

ARS

JOURNAL

LOS ANGELES PUBLIC LIBRARY

A PUBLICATION OF THE AMERICAN ROCKET SOCIETY

OCT 2 1961

VOLUME 31 NUMBER 9

SEPTEMBER 1961

BIND

EDITORIAL

Martin Summerfield: Ten Years as Editor Theodore von Kármán 1182

SURVEY ARTICLE

The Fuel Cell in Space H. A. Liebhafsky and W. T. Grubb Jr. 1183

CONTRIBUTED ARTICLES

Internal Animal Telemetry: a Feasibility Test Program
Ben L. Ettelson, Wilfred N. Cooper, Merle A. Beaupre, Toby Freedman,
Laurance G. Throssell and Bruce Pine 1190

Reactor Heat Removal Limitations of Nuclear Rockets George Yasui 1195

Experimental Study of Flow and Separation in Vortex Tubes With Application
to Gaseous Fission Heating J. J. Keyes Jr. 1204Magnetic Damping of the Angular Motions of Earth Satellites
Robert E. Fischell 1210Hodograph Analysis of the Orbital Transfer Problem for Coplanar Nonaligned
Elliptical Orbits Samuel P. Altman and Josef S. Pistiner 1217Planar Motions About an Oblate Planet
Maurice L. Anthony and George E. Feedich 1225

Interplanetary Maneuvers Using Radial Thrust C. M. Petty 1233

Satellite Orbit Sustaining Techniques Richard W. Bruce 1237

Recording of Pressure Step Functions of Low Amplitude K. Posel 1242

The Traveling-Wave Pump Eugene E. Covert and Charles W. Haldeman 1252

Effect of Glass Fiber Geometry on Composite Material Strength James E. Ball 1260

Use of Binary Light Metal Mixtures and Alloys as Additives for Solid
Propellants A. W. Blackman and D. E. Kuehl 1265

TECHNICAL NOTES

Low Thrust Orbit Penalty Paul D. Arthur 1273

Rocket Nozzle as Temperature Indicators Y. Benkin and D. C. Schell 1276

Burning Rates of Composite Solid Propellants at Subatmospheric Pressure Harry Sils 1277

Direct Thrust and Efficiency Measurements of a Continuous Plasma Accelerator
Stargo T. Demetriades and Richard W. Ziemer 1278

Time Relationships for Interplanetary Trajectories Werner M. Pauson 1281

Summary of Solid Propellant Residual Thrust Studies J. A. Morris 1283

Plateau Ballistics in Nitrocellulose Propellants R. F. Prochel 1286

Practical Methods for Compensation of Erosive Pressure Peaks William C. Stone 1288

Nonuniform Deceleration of a Slender Cone in Supersonic, Transonic and Subsonic Flight Cheng-Ting Hsu 1289

DEPARTMENTS

Technical Comments 1292

Patents 1293

Book Notes 1295

Technical Literature Digest 1296

RUSSIAN SUPPLEMENT...1305-1360

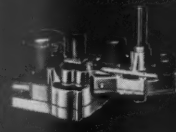
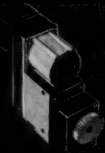
*Exclusive with Lear**



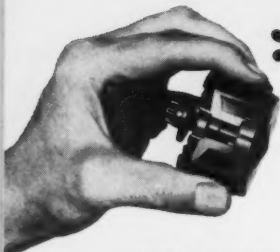
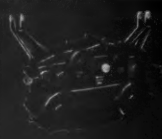
LEAR ELECTRIC SERVOS



Model 1000
1000 RPM
1/2" x 1" x 1" (approx.)



Model 1000
1000 RPM
1/2" x 1" x 1" (approx.)



**LEAR
MAGNETIC
POWDER
CLUTCH**

Unmatched reliability and performance for smooth, precise, fast-response control and transmission of mechanical power in all environmental extremes.

EM-8

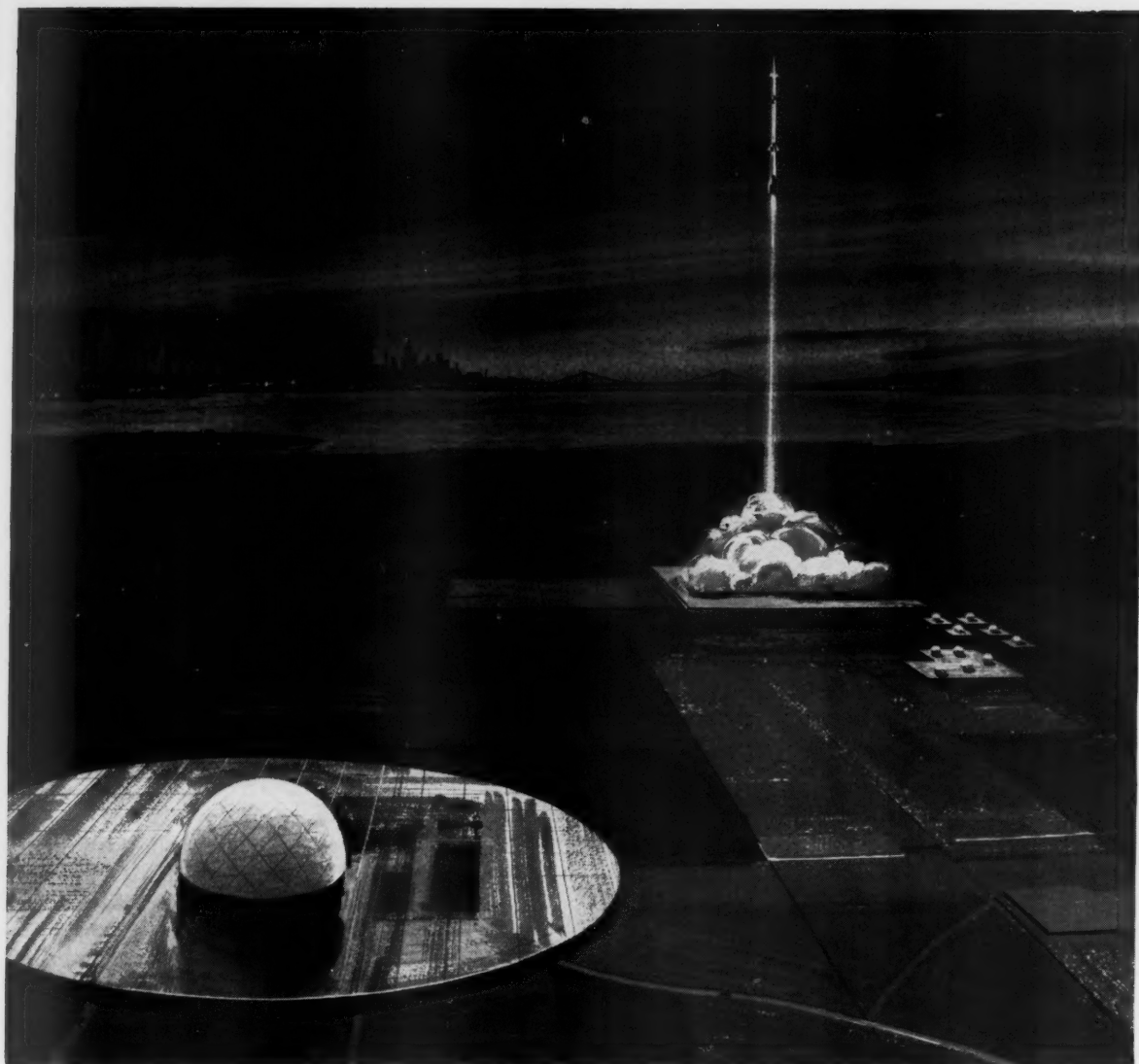
"OFF-THE-SHELF" VERSATILITY — Lear produces electric motors by the million...clutches by the thousands...and almost limitless assemblies of precision gearing. *Here is exceptional in-house availability* — a wide range of ratings and configurations of interchangeable building-blocks for fast, economical production of electric servos — truly, "off-the-shelf" versatility. Aerospace applications include sub-miniature types for instruments and computers; control surface actuation for aircraft, drones and missiles; positioning of gimbal-mounted rocket engines; telemetry tracking; and many other exacting control/actuation projects requiring high frequency response with *exceptional* accuracy, reliability, and environmental capabilities.



WRITE OR TELEPHONE FOR
SERIES SPECIFICATIONS TO:

LEAR

ELECTRO-MECHANICAL DIVISION
110 IONIA AVE. N. W., GRAND RAPIDS, MICH.



More than 450,000 pounds of thrust lifts the U. S. Army's Nike Zeus missile skyward in a cloud of vapor. The Nike Zeus missile being developed for the project by the Douglas Aircraft Company will be designed to intercept ballistic missiles traveling over 15,000 miles per hour, and destroy them at a safe distance from the defended area.

How do you stop an ICBM?

How do you detect, track, intercept—and destroy within minutes—an ICBM that is moving through outer space ten times faster than a bullet?

Bell Telephone Laboratories may have designed the answer: Nike Zeus, a fully automated system designed to intercept and destroy all types of ballistic missiles—not only ICBM's but also IRBM's launched from land, sea or air. The system is now under development for the Army Ordnance Missile Command.

Radically new radar techniques are being developed for Nike Zeus. There will be an acquisition radar designed to detect the invading missile at great distances. And a discrimination radar designed to distinguish actual war-

heads from harmless decoys that may be included to confuse our defenses.

The system tracks the ICBM or IRBM, then launches and tracks the Nike Zeus missile and automatically steers it all the way to intercept the target. The entire engagement, from detection to destruction, would take place within minutes and would span hundreds of miles.

Under a prime Army Ordnance contract with the Western Electric Company, Bell Laboratories is charged with the development of the entire Nike Zeus system, with assistance from many subcontractors. It is another example of the cooperation between Bell Laboratories and Western Electric for the defense of America.

BELL TELEPHONE LABORATORIES

World center of communications research and development



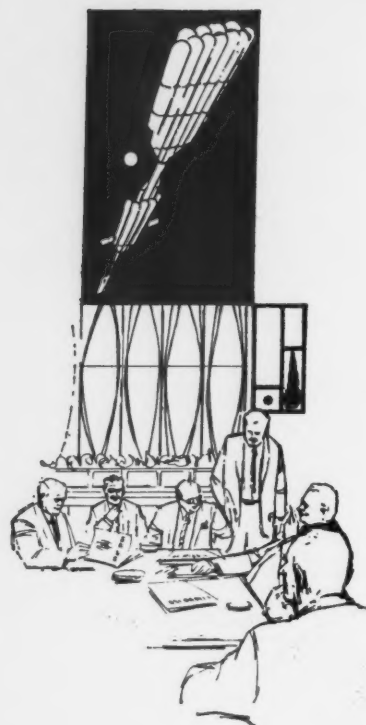
New York Coliseum

October 9-15, 1961

AMERICAN ROCKET SOCIETY

SPACE FLIGHT REPORT

TO THE NATION



Through the medium of the ARS SPACE FLIGHT REPORT TO THE NATION, the American Rocket Society, during the week of October 9-15, 1961, in New York Coliseum, will present a thorough and comprehensive review of the U. S. space program.

The SPACE FLIGHT REPORT TO THE NATION will present for the first time under one roof a complete review of the most significant work being done in each of the major technical disciplines contributing to current progress in rocketry, missiles, and space flight, and one of the largest and most extensive technical exhibits ever undertaken in these fields.

More than 300 technical papers will detail major space projects; will explore problems that must be solved to insure further, faster progress; and will stimulate penetrating discussions by outstanding authorities in the audience.

There will be three floors of technical exhibits and displays by more than 350 manufacturers, suppliers, engineering organizations, and governmental agencies, disclosing latest achievements, concepts, products, and ideas.

ARS SPACE FLIGHT REPORT TO THE NATION will present:

- Under one roof, at one time, in one place the most comprehensive review of all the contributing technologies to the U. S. space effort.

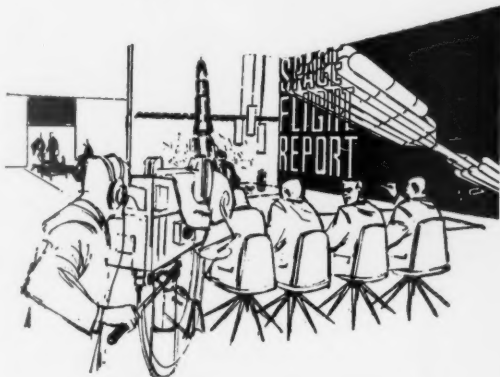
- Forty-two specialized technical sessions, all on the same floor with comfortable lounge areas and conference rooms for informal discussions.

- Three unique Space Flight Report panels that will explore and interpret space missions, space vehicles, and the global impact of space events for the technical community at large.

- A new exhibiting technique called "Exhibiting in Depth", permitting for the first time 3-dimensional displays with the main aisle running *through* the booths instead of by them.

- Main exhibit organized by NASA and DOD, representing U. S. space capability, which will be 88'x50' in floor area and will extend 60' into the air.

- The history, purposes, and plans of ARS graphically displayed in a booth designed by Raymond Loewy.



For further information about reservations, program information or exhibit space contact

ARS SPACE FLIGHT REPORT TO THE NATION

American Rocket Society

500 Fifth Ave., New York 36, N. Y.

Honorary Committee

Wernher von Braun, Chairman

Harold Boyer

Detlev W. Bronk

Overton Brooks

Milton U. Clauser

James R. Dempsey

Gen. James H. Doolittle

C. Stark Draper

Hugh L. Dryden

Trevor Gardner

Mrs. Robert H. Goddard

Harry F. Guggenheim

Willis M. Hawkins

Rear Adm. John T. Hayward

Samuel K. Hoffman

Robert H. Jewett

Arthur Kantrowitz

Dan A. Kimball

Maj. Gen. John B. Medaris

George F. Metcalf

Maj. Gen. Don R. Ostrander

William H. Pickering

Richard W. Porter

Simon Ramo

Harold W. Ritchey

Lt. Gen. Bernard A. Schriever

Howard S. Seifert

Abe Silverstein

Col. John P. Stapp

George P. Sutton

Maj. Gen. Holger N. Toftoy

George S. Trimble, Jr.

Lt. Gen. Arthur G. Trudeau

Harold Urey

Theodore von Karman

Alan Waterman

Elmer P. Wheaton

Herbert F. York

ARS JOURNAL

A PUBLICATION OF THE AMERICAN ROCKET SOCIETY

EDITOR Martin Summerfield
ASSOCIATE TECHNICAL EDITOR Irvin Glassman
MANAGING EDITOR Margaret Sherman
STAFF EDITOR Barbara Nowak
ART EDITOR John Culin

ASSOCIATE EDITORS

Igor Jurkevich, G. E. Space Sciences Laboratory, Russian Supplement;
 George F. McLaughlin, Patents; Charles J. Mundo, Jr., Raytheon Co.,
 Guidance; Bernard H. Paiewonsky, Aeronautical Research Associates
 of Princeton, Flight Mechanics; M. H. Smith, Princeton University,
 Technical Literature Digest

ASSISTANT EDITORS

Carol Falcetti, Eleanor Rosman, Carol Rubenstein

DIRECTOR OF MARKETING

Owen A. Kean

ADVERTISING PRODUCTION MANAGER

Walter Brunke

ADVERTISING REPRESENTATIVES

New York

D. C. Emery and Thomas Harford
 400 Madison Ave., New York, N. Y.
 Telephone: Plaza 9-7460

Chicago

Thomas M. Bryne, Jr.
 2316 Sherman Ave., Evanston, Ill.
 Telephone: 869-1831

Atlanta

Joe H. Howell
 1776 Peachtree Bldg., Atlanta, Ga.
 Telephone: 873-2136

Los Angeles

James C. Galloway and Co.
 6335 Wilshire Blvd., Los Angeles, Calif.
 Telephone: Olive 3-3223

London

B. C. Nichols
 151 Fleet St.
 London E. C. 4, England

American Rocket Society

500 Fifth Avenue, New York 36, N. Y.

Founded 1930

OFFICERS

President	Harold W. Ritchey
Vice-President	William H. Pickering
Executive Secretary	James J. Harford
Treasurer	Robert M. Lawrence
General Counsel	Andrew G. Haley
Director of Publications	Irwin Hersey

BOARD OF DIRECTORS

(Terms expire on dates indicated)

Ali B. Cambel	1962	Samuel Herrick	1963
Richard B. Canright	1962	Arthur Kantrowitz	1963
William J. Cecka, Jr.	1963	A. K. Oppenheim	1961
James R. Dempsey	1961	Simon Ramo	1963
Herbert Friedman	1962	David G. Simons	1961
George Gerard	1961	John L. Sloop	1961
Robert A. Gross	1962	Martin Summerfield	1962
Abe M. Zarem	1963		

TECHNICAL COMMITTEES AND CHAIRMEN

Aerodynamics , Robert M. L. Baker, Jr.	Physics of the Atmosphere and Space , Herbert Friedman
Communications and Instrumentation , Frank W. Lehan	Power Systems , John H. Huth
Electric Propulsion , Ernst Stuhlinger	Propellants and Combustion , Peter L. Nichols, Jr.
Guidance and Control , James S. Farrior	Ramjets , William H. Avery
Human Factors and Bioastronautics , Eugene B. Konecki	Solid Propellant Rockets , G. Daniel Brewer
Hypersonics , William H. Dorrance	Space Law and Sociology , Andrew G. Haley
Liquid Rockets , Martin Goldsmith	Structures and Materials , George Gerard
Magnetohydrodynamics , Milton M. Slawsky	Test, Operations, and Support , Bernhard L. Dorman
Missiles and Space Vehicles , William M. Duke	Underwater Propulsion , Herman E. Sheets
Nuclear Propulsion , Robert W. Bussard	

Scope of ARS JOURNAL

This Journal is devoted to the advancement of astronautics through the dissemination of original papers disclosing new scientific knowledge and basic applications of such knowledge. The sciences of astronautics are understood here to embrace selected aspects of jet and rocket propulsion, spaceflight mechanics, high speed aerodynamics, flight guidance, space communications, atmospheric and outer space physics, materials and structures, human engineering, overall system analysis and possibly certain other scientific areas. The selection of papers to be printed will be governed by the pertinence of the topic to the field of astronautics, by the current or probable future significance of the research, and by the importance of distributing the information to the members of the Society and to the profession at large.

Information for Authors

Manuscript must be as brief as the proper presentation of the ideas will allow. Exclusion of dispensable material and conciseness of expression will influence the Editors' acceptance of a manuscript. In terms of standard-size double-spaced typed pages, a typical maximum length is 22 pages of text (including equations), 1 page of references, 1 page of abstract and 12 illustrations. Fewer illustrations permit more text, and vice versa. Greater length will be acceptable only in exceptional cases.

Short manuscripts, not more than one quarter of the maximum length stated for full articles, may qualify for publication as Technical Notes or Technical Comments. They may be devoted to new developments requiring prompt disclosure or to comments on previously published papers. Such manuscripts are published within a few months of the date of receipt.

Sponsored manuscripts are published occasionally as an ARS service to the industry. A manuscript that does not qualify for publication, according to the above-stated requirements as to subject, scope or length, but which nevertheless deserves widespread distribution among jet propulsion engineers, may be printed as an extra part of the Journal or as a special supplement, if the author or his sponsor will reimburse the Society for actual publication costs. Estimates are available on request. Acknowledgment of such financial sponsorship appears as a footnote on the first page of the article. Publication is prompt since such papers are not in the ordinary backlog.

Manuscripts must be double spaced on one side of paper only with wide margins to allow for instructions to printer. Include a 100 to 200 word abstract. State the authors' positions and affiliations in a footnote on the first page. Equations and symbols may be handwritten or typewritten; clarity for the printer is essential. Greek letters and unusual symbols should be identified in the margin. If handwritten, distinguish between capital and lower case letters, and indicate subscripts and superscripts. References are to be grouped at the end of the manuscript and are to be given as follows. For journal articles: Authors first, then title, journal, volume, year, page numbers; for books: Authors first, then title, publisher, city, edition and page or chapter numbers. Line drawings must be clear and sharp to make clear engravings. Use black ink on white paper or tracing cloth. Lettering should be large enough to be legible after reduction. Photographs should be glossy prints, not matte or semi-matte. Each illustration must have a legend; legends should be listed in order on a separate sheet.

Manuscripts must be accompanied by written assurance as to security clearance in the event the subject matter lies in a classified area or if the paper originates under government sponsorship. Full responsibility rests with the author.

Preprints of papers presented at ARS meetings are automatically considered for publication.

Submit manuscripts in duplicate (original plus first carbon, with two sets of illustrations) to the Managing Editor, ARS JOURNAL, 500 Fifth Avenue, New York 36, N. Y.

ARS JOURNAL is published monthly by the American Rocket Society, Inc. and the American Interplanetary Society at 20th & Northampton Sts., Easton, Pa., U. S. A. Editorial offices: 500 Fifth Ave., New York 36, N. Y. Price: \$18.00 per year, \$3.00 per single copy. Second-class postage paid at Easton, Pa., with additional entry at New York, N. Y. This publication is authorized to be mailed at the special rates of postage prescribed by Section 132.122. Notice of change of address should be sent to the Secretary, ARS, at least 30 days prior to publication. Opinions expressed herein are the authors' and do not necessarily reflect the views of the editors or of the Society. © Copyright 1961 by the American Rocket Society, Inc.

HOW TO TURN LIGHT INTO MICROWAVES

Led by physicist Vernon Derr, a research team investigating optical pumping of vapors at The Martin Company in Orlando, Florida, made theoretical calculations on the energy levels of various elements — including the highly active cesium. ■ Dr. Derr felt that, if their conclusions were correct, an input solely of visible light could make cesium emit microwave energy with the strength and precision needed to power an ultrastable frequency source. Others had made the transition from light to microwaves, but always with the addition of a supplementary rf signal. ■ In less than six months, a special development group set up to check Derr's approach began to get results: light from a cesium lamp directed into a resonant cavity containing cesium vapor produced a coherent microwave signal. ■ *This — the first continuous conversion of light into microwaves — is a product of the creative environment that exists for scientists and engineers at Martin in Florida.*



MARTIN
ORLANDO

Scientific firsts like this are achieved when management backs up creative research with sound development programs. At The Martin Company in Florida there is a continuing need for engineers and scientists with the professional ability to help push forward technological frontiers. ■ For information about your place in one of our six major missile and electronics systems — or in our advanced programs, write:

C. H. Lang, The Martin Company, Orlando 61, Florida.

Immediate technical staff openings include:

GUIDANCE & CONTROL SYSTEMS / HIGH RESOLUTION RADAR / FLUID DYNAMICS / AEROSPACE DYNAMICS / INFORMATION THEORY / COMMUNICATIONS / DIGITAL COMPUTER RESEARCH / HUMAN FACTORS / OPERATIONS RESEARCH / WEAPONS SYSTEMS ANALYSIS
All qualified applicants will receive consideration for employment without regard to race, creed, color or national origin.

Martin Summerfield: Ten Years as Editor



Scientific and technical journals can be numbered in the thousands in the world today. Some are good, some are poor, only a few are outstanding. As one looks back over the development of science and technology since the Renaissance, one finds that certain fields of endeavor occasionally experienced explosive growth—like novae in the sky. The methods of communicating ideas and new knowledge during such extraordinary times assume very great importance. In spite of the great progress we have made in information theory, data handling and communication, the printed word is still the most effective method, and the periodic journal the most rapid vehicle, for diffusing complex material.

Space flight engineering, and the sciences and industry it nourishes, is without question of the nova category, which would lead one to the expectation of finding an outstanding journal as one of its manifestations. There is no doubt in my mind that ARS JOURNAL is that journal.

Although the circumstances were favorable for the creation of an outstanding journal for the Society, the fact that it has achieved such a position in the world depends finally on the guiding hand of its editor.

A journal of highest quality with an agreeable style of presentation and sustained vigor does not just happen. It is the achievement of someone who has a deep understanding of the field to be served, of someone who has the persistence to find good manuscripts and to stimulate authors to prepare them, of someone with the strength to refuse poor manuscripts and to accept manuscripts with novel ideas. Furthermore, it is the result of continuous effort of meeting and talking with people who work within the domain of the journal, of getting along with and listening to those who formulate long- and short-term publication policies, of maintaining a spirit of good cooperation among those directly concerned with the journal's production. And, especially in our time, it requires one who is able to placate the spectre of secrecy without allowing the breath of science to be strangled by the lack of free flow of new information.

In Martin Summerfield, the American Rocket Society has been fortunate to find an Editor who has these attributes. He has grown up with and contributed in good measure to the basic research upon which rests the development of rocket power and astronautics in America. In 1940, he became a part of the "Galcit Project," the nucleus at the California Institute of Technology from which have flowered both the Jet Propulsion Laboratory and the Aerojet-General Corporation. He has made important contributions to the theory and design of liquid- and solid-propellant rocket engines, and in recent years has been particularly concerned with combustion problems. In 1945, he wrote with Frank J. Malina a paper on "The Problem of Escape from the Earth by Rocket" which is recognized as a classic in the literature on step-rockets.

In 1949, I became Chairman of the Editorial Board of the 12-volume series *High Speed Aerodynamics and Jet Propulsion*; then I invited Dr. Summerfield to become the first general editor of the series, which was to be published by the Princeton University Press. He played a large part in formulating the scope and content of the series and also wrote the section on the liquid-propellant rocket engine in Volume XII.

As Professor of Jet Propulsion and Aeronautical Engineering at Princeton University, he has actively pursued his own research and devoted much time and thought to the teaching of advanced courses in jet propulsion. The challenge to the nation of modernizing higher education has in recent years been of much concern to him.

This month marks the Tenth Anniversary of Dr. Summerfield's editorship of the JOURNAL since he took over as Editor-in-Chief with the September 1951 issue. During his ten years as Editor, the Society has grown in membership from 1600 to 19,000 members, and nonmember subscriptions to the JOURNAL have increased from 250 to 2100. One criterion for judging the quality of a journal is the number of subscriptions above the membership of a society and its international circulation. There is no doubt that by this criterion alone ARS JOURNAL is the outstanding journal of its kind in the world today.

The statement of the fact that knowledge has no national frontiers cannot be repeated too often. Foreign authors have been welcomed to appear on the pages of ARS JOURNAL. The introduction into the JOURNAL in 1959 of translations from the Russian language of important articles by Soviet authors has been an important contribution to the development of the astronautical sciences.

It is interesting to note that, when Martin Summerfield took over the editorship of the JOURNAL in 1951, there were many in the Society who resisted the publication of articles dealing with space flight. However, at the meeting of the Directors of the Society in November of that year, Andrew G. Haley took a strong stand in favor when he stated that he felt "there was no irreconcilable difference between the present engineering problems in the rocket field and future developments in the astronautical field." He felt that the American Rocket Society had to have a reason for its future existence, and space travel provided this. Also, H. R. J. Grosch, President of the Society, stated: "It is obvious that the engineering problems presented in the JOURNAL are essential and must be continued in an effort to do our part in the defense program, but it would be a mistake to completely exclude consideration of the long-term project—space travel. We must definitely not shirk our responsibilities to the rocket field, but we must keep this long-term project in mind—for instance, such things as satellite stations, space ships, interplanetary travel, etc."

In ten short years after this debate, the JOURNAL finds itself bringing to its readers articles which will help to achieve the national goal of placing a man on the moon within the next ten years!

One can be sure that ARS JOURNAL, under the editorship of Martin Summerfield, will keep pace with the rapid growth of the scientific and technological knowledge in the fields of rocketry and space flight. I am sure, too, that it is on behalf of all members of the Society, editors and readers, that we wish him good health and vigor for his future activities.

Theodore von Kármán
(With the cooperation of
Frank J. Malina)

The Fuel Cell in Space

H. A. LIEBHAFSKY
and W. T. GRUBB Jr.

General Electric Research
Laboratory
Schenectady, N. Y.

OF THE methods of energy conversion currently receiving renewed, major research attention (1),¹ three, power sources, represented by the thermionic converter, the thermoelectric generator, and the fuel cell, are particularly attractive for possible use in space. Such power sources must above all be reliable, otherwise the electrical equipment will not function properly and satisfactory communication cannot be maintained. They must have at least the needed life, which will be short in a rocket but long in a satellite. Power sources should be light and compact, e.g., a saving of 1 lb in the weight of an orbiting satellite may reduce the weight of propulsion vehicle and fuel required for launching by 50 to 1000 lb.

The fuel cell is a promising power source of great versatility. It can serve as a primary converter of chemical energy or as a component of systems into which other kinds of energy (heat, solar, nuclear) are introduced and stored to be consumed as electricity when needed. Compact and flexible as to form, it gives promise of simplicity, high efficiency and long life. It uses fuels of high energy. In certain modifications, it is light and adaptable to gravity free operation.

As yet, the emphasis in the preceding paragraph must be upon "promising." Because more research and development activity will be directed toward fuel cells during the next decade than has been in all their long previous history, rapid progress is assured. Yet it is well to remember that other power sources are also receiving greatly increased attention, and that fuel cells will have to compete for space applications against devices—even long established devices such as conventional batteries—that are still being developed.

Received June 14, 1961.

¹ Numbers in parentheses indicate References at end of paper.

Fuel Cell Described

In the current literature, "fuel cell" is used indiscriminately to include many electrochemical devices. The following definition will apply here: A fuel cell is an electrochemical device in which energy of reaction between a conventional fuel and oxygen is converted directly and usefully into low voltage d-c electrical energy. Individual fuel cells when combined in parallel or in series make fuel batteries; here the term "fuel battery" will not be used.

Fuel cells differ from ordinary batteries in several important ways. Ordinary batteries store in themselves the chemical energy to be converted; the substances these batteries consume at anodes (e.g., zinc, magnesium, or lead) are not really fuels—certainly not conventional fuels.

Ordinary batteries, both primary and secondary, can deliver large amounts of electricity in sudden discharges because they convert chemical energy stored within them. The fuel cell cannot do this because it is the converter alone; fuel and oxygen must be brought to it just as they must be brought to a central station generating electricity. Consequently, fuel cells will have greatest advantage over ordinary batteries when loads are moderate and long continued.

As ordinary batteries do not consume conventional fuels, it follows that the electrochemical reactions at their anodes are greatly different from those at the anodes of fuel cells. In general, there is also a great difference at the cathodes. In ordinary batteries, the substance reduced is usually a compound—manganese dioxide, lead dioxide, silver oxide—but in fuel cells it is always the element oxygen, either as such or as a constituent of air.

Conventional fuels are the fossil fuels, coal and hydrocarbons found in nature, and substances easily derived therefrom, such as hydrogen, carbon monoxide, and the simpler

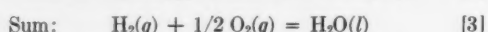
Dr. Herman A. Liebhafsky is manager of the Physical Chemistry Section of the General Electric Research Laboratory in Schenectady, N. Y. He joined the staff of the Laboratory in 1934 and assumed his present position in 1951. His fields of specialization are physical and analytical chemistry. Dr. Liebhafsky received his B.S. from Texas A & M, his M.S. from the University of Nebraska, and his Ph.D. from the University of California, where he was a member of the faculty from 1929 to 1934. During World War II, he served as a technical observer for the Armed Forces in the European Theater of Operations. He is the author of more than 100 scientific papers and is an authority on the use of X rays in chemical analysis, a field in which he is coauthor of a recent book.

Dr. Willard Thomas Grubb studied chemistry at Harvard University, where he was a member of Phi Beta Kappa, receiving his B.S. summa cum laude in 1946. After receiving a Ph.D. in physical chemistry from Harvard in 1949, he joined the General Electric Research Laboratory, where he has engaged in research in several fields including polymers, ion exchange membranes, and fuel cells. Dr. Grubb holds the basic patent on the ion exchange membrane fuel cell and is the author of 15 papers.

alcohols. In general, the cheapest fuels are the most abundant, but cheap fuels tend to react sluggishly at fuel cell anodes, especially if the fuels are solid. Fortunately, even the most costly conventional fuel is economical for space applications, and it is thus unnecessary to discuss here the difficult problem of using coal, carbon monoxide, or natural gas (methane). The other hydrocarbons, hydrogen, alcohols, and similar compounds are available for use in space.

Fig. 1 shows a simple fuel cell close to practical realization. Some years ago Grubb (2,3,4) introduced ion exchange membranes as the sole electrolytes in various devices, fuel cells included. In acid membranes, only the hydrogen ion carries current, since no other ion is free to move. Niedrach (5) succeeded in raising the current density in hydrogen fuel cells incorporating such electrolytes; further development was reported by Oster (6).

As all fuel cells, the one in Fig. 1 consists of an anode and a cathode with an electrolyte between. The reactions are



Abbreviations: e^- , electrons; g , gas; l , liquid

The directness of the fuel cell is its main attraction. There is nothing random about the principal processes in the ideal fuel cell. The electrons want to leave the fuel at the anode (Reaction [1]) and to be captured by oxygen at the cathode (Reaction [2]), and they are willing to work en route. Contrast this simplicity with what happens in the present central stations. The chemical energy is randomized as heat when the fuel is burned under the boiler. But work is a directed process, and to acquire the needed direction, which in the fuel cell is never lost, steam must be put through a guided expansion, as in a turbine. Carnot discovered the price that must be paid when heat (random) is converted into work (directed). The fuel cell escapes this penalty; it is not Carnot cycle limited.

The fuel cell can thus convert the energy of the reaction



directly into electrical energy, bypassing wasteful intermediate conversion into heat. The maximum useful obtainable work (here, electrical) ΔG is related to the reversible electromotive force E_r of the fuel cell

$$\Delta G = -E_r It \quad (\text{the minus sign is arbitrary}) \quad [5]$$

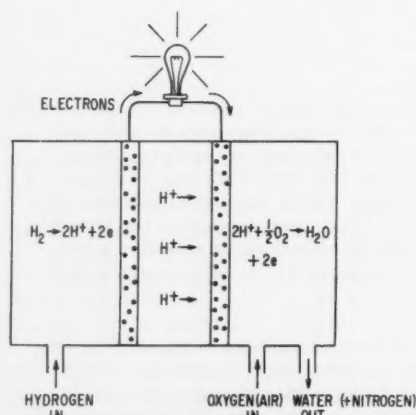


Fig. 1 Schematic cross-section diagram of ion exchange membrane fuel cell

In Eq. 5, E_r is the electromotive force of the fuel cell in which Reaction [4] is being carried out isothermally and reversibly to deliver a current I for the time t required to consume 1 mole of fuel. The ideal efficiency is

$$\eta_i = -E_r It / \Delta H \quad [6]$$

where ΔH is the heating value, usually the higher heating value, of 1 mole of fuel. E_r is the maximum driving force available to send electrons from anode to cathode in Fig. 1. The energy changes in the various Reactions [4] limit E_r to about 1 v.

Actual Operation

In a fuel cell under load, the actual electromotive force E_a will drop below E_r for some or all of these reasons:

- 1 An unwanted reaction may be occurring at anode or cathode (or elsewhere in the cell).
- 2 Hindrance to reaction at anode or cathode.
- 3 Concentration gradients in the electrolyte.
- 4 I^2R heating in the electrolyte.

The actual efficiency of the fuel cell is

$$\eta_a = -E_a It / \Delta H \quad (\text{see Eq. 6}) \quad [7]$$

In general, the three quantities in the numerator above are dependent variables. The difference between the useful work in actual operation $-E_a It$ and the maximum useful work in reversible isothermal operation $-E_r It$ must appear as rejected heat. The rejected heat q (see Table 1) is an important design parameter, particularly in space applications.

Performance Requirements

In an ideal fuel cell, maximum performance is obtained under convenient conditions for maximum time. This can be translated into more scientific terms.

Obviously I^2R losses should be minimized. To this end electrodes must be close spaced, and the electrolyte must have high ionic and negligible electronic conductivity.

The other less obvious but important performance requirements are conveniently grouped under two headings: reactivity requirements and invariance requirements.

Reactivity Requirements

An ideal fuel cell will satisfy the following reactivity requirements:

1 Proper stoichiometry: complete oxidation of fuel; H_2O and/or CO_2 the only substances formed in the usual case.

2 High and unimpeded electrode reactivity: high current density, E_a/E_r approaching unity.

It will be noticed that the reactivity requirements relate to the rates and mechanisms of electrode reactions. In more detail:

1 Practical fuel cells have maximum voltages not much different from 1 v. Voltages may be disregarded in discussing proper stoichiometry. The quantity of electricity from one mole of fuel, $I \cdot t$, will not be a maximum unless the fuel is oxidized to CO_2 and/or H_2O . For example, carbon oxidized to CO yields only 2 Faradays of electricity per mole instead of the 4 that pass through the circuit if CO_2 is produced at the anode. Therefore, other things equal, only half as much useful work will be done in the former case. Thus, maximum performance requires proper stoichiometry.

2 High and unimpeded electrode reactivity will naturally bring high current density with it. But if I^2R losses are low, it will also make possible a close approach of E_a to E_r , the maximum possible electromotive force, which is attained only in a cell operating reversibly.

The current density I/A (A is electrode area) is of par-

Table 1 Operating data for 100-w hydrogen ion exchange membrane fuel cell^c

Current density, amp/ft ²	E_a , v	I , amp	t , ^a hr	$E_a It$, ^b cal	η_a , ^c	q , ^d cal	D , ^e
10	0.82	122	0.44	37,850	0.55	30,470	81
25	0.70	143	0.375	32,250	0.47	36,070	112

^a Hours to consume 1 mole (2 gm) of hydrogen. See Eqs. 6 and 7.

^b 1 w-hr = 860 cal.

^c The higher heating value of hydrogen at 25 °C is $\Delta H = 68,320$ cal. See Eqs. 6 and 7.

^d Note that the rejected heat q is the difference between ΔH and $E_a It$. D is the rate of heat rejection in watts.

^e Data on the characteristics of ion exchange membrane fuel cells were supplied by D. L. Douglas, Manager, Fuel Cell Engineering, Aircraft Accessory Turbine Dept., General Electric Co., Lynn, Mass.

ticular importance in space applications because it has an important influence on the size and weight of the cell. As will appear later, one cannot arbitrarily say that a fuel cell ought to operate at the highest possible current density. Each fuel cell parameter must be a compromise, and good design must ensure that each compromise be the best for the application under consideration.

The chief ways of meeting reactivity requirements are by increasing the gas electrode electrolyte interface, such as by using porous electrodes; by using catalysts, either as electrode materials or incorporated in them; by raising pressure; by raising temperature; and, particularly for space applications, by proper choice of fuel.

Invariance Requirements

The fuel cell is solely a converter of energy. The converter, to start with, should be built as well as possible, and should remain invariant to insure long life. Invariance, or long life, requirements are:

- 1 No corrosion or side reactions.
- 2 Invariant electrolyte.
- 3 No change in electrodes.

The invariance requirements are more drastic and less obvious than might appear. A few examples follow. In the hydrogen fuel cell of Fig. 1, diffusion of hydrogen through the electrolyte could lead to undesirable side reactions; mixing of fuel and oxygen ought always to be avoided. Catalysts can be poisoned. The pores in porous ("gas diffusion") electrodes can become filled with too much liquid, gas, or extraneous materials; in any such case, they are put out of action. If the wrong ions carry current, the electrolyte will not remain invariant, and the anode and cathode reactions (only fuel oxidized at anode; only oxygen reduced at cathode) may be thrown out of balance. In general, invariance requirements are met by a proper choice of materials and of operation conditions.

Reactivity and invariance requirements are interrelated. If, for example, one must go to high temperatures to obtain high reactivity, it will usually be more difficult to keep the fuel cell invariant.

The ultimate goal of fuel cell research would seem to be a cell in which a cheap hydrocarbon, say methane or propane, is consumed at room temperature and pressure, all invariance and reactivity requirements being met. No fuel cell today achieves this goal. But encouraging progress is being made; in general, gains made with hydrogen are subsequently applied to hydrocarbons.

Particularly striking is the great improvement in gas diffusion electrodes. Here high porosity provides an extended interface at which electrode, gas, and electrolyte meet, i.e., Grove's "notable surface of action" (7). The difficulties indicated above for these electrodes have been greatly mitigated by Bacon (8), Justi (9) and others by building them of two layers differing in pore size, the layer facing the elec-

trolyte having the smaller pores. The gas enters the larger pores, and the reactive interface is near the junction of the two layers within the electrode.

In the case of carbon gas diffusion electrodes, outstanding progress (10) has resulted from incorporating catalysts into electrodes of controlled porosity on which water repellent materials act as an adjunct to prevent filling of the pores with electrolyte.

Hydrocarbons in cells with aqueous alkaline electrolytes can lead to serious lack of electrolyte invariance. Anodic oxidation of the hydrocarbons yields products such as CO_2 that react with these electrolytes. A cheap and simple remedy, i.e., a suitable way of regenerating a spent electrolyte, is badly needed.

The Esso Research and Engineering Co. (11) has made welcome progress in the anodic oxidation of hydrocarbons. Ethane has been oxidized almost completely to carbon dioxide and water, an experimental value of 13.8 having been obtained for n , the number of Faradays per mole, as against a theoretical value of 14. At these conversions, the sustained current density was 7 amp/ft² and the open circuit voltage was 0.92 v.

Efficiency, Current Density and Rejected Heat

When small currents are drawn, values of η_a will approach those of η in a good fuel cell; this means that efficiencies above, say 0.80, can be realized. But high efficiency at low current density is a will-o'-the-wisp because one cannot usually afford to build an outrageously large fuel cell. Consequently, efficiencies must never be dissociated from the corresponding current densities. At the higher current densities, say above 50 amp/ft², efficiencies η_a are usually between 0.40 and 0.70; this is still very good in comparison with those of most other power sources.

One might be tempted to conclude that the efficiencies just quoted give the fuel cell a marked advantage over the thermoelectric generator and the thermionic converter, for each of which the Carnot cycle efficiency is an upper limit not yet reached. But efficiency is only one factor, and decisions cannot be based on it alone.

As an illustrative example, consider two 100-w hydrogen ion exchange membrane fuel cells for a space ship. For such cells, the data in Table 1 might apply. At the higher current density, the cell is smaller, but it uses fuel, and oxygen, at a higher rate than at the lower current density with its concomitant higher efficiency. Further, there is more rejected heat in the former case, and this heat will be rejected in a smaller volume.

The simplicity of the illustrative example is deliberate. It is intended to emphasize the lack of knowledge on which sound decisions can be based. For example, the following are among the things one needs to know in order to decide between the two cells described above: operating life at each

current density; the extent to which rejected heat must be disposed of, and by what means; the relative weights and volumes of the complete fuel cell assemblies. The cell areas, which are in the ratio of about 2.1 to 1, do not begin to tell the story. Anyone facing the design of an actual space vehicle is unlikely to find the fuel cell literature overburdened with useful data.

It should be noted that the fuel cell is not the only source of rejected heat. Much of the energy furnished by the cell and usefully employed for electronic and control systems also appears eventually as heat; this heat must also be rejected.

Present Status of Fuel Cell Development

Present day fuel cells, as tabulated in Tables 2 and 3, fall into three broad classes according to their operating conditions: Type 1, high temperature, low pressure; Type 2, moderate temperature, high pressure; Type 3, low temperature, low pressure. No work has been done on high temperature, high pressure cells because of the serious technical difficulties to be expected.

Performance data for fuel cells must be loosely interpreted. For one thing, nearly all cells listed are under continuing investigation with constant improvement. In addition, the performance of some cells, especially those of Type 1, can be varied over wide ranges by changing the operating temperature. The following performance data are guides to what has been done: Type 1, smaller than 100 w, continuous operation up to six months. Type 2, up to 5 kw, continuous operation over 1000 hr. Type 3 (Allis-Chalmers), 15 kw with continuous operation probably measured in hours. Type 3 (National Carbon), 100 w with continuous operation for more than a year.

Prime contenders for space power are Types 2 and 3. Type 3 has operational advantages deriving from the absence of elevated temperatures and elaborate pressure controls.

Problems of Gravity Free Operation

If gravity is absent, or if the gravitational field changes, it is difficult to keep fluid electrolytes where they belong, i.e.,

Table 2 Partial log of fuel cell activity

No.	Organization	Country	Type of fuel cell ^a	Remarks
1	G. E. Research Lab.	U.S.A.	1
2	Sondes Place Research Lab.	Great Britain	1
3	University of Amsterdam	Netherlands	1
4	Messrs. Marshall Ltd.	Great Britain	2	Cell developed by F. T. Bacon
5	Patterson-Moos (Div. of Leeson Corp.)	U.S.A.	2	U. S. Licensee of Bacon fuel cell patents
6	Esso Research Lab.	U.S.A.	2
7a	G. E. Research Lab.	U.S.A.	3	Units for military applications being built by departments
7b	G. E. Aircraft Accessory Turbine Dept.	U.S.A.	3
7c	G. E. Missile Space Vehicle Dept.	U.S.A.	3
8	National Carbon Co.	U.S.A.	3
9	Allis-Chalmers Co.	U.S.A.	3
10	STEAG, Ruhrchemie and T. H. Braunschweig	Germany	3	Research directed by E. Justi
11	Ionics, Inc.	U.S.A.	3

	Temperature	Pressure
^a Type 1	Above 300 °C	Approximately atmospheric
Type 2	100 to 300 °C	High (up to 600 psi)
Type 3	Below 100 °C	Approximately atmospheric

Table 3 Approximate data for fuel cells on Table 2

No. (see Table 2)	Electrodes	Electrolyte	Principal fuel (other fuels)	Current density ^a
1	porous metal	fused carbonates	H ₂ (CO)	low
2	porous metal	fused carbonates	H ₂ (CO, CH ₄)	low
3	porous metal	fused carbonates	H ₂ (CO, CH ₄)	low
4	porous metal	aqueous KOH	H ₂	high
5	porous metal	aqueous KOH	H ₂	high
6	porous metal	aqueous KOH	H ₂ , C ₂ H ₆	high
7	metal powder	ion exchange membranes	H ₂	low
8	activated porous carbon	aqueous KOH	H ₂	high
9	unpublished	unpublished	gas mixture said to be largely propane	low
10	porous metal	aqueous KOH	H ₂ (alcohols glycols)	high
11	unpublished	aqueous KOH between anion membranes	H ₂	low

^a low—below 100 amp/ft² at 0.8 v.
high—above 100 amp/ft² at 0.8 v.

between and in contact with the electrodes. Normally an electrolyte solution such as the sulfuric acid in an automobile battery takes the shape of the container (battery case) under the pull of gravity, and it remains as a continuous ionically conducting path between the electrodes as the acid fills the case from the bottom to a level surface which is determined by the total volume of liquid present. That this simple situation will not exist at zero gravity seems certain. In the absence of gravity, discontinuities in electrolyte path over part or all of the active area of the cell become possible. Leakage protection will be required all around the unit since the electrolyte is now as capable of flowing out at the top as of staying at the bottom. In a fuel cell, weightlessness could increase the risk of mixing gaseous fuel and oxygen, always undesirable and possibly fatal.

Most fuel cells now being considered for practical applications have a gas reacting at each electrode and have water formed as reaction product. Consequently, the problems of gravity free operation are likely to be more difficult with fuel cells than with primary or secondary batteries, both of which can be sealed and in which gases are usually involved only as products of undesirable side reactions.

A few obvious possibilities to help control the location of fluids in zero gravity are:

1 Use of rotational motion to produce forces to replace gravity (12).

2 Use of capillary action to prevent unwanted migration of electrolyte as is done in the double-layer gas diffusion electrodes.

3 Use of solid or quasi-solid electrolytes.

The third solution seems the best. Ion exchange membranes, as in No. 7, Tables 2 and 3, appear to be the only such electrolytes used in fuel cells today. Because these membranes are mechanically coherent, and because satisfactory operation of the electrodes is not contingent upon the establishment of a particular gas-liquid-solid interface, No. 7 type cells should operate satisfactorily in a gravitational field that is zero or variable.

A No. 7 type cell has operated satisfactorily at low current density in this Laboratory for two years. Operation has been continuous with hydrogen and oxygen each under static head, a simple arrangement attractive for space applications. On Oct. 13, 1960, a cell of this type was launched into space and retrieved after having operated satisfactorily for about 30 min in accordance with expectations (13).

Power and Weight Considerations

Because the fuel cell is distinguished by separation of the energy conversion function from the energy storage function, it can be sized according to the power (watts) required. The fuel and oxygen supplies are sized according to the total power-time integral (total w-hr) of the mission. These ideas are expressed in Eq. 8. The analogy to the corresponding rocket problem is obvious.

$$W = A W_e + AB W_{FO} \quad [8]$$

where

W = total system weight

W_e = weight of fuel cell per w of power output

W_{FO} = weight of fuel, oxygen and containers per w-hr

A = power output, w

B = duration of mission (operation), hr

W_e and W_{FO} both depend upon E_a . W_e has its minimum value at maximum power output, where E_a is about one half E_r . W_{FO} is at a minimum when $E_a = E_r$, where W_e is infinitely large.

The optimization of total weight W requires choosing the proper value of E_a in the range 0.5 E_r to E_r . This can be done mathematically if an analytical expression for the

Table 4 Comparative system weights for two 10,000 w-hr missions

Mission	E_a , v	AW_e , lb	$AB (E_r/E_a) W_{FO}'$, lb	W , lb
1	0.70	23.0	148	171
1	0.82	49.0	126	175
2	0.70	0.46	148	148.5
2	0.82	0.98	126	127

polarization curve E_a as a function of current density is available.

E_r , the limiting value of E_a , is given by Eq. 5. Again we deal here with the complete oxidation of one mole of fuel. As this mole contains n equivalents, each of which represents one Faraday ($F = 96,500$ coulombs) of electricity, nF may be substituted for It in Eq. 5.

For the calculation of W_{FO} , it is convenient to express the free energy change as w-hr/lb-mole, and to denote it by $\Delta G'$. We then have

$$W_{FO} = \frac{E_r (M_f + 32m + C)}{\Delta G'} = W_{FO}' E_r/E_a \quad [9]$$

where

M_f = molecular weight of fuel

m = number of moles of oxygen consumed in the combustion of one mole of fuel (molecular weight of oxygen is 32)

C = weight of containers allocated to one mole of fuel + m moles of oxygen

Substitution in Eq. 8 gives

$$W = AW_e + AB (E_r/E_a) W_{FO}' \quad [10]$$

For the fuel cell of Table 1, a reasonable value of W_e is 0.046 lb/w at 25 amp/ft², and $E_a = 0.7$ v. With weight proportional to cell area, $W_e = 0.098$ lb/w at 10 amp/ft² where $E_a = 0.82$ v. For hydrogen and oxygen in high tensile strength steel containers,⁴ $W_{FO}' = 0.0084$ lb/w hr. If the cell operates at 25 °C, $E_r = 1.23$ v.

Let us now consider two 10,000 w-hr missions:

Mission 1	500 w for 20 hr
	$A = 500$ $AB = 10,000$
Mission 2	10 w for 1000 hr
	$A = 10$ $AB = 10,000$

Table 4 shows the weights of fuel cell and fuel for the two missions for two values of E_a .

For high power levels and short times the cell should be run at high current density to minimize cell weight; but for small power level and long times the current density should be low in order to minimize total fuel weight by taking advantage of higher efficiency. It has already been pointed out that for short discharge times at high current densities, fuel cells are generally inferior to ordinary batteries.

On the other hand, the fuel cell is distinctly superior to such batteries for missions long enough so that the first term of Eq. 8 is small compared with the second. For the best fuel cells available today, this probably occurs when the length of the mission is about 24 hr. The energy density of the fuel oxidant system and the operating voltage of the fuel cell then determine the number of w-hr per lb of total system. Of course, the weight of containers for fuel and oxygen must be included; this is especially important when gases are involved. Some approximate energy densities for several hydrogen-oxygen packaging systems are listed in Table 5.

⁴ Bottled gas is an unlikely choice for space application but may be used for illustrative calculations.

Because hydrocarbon cells suitable for space missions are still in the future, hydrocarbons have not been considered in Table 5. Hydrocarbons, especially those readily liquefiable, possess the advantages of high energy density and ease of packaging. Liquid fuels of lower energy, such as alcohols, give promise of greater anodic reactivity than hydrocarbons and may consequently find earlier use in fuel cells for space missions.

Long Mission Problem

Reliability and long life are likely to override other considerations governing the choice of power sources for long missions.

Assuming a value of 100 w-hr/lb of total system (see Table 5), one may calculate the total weight for a mission in which a fuel cell operates continuously at 100 w for 2 years. Such a mission would require 1,752,000 w-hr or a total weight W of 17,520 lb, which is prohibitive. For missions of this kind, the fuel cell can be useful only if it is integrated with a primary source of energy that does not overload the space vehicle.

Nuclear energy, derived from radioisotopes or fissionable fuels, and solar energy are the two kinds of energy primarily to be considered for long missions. Each will be characterized only as required by this discussion of the fuel cell.

Today nuclear energy must undergo intermediate conversion to heat if it is to serve as a practical source of electrical energy (14), the production of which is then subject to the Carnot cycle limitation. Converters such as the thermoelectric generator and the thermionic converter which are subject to this limitation in any case are natural choices for nuclear energy systems. If these converters could be made to operate satisfactorily near the highest temperature of which a nuclear reactor is capable, the Carnot cycle limitation would not be serious. (The materials problems at high temperatures need further study for both converters.) Nuclear energy cannot be used without adequate shielding or remote

positioning of the source; this is not easy to do for manned flights. Finally, the useful life of a given nuclear energy source depends either on its half life (radioisotope) or upon the "burnup" attained (fissionable fuel). In both cases, however, operating life could eventually be measured in years. To compete successfully, the fuel cell would need to outperform the thermionic converter and the thermoelectric generator.

Solar energy (15) is being converted directly into electrical energy via silicon solar cells at efficiencies near 10%. Solar energy can also be changed through heat to electricity in a thermionic converter, and it may be used in still other ways. The point of importance here is this: Solar energy itself is weightless, but it is available only during the orbital day. There must be provision for energy storage (16) if energy is needed during the orbital night. The fuel cell might qualify here as a storage device.

A fuel cell used thus in conjunction with either a nuclear energy source or a solar converter is said to be coupled to, or integrated with, the energy source for regenerative operation. "Regenerative" means that fuel and oxidant are regenerated in the operation of the system either thermally as in a nuclear energy source, or electrochemically as by use of a solar converter that supplies electrical energy in sufficient excess over the normal requirements of a space vehicle.

The Fuel Cell and the Carnot Cycle

The following should be almost self-evident: If heat is converted into work in a cyclic system, the Carnot cycle limitation applies (17). Integration of a fuel cell into such a system will not suspend the Second Law of Thermodynamics even though the fuel cell as an isolated device escapes the Carnot cycle restriction.

The system in question might consist of a nuclear reactor in which water is dissociated thermally, joined by a heat exchanger to a fuel cell in which hydrogen and oxygen are recombined at a lower temperature. For purposes of illustration, it is convenient to decompose the water in the nuclear reactor by reversible electrolysis. The reader interested in details of the thermodynamics will wish to consult the literature (17,18).

The hydrogen oxygen water system is a candidate for regenerative operation. In such operation, the necessary separations of these three substances from each other are obviously going to be difficult, especially in the absence of gravity. Electrolysis is an excellent method of separation, but electrolysis at nuclear reactor temperatures would pose serious problems. Also, there is need for mass transport between nuclear reactor and fuel cell. The fuel cell must overcome these handicaps if it is to compete successfully with thermionic converter or thermoelectric generator for coupling to a nuclear reactor in a satellite.

The comments just made apply with appropriate modification to the regenerative metal hydride systems (19,20). There is, however, no wish to depreciate the interesting work done on these systems, which has already yielded gratifying current densities albeit at low voltages; 67, 123 and 330 amp/ft² at 0.17 v with different electrodes at 520 °C are illustrative data (19).

Electrochemical Energy Storage

The metal hydride system just referred to does not, by the present definition, contain a fuel cell; lithium is scarcely a conventional fuel. In a regenerative system, the matter is only of academic importance because the substances that generate electricity are regenerated after they have done so. They are thus analogous to a working fluid.

The hydrogen-oxygen-water system was actually operated regeneratively by Grove (7), though not for the purpose of energy storage. The regenerative cycle consists of

Table 5 Comparative energy densities of hydrogen and oxygen in various packaging systems

Fuel oxidant system	Fuel cell operating voltage E_a , v	Approx. energy density of fuel plus oxidant plus containers, w-hr/lb
H ₂ and O ₂ gases at ^d 5000 psi in high strength steel tanks	0.80	78
H ₂ and O ₂ gases at ^e 3000 psi in resin-fibre glass containers	0.80	150
Liquid H ₂ and O ₂ in cryogenic containers ^d	0.80	700
Chemical H ₂ and O ₂ ^{a,d} generation	0.80	220 ^b
Comparison ^c		
Lead acid batteries		10
Silver-zinc batteries		40-80

^a For example, H₂O reacting with NaBH₄ to form H₂, and with KO₂ to form O₂.

^b Weight of control and water input systems and completeness of reaction are uncertain.

^c Comparison is valid only for missions above 24 hr (see text).

^d Data for gas and liquid storage were supplied by D. L. Douglas (see Table 1).

^e Calculated from data of F. T. Bacon, *Fuel Cells*, ed. by G. J. Young, Reinhold Publishing Corp., N. Y., 1960, p. 76.

Electrolytic charge: $\text{H}_2\text{O}(l) = \text{H}_2(g) + 1/2 \text{O}_2(g)$ emf, F_e
 Fuel cell discharge: $\text{H}_2(g) + 1/2 \text{O}_2(g) = \text{H}_2\text{O}(l)$ emf, E_a

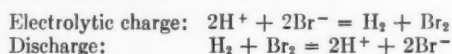
The percentage efficiency of the cycle is $100 E_a/E_e$ if no side reactions occur.

Bacon (21), Justi (22), and their co-workers have used gas diffusion electrodes to carry out the cycle. Justi et al. (22) quote efficiencies near 60% at a current density near 100 amp/ft² at 85 °C with an alkaline electrolyte; this is good performance.

From earlier discussion, it is clear that a cell modeled after Fig. 1 might be simpler for regenerative operation in space than the cells just mentioned. One might hope to design a single cell for both the electrolysis and fuel cell functions which can operate sealed off without requiring external aids to accomplish separation or mass transport. Work in this Laboratory by L. W. Niedrach and S. Gilman, and in the General Electric Missile and Space Vehicle Dept. (23) encourages the belief that this hope can be realized.

Fig. 2 shows a current-voltage curve for the regenerative operation of an ion exchange membrane cell. One sees immediately that the efficiency (about 40% near 20 amp/ft²) is not as good as that of the Justi cell; of course, the membrane cell is simpler and it operates at room temperature. On the basis of information available today, it is premature to go into detailed discussions or into fuel battery design.

It is well known that ion exchange membranes retain their conductivity better (4,24,25) if a supporting aqueous electrolyte is present. It is also well known that it is difficult to avoid polarization at oxygen electrodes. Juda, Tirrell, and Lurie (25) propose an electrochemical system advantageous from both these points of view. The electrolyte consists of an ion exchange membrane in contact with a bromine-hydrobromic acid solution, and the reactions during regenerative operation are



The polarization curve for this hydrogen-bromine battery, which is not a fuel cell by our definition, is shown in Fig. 2. The linearity of the curve is noteworthy and points to IR drop as the principal loss present during operation. The efficiency is consequently high at low current densities, and it would be higher for thinner membranes. This battery seems interesting for regenerative operation, especially if it operates satisfactorily sealed off, without auxiliaries, and remains invariant.

In consideration of electrochemical energy storage in space vehicles, improved secondary batteries (26) must never be overlooked. They are in use today, and they will probably be better in the future. They are not likely to become as nearly immune as fuel cells to damage from overcharging or deep discharging, and they may always have difficulty in meeting the reliability requirements for satellite power sources that must operate for years, not months. This situation presents the fuel cell with its best opportunity for early spectacular success.

Conclusion

The outlook for the fuel cell in space seems to be this: If the severe reactivity and invariance requirements can be met even moderately well, the device should prove useful on missions too long for primary batteries. It should also prove an attractive alternative to secondary batteries on extremely long missions in which the fuel can be regenerated by using another form of energy, preferably that of the sun. Intensive research on all kinds of fuel cells can therefore be justified also on the basis of space age needs (27).

It seems unnecessary to add that this résumé of the fuel cell in space was made primarily from the point of view of research and does not pretend to treat the many important

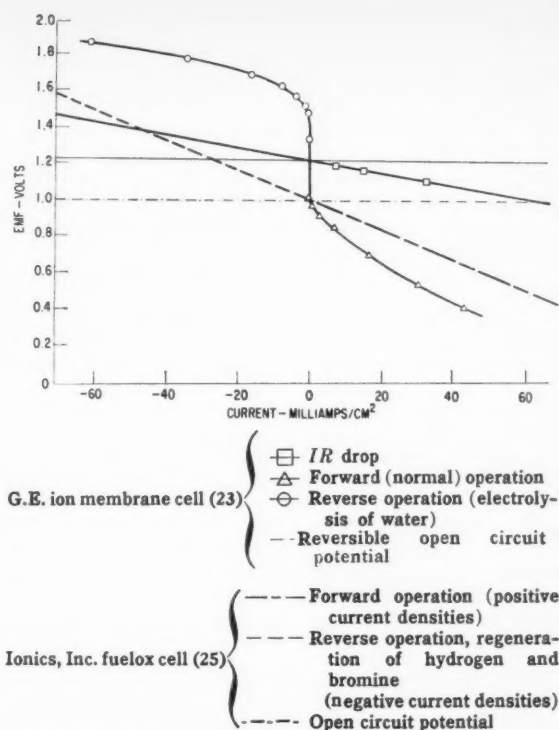


Fig. 2 Polarization curves for regenerative fuel cell systems

engineering problems involved. Among these are the calculation of "trade off" curves, the need for voltage regulation, the details of heat rejection, and problems arising from the different requirements posed by different missions (28). Also, the principal comparison has been of fuel cells with ordinary batteries, which is justifiable because the devices are similar and because the batteries currently occupy an important position. A comprehensive look at the future, which compares numerous power sources not yet fully developed, is given by Klass (29).

References

1. Kaye, J. and Welsh, J. A., *Direct Conversion of Heat to Electricity*, John Wiley and Sons, Inc., N. Y., 1960.
2. Grubb, W. T., "Batteries with Solid Ion-Exchange Electrolytes, 1. Secondary Cells Employing Metal Electrodes," *J. Electrochem. Soc.*, vol. 106, 1959, pp. 275-278.
3. Grubb, W. T., "Fuel Cell," U. S. Patent 2,913,311, Nov. 17, 1959.
4. Grubb, W. T. and Niedrach, L. W., "Batteries with Solid Ion-Exchange Electrolytes, 2. Low Temperature Hydrogen Oxygen Fuel Cells," *J. Electrochem. Soc.*, vol. 107, 1960, pp. 131-135.
5. Niedrach, L. W., "The Ion-Exchange Membrane Fuel Cell," *Proc. Thirteenth Annual Power Sources Conf., Power Sources Div., U. S. Army Signal R. and D. Laboratory, Fort Monmouth, N. J., May 1959*, pp. 120-121.
6. Oster, E. A., "Cation-Exchange Membrane Fuel Cells," *Proc. Fourteenth Annual Power Sources Conf., Power Sources Div., U. S. Army Signal R. and D. Laboratory, Fort Monmouth, N. J., May 1960*, pp. 59-62.
7. Grove, W. R., "On A Gaseous Voltaic Battery," *Phil. Mag. and J. of Sci.*, vol. 21, 1842, pp. 417-420.
8. Bacon, F. T., "Research Into Properties of Hydrogen-Oxygen Cell," *BEAMA J.*, vol. 61, no. 199, Jan. 1954, pp. 6-12.
9. Justi, E., Pilkuhn, M., Scheibe, W. and Winsel, A., "High Drain Hydrogen Diffusion Electrodes Operating at Ambient Temperature and Low Pressure," *Academy of Sciences and Literature (Mainz) Komm.-Verlag F. Steiner, Wiesbaden*, 1959, pp. 33, 81.
10. Kordesch, K., "The Hydrogen-Oxygen (Air) Fuel Cell With Carbon Electrodes," *Fuel Cells*, ed. by G. J. Young, Reinhold Publishing Corp., N. Y., 1960, pp. 11-22.
11. Esso Research and Engineering Company, Process Research Div., *Pe RD Mem. 60-8*, Jan. 7, 1960.
12. Podolny, W. H., "Regenerative H_2O_2 Fuel Cell System," *Proc. Fourteenth Annual Power Sources Conf., Power Sources Div., U. S. Army Signal R. and D. Laboratory, Fort Monmouth, N. J., May 1960*, pp. 64-67.

- 13 Private Communication from General Electric Co. Missile and Space Vehicle Dept., Phila., Pa.
- 14 Ogburn, G. H., "Nuclear Energy Power Sources," *Proc. Fourteenth Annual Power Sources Conf.*, Power Sources Div., U. S. Army Signal R. and D. Laboratory, Fort Monmouth, N. J., May 1960, pp. 12-18.
- 15 Dale, B. and Rudenburg, H. G., "Photovoltaic Conversion 1. High Efficiency Silicon Solar Cells," *ibid.*, pp. 22-25.
- 16 Winkler, S. H., "Optimum Design of a Space Vehicle Storage System," *ibid.*, pp. 90-93.
- 17 Liebhafsky, H. A., "The Fuel Cell and the Carnot Cycle," *J. Electrochem. Soc.*, vol. 106, 1959, pp. 1068-1071.
- 18 deBethune, A. J., "Fuel Cell Thermodynamics," *J. Electrochem. Soc.*, vol. 107, 1960, pp. 937-939.
- 19 Shearer, R. E., Mausteller, J. W., Ciariello, T. A. and Werner, R. C., "Regenerative Metal Hydride System," *Proc. 14th Annual Power Sources Conf.*, Power Sources Div., U. S. Army Signal R. and D. Lab., Fort Monmouth, N. J., May 1960, pp. 76-77.
- 20 Del Duca, M. A., Fuscoe, J. M. and Johnston, T. A., "Fuel Cells for Space Vehicles," *ASTRONAUTICS*, vol. 5, 1960, pp. 36-44.
- 21 Bacon, F. T., "The High-Pressure Hydrogen-Oxygen Fuel Cell," in

- Fuel Cells*, ed. by G. J. Young, Reinhold Publishing Corp., N. Y., 1960, pp. 51-77.
- 22 See (9), pp. 208-214.
 - 23 Bone, J. S., "Regenerative Ion-Exchange Fuel Cell System," *Proc. Fourteenth Annual Power Sources Conf.*, Power Sources Div., U. S. Army Signal R. and D. Lab., Fort Monmouth, N. J., May 1960, pp. 62-64.
 - 24 Juda, W. and McRae, W. A., U. S. Patent 2,636,851, April 28, 1953.
 - 25 Juda, W., Tirrell, C. E. and Lurie, R. M., "Fuel Cells with Ion-Exchange Membranes," presented at the ARS Space Power Systems Conf., Santa Monica, Calif., Sept. 27-30, 1960 (ARS preprint 1304-60).
 - 26 "Session on Secondary Batteries," A. Fleischer, Chairman, *Proc. Fourteenth Annual Power Sources Conf.*, Power Sources Div., U. S. Army Signal R. and D. Lab., Fort Monmouth, N. J., May 1960, pp. 78-99.
 - 27 Eisenberg, M., "Electrochemical Energy Sources for Space Flight Applications," presented at the ARS Semi-Annual Meeting, San Diego, Calif., June 8-11, 1959 (ARS preprint 866-59).
 - 28 Bossart, K. J., "An Engineer Looks at Space Flight," *Elec. Engng.*, vol. 79, 1960, pp. 960-962.
 - 29 Klass, P. J., "USAF Expands Energy Conversion Effort," *Aviation Week*, vol. 73, Aug. 15, 1960, pp. 83-90.

Internal Animal Telemetry: a Feasibility Test Program¹

BEN L. ETTELSON²

Spacelabs, Inc.
Van Nuys, Calif.

WILFRED N. COOPER,³
MERLE A. BEAUPRE⁴
and **TOBY FREEDMAN⁵**

North American Aviation, Inc.
Los Angeles, Calif.

LAURANCE G. THROSSELL

Wyle Laboratories
El Segundo, Calif.

BRUCE PINC⁷

Air Force Ballistic Missile Div.
Inglewood, Calif.

An improved method of animal instrumentation is described. This method uses an implanted sensor and telemeter to allow transmission of physiological data from unencumbered, intact test animals to a receiver-signal conditioner for subsequent air to ground telemetry. To investigate the possible advantages of this system, a program, under the direction and sponsorship of the Bio-Astronautics Projects Office, Air Force Ballistic Missile Div., USAF, was initiated to demonstrate feasibility of transmitting a single channel of physiological data through the intact skin of a chronically instrumented simian under combined environmental conditions.

Presented at the ARS 15th Annual Meeting, Washington, D. C., Dec. 5-8, 1960.

¹ This work was supported in part by the Ballistic Missile Div. of the U. S. Air Force under Contract AF 04(647)-585.

² Pres., Spacelabs, Inc., Van Nuys, Calif.

³ Physiologist, Weapon System Advance Design, North American Aviation, Inc., Los Angeles, Calif.

⁴ Project Engineer, Weapon System Advance Design, North American Aviation, Inc., Los Angeles, Calif.

⁵ Corporate Flight Surgeon, North American Aviation, Inc., Los Angeles, Calif.

⁶ Test Project Engineer, Wyle Laboratories, El Segundo, Calif.

⁷ Captain-USAF (MSC), Bio-Astronautics Projects Office, Air Force Ballistic Missile Div., Inglewood, Calif.

IN A PREVIOUS paper (1)^{*} it was suggested that internally instrumented animals could serve as compact, self-contained biophysical test packages to sample comprehensively the biological effects of space environments. The paper also described a first attempt at internally instrumenting a dog with a small VHF transmitter to telemeter his electrocardiogram a short distance.

To explore further the potential advantages of this system in high stress situations, a program was initiated under the direction and sponsorship of the Bio-Astronautics Projects Office, Air Force Ballistic Missile Div., USAF. The purpose was to demonstrate feasibility of transmitting a single physiological parameter through the intact skin of an internally instrumented simian under combined environmental conditions.

To accomplish the work, a team was formed consisting of North American Aviation, Inc., Spacelabs, Inc., and Wyle Laboratories. In this effort, North American Aviation, in addition to serving as prime contractor and project manager, provided the life support system, Spacelabs provided the system of surgically implanted transmitters plus receiving and decoding equipment, and Wyle Laboratories the facilities and personnel for performing omni-environmental testing.

Description of the Transmitter, Receiver, and Decoder

The original dog implant was made using a straight frequency modulated transmitter operating just below the FM broadcast band. The oscillator was modulated by a capacitively coupled single transistor amplifier which had its input connected to sutures acting as ECG electrodes. The ECG was selected merely as a matter of convenience. A miniature nickel-cadmium battery contained within the package was recharged by an external 1.8 mc RF generator which coupled into a tuned circuit within the implanted instrument.

Several problems led us to redirect our efforts toward other modulation methods. These were primarily detuning of the FM carrier caused by movement of the transmitter with respect to body tissue and organs, and the inherent power inefficiency of frequency modulation. Additional problems encountered were tissue heating caused by the 1.8 mc recharging power, and battery unreliability caused by using cells in series and allowing them to discharge completely.

To overcome these problems, a pulse rate modulated transmitter was developed which switches on the RF oscillator briefly at a rate which is proportional to the amplitude of the input signal. This approach rendered the information content independent of carrier frequency, and reduced current drain by 70% so that operating time after charging could be increased to approximately 12 hr from the previous 4 hr. The new design utilized was tailored to a single Ni-Cd cell to increase battery reliability. Fig. 1 shows the unit before potting.

To minimize costs in the program, a surplus APR-1 AM receiver was used. The audio output was put on a speaker so that the R wave of the ECG was audible. The video output of the receiver was connected by coaxial cable to a simple decoder. The latter unit amplified the signal and differentiated it. The differentiated signal was used to trigger a multivibrator which was direct coupled to a cathode follower stage with low pass filters at the output. The filter output was used to drive a direct writing oscillograph.

Animal Support System

The simian couch and restraint system (Fig. 2) were designed

to provide adequate support and protection for a six to eight pound Rhesus monkey. The couch shell was fabricated with fibreglass formed over the posterior half of a plaster monkey dummy. The receiving antenna consisted of a longitudinal aluminum foil strip in the couch. Polyurethane foam was formed within the couch shell to a thickness of $\frac{1}{4}$ in. and then covered with $\frac{1}{8}$ in. thick sponge rubber.

The restraint system was made from nylon net (Nottingham weave). A single oval cutout was made in the facial area and lined with padded chamois.

Surgical Procedures

Surgeries were performed on two Balcones laboratory strain Rhesus monkeys (No. 150F and No. 122E) to implant transmitters and ECG electrodes. The operative procedure used was as follows:

After satisfactory anesthesia with intravenous pentobarbital, using the saphenous vein, the simian 150F was placed in the supine position. The abdomen was prepped first by shaving the hair and then by cleaning with alcohol, followed by tincture of iodine. The abdominal incision was midline from just below the xiphoid to below the umbilicus. The linea alba was identified and the midline incision was carried down through this structure. The peritoneum was opened in the direction of the incision. The intestinal contents, including the colon and small intestine were retracted to the right with wet sponges. The left kidney was identified

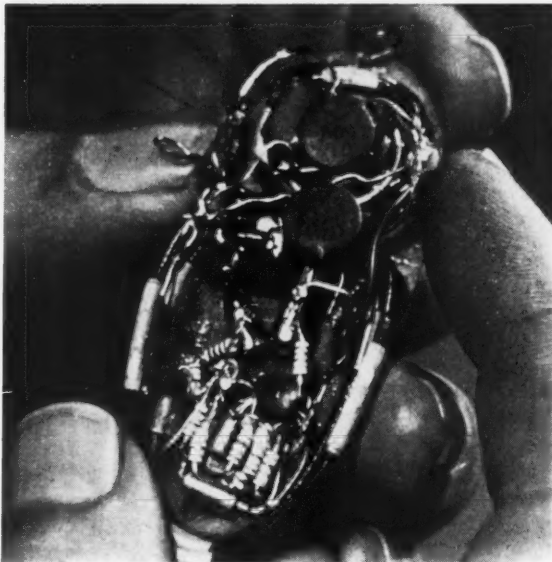


Fig. 1 Pulse rate modulated transmitter

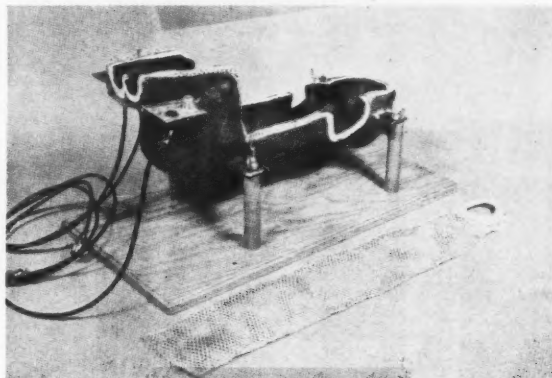


Fig. 2 Simian couch and restraint system

^{*} Numbers in parentheses indicate References at end of paper.



Fig. 3 Surgery on simian 122E

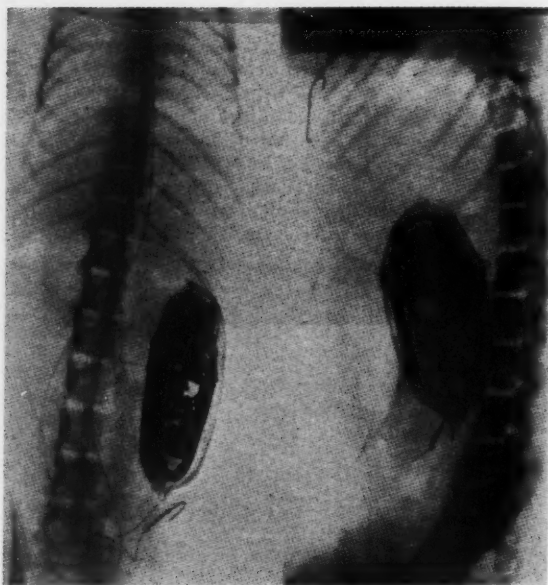


Fig. 4 Simian 150 X-ray

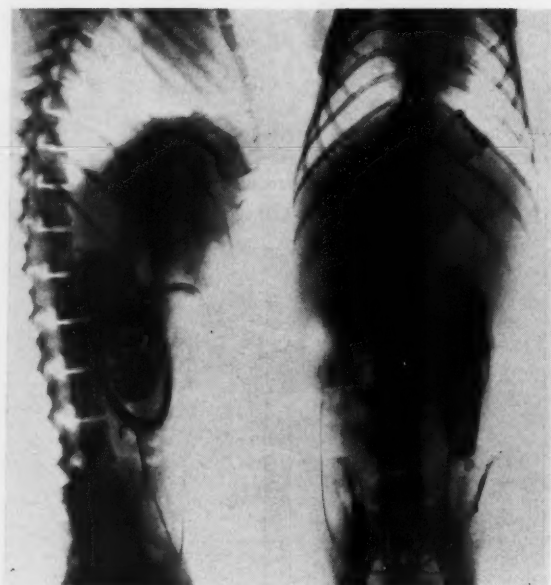


Fig. 5 Simian 122 X-ray

and the peritoneum covering it was divided. The kidney was reflected medially and the transmitter unit was placed in the left posterior gutter of the peritoneal cavity and the unit secured in place with No. 00 black silk. The kidney was then allowed to lay back on the unit. The electrodes next were fixed in place. The inferior electrode was brought down and anchored to the lateral portion of the crest of the ilium by making a small incision over the crest of the ilium and forcing the hook through the bony cortex and into the medullary cavity. The shank of the hook was then sutured in place. The superior electrode then was directed from the incision up through the subcutaneous tissue to the presternal region. A small incision exposed the sternum and the hook electrode was impaled in the substance of the sternum. The shank was then sutured in place. The skin incision was closed with No. 000 black silk. The peritoneal cavity was closed with running No. 000 chromic catgut and the skin was closed with interrupted sutures of No. 000 black silk.

Surgery on simian 122E (Fig. 3) was identical to that on simian 150F with the exception of the superior or sensing electrode and its placement within the simian. This electrode was a screen mesh type measuring 2×2 cm. It was fixed to the abdominal side of the left diaphragm over the pericardial reflexion with No. 000 black silk.

Post operative convalescence was completely uneventful. Fig. 4 shows an X ray taken of subject 150F immediately following surgery, and Fig. 5 is taken of subject 122E.

Environmental Testing

The environmental testing was divided into three major categories: bench mark testing of the transmitter, testing of the life support system with a dummy load, and simian testing under single and combined environments.

The Wyle centrifuge was fitted with a shaker capable of generating both sinusoidal and random vibration and acoustic transducers for noise generation. A capsule support frame was installed at the end of the centrifuge (Fig. 6). The capsule was a round nosed cone of fibreglass and other plastic split longitudinally and mounted by quick lock screws and toggle fasteners (Fig. 7). The shaker was mounted on the centrifuge arm such that the specimen could be vibrated within a second support frame which held the acoustic transducers, a motion picture camera, and photographic lights. A vibration and holding fixture was mounted to the exciter for attachment of the specimen.

Bench mark testing of the transmitter consisted of radio interference testing, acoustic noise, random vibration, sus-

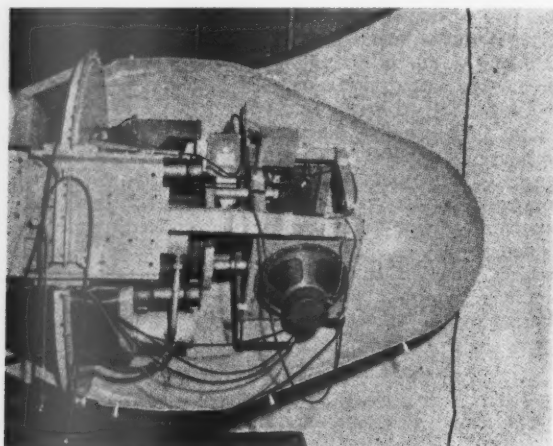


Fig. 6 Capsule and support frame

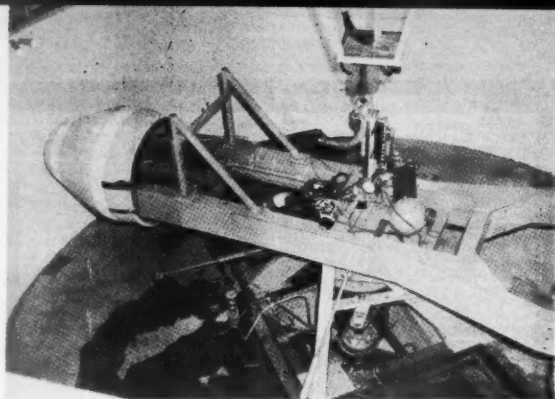


Fig. 7 Centrifuge with capsule installed

tained acceleration, and combined environment. The objective of the tests was to determine the performance of the transmitter under single and combined environments more severe than those specified for the simian tests which were to follow. A further objective was to provide reference data for operation of the transmitter by itself so that comparisons could later be made of the implanted unit. The tests were satisfactory except for the random vibration test during which the output from the system was intermittently abnormal. In a later retest, the condition could not be repeated and it was concluded that low battery voltage at the time of the first test contributed to the problem.

Dummy load testing of the couch and capsule was performed primarily to demonstrate structural integrity of the configuration and to check out the camera system. A secondary objective was to determine temperature control needed to protect the simian from photo-flood lamps and ambient air temperature fluctuations. Sustained acceleration, random vibration, sinusoidal vibration, and combined environmental tests were run to validate the system. The tests revealed that the temperature rise in the capsule was excessive. Improvements were made in cooling air provisions and in camera light sequencing to eliminate this condition. There were no structural problems.

Simian tests were scheduled over a period of 11 days to provide a certain amount of conditioning and to allow the animal to rest at least every other day.

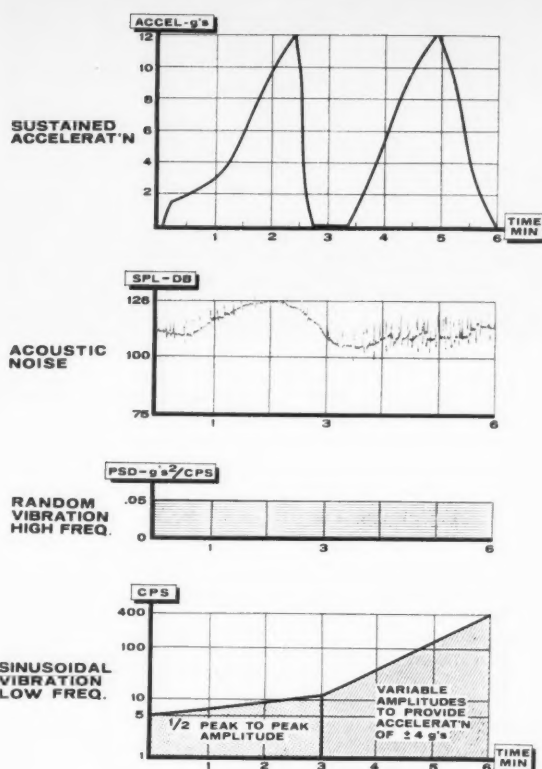


Fig. 8 Combined environment test program

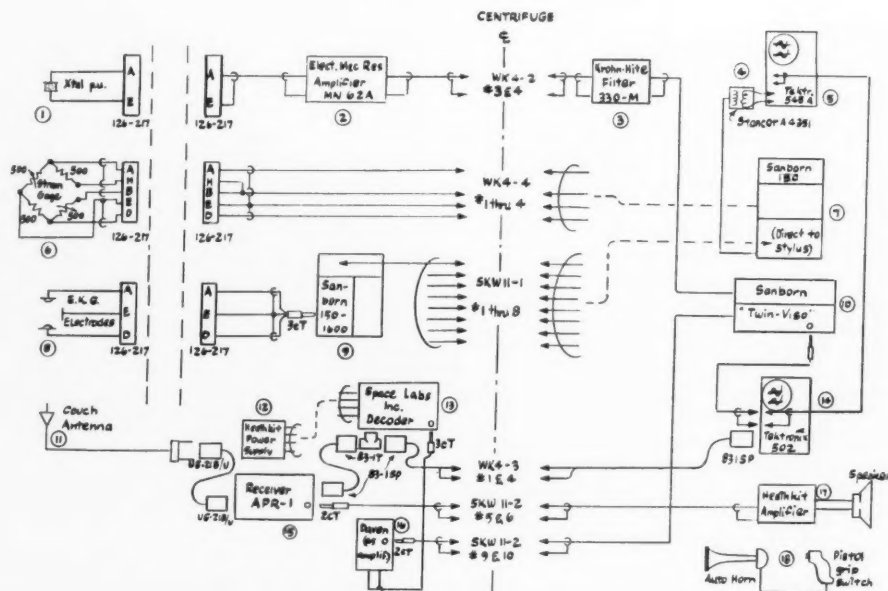


Fig. 9 Simian test instrumentation

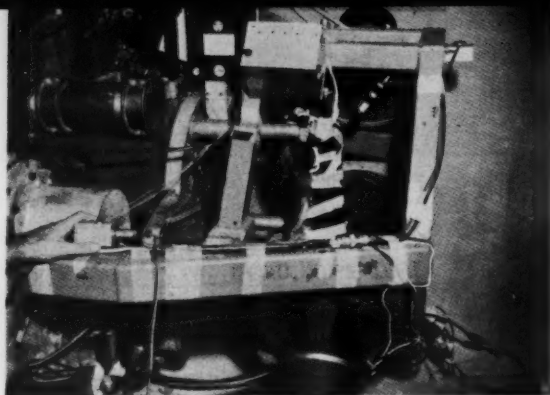


Fig. 10 Animal installed on fixture

Monkey 122E was selected as a test subject. To afford a comparative measure, an external ECG was taken. External respiration signals were also presented to provide viability indication to assure animal safety.

The tests were performed as follows:

Test day 1	Radio interference	8-5-60
Test day 2	Acoustic noise (107 db and 110 db: ref. 0.0002 dynes/cm ² , 6 min each)	8-8-60
	Acceleration (6 g peak and 12 g peak, 6 min each)	
	Random vibration (15-2000 cps; power spectral density 0.05 g ² /cps, 6 min)	
Test day 3	Low frequency vibration (5-12 cps 1/4 in. double amplitude, 3 min; 12-400 cps, 2 g, 3 min)	8-10-60
Test day 4	Low frequency vibration (5-12 cps 1/2 in. double amplitude, 3 min; 12-400 cps, 4 g, 3 min)	8-12-60
Test day 5	Combined environment	8-15-60
	Test 1	
	Acceleration	12 g's peak
	Acoustic noise	123 db
	Random vibration	0.05 g ² /cps
	Sinusoidal vibration	5-12 cps 1/4 in. double amplitude
		12-400 cps, 2 g
		6 min
	Test 2	
	Acceleration	12 g's peak
	Acoustic noise	126 db
	Random vibration	0.05 g ² /cps
	Sinusoidal vibration	5-12 cps 1/2 in. double amplitude
		12-400 cps, 4 g
		6 min

Fig. 8 indicates the manner in which the combined environments were applied, and Fig. 9 the test set up.

Prior to each day's testing and at the conclusion of each test, the animal was given a physical examination and found to be in excellent condition and suffering no ill effects from the exposure with the implanted instrument. Furthermore, long term tolerance to the implanted unit is excellent. The transmitters have been implanted about four months with no evidence of discomfort or pathology.

Fig. 10 shows the animal mounted on the fixture and Fig. 11 is a record taken during the second combined environment run at an acceleration of 6.5 g. While the transmitted cardiogram is clearly not of clinical quality, it does validate the basic premise that internally instrumented animals have great potential for bio-astronautic research. It should be noted that the external instrumentation was extremely poor under adverse environments in our experiments, despite the most rigid observance of electrode placement techniques.

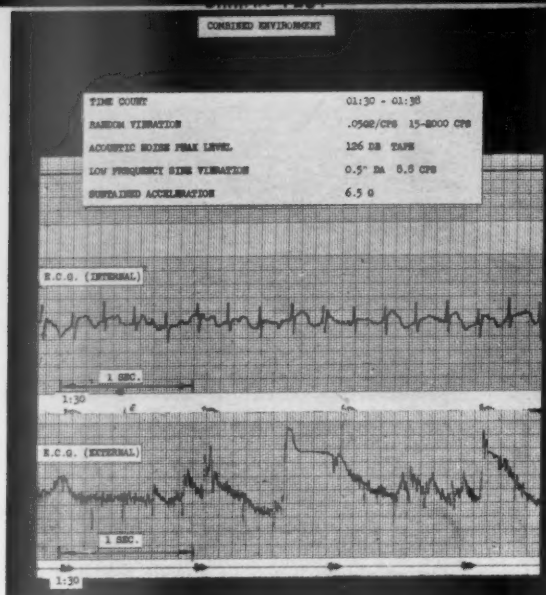


Fig. 11 Comparison between transmitted and external cardiograms

Conclusions

The purpose of the program was to demonstrate the feasibility of transmitting physiological data through the intact skin of chronically instrumented simians under combined environmental conditions. The main ideas were validated, i.e., that animals can tolerate implanted instruments in severe environments, and that useable data can be transmitted under these conditions. Obvious refinements that need further attention are the method of surgical attachment of the transmitter, reduction of self-generated electrical noise in the low level sections of the transmitter, and redesign of the recharging system to simplify the procedure. In addition, the decoder should be redesigned to prevent it

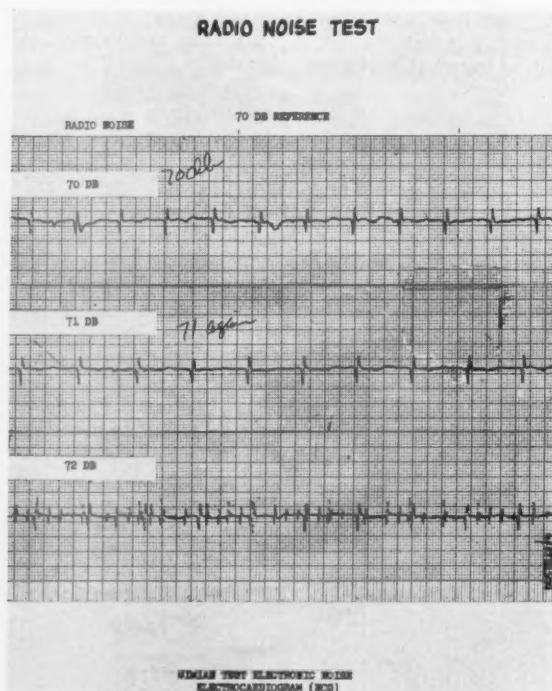


Fig. 12 Effects of radio noise on transmitted signal

from responding to noise spikes, and to force it to "recognize" only pulses which are characteristic of the biological transmitter system. Shown on Fig. 12 are transmitted cardiograms taken during radio interference testing which show the effects of noise. To minimize radio interference, electrical shielding of the entire animal must also be studied to compare the relative benefits with the alternative of further complications in transmitter and receiver-decoder. The whole area of electrode configuration and location needs further work. The program pointed out the difficulty with large screen electrodes located on moving muscle tissue. Respiration artifact was clearly evident on Monkey 122E, whereas Monkey 150F, equipped with two point electrodes, did not exhibit this problem. Some changes were also indicated in the animal support system to simplify animal handling and to save time.

Expansion of the Concept

While this purpose of the initial program was strikingly achieved, additional development is required to bring the concept into line with practical requirements. Furthermore, it appears evident that the greatest gains from internal animal instrumentation obtain in situations where measurements can be taken of physiological parameters that would otherwise be unmeasurable. A good example is that of cardiac output which is of interest to physiologists in prolonged weightlessness experiments. Using the techniques discussed herein, one can conceive of a flowmeter sectioned into the aorta which would modulate the transmitter. Another example might be the measurement of ureteral flow as an indication of kidney function.

Another obvious extension is the transmission of multiple physiological parameters in multiple stress environments. Under contract as the second phase of the previously described

program is work to design, implant, ground test, and flight test a three channel FM/FM telemetry system. This program again makes use of small Rhesus monkeys and measurements tentatively selected are the electrocardiogram, the phonocardiogram, and respiration. Cyclic data of both low and high frequencies have been selected not only for their physiological interest, but also because they will exercise the telemetry system more fully than, say, a body temperature channel. The system will again be short range, with signals being picked up in a couch antenna. While the composite FM signal could be directly relayed to ground, an alternate approach was chosen to facilitate testing and to make the system self sufficient. A small FM receiver and three channel discriminator will be contained within the life support system complete with its own battery supply. Signals will, therefore, be processed to the proper voltage levels for retransmission via the missile air to ground telemetry system. Capsule pressure and temperature will also be telemetered.

A unique feature of the life support system is a gimbed couch to provide proper orientation for re-entry, since it is not planned to reorient the vehicle as is done in the Mercury program.

The culmination of this second phase program is a rocket flight test scheduled for next year. The data obtained should provide a sound basis for extrapolation of the concept to larger animals and more sophisticated measurements, and contribute significantly to the technology of manned space flight.

Reference

- 1 Breckler, A., Kaeburn, L., Ettleson, B. and Dourlas, D. W., "Space Canaries—Implicit Biological Monitoring," presented at the ARS 14th Annual Meeting, Washington, D. C., Nov. 16-20, 1959 (ARS preprint 925-59).

Reactor Heat Removal Limitations of Nuclear Rockets

GEORGE YASUI¹

Lockheed Aircraft Corp.
Sunnyvale, Calif

Moderately detailed analyses of convective heat transfer in the core of a typical nuclear rocket engine were performed in order to determine the effects of major design parameters. An estimate of the permissible power density is given. Practical limitations imposed by design factors are discussed with respect to nuclear rocket application. In a comparison of relative efficiencies of different axial power density profiles, it is shown that a constant wall temperature operation is advantageous if the only limitation is allowable wall temperature. On the other hand, if an additional restriction is imposed of allowable power density, then a combination of power density profiles is shown to lead to better performance. The study also indicates that nuclear rockets are capable of throttling operation and can trade off in performance between specific impulse and thrust.

IN THE open literature on the design of solid core nuclear reactors for propulsion, the importance of heat transfer due to the extreme power densities and temperatures has been elucidated (1,2,3).² While not aimed at a broad systems analysis that is needed for overall optimization, this paper is an attempt to make a detailed analysis of how core size and power

are limited by heat removal problems at steady state conditions.

Using a simplified model of a "typical" reactor engine, heat transfer equations will be discussed to show how the variables affect engine size and performance. Comparisons will be made of cases which differ in axial power density profile; in addition, the range of power variation will be examined. The calculations suggest that, for reasons of high power density when power output is restricted by a limiting wall temperature, an isothermal reactor core is preferable. How-

¹ Presented at the ARS Semi-Annual Meeting, Los Angeles, Calif., May 9-12, 1960.

² Presently Research Scientist, Lockheed Missiles and Space Div., Palo Alto, Calif.

³ Numbers in parentheses indicate References at end of paper.

ever, if thermal stress and strain is such as to result in another restriction, called the limiting heat flux due to rupture or distortion, then the power density should be modified in the front portion of the reactor so that it tends more toward a uniform heat generation rate.

Basic Assumptions and Equations

General

The following model and assumptions are believed to be reasonable as regards a possible nuclear reactor for rocket motors. One of the reasons for specifying the main assumptions is the difficulty in trying to include all pertinent data in a single equation or graph.

- 1 The core is a graphite based solid.
- 2 The right circular cylindrical core has length equal to its diameter, except where separately treated.
- 3 Coolant is gaseous hydrogen.
- 4 Coolant channels are constant diameter holes parallel to the cylinder axis.
- 5 Holes are uniformly distributed with centers located at corners of equilateral triangles.
- 6 There is steady state case of heat transfer.
- 7 There is one dimensional heat transfer in the solid.
- 8 Coolant flow is turbulent.
- 9 Heat generation rate in solid is uniform at a given x plane, but may vary in the axial direction.
- 10 Gas flow rate is the same for each channel.

As an approximation, this model should be adequate to indicate the behavior of a typical reactor core under steady state operation. For example, nucleonic efficiency and weight savings usually suggest a core with diameter equal to its length. Furthermore, a good side reflector very likely will be included, in which case substantial radial flux flattening may be expected. For high specific impulse, hydrogen is the propellant choice. Because regenerative cooling and a pressure above its critical point are anticipated, the coolant in the core channels should behave like a gas. At the design point, turbulent flow prevails, while the assumption of one dimensional conduction (radially) for each channel appears reasonable. The choice of the hole locations was due to convenience in calculation using void fraction as a parameter.

Convective Heat Transfer

References (4) and (5) discuss the finer points of convective heat transfer. The approach taken next is believed to be reasonable. Because of extreme variations in conditions along the flow channel, the usual analysis based on average core conditions may be inadequate, hence, a correlation for the local heat transfer coefficient will be applied. In this manner, the heat transfer surface area or channel length required and axial profiles of temperatures and heat flux may be found.

For gas in turbulent flow, the correlation for local convection heat transfer coefficient, as experimentally determined by (6), may be written as

$$h_x = \frac{0.036 G^{0.8} k_f Pr_f^{0.4} \mu^{0.3}}{d^{0.1}(x+d)^{0.1} \mu_f^{0.3} T_f^{0.3}} \quad [1]$$

As a conservative gesture to account for hot channel factors, the value of the constant was changed from 0.036 to 0.034. The correlation of Taylor and Kirchgessner (7) may be simpler but was not used here. To obviate the need for pressure drop information required to find the static temperature t in Eq. 1, an approximation is suggested of substituting T_{AW} or T in place of t in Eq. 1. This simplification may be justified on the grounds that design values of exit Mach number substantially below one are expected, and that the added error is small compared to variance in the correlation itself.

Expanding upon the first item, we note that Bussard and DeLauer (2) state that sonic choke conditions should be avoided in multi-channel cores because of flow instability among the passages.

Additional problems anticipated for sonic flow are erosion and shock waves. To assure subsonic flow at the channel exit, a design exit Mach number of 0.5 appears to be reasonable, according to F. P. Durham (3), in view of the rapidly increasing Mach number in a short distance after that value.

If $M_2 = 0.5$, then for hydrogen the total temperature and static temperature differ at most by about 4%

$$T_2 = t_2 \left(1 + \frac{\gamma - 1}{2} M_2^2 \right) \sim 1.04 t_2 \quad [2]$$

The difference between "adiabatic wall" temperature and static temperature is somewhat less than this. Therefore, a common temperature approximating T_{AW} and denoted by T_g will be used in the basic heat transfer equations, which then become

$$(q/S)_x = h_x(T_w - T_g) \quad [3]$$

$$h_x = \frac{0.034 G^{0.8} k_f Pr_f^{0.4} T_g^{0.3}}{d^{0.1}(x+d)^{0.1} \mu_f^{0.3} T_f^{0.3}} \quad [4]$$

$$\int_{T_1}^T c_p dT_g = \frac{4}{dG} \int_0^x (q/S)_x dx \quad [5a]$$

$$H_{T_1}^T = \frac{4}{dG} (q/S)_{ave} x \quad [5b]$$

If one combines Eqs. 3 and 4, a relationship is obtained as follows

$$\frac{(q/S)_x d^{0.1}(x+d)^{0.1}}{G^{0.8}} = \frac{C k_f Pr_f^{0.4} T_g^{0.3} (T_w - T_g)}{\mu_f^{0.3} (T_w + T_g)^{0.3}} \quad [6a]$$

$$= \Phi(T_g, T_w) \quad [6b]$$

The equation is useful when the wall temperature is plotted as function of gas temperature and Φ .

In examining the foregoing equations, one sees that, for a given hole size and gas flow rate, the temperature difference between gas and wall depends on the local heat flux, indicating that the axial heat flux profile plays an important role where wall or solid temperature is limiting, as discussed more fully in subsequent sections.

Axial Power Density

Some possible profiles of axial heat flux distribution will be discussed now, since this information is found to be useful as explained in a later section. In an unreflected, uniformly loaded cylindrical nuclear reactor, the fission density proportional to the neutron flux has a sine curve shape along the axis, but the profile may be modified by adding reflectors, varying fuel loading, etc. (3), to produce a more desirable power density. A few of these profiles may be represented as follows.

Uniform heat generation rate

In this case q/S is constant along the channel length; obviously, its ratio of average to peak heat flux is unity. From the thermodynamic properties of the gas and Eq. 5b, the gas temperature profile is readily found, while Eq. 6 may be used to determine the wall temperature as a function of distance x .

End reflected core

Besides side reflection, the cold end may also be reflected to decrease core size still further. With uniform loading, the resultant heat flux profile may be represented approximately

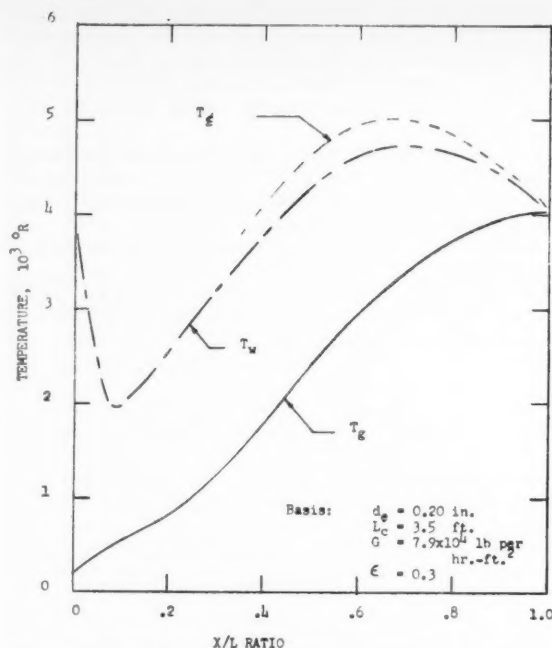


Fig. 1 Axial temperature profiles for cold end reflected nuclear core

by a modified sine curve as defined below

$$(q/S)_x = (q/S)_{\max} \left[\sin \frac{x}{L} \pi - B \left(1 - \sin \frac{mx}{L} \pi \right) \right] \quad [7]$$

From

$$0 \leq x/L \leq 1/2m$$

while from

$$1/2m \leq x/L \leq 1$$

$$(q/S)_x = (q/S)_{\max} \sin \frac{x\pi}{L} \quad [8]$$

For this case, the average heat flux may be expressed as

$$(q/S)_{\text{ave}} = \frac{(q/S)_{\max}}{\pi} \left[2 + \frac{0.57 B}{m} \right] \quad [9]$$

Inserting values of B and m respectively equal to 0.5 and 3, the heat flux and temperature profiles are illustrated in Figs. 1 and 2. Note how the wall temperature at the inlet is raised. This is a consequence of the properties of hydrogen at low inlet temperatures and of the relatively high heat flux at the entrance region which are related in the manner of Eq. 6a. Indeed, this pronounced tendency to a high wall temperature at the inlet area can set a limit, as will be illustrated later. In this respect, an unreflected core end with a simple sine-shape, axial power density will not be thus restricted, whereas there may be a limit to the amount of front end reflector one can add practically. Other schemes for altering the axial power density, such as by fuel loading variation, need to take into consideration this entrance region effect.

Constant wall temperature case

To facilitate analysis in the case of constant wall temperature, further simplifications can be made with the aid of the

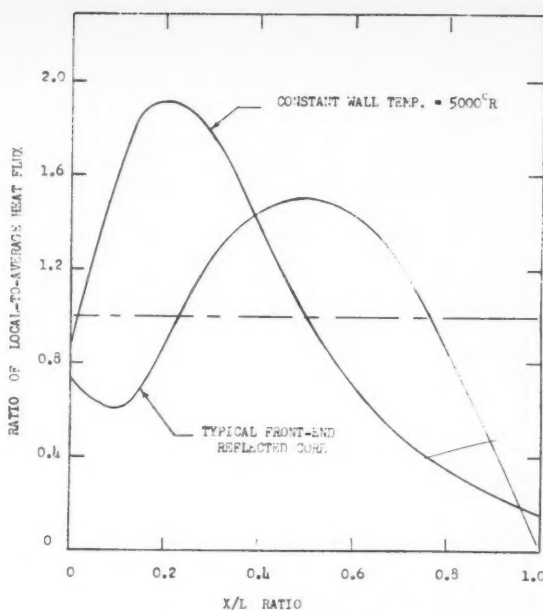


Fig. 2 Ratio of local to average heat flux for end reflected and for constant wall temperature cases

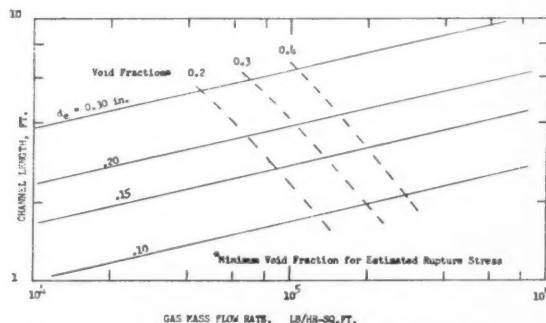


Fig. 3 Design point values of channel length for constant wall temperature of 5000 °R

following relationships

$$\frac{k_f Pr_f^{0.4}}{\mu_f^{0.5}} \equiv \frac{c_p \mu_f^{0.2}}{Pr_f^{0.6}}$$

$$c_p \approx c_{pf}$$

$$\left[\frac{Pr^{0.6}}{\mu^{0.2}} \right]_f \approx 5.5 T_f^{-0.19}$$

for hydrogen in the range of interest. These may be combined together with Eqs. 5a and 6a to obtain

$$\frac{0.042}{d^{1.1} G^{0.2}} \int_0^x \frac{dx}{(x + d_e)^{0.1}} = \int_{T_1}^T \frac{(T_w + T_g) dT_g}{(T_w - T_g) T_g^{0.5}}$$

Finally, let

$$x + d_e \approx x$$

$$\beta = T_g/T_w$$

$$x = (x/L) \cdot L$$

Then for the case of constant T_w

$$\frac{0.042 L^{0.9}}{d_s^{1.1} G^{0.2}} \left(\frac{x}{L} \right)^{0.9} = \frac{1}{T_w^{0.19}} \int_{\beta}^1 \frac{(1 + \beta)^{0.61} d\beta}{(1 - \beta) \beta^{0.8}} \quad [10]$$

By graphical integration one may find the temperature profile as a function of the ratio x/L for a fixed hole diameter, gas flow rate and wall temperature. Now, if the right-hand side of the equation is fixed, the required length is found to be proportional to $d^{1.22}$ and $G^{0.22}$ in the manner of Fig. 3, which also shows the estimated minimum void fraction as set by thermal stress which was determined, as described under the next section, Allowable Heat Flux. The utility of Eq. 10 lies in the quantitative relationship of the variables when the value of the integral is determined.

Similarly, an equation for heat flux along the axis may be shown to be

$$(q/S)_x = \frac{0.005 G^{0.8} T_w^{-1.42} \beta^{0.8} (1 - \beta)}{d^{0.1} (x + d)^{0.1} (1 + \beta)^{0.38}} \quad [11]$$

In Fig. 2, where local to average heat flux curves are presented, the maximum heat flux for the constant wall temperature case is seen to peak to the left of center and to exhibit a large departure from the average heat flux.

Constant centerline temperature case

In this case, the overall heat transfer coefficient U , which takes into account the solid conductivity as well as the coefficient h , is applicable in the usual heat transfer equation. The heat flux profile is shaped somewhat like that of the constant wall temperature case.

Allowable Heat Flux

In a nuclear rocket engine of the type under discussion, a design limit to the rate of heat transfer is set when adverse effects become significant. Thus, the power generation may

be fixed by:

1 Wall temperature above which excessive chemical reactions take place between the solid and the gas coolant.

2 Solid centerline temperature in the region where mechanical strength is unsatisfactory or where undesirable phase change occurs.

3 Excessive dimensional change, plastic deformation or rupture due to thermal stress or strain.

4 Some unforeseen effect of nuclear heating such as gas formation or fission fragment damage.

Evaluation of the first point is made difficult by scarcity of unclassified data on corrosion of carbon by hydrogen at high wall temperatures. There appear references which mention overcoming the chemical attack by coating the wall or with additives to the gas (3). Rom (9) suggests the use of W^{184} , which is believed to be compatible with hydrogen at very high temperatures.

Equations pertaining to wall and centerline temperatures of heat generating solids and thermal stress equations for elastic bodies are given in (2) and (8).

Available data would indicate that other limitations occur before the fourth item need to be considered, nevertheless it is a possibility.

With respect to thermal stress and strain, applicable data are not abundant in the open literature. It would be preferable, of course, to utilize data obtained from a nuclearly heated specimen, but in the absence of such appropriate high temperature high heat flux information in the literature, test results of electrically heated samples have to be used. Experiments along this line have been reported in (10) and (11), and some Los Alamos Laboratory results, together with an analytical solution for externally cooled tubes are given by Kammash (12), who took into account the plastic domain. Some heat transfer correlation papers contain data which indicate high values of heat flux, for example, (6).

However, interpretation of these results is made difficult by such matters as: lack of accurate material property data at high temperatures—even for the same type of sample, there is considerable scatter of data in the case of graphite; the nonuniform heating to be expected in an electrically heated specimen because of the variation in electrical and thermal conductivities with temperature; and the presence of a thermo-plastic region in graphite where transition from the elastic domain is not sharply defined, with the element of operating time entering into the picture. Therefore, further theoretical and experimental investigations would be helpful in the determination of the allowable heat flux.

As an approximation suggestive of the role of variables, the elastic theory of thermal stress was used to convert the flat plate data of (11) to the case of internally cooled, heat generating tubes. A design stress was chosen and the physical properties and dimensions were evaluated at some temperature, so that the allowable solid power density could be related to the void fraction and hole diameter, as graphically represented in Fig. 4. The problem remains, however, of determining the magnitude of allowable heat flux more accurately than by this method, for when this method is applied to the externally cooled tubes of Kammash's paper, the Los Alamos experimental data were several times larger than those obtained by the elastic theory method and data of (12).

Material Properties

Besides data found in references already mentioned, hydrogen and graphite properties given in (13 through 20) were picked for use in the work of this report. Considerable differences among reported values were noted, especially for graphite.

Core Size Parameters

The objective of rocket engine design may be stated as obtaining the highest specific impulse and thrust with the

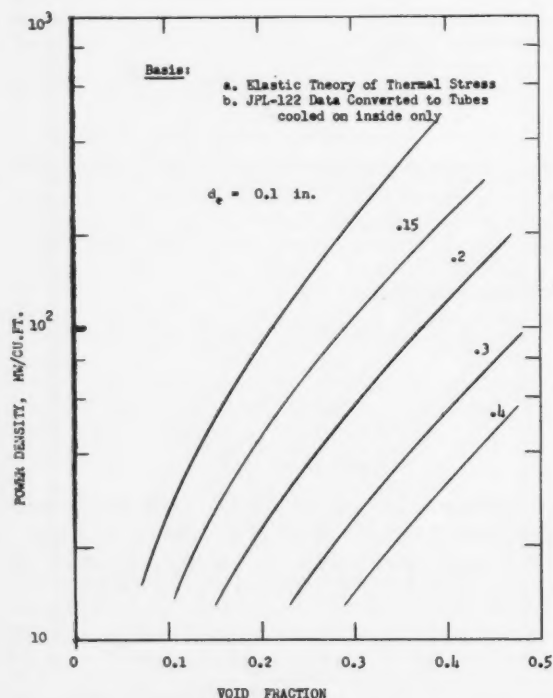


Fig. 4 Solid power density variation with void fraction for various hole diameters of coolant passage

minimum engine weight; however, as pointed out in (4), a compromise must be made between high thrust coefficient and high specific impulse. This will depend on specific mission analysis which is not in the scope of this work. Instead, we will concern ourselves with the important parameters relating to size and performance.

A simple heat balance on our model will show that the reactor core size is given by

$$D_c = \left[\frac{d P}{\pi \epsilon (q/S)_{ave}} \right]^{1/3} \quad [12]$$

where P is total power which is convectively removed by the propellant within the core or by

$$D_c = \frac{d G H}{4 (q/S)_{ave}} \quad [13]$$

From the forementioned equations, it is readily seen that a decrease in core diameter may be effected by going to a smaller hole size. Earlier in the discussion, the allowable heat generation rate was estimated to be related to hole diameter and void fraction in the manner shown in Fig. 4. For a given hole diameter, the permissible average heat flux will also increase with void fraction.

A visual representation of Eq. 12 is given by Fig. 5 for the case of an end reflected reactor core at $P = 1000$ Mw. Rather than the average heat flux, the parameter in the graph uses the maximum heat flux $(q/S)_{max}$. Also included in the graph is a line symbolizing the trend of nucleonic size with void fraction for a given fuel loading. Some compromise solution between nucleonic and heat transfer requirements is thereby indicated.

The power to core weight ratio can also be derived

$$P/W_c = \frac{4 \epsilon (q/S)_{ave}}{(1 - \epsilon) d \rho_s} \quad [14a]$$

where ρ_s denotes core solid density or, simply

$$P/W_c = \frac{\tau_{ave}}{\rho_s} \quad [14b]$$

When the core solid density is known through choice of a suitable core material, Eq. 14b can be used, together with the estimated allowable power density curves of Fig. 4, to obtain probable power to core weight values.

One of the items of interest in rocketry, specific thrust based on core weight, may be expressed as follows

$$F/W_c = \frac{w I_{sp}}{W_c} \quad [15a]$$

$$\alpha \frac{\epsilon G H^{0.5}}{(1 - \epsilon) \rho_s L_c} \quad [15b]$$

One can also divide through by the inlet pressure p_1 to get

$$\frac{F}{p_1 W_c} \propto \frac{\epsilon M_1 H^{0.5}}{(1 - \epsilon) \rho_s L_c} \quad [16]$$

Influence of Axial Power Density Profile

When the limiting factor is the channel wall temperature alone, it will be demonstrated that the constant wall temperature design point operation results in the highest efficiency of attaining the specific impulse associated with the wall temperature. On the other hand, if there is a limit on local heat flux due to thermal stress in one section of the core, while the downstream channel section is restricted by a maximum wall temperature condition, the greater overall power density will be obtained when uniform heat flux heating is applied to the forepart and constant wall temperature is kept at the aft section.

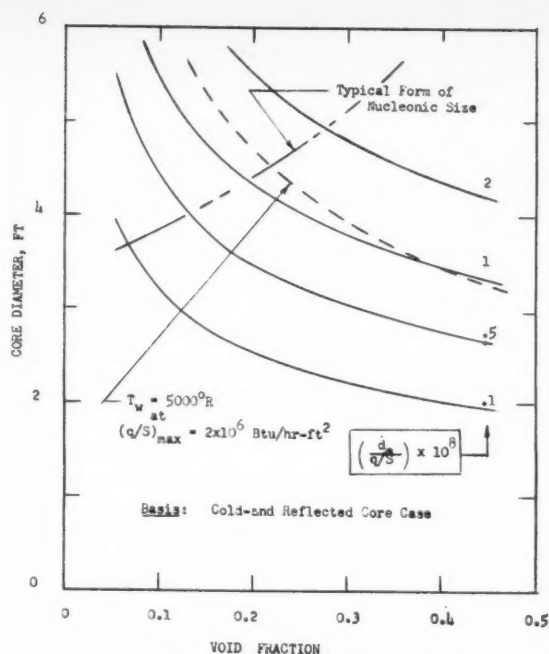


Fig. 5 Reactor size vs. void fraction based on heat transfer requirements for end reflected reactor core

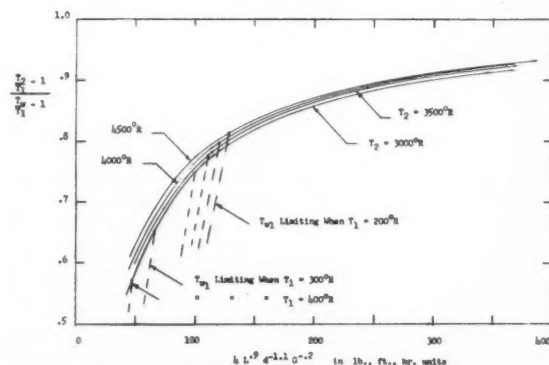


Fig. 6 Heating "efficiencies" for uniform heat flux case

Following the relation expressed by Eq. 10, the approach of the gas temperature to the maximum wall temperature may be compared on the basis of the group $L^{0.9}/d^{1.1} G^{0.2}$. The same expression can be derived for the uniform heat generation case, and bears out the simplified approach of Stenning (4), with the exception to be noted. His representation will be modified, therefore, by plotting $(T_2/T_1 - 1)/(T_{w \max}/T_1 - 1)$ against $L^{0.9}/d^{1.1} G^{0.2}$. (The analogy between his expression and this is seen to lie in the fact that the friction factor f is inversely proportional to $G^{0.2}$.)

To illustrate the influence of system variables, Fig. 6 is presented for the uniform heat generation case. Since the basic model ignores axial conduction and end heat losses, the analysis indicates that inlet gas temperature can restrict the heat removal of a typical nuclear rocket engine. For a given constant exit gas temperature and low gas mass flow rate, one may start from the right side of the graph and proceed to the left as the reactor power (and hence gas flow rate) is increased for a given core, until the condition is reached when

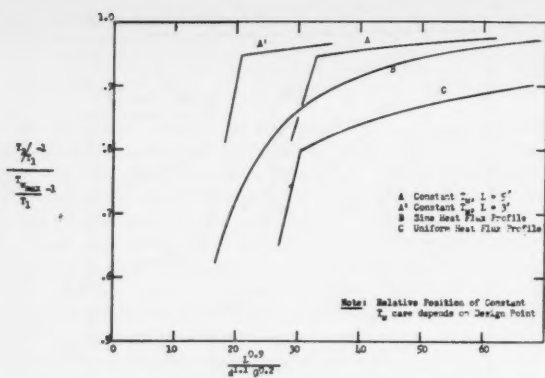


Fig. 7 Relative "efficiencies" of various axial heat flux profiles for 4000 °R hydrogen gas

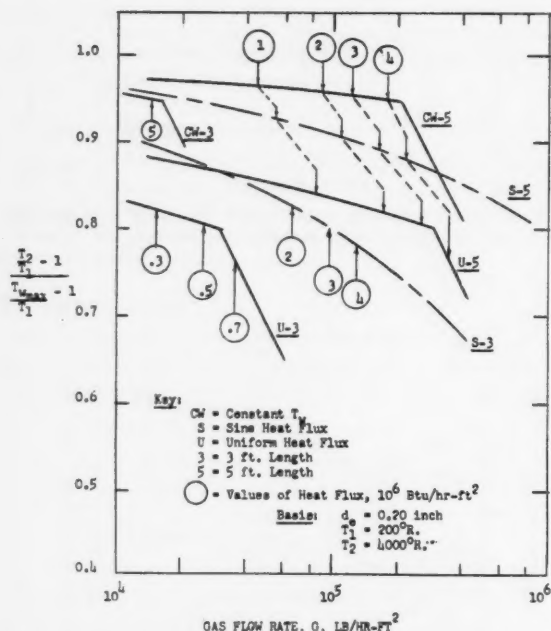


Fig. 8 Further comparison among modes of heating to show effects of channel length and gas flow rate

the entrance wall temperature becomes the limiting one, after which the temperature ratio of the ordinate drops steeply. This is the noted difference between the simplified approach of (4) and the present detailed one. This restriction occurs earlier the colder the inlet gas temperature. Hence, it pays to warm up the coolant before it enters the core.

The variation with exit gas temperature is seen to be small. In Fig. 7 the axial heat flux profile may be observed to have a strong influence on the attainment of the maximum possible gas temperature or specific impulse as limited by the maximum wall temperature. It will be remarked that the relative position of the constant wall temperature case depends on the design point chosen, and deviation from the design point implies that the wall temperature is no longer constant. Nevertheless, the order of "efficiency" is interesting to observe in the graph: A, B, C.

Although not shown in Fig. 7, the case where the front end is reflected (in addition to the sides) lies intermediate in position between the plain sine profile and the design point constant wall temperature case.

Still referring to the same graph, we note again the marked influence of the limiting inlet wall temperature on the cases of Curves A, A' and C. Curve B, of course, is not similarly affected because the heat flux starts from zero at the entrance.

If the same information is plotted as shown in Fig. 8, the influence of channel length is made more apparent. Values of the maximum heat fluxes were also indicated on each curve. Provided that the maximum allowable heat flux is not exceeded, heat transfer and weight considerations indicate the desirability of having L/D greater than one. There is a favorable trade-off in gas mass flow rate increase by going to a longer channel length, resulting in greater thrust to weight ratio, as found by Eq. 15b. On the other hand, counterbalancing such a move are the limiting allowable heat flux and the increased pressure drop for the longer channel.

The desirability of small channel diameter is also evident from the parameter used as abscissa in Figs. 6 and 7.

Another useful function of plots just mentioned is that end conditions may be inferred from them for off design operation. For example, if the same inlet and exit gas temperatures are to be maintained while core power and gas mass flow rate are varied proportionately, the maximum wall temperature may be found from the ordinate parameter.

Now, considering the case mentioned at the beginning of this section where a given core may be faced with both heat flux and wall temperature limitations, it may be shown under certain practical conditions that a higher average power density is achieved by combining the uniform heat generation

Table 1 Core thrust to weight ratio comparisons between heating schemes

T_w , °R	Limitations assumed		T_2/T_w	Heating profile ^a	d_c , in.	T_1^b , °R	G , lb hr-ft ²	L_c , ft	$(F/W)_A/(F/W)_B$
	q/S , 10 ³ Btu hr-ft ²	Void							
5000	2.6	...	0.95	A	0.1	4100	1.75	2.66	1.7
5000	2.6	...	0.95	B	0.1	...	0.59	1.50	...
5000	1.0	...	0.95	A	0.2	4100	0.63	5.0	1.6
5000	1.0	...	0.95	B	0.2	...	0.22	2.8	...
3400	...	0.1	0.95	A	0.1	2800	1.50	3.50	1.6
3400	...	0.1	0.95	A	0.1	2500	0.86	2.35	1.4
3400	...	0.1	0.95	B	0.1	...	0.42	1.55	...
3400	...	0.3	0.95	A	0.1	2800	4.16	4.50	1.5
3400	...	0.3	0.95	A	0.1	2500	2.48	2.88	1.4
3400	...	0.3	0.95	B	0.1	...	1.19	1.95	...

^a Scheme A: Uniform heat flux followed by constant wall temperature heating. Scheme B: Constant wall temperature heating only.

^b Temperature of gas at end of uniform heat flux section.

scheme with the constant wall temperature axial profile. To be practical, the channel diameter should be small enough so that the increase in channel length can be tolerated, since nuclear considerations favor L/D ratio close to one, while core diameter has a practical limit too. Examples of the calculated favorable power density increase for special cases are given in Table 1. Further use of Eq. 15b with the information in Table 1 shows that the thrust to weight ratio at 0.3 void fraction is about eight times that as 0.1 void fraction.

As higher temperatures and heat fluxes become permissible, the limiting factor will become the maximum allowable centerline temperature of the solid fuel elements. If this is true along the entire channel length, the most efficient heating scheme will then be that of constant solid centerline temperature.

Pressure Level and Friction Loss

Thus far the influence of pressure has been avoided in the interest of clarity, but in forced convection heat transfer the fluid flow characteristics must be examined. We shall consider how the ratio of exit to inlet pressure and Mach number are affected by the pressure level. In the cryogenic temperature region, pressure level has significant effects on hydrogen gas properties, but since the gas is heated up very quickly near the entrance of the flow channel, its influence has been regarded as second order and neglected.

For hydrogen gas in turbulent flow through the model core, the pressure drop for the channel, not including entrance and exit losses, may be estimated by standard equations, but because of the large change in gas density along the flow channel, such equations should be used over incremental lengths and each incremental pressure drop summed to yield the overall result. An iterative solution must be performed, using the total temperature (calculated by the previous heat transfer equations), assumed Mach number and the ideal gas law to relate density to static temperature and pressure. A computer solution would be a time saver if many increments and problems are involved. A set of solutions indicated that the pressure ratio p_2/p_1 and exit Mach number M_2 were related to the initial Mach number M_1 in the manner of Fig. 9. As a matter of interest, for a fixed inlet temperature T_1 , the initial Mach number is proportional to G/p_1 ; therefore, for a given gas mass flow rate, the exit Mach number increases if pressure is decreased, until sonic velocity is reached. At a given gas temperature and in turbulent flow regime if the ratio of G/p_1 is maintained constant, the exit Mach number is relatively unaffected.

Experimental values of friction coefficient generally are obtained as the average over the entire length of the test section, and local values of f under conditions of sizable T_w/T_o ratios are not readily found.

Average friction coefficients reported in (7) and (21) suggest that the ratio T_w/T_o does affect the correlation; but for the present work the Colburn-Reynolds analogy was deemed adequate.

Other Considerations of Parameter Effects

Besides their effects on size from the heat transfer viewpoint, the variables mentioned are related to nucleonic and other considerations, requiring a careful analysis before choosing a set of conditions. Some of the implications will be touched upon here.

Void fraction

According to Eq. 12, a large value of void fraction leads to small core size, where void fraction is the fraction of the core volume occupied by the gas channel. Other factors being constant, the neutronic critical size increases with void fraction in the manner illustrated by a dotted line in Fig. 5. Since there may be practical limits to increasing fuel loading

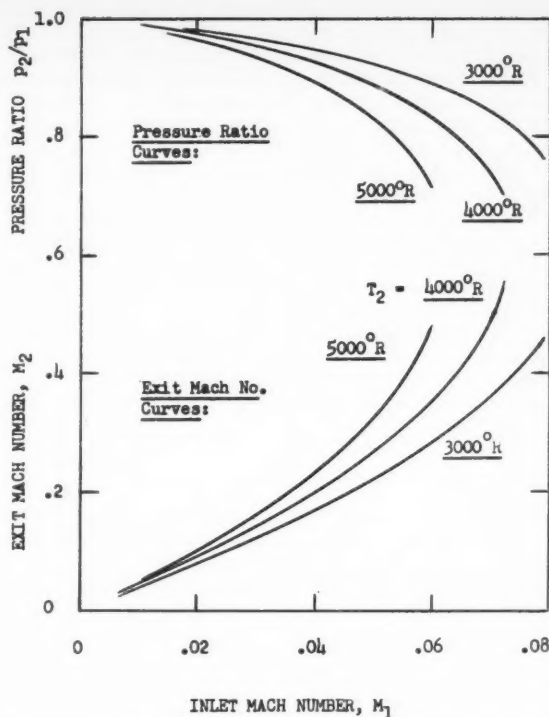


Fig. 9 Exit Mach numbers and ratios of exit to inlet total pressures as functions of inlet Mach number for various gas temperatures

and reflector thickness to offset the effect of larger void, some balance must be reached between heat transfer and neutronic requirements. Furthermore, at high fuel loadings the control system may become more complex to cope with the intermediate to fast reactor.

Although the allowable heat tends to increase with void fraction, the solid web thickness may become so thin that mechanical strength or fabrication difficulties become limiting.

Hole diameter

While small hole size would alleviate heat removal restrictions, here again the matter of fabrication difficulty may set the lower limit. In addition, the total number of holes would increase as hole size decreased and void fraction were kept constant. If the flow channel were constructed from short sections, exact alignment of the holes becomes more critical as hole size decreases. Pressure drop varies inversely with the hole size; so again a compromise is indicated.

Temperature level

While high exhaust gas temperature is desired for its high specific impulse, it was previously mentioned that adverse chemical reactions, mechanical strength and thermal properties were likely to set some upper temperature limit within the core. It is to be noted, too, that with the expected negative temperature coefficient of reactivity, additional reactivity for this effect must be provided.

Heat loss from the core is also accentuated as temperature level increases, presenting a greater cooling problem.

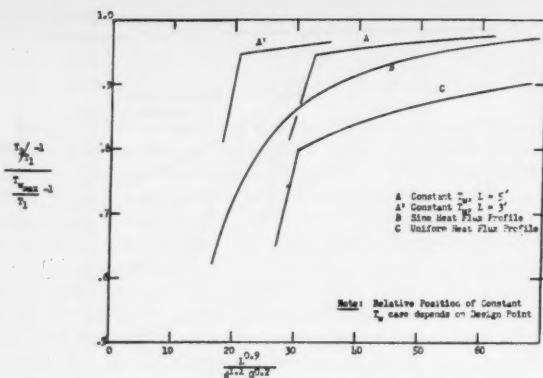


Fig. 7 Relative "efficiencies" of various axial heat flux profiles for 4000 °R hydrogen gas

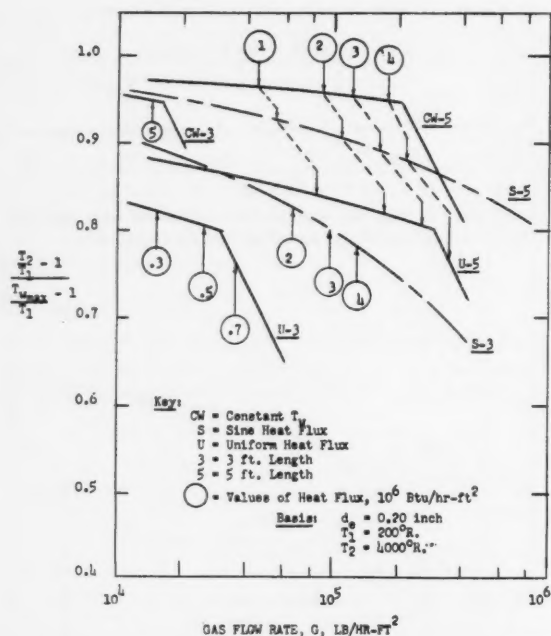


Fig. 8 Further comparison among modes of heating to show effects of channel length and gas flow rate

the entrance wall temperature becomes the limiting one, after which the temperature ratio of the ordinate drops steeply. This is the noted difference between the simplified approach of (4) and the present detailed one. This restriction occurs earlier the colder the inlet gas temperature. Hence, it pays to warm up the coolant before it enters the core.

The variation with exit gas temperature is seen to be small. In Fig. 7 the axial heat flux profile may be observed to have a strong influence on the attainment of the maximum possible gas temperature or specific impulse as limited by the maximum wall temperature. It will be remarked that the relative position of the constant wall temperature case depends on the design point chosen, and deviation from the design point implies that the wall temperature is no longer constant. Nevertheless, the order of "efficiency" is interesting to observe in the graph: A, B, C.

Although not shown in Fig. 7, the case where the front end is reflected (in addition to the sides) lies intermediate in position between the plain sine profile and the design point constant wall temperature case.

Still referring to the same graph, we note again the marked influence of the limiting inlet wall temperature on the cases of Curves A, A' and C. Curve B, of course, is not similarly affected because the heat flux starts from zero at the entrance.

If the same information is plotted as shown in Fig. 8, the influence of channel length is made more apparent. Values of the maximum heat fluxes were also indicated on each curve. Provided that the maximum allowable heat flux is not exceeded, heat transfer and weight considerations indicate the desirability of having L/D greater than one. There is a favorable trade-off in gas mass flow rate increase by going to a longer channel length, resulting in greater thrust to weight ratio, as found by Eq. 15b. On the other hand, counterbalancing such a move are the limiting allowable heat flux and the increased pressure drop for the longer channel.

The desirability of small channel diameter is also evident from the parameter used as abscissa in Figs. 6 and 7.

Another useful function of plots just mentioned is that end conditions may be inferred from them for off design operation. For example, if the same inlet and exit gas temperatures are to be maintained while core power and gas mass flow rate are varied proportionately, the maximum wall temperature may be found from the ordinate parameter.

Now, considering the case mentioned at the beginning of this section where a given core may be faced with both heat flux and wall temperature limitations, it may be shown under certain practical conditions that a higher average power density is achieved by combining the uniform heat generation

Table 1 Core thrust to weight ratio comparisons between heating schemes

T_w , °R	Limitations assumed		T_2/T_w	Heating profile ^a	d_e , in.	T_2^b , °R	G , lb/hr-ft ²	L_c , ft	$(F/W)_A/(F/W)_B$
	q/S , Btu/hr-ft ²	Void							
5000	2.6	...	0.95	A	0.1	4100	1.75	2.66	1.7
5000	2.6	...	0.95	B	0.1	...	0.59	1.50	...
5000	1.0	...	0.95	A	0.2	4100	0.63	5.0	1.6
5000	1.0	...	0.95	B	0.2	...	0.22	2.8	...
3400	...	0.1	0.95	A	0.1	2800	1.50	3.50	1.6
3400	...	0.1	0.95	A	0.1	2500	0.86	2.35	1.4
3400	...	0.1	0.95	B	0.1	...	0.42	1.55	...
3400	...	0.3	0.95	A	0.1	2800	4.16	4.50	1.5
3400	...	0.3	0.95	A	0.1	2500	2.48	2.88	1.4
3400	...	0.3	0.95	B	0.1	...	1.19	1.95	...

^a Scheme A: Uniform heat flux followed by constant wall temperature heating. Scheme B: Constant wall temperature heating only.

^b Temperature of gas at end of uniform heat flux section.

scheme with the constant wall temperature axial profile. To be practical, the channel diameter should be small enough so that the increase in channel length can be tolerated, since nuclear considerations favor L/D ratio close to one, while core diameter has a practical limit too. Examples of the calculated favorable power density increase for special cases are given in Table 1. Further use of Eq. 15b with the information in Table 1 shows that the thrust to weight ratio at 0.3 void fraction is about eight times that as 0.1 void fraction.

As higher temperatures and heat fluxes become permissible, the limiting factor will become the maximum allowable centerline temperature of the solid fuel elements. If this is true along the entire channel length, the most efficient heating scheme will then be that of constant solid centerline temperature.

Pressure Level and Friction Loss

Thus far the influence of pressure has been avoided in the interest of clarity, but in forced convection heat transfer the fluid flow characteristics must be examined. We shall consider how the ratio of exit to inlet pressure and Mach number are affected by the pressure level. In the cryogenic temperature region, pressure level has significant effects on hydrogen gas properties, but since the gas is heated up very quickly near the entrance of the flow channel, its influence has been regarded as second order and neglected.

For hydrogen gas in turbulent flow through the model core, the pressure drop for the channel, not including entrance and exit losses, may be estimated by standard equations, but because of the large change in gas density along the flow channel, such equations should be used over incremental lengths and each incremental pressure drop summed to yield the overall result. An iterative solution must be performed, using the total temperature (calculated by the previous heat transfer equations), assumed Mach number and the ideal gas law to relate density to static temperature and pressure. A computer solution would be a time saver if many increments and problems are involved. A set of solutions indicated that the pressure ratio p_2/p_1 and exit Mach number M_2 were related to the initial Mach number M_1 in the manner of Fig. 9. As a matter of interest, for a fixed inlet temperature T_1 , the initial Mach number is proportional to G/p_1 ; therefore, for a given gas mass flow rate, the exit Mach number increases if pressure is decreased, until sonic velocity is reached. At a given gas temperature and in turbulent flow regime if the ratio of G/p_1 is maintained constant, the exit Mach number is relatively unaffected.

Experimental values of friction coefficient generally are obtained as the average over the entire length of the test section, and local values of f under conditions of sizable T_w/T_g ratios are not readily found.

Average friction coefficients reported in (7) and (21) suggest that the ratio T_w/T_g does affect the correlation; but for the present work the Colburn-Reynolds analogy was deemed adequate.

Other Considerations of Parameter Effects

Besides their effects on size from the heat transfer viewpoint, the variables mentioned are related to nucleonic and other considerations, requiring a careful analysis before choosing a set of conditions. Some of the implications will be touched upon here.

Void fraction

According to Eq. 12, a large value of void fraction leads to small core size, where void fraction is the fraction of the core volume occupied by the gas channel. Other factors being constant, the neutronic critical size increases with void fraction in the manner illustrated by a dotted line in Fig. 5. Since there may be practical limits to increasing fuel loading

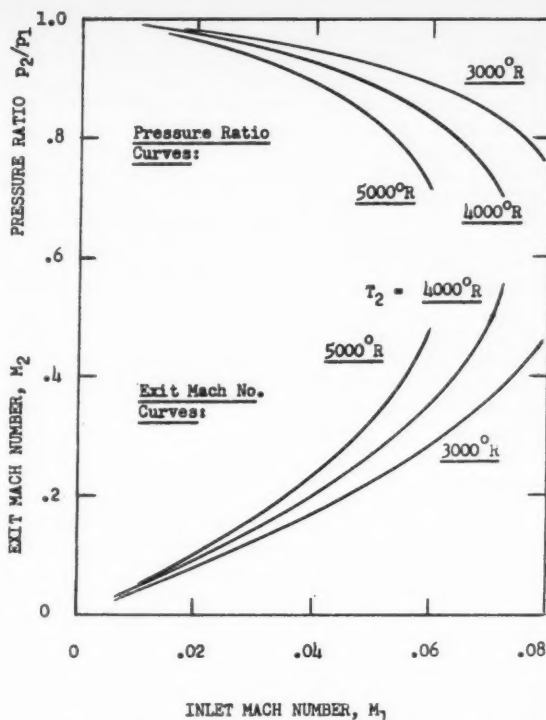


Fig. 9 Exit Mach numbers and ratios of exit to inlet total pressures as functions of inlet Mach number for various gas temperatures

and reflector thickness to offset the effect of larger void, some balance must be reached between heat transfer and neutronic requirements. Furthermore, at high fuel loadings the control system may become more complex to cope with the intermediate to fast reactor.

Although the allowable heat tends to increase with void fraction, the solid web thickness may become so thin that mechanical strength or fabrication difficulties become limiting.

Hole diameter

While small hole size would alleviate heat removal restrictions, here again the matter of fabrication difficulty may set the lower limit. In addition, the total number of holes would increase as hole size decreased and void fraction were kept constant. If the flow channel were constructed from short sections, exact alignment of the holes becomes more critical as hole size decreases. Pressure drop varies inversely with the hole size; so again a compromise is indicated.

Temperature level

While high exhaust gas temperature is desired for its high specific impulse, it was previously mentioned that adverse chemical reactions, mechanical strength and thermal properties were likely to set some upper temperature limit within the core. It is to be noted, too, that with the expected negative temperature coefficient of reactivity, additional reactivity for this effect must be provided.

Heat loss from the core is also accentuated as temperature level increases, presenting a greater cooling problem.

Pressure level

Under the section discussing Pressure Level and Friction Loss the favorable effects of high pressure level on core pressure drop and on gas Mach number were presented. On the other hand, an increase in pressure level means greater weight of the pressure shell around the reactor and of associated plumbing. Furthermore, it implies more work diverted for pumping purpose.

At high altitudes where the ambient pressure is practically zero, the nozzle pressure ratio is determined by the chamber gas temperature and the nozzle area expansion ratio so that with the latter variables fixed an increase in chamber pressure does not increase the I_{sp} , but it does increase the nozzle flow rate and hence engine thrust. Operation at low chamber pressure tends to increase the molecular dissociation and hence I_{sp} , but for practical missions which require large thrust the low pressure system would result in an engine size too large.

Power level

With nuclear reactors, the radiation level increases with power, so shielding weight will increase and radiation heating and damage problems become more acute.

If a limiting power density is attained, further increase in power must be accommodated by an increase in reactor size and pressure vessel.

Power density profile

In a previous section the heat transfer aspects of modifying the axial power density profile were discussed. The advantages to be gained may be offset by the more complicated neutronic analysis and effects of nonuniform fuel loading. Certainly the fabrication and assembly of the core are made more complex, and it may be that such changes in fuel loading are limited. Similarly, the prediction of neutronic characteristics by the computer may become quite expensive. A secondary effect on the heat loss from the core boundary is expected, too.

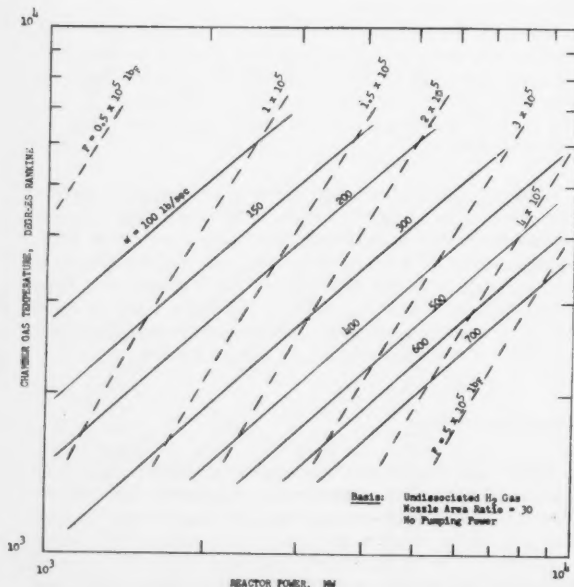


Fig. 10 Theoretical performance of nuclear engine. Constant flow rate and constant thrust lines as functions of temperature and power

Basic data

The importance of basic data and correlations is reflected in the reliability of the design limit figures. In the pioneering effort of nuclear rocket engine development, there still appears to be inadequate information on material properties. It is hoped, too, that correlations can be improved so that greater resolution of parameters can be made. On the basis of unclassified literature, it seems that some materials property data and allowable heat flux information are tenuous. Sometimes, present theory or the extrapolation of existing data may differ significantly from the true values. This seems to have been the case for thermal conductivity of hydrogen at high temperature, judging from the recent data in LA-2316 (14). Other undetermined properties then become questionable. If the recent thermal conductivity data is used to calculate Prandtl number, the usual assumption of constant Pr is no longer a good approximation over the range of temperature involved. To cite another example, graphite property measurements at high temperature exhibit considerable variance of data, leading to uncertainty in the estimation of the heat generation rate limit due to thermal stress and strain. It would be desirable to more firmly establish the trend for allowable power density to increase with solid temperature which was indicated by data in the JPL Report 122 (11). In the area of fluid flow with heat transfer, the transition point from turbulent to laminar flow under conditions of high heat transfer rates might be established with greater accuracy than now.

Off Design Operations

For the hydrogen cooled nuclear rocket, the theoretical values of gas weight flow rate and resultant thrust may be determined for a given chamber stagnation temperature and reactor power by the usual rocket equations and through the use of theoretical specific impulses. In Fig. 10 such information has been plotted as constant weight flow rate and constant thrust lines on temperature reactor power chart. Reactor power refers to the power required to heat liquid hydrogen at 1 atm boiling point temperature to the chamber temperature, while thrust is based on the theoretical specific impulse of isentropically expanding, undissociated hydrogen in a nozzle with an area ratio of 30. Pumping power was disregarded. If power is fixed, the thrust varies inversely as the specific impulse and there is some latitude for trade-off between the last two items.

Even if power is not kept constant, thrust may be increased at the expense of specific impulse. Referring to the curves of either Fig. 6 or Fig. 7, the temperature ratio can be decreased to permit greater gas mass flow rate for a given reactor. Assuming that pumping capacity is not exceeded, there are portions of the curves where the increase in flow rate is faster than the decrease in specific impulse resulting from reduced temperature operation. This is clear if it is assumed that T_w max is fixed.

The degree to which the gas temperature should approach the solid wall temperature at the design point requires a system optimization study which is beyond the scope of this report. Before leaving this subject, however, it will be added that a separate study indicates that when the reactor is operating near its maximum allowable power density, there would be no advantage in increasing thrust at the expense of the specific impulse. But if reactor operation is limited only by wall temperature and not by power density considerations over the range to be analyzed, then the considerable increase in thrust gained by operating at a lower temperature and increasing the gas flow rate and total power makes such a move attractive under certain conditions. It may be shown using Eq. 10 that, in the manner just described, thrust can be doubled as the ratio of T_2/T_w is reduced from 0.95 to 0.90.

Let us now consider off-design aspects such as reduced power operation or changes made feasible by advances in technology.

Reduced Power Operation

Someone has suggested that flight testing of a nuclear rocket can be made at a fraction of some design point power, a power which should be large enough for heavy payload missions and be competitive with chemical propulsion. It is presumed that the exhaust gas temperature will be the same as the design point value, signifying that the gas flow rate is at a fraction of the design value, together with power density. This means that the axial profile of the solid temperature will be lower than that of the design point, especially in the front portion of the core. Furthermore, it is suggested that, assuming present technology is limited by the solid wall temperature, when higher temperatures are possible in the future, the same sized reactor will be still usable under the new conditions.

Assume a full power design point of 10,000 Mw and chamber temperature of 4000 °R. This means a gas flow rate of 653 lb/sec and resultant thrust of 5.18×10^6 lb. For a flight test it may be desired to operate at one tenth design power with the same 4000 °R temperature, requiring a gas flow rate of 65.3 lb/sec. Can this be done? The answer is yes, if the Reynolds number of the reduced power run is above that at transition from turbulent to viscous flow, or about 5000. This means the design point Reynolds number should be at least 50,000. At reduced power, the operating pressure will decrease nearly proportionally with the decrease in gas flow rate, so sonic choke can be avoided by choosing the proper design point Mach number with this in mind. This throttling capability may, however, be restricted by some other consideration such as pump characteristics.

The above discussion also holds true for reduced power operation during actual mission flight, such as in the early cooling period to remove fission product decay heat.

If some values of the design limitations assumed in this paper were to become raised, what kind of improvement in engine performance might one expect from just the heat transfer considerations? Quite significant improvement may be expected for the graphite cone if thermal conductivity and resistance to hydrogen attack are raised.

An increase in operating temperature certainly implies that specific impulse would be increased due to the higher gas temperature possible. As for the allowable heat generation rate due to thermal stress rupture, the previously mentioned JPL-122 data indicates that the allowable heat flux would increase nearly proportionately with temperature up to about 5500 °R if a limiting centerline temperature is not reached in the change. Further experimental verification on this point is desirable.

An improvement in allowable heat flux alone with a fixed, limiting wall temperature would not be expected to improve the specific impulse, but a higher specific thrust or greater power density is made possible up to the point when solid centerline temperature may become limiting.

A change in material which would permit a higher chamber gas temperature while resulting in higher specific impulse, would have to be examined to see if the density and allowable heat generation rate would result in improvement of thrust to weight.

As noted in the opening paragraph of this report, the present observations are confined to a narrow aspect of nuclear propulsion system design. An overall system optimization will entail a much more involved study.

Summary and Conclusions

By means of detailed analyses of the heat transfer process in a typical model of a nuclear rocket engine, the influence of core design parameters were studied. Power density limitations were estimated and related to equivalent coolant channel diameter and core void fraction.

Typical axial power density profiles were also compared for efficiency as defined in the text. It was shown that the

core with constant wall temperature was desirable if the only restriction to heat removal was a limiting wall temperature. But, if in addition there happened to be some critical allowable heat flux limit, a combined approach is better. In this case, with due correction for the entrance effect, the power density in the front portion should operate close to the allowable value, while the downstream zone should operate near the allowable wall temperature.

This study also indicated that the nuclear engine is capable of considerable throttling capability and that it should be possible to operate at a reduced I_{sp} , but higher thrust under nondesign point conditions.

Acknowledgment

The counsel and encouragement given by H. F. Plank in preparing this paper is gratefully acknowledged.

Nomenclature

B	= constant
c_p	= specific heat
C	= constant
d	= channel hole diameter
D_c	= core diameter
f	= friction coefficient
F	= propellant thrust
G	= mass flow rate of coolant per unit flow area
h	= heat transfer coefficient of gas film at channel wall
H	= gas enthalpy
I_{sp}	= specific impulse of propellant
k	= thermal conductivity
L_c	= length of coolant channel or core
m	= constant
M	= Mach number of coolant gas
p	= gas pressure
P	= total power absorbed by gas in core except where noted
Pr	= Prandtl number
q	= heat transfer rate
S	= heat transfer surface area
t	= static temperature of gas
T	= total or stagnation temperature of gas
T_{aw}	= "adiabatic wall" temperature
T_f	= gas film temperature
T_g	= gas temperature as defined in text
T_w	= channel wall temperature
\dot{w}	= gas flow rate, mass per unit time
W_c	= core weight
x	= distance downstream from entrance of coolant channel
β	= T_g/T_w
γ	= ratio of specific heats of gas
ϵ	= void fraction of core
μ	= gas viscosity
ρ	= density
Φ	= parameter described in text

Subscripts

1	= inlet to coolant channel
2	= exit from coolant channel
ave	= average
f	= "film temperature" condition
s	= refers to solid material of core
x	= local value at point x

References

- 1 Levy, M. M. and Newgard, S. J., "Rocket Reactor Design," *Nuclear Engineering*, vol. 16, July 1958, pp. 66-68.
- 2 Bussard, R. W. and DeLauer, R. D., *Nuclear Rocket Propulsion*, McGraw-Hill Book Co., Inc., N. Y., 1958.
- 3 Durham, F. P., "Solid-Core Nuclear Rocket Design," *ASTRONAUTICS*, vol. 4, October 1959, pp. 26, 27, 102-104.
- 4 Stenning, A. H., "Rapid Approximate Method for Analyzing Nuclear Rocket Performance," *ARS JOURNAL*, vol. 30, February 1960, pp. 169-72.
- 5 Lapidus, M. E. and Goldstein, M. B., "Heat Transfer Source File Data," APEX-425, September 1957.
- 6 Durham, F. P., Neal, R. C. and Newman, H. J., "High Temperature Heat Transfer to a Gas Flowing in Heat Generating Tubes with High Heat Flux," presented at Reactor Heat Transfer Conf., N. Y., Nov. 1 and 2, 1956.

7 Taylor, M. F. and Kirchgessner, T. A., "Measurements of Heat-Transfer and Friction Coefficient for Helium Flowing in a Tube at Surface Temperatures up to 5900° R," presented at ARS Semi-Annual Meeting, San Diego, Calif., June 8-11, 1959 (ARS preprint 850-59).

8 Field, F. A., "Temperature Gradient and Thermal Stresses in Bodies with Uniformly Distributed Volume Heat Sources," AEC-D-3650, February 1955.

9 Rom, F. E., "Advanced Reactor Concepts for Nuclear Propulsion," *ASTRONAUTICS*, vol. 4, October 1959, p. 46.

10 Powell, W. B. and Massier, P. F., "Heat Flux-Rupture Limits with Internal Heat Generation of Several Graphites up to 5000°F," Jet Propulsion Laboratory Progress Rep. no. 20-322, Calif. Inst. of Technology, June 10, 1957.

11 Powell, W. B., "Heat Flux Rupture with Internal Heat Generation of Graphites," prepared by Los Alamos Scientific Laboratory of the Univ. of Calif., Jet Propulsion Lab. Publ. no. 122, Feb. 27, 1958.

12 Kammas, T., "Elastic-Plastic Thermal Stresses in Tubes Subjected to Uniform Heat Generation Evaluation of Experimental Results Obtained Using Graphite Tubes," *Nuclear Science and Engineering*, vol. 7, May 1960, pp. 425-434.

13 *Handbook of Chemistry and Physics*, Chemical Rubber Publication Co., Cleveland, 40th ed., p. 2288.

14 Mann, J. B. and Blais, N. C., "Thermal Conductivity of Helium and Hydrogen at High Temperatures," L.A.-2316, OTS, U. S. Dept. of

Commerce, Wash., D. C., September 1959.

15 Rossini, F. D., *Thermodynamics and Physics of Matter*, Princeton Univ. Press, 1955, pp. 374-375.

16 Chelton, D. B. and Mann, D. B., *Cryogenic Data Book*, UCRL-3421, May 15, 1956.

17 Green, L., Jr., Stehsel, M. L. and Waller, C. E., "Measurements of Mechanical Properties of Pure and Uranium-Loaded Graphites at Elevated Temperatures," Aerojet-General Corp. Rep. no. 1537, Dec. 23, 1958.

18 Hove, J. E., "Some Physical Properties of Graphite as Affected by High Temperature and Irradiation," presented at the American Nuclear Society Meeting, N. Y., Fall 1957.

19 Wagner, P., Driesner, A. R. and Kmetko, E. A., "Some Mechanical Properties of Graphite in the Temperature Range 20 to 3000° C," *Proc. Second U. N. International Conf. on Peaceful Uses of Atomic Energy*, vol. 7, U. N., Geneva, 1958, pp. 378-388; excerpts appearing in *J. Appl. Phys.*, vol. 30, no. 2, 1959, pp. 148-151, 152-154. (Work Performed at Los Alamos Scientific Laboratory, Univ. of Calif., Los Alamos, New Mexico.)

20 Currie, L. M., Hamister, V. C. and MacPherson, H. G., "The Production and Properties of Graphite for Reactors," National Carbon Co., paper presented at the UN International Conf. on the Peaceful Uses of Atomic Energy, Geneva, Switzerland, Aug. 8-20, 1955.

21 Fowler, J. M. and Warner, C. F., "Measurements of the Heat Transfer Coefficients for Hydrogen Flowing in a Heated Tube," *ARS JOURNAL*, vol. 30 no. 3, March 1960, p. 267.

Experimental Study of Flow and Separation in Vortex Tubes With Application to Gaseous Fission Heating

J. J. KEYES Jr.¹

Oak Ridge National Laboratory
Oak Ridge, Tenn.

An experimental investigation of the flow in simple jet driven vortex tubes under conditions dynamically similar to those estimated to be necessary for operation of a vortex cavity reactor has indicated that viscous retardation of the vortex motion near the periphery is severe. Estimates of virtual viscosities and skin friction coefficients based on an assumed two dimensional flow field have been correlated in terms of the peripheral tangential Reynolds number based on the tube diameter. Friction coefficients so defined for vortex flow appear to be high by a factor of about two compared with those for turbulent flow along a flat plate with zero pressure gradient. Observed tangential velocities are compared with theoretical calculations for viscous vortex flow in terms of the turbulent radial Reynolds number. This comparison suggests that virtual viscosity probably decreases with decreasing radius. Extrapolation of the experimental results to typical reactor operating conditions as calculated by Kerrebrock and Meghreblian has indicated the need for small diameter tubes and recirculation of a large fraction of the inlet gas in order to achieve adequate vortex strength without exceeding an allowable exit mass flow rate. Quantitative measurements of concentration profiles for separation of helium and a heavy fluorocarbon vapor were made using a radial gas sampling probe and thermal conductivity analysis. The data are compared with laminar flow separation theory.

THE FEASIBILITY of utilizing a vortex field to contain a fissioning gas is strongly dependent upon the magnitude of the tangential velocities that can be generated at low propellant mass flow rates. It was shown by Kerrebrock and Meghreblian (1)² that it should be possible to obtain

vortices of sufficient strength for separation of U and H₂, provided the flow field remained laminar. The effects of turbulence were not included in the analysis.

In order to achieve criticality in gaseous reactors, it is necessary that the ratio of fissionable material density to propellant density be large in the fuel zone, and that the propellant pressure be high (2). Since the tangential velocity required for separation is also high, the characteristic Reynolds number for the flow will be large and turbulence will most likely exist. Furthermore, the diffusional velocity of

¹ Presented at the ARS 15th Annual Meeting, Washington, D. C., Dec. 5-8, 1960; revision received July 5, 1961.

² Development Engineer.

³ Numbers in parentheses indicate References at end of paper.

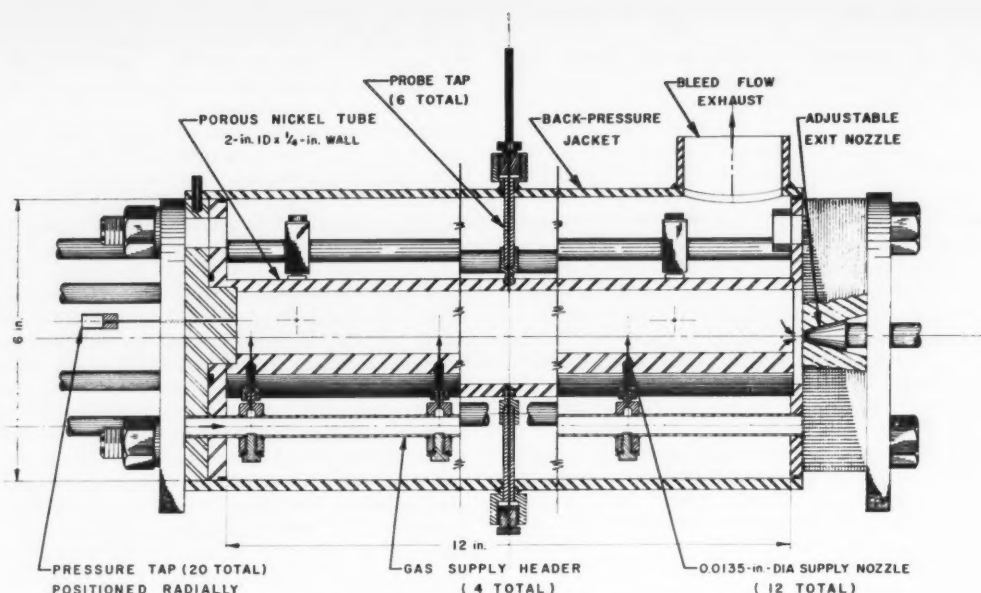


Fig. 1 2-in. porous vortex tube assembly

propellant through the fuel zone limits the exit mass flow rate to a very low value. There is obviously a limit also to the amount of energy which can be expended in maintaining the vortex. These factors impose severe limitations on the operation of gaseous vortex cavity reactors.

An experimental program at the Oak Ridge National Laboratory had as its objective the study of flow and separation in jet driven vortex tubes under conditions estimated to be dynamically similar to those believed necessary for reactor operation. This program included both an exploratory gas dynamics investigation, in which the effects on vortex strength of such variables as tube diameter, pressure, temperature, mass flow rate and injection velocity were investigated, and a preliminary separation study. Details of the experimental work at ORNL are presented in (3,4,5). This paper summarizes the major results of the investigation, with an interpretation of the gas dynamics studies in terms of the application to a gaseous reactor for rocket propulsion. Experimental work carried out by the NASA is described by Ragsdale (6).

Apparatus

Experiments were carried out in tubes ranging in size from about 0.3 in. to 2.0 in. ID, with length to diameter ratios of 6 to 20. Fig. 1 is a diagram of one of the 2.0-in. diameter tubes in which the vortex was generated by means of twelve 0.0135-in. diameter nozzles located in a staggered configuration along the tube length. Gas was exhausted by means of a conical valve at the center of one end of the tube. The radial static pressure distribution, from which tangential velocities were determined by a method discussed in (4,5), was measured by means of pressure taps drilled in the closed end of the tube. This particular tube had a porous wall for study of the effects of boundary layer suction and injection. The porous wall was also used to achieve uniform introduction of a heavy gas for the separation studies. Taps were provided for insertion of a gas sampling probe used for measurement of the concentration gradient in the separation work.

Fig. 2 is a photograph of the 2-in. tube with the outer jacket and end plates removed. The two smaller tubes are 1- and 0.64-in. diameter inserts which were used to study effects

of tube diameter and length/diameter ratio. Nozzles drilled directly in the wall and fed from the surrounding annulus served for vortex generation. In some of the experimental tubes, the vortex was generated by means of a continuous slit a few mils wide, rather than by discrete nozzles.



Fig. 2 2-in. porous vortex tube and inserts: A = 1 in.-diam, B = 0.64 in.-diam

Experimental Results

The values of peripheral tangential Mach number M_p , which were observed in 0.64- and 2.0-in. diameter tubes with N_2 gas injected at room temperature and at sonic velocity $M_i = 1$ are indicated in Fig. 3 as a function of the mass flow rate m . M_p is the rotational Mach number near the periphery of the tube and can be considered as a direct indication of the vortex strength. The data include measurements with tube wall pressures of 83 and 108 psia. It must be pointed out that, based on the original laminar flow analysis (1), a peripheral Mach number approaching unity should be achievable at the allowable mass flow rates of 0.01 to 0.02 lb/sec-ft. Note, however, that in this range of mass flows the values of M_p actually observed varied from approximately 0.10 to 0.18 for the 2-in. tube, and from approximately 0.2 to 0.3 for the 0.64-in. tube. The highest peripheral Mach number of 0.49 was observed in a 0.64-in. diameter tube, and required a mass flow rate of 0.06 lb/sec-ft. Since the observed velocities were significantly lower than would be expected for laminar flow, it may be concluded that boundary layer turbulence existed with correspondingly high wall shear.

Preliminary estimates of the degree of turbulence in vortex flow were made by comparison of observed velocity profiles with published solutions of the Navier-Stokes equations in terms of virtual viscosity (molecular viscosity plus eddy viscosity) (7). Fig. 4 shows the observed ratio μ^*/μ of virtual to molecular viscosity near the periphery as a function of tangential peripheral Reynolds number $N_{Re,p}$ for three tubes

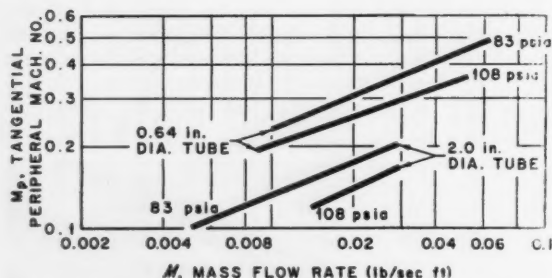


Fig. 3 Tangential peripheral Mach number vs. mass flow rate, $M_i = 1.0$; based on experimental results for N_2 gas, 75°F

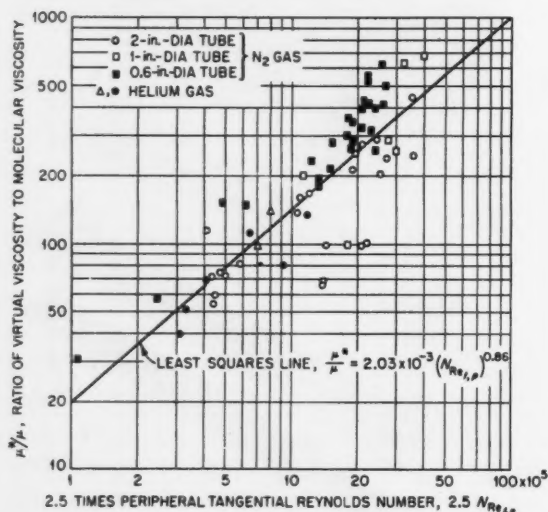


Fig. 4 Variation of ratio of virtual viscosity to molecular viscosity with peripheral tangential Reynolds number; 0.6-, 1.0-, and 2-in. diam tubes; N_2 and He gas

sizes, N_2 and He gas. At the lowest Reynolds number 4×10^4 , $\mu^*/\mu \approx 30$, and at the highest Reynolds number 1.6×10^5 , the ratio is nearly 700. The ratio would, of course, be unity for laminar flow. Since the operating Reynolds number may be in the range from 3×10^4 to 6×10^4 , it is suggested that turbulence will probably exist, unless the strong density gradients resulting from the internal heating produce sufficient stabilization.

It must be pointed out that the estimates of virtual viscosity are based on a two-dimensional flow analysis in which the radial mass flow rate is assumed uniform and equal to that which exhausts at the center of the tube. Measurements by Kendall (8) at the Jet Propulsion Laboratory indicate that this is not necessarily true, and that some of the flow is carried in the boundary layers on the wall and end plate. Neglect of this component of the flow means that the viscosities estimated in this work are upper limits. It is the opinion of the author, however, that with tube length to diameter ratios of six or more as employed, the effect of the secondary flow may be neglected to a first approximation. This view is supported by reasonable agreement of the observed and calculated position of the heavy gas concentration peak when secondary flow effects are neglected (see paragraph on separation). This aspect of the problem should, nevertheless, be investigated in detail in order to more clearly understand the flow phenomena.

The observed influence of peripheral tangential Reynolds number on vortex strength is shown in Fig. 5, in which the effective jet input power $P^* = (\gamma/2)m M_i^2$ required to sustain vortices with varying M_p is plotted as a function of the Reynolds number. The discrepancy in the results for $0.30 < M_p < 0.38$ is not understood. It is inferred from the plot that maintenance of constant M_p with increase in $N_{Re,p}$

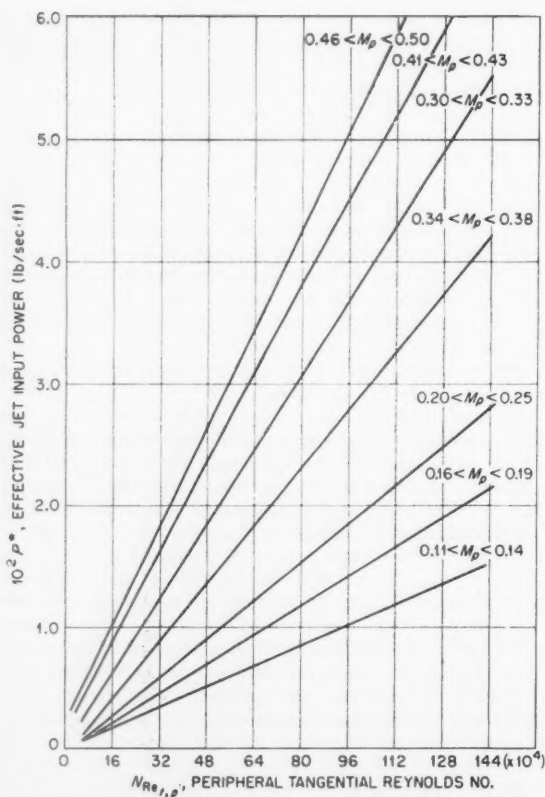


Fig. 5 Vortex tube performance characteristics summary plot: peripheral tangential Reynolds number vs. jet input power; linear fit to data for 0.6-, 1.0- and 2-in. diam tubes; N_2 and He gas

requires an approximately proportional increase in input power. For fixed injection velocity, this means that an increase in inlet mass flow is required to maintain a given vortex strength as the Reynolds number increases.

Comparison of a typical experimentally determined velocity profile with theoretical profiles for two-dimensional viscous vortex flow is presented in Fig. 6. The experimental profile is based on data for a 2-in. diameter tube operating at 40 psia with an injection Mach number of 0.98 and a peripheral tangential Mach number of 0.24. Note that the exit radius ratio r_e' was 0.25. The assumption of an isentropic expansion process was made in obtaining the velocity profile from the Mach number profile determined directly from static pressure data. A value of the turbulent radial Reynolds number A of 2.5 was ascertained by comparison of the observed velocity profile near the wall with the theory of Einstein and Li (7), as discussed in (4, 5). The complete profile was then calculated making use of the appropriate relationships given by Einstein and Li for $r' > r_e'$ and $r' < r_e'$. The curve calculated from the theory of C. D. Pengelley (9) was obtained by matching the calculated and observed profiles at a point inside the exit radius where viscous stress vanishes. It is suggested by a comparison of the slopes of either theoretical curve for constant turbulent radial Reynolds number with the experimental data that the Reynolds number is probably not constant as assumed, but increases (i.e., μ^* decreases) with decreasing radius. This apparent decrease in the turbulence level at small radii may result from stabilizing effects of the strong density gradient and the corresponding decrease in the tangential Reynolds number near the center of the tube.

The intensity of turbulent wall shear is of obvious interest in relation to fluid friction characteristics of vortex tubes. Estimates of average coefficients of skin friction C_f have been made from tangential velocity and virtual viscosity data, making use of a torque balance in which the driving torque due to the decrease in momentum of the feed jets is equated to the sum of the torque due to wall shear and the internal fluid torque

$$\underbrace{\frac{m}{g_c} (u_j - u_a) \times r_a}_{\text{Driving torque}} = \underbrace{C_f \times \frac{\rho_p u_p^2}{2g_c} \times 2\pi R^2}_{\text{Wall shear torque}} + \underbrace{\frac{\mu^*}{g_c} \left(\frac{du}{dr} - \frac{u}{r} \right) \times 2\pi r a^2}_{\text{Internal fluid torque}}$$

If it is assumed that $u = K/r^n$, $r_a = R$, $u_a = u_p$

$$C_f \cong \frac{4 N_{Re,r}}{N_{Re,t,p}} \left[\frac{u_j}{u_p} - \left(1 - \frac{n+1}{A} \right) \right]$$

$N_{Re,r}$ and $N_{Re,t,p}$ are the radial and tangential Reynolds numbers, respectively; u_j/u_p is the ratio of jet velocity to peripheral tangential velocity, n is the exponent in $u = K/r^n$, and A is the turbulent radial Reynolds number.

Fig. 7 is a graph of C_f versus peripheral tangential Reynolds number, including data for $\frac{3}{8}$ -, 1-, and 2-in. diameter vortex tubes. The data scatter about the least squares line represented by the equation

$$C_f = 0.35 (N_{Re,t,p})^{-0.27}$$

The lower (dashed) curve is a plot of the Schoenherr average law for turbulent C_f on a flat plate with zero pressure gradient (10). Since the Schoenherr equation is based on a length Reynolds number, which is not directly comparable with the Reynolds number as defined for vortex flow, the lower curve should be considered for reference purposes only. It is not unreasonable, however, that the friction coefficient for vortex

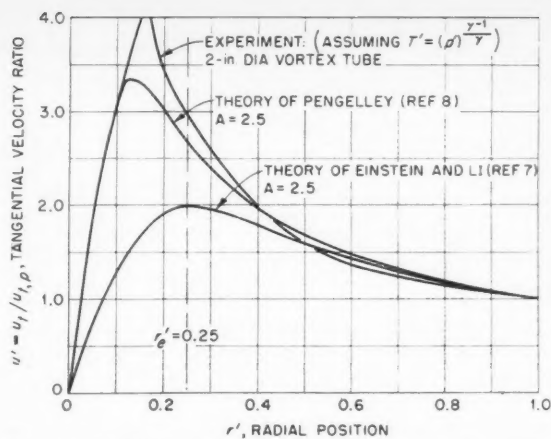


Fig. 6 Comparison of an experimentally determined tangential velocity profile with theory: 2-in. tube

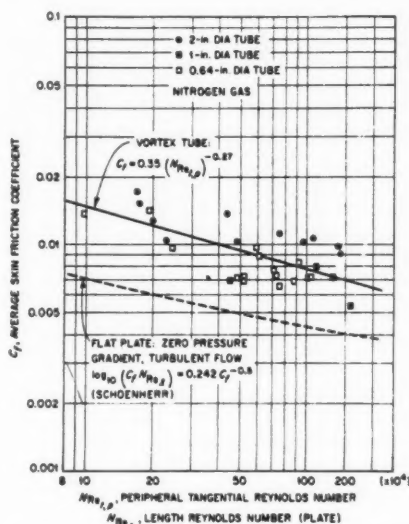


Fig. 7 Comparison of skin friction coefficients for vortex tube and flat plate

flow may be higher than that for flow along a flat plate, as a consequence of the well-known destabilizing effect of concave curvature.

The ratio of wall shear to internal fluid shear is given approximately by the expression

$$\frac{C_f A N_{Re,t,p}}{4(n+1) N_{Re,r}}$$

This ratio was found to vary from about 2 for 0.64-in. diameter tubes to about 7 for 2.0-in. diameter tubes, indicating the significance of the internal shear component.

Some experiments were carried out with uniform wall bleed-off, utilizing 2-in. diameter nozzle and slit fed tubes with porous walls (sintered Ni) having approximately 100- μ in. surface finish. These experiments were for the purpose of determining if reduction in wall shear by boundary layer stabilization could be observed. In no case was a significant increase in vortex strength measured for bleed flows up to three times the exit flow. The vortex strength was observed to increase with extreme wall cooling, however, suggesting that strong density and viscosity gradients in the boundary layer may reduce turbulent shear.

Table 1 Conditions of operation of a vortex cavity reactor based on calculations of Kerrebrock and Meghreblian (1)

Case	Peripheral Mach number, M_p	Peripheral gas temp, (T_p) , °R	Exit gas temp, (T_e) , °R	Mass flow rate, m , lb/sec-ft	Peripheral gas pressure, p_p , atm	Peripheral tangential Reynolds number for a 0.64-in. diam tube, $N_{Re,t,p}$
1	1.00	4500	7,020	1.98×10^{-2}	213	3.6×10^8
4	1.00	2470	10,000	1.21×10^{-2}	171	5.6×10^8

Application

An interpretation of the experimental gas dynamics results in terms of the application to a gaseous reactor for rocket propulsion is of interest. Table 1 reviews conditions of operation of a vortex cavity reactor based on the calculations of Kerrebrock and Meghreblian (1). Case 1 is for a hybrid core in which the propellant is heated to 4500 °R by solid fuel elements located between the vortex tubes, and the temperature increased to approximately 7000 °R by the gaseous core. Case 4 is for an all gaseous core with propellant inlet temperature of 2470 °R and exit temperature of 10,000 °R. Note that pressures of 213 and 171 atm are required for criticality, and that the corresponding tangential Reynolds numbers are 3.6×10^8 and 5.6×10^8 . Note also that a peripheral tangential Mach number of 1.0 is assumed, with mass flow rates of 0.0198 and 0.0121 lb/sec-ft. On the other hand, because of turbulence, the maximum tangential Mach number, which could be generated experimentally at a mass flow of 0.02 lb/sec-ft, was of the order of 0.3, as indicated in Fig. 3. In order to increase the vortex strength, it is necessary to introduce excess mass flow, with bleed-off and recirculation of all but the allowable exhaust flow. Table 2 presents estimates based on extrapolation of the experimental results (Figs. 3 and 5) using Reynolds and Mach number similitude criteria, of the recirculation ratio R (defined as the ratio of mass flow recirculated to mass flow exhausted) required for generation of vortices having M_p of 0.25, 0.5 and 1.0 under conditions of constant exit mass flow rate. The two examples chosen for illustration are based on cases 1 and 4 of Table 1 and (1). For case 1, recirculation ratios required for 0.64-in. tubes increase from 0.4 to 29 as M_p increases from 0.25 to 1.0. Larger ratios are required if 2.0-in. tubes are used. Assuming that M_p of at

least 0.5 will be necessary for preliminary interest in vortex reactors, it is seen from the table that attainment of this will require a recirculation ratio of 5.³ In order to obtain R of 5, it would be necessary to provide extra heat rejection capacity, such as additional liquid H_2 . A rough estimate of the amount of additional liquid H_2 required indicates that for case 1 the minimum take off weight of coolant would be several times that of the reactor. For case 4, the recirculation ratio required for $M_p = 0.5$ is about 13, and the additional weight of coolant amounts to possibly five times the reactor weight. These penalties must be taken into account in evaluating the vortex reactor concept for rocket propulsion. Furthermore, with a peripheral Mach number of 0.5, the peak in fuel concentration will occur at a radial position of at most 0.5, and the diameter of the exit nozzle cannot be greater than say 0.25 of the tube diameter. The consequence of this is that the individual tubes must be short in order to limit the mass flow per tube; a very large number of them will therefore be required to achieve high total thrust. Thus turbulence imposes a geometrical limitation as well as a weight penalty.

Separation

Separation experiments were carried out utilizing helium and a heavy fluorocarbon vapor C_8F_{18} (molecular weight 400). Note that the ratio of masses is nearly the same as for H_2 -U. The heavy gas was introduced as a dilute mixture with helium through the porous wall of the 2-in. diameter vortex tube described in Fig. 1. This method of introducing the trace gas insured uniform peripheral distribution and eliminated the possibility of condensation which might occur, for example, if nozzle injection were used. To minimize condensation resulting from the vortex radial cooling effect, the peak mole fraction of C_8F_{18} was maintained below saturation, based on an assumed isentropic expansion process. To fulfill this requirement, the vapor mole fraction had to be less than 100 ppm.

An 0.008-in. OD probe introduced radially at the midaxial position was used to withdraw gas for analysis by measurement of thermal conductivity. Inherent disadvantages associated with use of such a probe must be recognized, since the probe itself introduces turbulence, thereby decreasing the vortex strength and the separation effect; and withdrawal of even a very small gas sample disturbs the diffusion equilibrium, and hence the gas concentration at the point of sampling.

A relationship between the tangential Mach number at the radius of maximum mole fraction of heavy component and the exit mass flow rate is derived in (1) for laminar flow. For the special case of a very dilute mixture, as employed in the experiments, the relationship is

$$M_m^2 = \frac{m_e(1 - x_e/x_m)}{2\pi(\rho D_{12})_m(m_2/m_1 - 1)\gamma}$$

M_m is the tangential Mach number at the radius of maximum mole fraction, m_e is the exit mass flow rate per unit tube length, x_e/x_m is the ratio of mole fractions of heavy component in the

³ Recirculation techniques are discussed in (2).

Table 2 Estimates of mass flow recirculation ratios required for operation of a vortex cavity reactor based on ORNL experimental results

Constant exit mass flow rate				
Case	Peripheral Mach no., M_p	Exit mass flow rate, M_E lb/sec-ft	Tube diameter, in.	Mass flow recirculated/ft, mass flow exhausted/ft $R = M_R/M_E$ ($M_j = 1.0$)
1	1.00	1.98×10^{-2}	0.64	29.0
	0.50	1.98×10^{-2}	0.64	5.0
	0.25	1.98×10^{-2}	0.64	0.4
1	1.00	1.98×10^{-2}	2.00	109
	0.50	1.98×10^{-2}	2.00	25
	0.25	1.98×10^{-2}	2.00	4
4	1.00	1.21×10^{-2}	0.64	74.0
	0.50	1.21×10^{-2}	0.64	12.5
	0.25	1.21×10^{-2}	0.64	2.5
4	1.00	1.21×10^{-2}	2.00	259
	0.50	1.21×10^{-2}	2.00	57
	0.25	1.21×10^{-2}	2.00	12

exit gas stream and at the peak, $(\rho D_{12})_m$ is the density-molecular diffusivity product at the peak, m_2/m_1 is the mass ratio, and $\gamma = c_p/c_v$. From an examination of this equation, it is seen that M_m varies directly as the square root of the exit mass flow rate and inversely as the square root of the diffusivity. In view of the small magnitude of diffusivity for C_3F_8 in helium near room temperature, the equation can be satisfied for values of M_m which are experimentally attainable only if the exit mass flow rate is low. Thus it was necessary in the experiment to introduce excess mass flow in order to generate the required vortex strength, and to bleed off all but the allowable exit flow.

Operating conditions and results for three typical separation runs are summarized in Table 3. Note that large bleed ratios were required, and that wall pressures ranged from 41 to 56 psia. In run 1 the gas was bled off axially by means of annular rings of holes located in the exit end plate at two radial positions, 0.25 and 0.4 in. In run 2 bleed off was radially outward through a slit in the wall, and in run 3 bleed off was axial at a radial position of 0.4 in. The peaks in mole fraction of heavy component were observed to occur at positions varying from 11 to 21% of the radius. The tangential Mach numbers observed at the radius of peak mole fraction were determined with the sample probe inserted, and thus reflect the effect of the probe on the vortex strength. These Mach numbers were 0.70, 0.70 and 0.55, respectively.

Mole fraction ratios x_e/x_m of 0.5 and 0.67 were measured for runs 1 and 2; no measurement was made for run 3. The calculated Mach numbers at the peak position for runs 1 and 2 were obtained from the preceding equation, using an experimental value of molecular diffusivity for C_3F_8 -He, corrected for temperature. Note that the observed and calculated values of M_m agree to within 20%.

Fig. 8 is the separation profile observed in run 1; the ratio of the mole fraction C_3F_8 at radial position r' to that at the wall is plotted as a function of r' . Note the definite peak at $r' = 0.15$ and the sharp dropoff toward the center of the tube. The peak is seen to occur just outside the exit opening ($r_e' = 0.11$), but inside the inner bleed position ($r' = 0.25$). The dashed curve is the corresponding tangential Mach number profile obtained with the probe inserted to $r' = 0.15$.

Summary

It must be recognized that the experimental work was exploratory in nature and that a number of important ques-

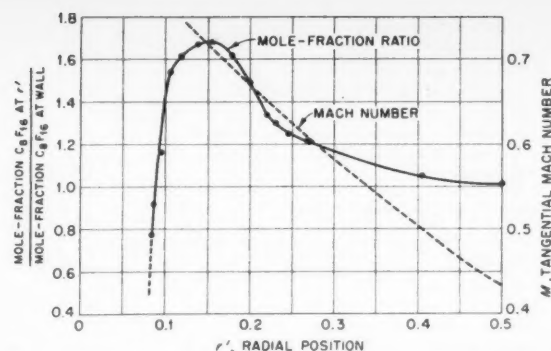


Fig. 8 Separation of He- C_3F_8 in vortex flow: run 1, Table 3

tions remain unanswered. In particular, the influence of possible secondary boundary layer flow was not investigated. The extrapolation to reactor conditions is a long one, of course, but some tentative conclusions may be drawn pertinent to the application of simple jet driven vortex tubes to a gaseous fission rocket. Further experimentation is admittedly needed to test the following conclusions:

1 Flow in the tubes can be expected to be turbulent, especially near the wall; the actual turbulence level will depend on the degree of stabilization effected by the temperature and pressure gradients in a manner which cannot at this time be quantitatively determined.

2 Due to turbulence, the achievement of vortex strengths adequate for separation may require the use of small diameter tubes with recirculation of a significant fraction of the inlet mass flow. Unless the excess flow can be used advantageously for boundary layer stabilization, recirculation ratios may be sufficiently high to necessitate auxiliary cooling capacity, thus increasing the weight and decreasing the payload capability as compared with the idealized model. A detailed design optimization is needed to determine overall performance characteristics.

3 Separation of U and H_2 may be achieved in a vortex flow field of limited turbulence provided the size of the exhaust opening is sufficiently small. This implies a geometrical configuration consisting of a large number of short tubes in parallel. The problems of feeding such a configuration and of nuclear criticality are formidable ones.

Acknowledgment

This experimental program was initiated at the suggestion of R. V. Meghreblian; methods of driving the vortex and of pressure measurement were proposed by J. L. Kerrebrock. The author wished to acknowledge also the contributions of R. E. Dial for general design assistance, operation, and data reduction.

Nomenclature

A	= turbulent radial Reynolds number, $m/2\pi\mu^*$
C_f	= skin friction coefficient
D_{12}	= molecular diffusivity, ft^2/sec
K	= a constant
m	= mass flow rate per unit of tube length, lb/sec-ft
M	= Mach number
m	= molecular weight, lb-mole/lb
n	= exponent
N_{Re}	= Reynolds number
P^*	= effective jet input power per unit of tube length, lb/sec-ft
p	= pressure, psia
R	= tube radius, ft

Table 3 Summary of operating conditions and results for He- C_3F_8 separation experiments in a 2-in. diam vortex tube

Parameter	Run		
	1	2	3
Inlet helium mass flow rate, m_i (lb/sec-ft)	0.023	0.030	0.030
Bleed ratio, R_B	15.6	9.4	17.5
Wall pressure p_w , psia	56.3	40.8	53.0
Exit diameter $2r_e$, in.	0.221	0.250	0.250
Bleed off position, r'	0.25, 0.40 (axial)	1.00 (wall slit)	0.40 (axial)
Observed mole fraction peak position, r_m'	0.15	0.11	0.21
Observed mach number at r_m' , M_m	0.70	0.70	0.55
Observed ratio of exit mole fraction to that at r_m' , x_e/x_m	0.5	0.67	—
Calculated M_m	0.58	0.81	—
Ratio of observed M_m to calculated M_m	1.2	0.87	—

- r = radial distance, ft
 T = absolute temperature, °R
 u = tangential velocity, fps
 x = mole fraction heavy component
 γ = c_p/c_v
 μ = absolute molecular viscosity, lb/sec-ft
 μ^* = absolute virtual viscosity, lb/sec-ft
 ρ = density, lb/ft³

Superscripts and Subscripts

- ['] = denotes value divided by value at periphery
 a = jet inlet
 e = exit
 j = jet
 m = maximum mole fraction
 p = periphery
 r = radial
 t = tangential
₁ = light component
₂ = heavy component

References

- 1 Kerrebrock, J. L. and Meghreblian, R. V., "An Analysis of Vortex Tubes for Combined Gas-Phase Fission Heating and Separation of the Fissionable Material," ORNL CF-57-11-3, revision 1, April 11, 1958.
- 2 Kerrebrock, J. L. and LaFyatis, P. G., "Analytical Study of Some Aspects of Vortex Tubes for Gas-Phase Fission Heating," ORNL CF-58-7-4, July 1958.
- 3 Kerrebrock, J. L. and Keyes, J. J., Jr., "A Preliminary Experimental Study of Vortex Tubes for Gas-Phase Fission Heating," ORNL-2660, February 1959.
- 4 Keyes, J. J., Jr. and Dial, R. E., "An Experimental Study of Vortex Flow for Application to Gas-Phase Fission Heating," ORNL-2837, April 1960.
- 5 Keyes, J. J., Jr., *Heat Transfer and Fluid Mechanics Institute*, Stanford Univ. Press, 1960, pp. 31-46.
- 6 Ragsdale, R. G., "NASA Research on the Hydrodynamics of the Gaseous Vortex Reactor," NASA-TN-D-288, June 1960.
- 7 Einstein, H. A. and Li, H., *Heat Transfer and Fluid Mechanics Institute*, Stanford Univ. Press, 1951, pp. 33-43.
- 8 *Jet Propulsion Laboratory Research Summary* no. 36-3, vol. 1, part 2, June 1960.
- 9 Pengelly, C. D., "Flow in a Viscous Vortex," *J. of Appl. Phys.*, vol. 28, no. 1, January 1957, p. 86.
- 10 Schoenherr, K. E., *Trans. of the Soc. of Naval Architects and Marine Engineers*, Vol. 40, 1932, pp. 279-313.

Magnetic Damping of the Angular Motions of Earth Satellites

ROBERT E. FISCHELL¹

The Johns Hopkins University
Applied Physics Laboratory
Silver Spring, Md.

Multiple, cylindrical rods of a high permeability magnetic alloy can be employed for damping both oscillatory and spin motions of an orbiting satellite. These rods are oriented perpendicular to that axis of the satellite about which it is desired to damp out motion. This system has been used on the TRANSIT 1B and 2A navigational satellites. As a result, all oscillatory motions of these satellites appear to have been damped out, and their spin has been essentially stopped.

TO DAMP the spinning or oscillating motions of an artificial Earth satellite it is necessary to have something to push against. Although internal mechanical devices can provide motion of one part of the satellite relative to another, they do not offer a system whereby the total angular momentum vector can be altered. To accomplish a change in the angular momentum of an Earth satellite, it is necessary to transfer momentum to another body. Several media, e.g., gas molecules, photons (usually those radiating from the sun), the Earth's gravitational field and the Earth's magnetic field are available in the environment of an Earth satellite to effect this momentum transfer. Of all these media for momentum transfer, the relatively large torque that can be

exerted on an Earth satellite by the Earth's magnetic field make it appear the most feasible means for damping the angular motions. This paper describes explicit methods by which the magnetic materials internal to the satellite can be used to remove spin energy and to damp out oscillatory motions.

Requirement for Spin Removal and Damping of Oscillatory Motions

To stabilize the satellite as it is injected into orbit, satellites are usually caused to spin about their axes as part of the launching process. However, spin removal is required for several reasons, of which most common is that the satellite's attitude can then be controlled. For example, a system of magnetic attitude control has been employed on the

Presented at the ARS 15th Annual Meeting, Washington, D. C., Dec. 5-8, 1960; revision received July 14, 1961.

¹ Project Supervisor, Power Systems and Attitude Control.

TRANSIT 1B and 2A satellites. This control consists of a strong, permanent magnet mounted parallel to the satellite's spin axis. When the spin of the satellite was reduced below approximately 0.01 rps, this magnet caused the satellite to align its axis along the direction of the Earth's magnetic field. The spin had to be removed from the TRANSIT satellites in order to make this orientation possible.

For solar or gravity gradient oriented satellites, the satellite's spin must be reduced considerably below 0.01 rps.

Another reason for spin removal stems from the fact that the frequency of radio transmission from the satellite is modulated at twice the spin rate. This is undesirable because it affects the precise doppler tracking of an Earth satellite. Thus in the TRANSIT satellites where transmission frequency stabilities are on the order of 0.01 cps in 108 mc, the spin rate had to be reduced below 0.005 rps in order to avoid significant modulation of the doppler transmission.

The reason for damping the oscillatory motions of Earth satellites are quite obvious. If a particular attitude control system is developed there usually results an oscillation of the satellite about the desired attitude. Magnetic materials can be employed to damp out such oscillations, thereby allowing the attitude control system to be more effective.

Use of Magnetic Materials for Damping Angular Motions

Fig. 1 illustrates a cylindrical rod spinning in the Earth's magnetic field. Due to demagnetization (1),² only the magnetic field component along the rod's longitudinal axis need be considered. If we let T represent the period for one rotation of the rod, and H_m represent the maximum value of the magnetic field component along the rod's longitudinal axis, then the effective magnetic field on the rod will vary sinusoidally as shown in Fig. 1. The changing magnetic field will cause the flux density in the rod to vary. This will result in eddy current and hysteresis losses in the rod. If a shorted coil is wrapped around the rod, the flux changing in the rod will result in a flow of current in the coil which further increases the rate of energy dissipation.

Several magnetic materials were tested for use in the TRANSIT satellite (having a nominal altitude of 500 miles). These materials were: AEM 4750, Mu-Metal, high purity iron, 3.4% silicon-iron, and Orthonol.

A comparison of the hysteresis loops of two of these materials is shown in Fig. 2. For the magnetic fields encountered at a 500 mile altitude, the AEM 4750 offered the greatest energy dissipating ability of any of the materials tested. AEM 4750 is a nickel-iron alloy having the nominal composition 47.5% nickel, 52.5% iron.

The ordinate in Fig. 2 represents the average flux density in the rod. The actual calculation of energy loss is complicated by the fact that the flux density varies along the length of the rod, being a maximum at the center and falling off sharply at each end.

The magnetic properties of rods are very sensitive to the ratio of the rod's length to the rod's diameter. Fig. 3 shows the effect of L/D ratio on the hysteresis loop of AEM 4750. In order to increase magnetic damping, it is desirable to use many rods each with a high L/D ratio. However, if we put two rods close together with their longitudinal axes parallel, we get the same effect as if we had decreased the L/D ratio of each of them. This phenomenon, which we shall call "separation effect," is illustrated in Fig. 4. As a result of this effect, if two rods having an L/D ratio of 248 are placed together with their longitudinal axes parallel, they will exhibit a smaller total energy dissipating capability than one rod by itself.

We shall define separation effect coefficients σ_e , σ_h and σ_s for eddy current, hysteresis and shorted coil damping respec-

* Numbers in parentheses indicate References at end of paper.

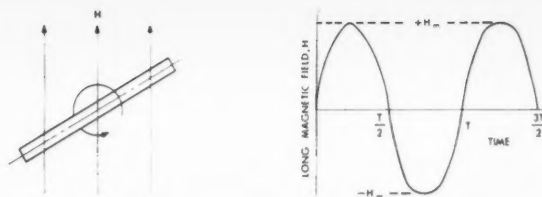


Fig. 1 Magnetic field experienced by a permeable rod spinning in the Earth's magnetic field

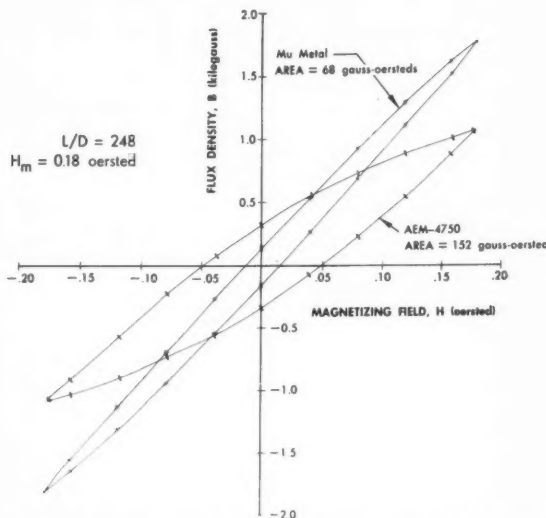


Fig. 2 Hysteresis loops for two different magnetic materials

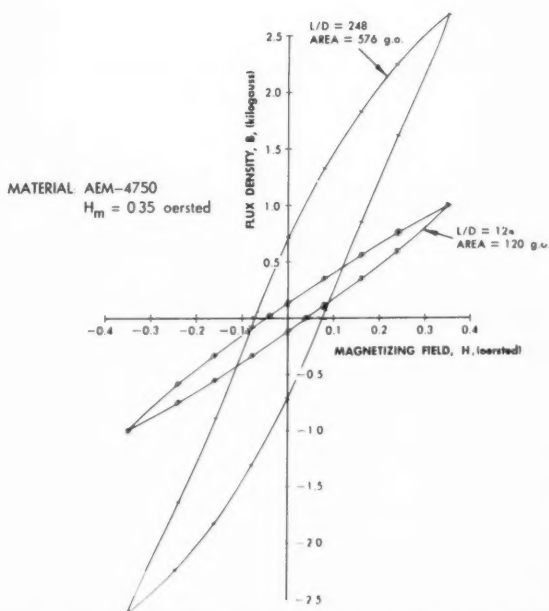


Fig. 3 The effect of L/D ratio on the hysteresis loop of AEM 4750

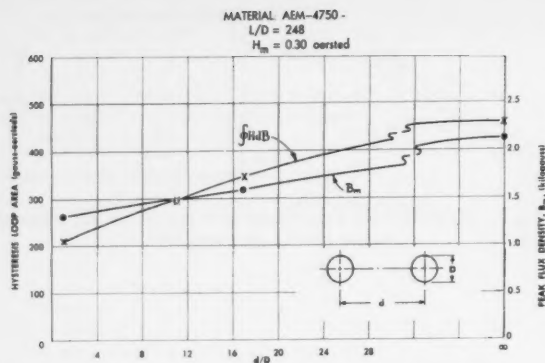


Fig. 4 The hysteresis loop area and peak flux density as a function of separation distance

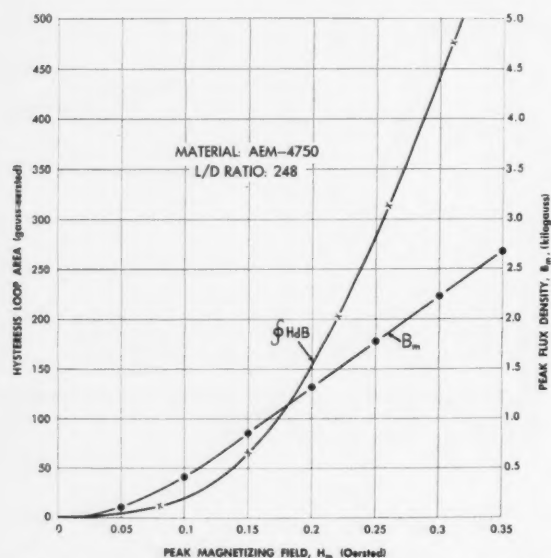


Fig. 5 Hysteresis loop area and peak flux density as a function of peak magnetizing field

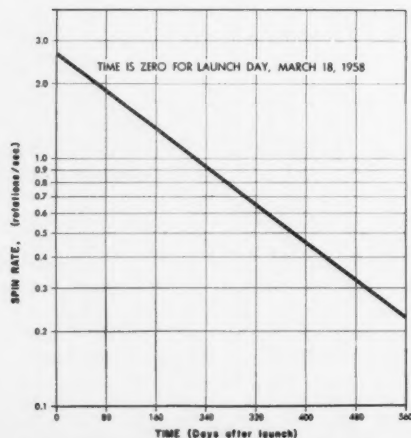


Fig. 6 Spin rate of the Vanguard satellite (1958 $\beta 2$) as a function of time

tively. When the separation distance is infinite, each one of these coefficients is unity. The values σ_s and σ_r are dependent on the decrease of peak flux density due to close proximity of multiple rods. The value of σ_h is dependent on the decrease of hysteresis loop area.

For a magnetic material the hysteresis loop area and the peak flux density (as averaged along the length of the rod) will be a function of the impressed magnetic field. The effect of the peak magnetizing field on a cylindrical rod of AEM 4750 is illustrated in Fig. 5.

Spin Removal by Means of Eddy Current Damping

The fact that the spin rate of satellites is reduced by eddy currents which result from spinning in the Earth's magnetic field has been established by long term observations of the Vanguard satellite, 1958 $\beta 2$. The curve (drawn on a logarithmic scale) for spin rate as a function of time for 1958 $\beta 2$ is shown in Fig. 6 (2).

Since the Vanguard satellite does not contain an appreciable amount of ferromagnetic material, the eddy current losses are due almost entirely to the spinning aluminum structure of the satellite. From Fig. 6 it is seen that the spin velocity drops to $\frac{1}{2}$ its value in approximately 155 days.

Magnetic materials of the proper material and geometry can greatly increase the spin reduction due to eddy currents. For a permeable bar spinning in a magnetic field, the intensity of the field in the longitudinal direction is given by

$$H = H_m \sin \omega t \quad \text{oersted} \quad [1]$$

As a result of the time varying intensity of the magnetic field, there will be a variation of the flux density within the rod. For a sinusoidal variation of the magnetic field, the flux density in the bar will also, to a good approximation, vary sinusoidally. If we take $(B_m)_s$ to be the maximum flux density in the rod (averaged over its entire length) corresponding to the peak magnetizing field H_m , then the flux density at any instant is given by

$$B = B_m \sin \omega t \quad \text{gauss} \quad [2]$$

The voltage around a cylindrical element in the bar of radius r , thickness dr , and length L is given by Faraday's Law

$$v = -N \frac{d\phi}{dt} \times 10^{-8} \quad \text{volts} \quad [3]$$

For this case $N = 1$

$$\phi = \pi r^2 (B_m)_s \sin \omega t \quad \text{maxwell} \quad [4]$$

and

$$\frac{d\phi}{dt} = \pi r^2 (B_m)_s \omega \cos \omega t \quad [5]$$

It can also be shown that the resistance of the cylindrical element is given by

$$R = \frac{2\pi\rho r}{L dr} \quad \text{ohms} \quad [6]$$

Therefore the power dissipated in the cylindrical element is given by

$$d \left(\frac{\Delta E_s}{\Delta t} \right) = \frac{-v^2}{R} = \frac{-\pi \omega^2 r^3 (B_m)_s^2 L \cos^2 \omega t dr \times 10^{-9}}{2\rho} \quad \text{ergs/sec} \quad [7]$$

where the negative sign is taken because the energy is decreasing. Over a complete spin cycle, the average value of $\cos^2 \omega t = 1/2$. The total power dissipated in the rod is

then found by integrating over all cylindrical elements from $r = 0$ to $r = D/2$

$$\frac{\Delta E_s}{\Delta t} = \frac{-\pi}{4\rho} \omega^2 (B_m)^2 L \int_0^{D/2} r^3 dr \times 10^{-9} \quad \text{ergs/sec} \quad [8]$$

Here $\Delta E_s/\Delta t$ represents the rate of loss of energy when averaging over a complete revolution of the rod. Setting $V = \pi(D/2)^2 L$, after integrating in Eq. 8 yields

$$\frac{\Delta E_s}{\Delta t} = -\frac{\omega^2}{64\rho} (B_m)^2 V D^2 \times 10^{-9} \quad \text{ergs/sec} \quad [9]$$

For a satellite containing n rods, having a separation effect coefficient for eddy currents σ_s , the energy dissipation is given in terms of the spin rate f by the equation

$$\frac{\Delta E_s}{\Delta t} = -6.25\pi^2 \sigma_s \rho^{-1} n f^2 \langle B_m^2 \rangle_s V D^2 \times 10^{-11} \quad \text{ergs/sec} \quad [10]$$

where $\langle B_m \rangle_s$ represents the average value of the square of the maximum flux density (over the entire length of the rod) as the satellite traverses its orbit. If we let

$$k_s = 6.25\pi^2 \sigma_s n \rho^{-1} \langle B_m^2 \rangle_s V D^2 \times 10^{-11} \quad \text{erg-sec} \quad [11]$$

then

$$\frac{\Delta E_s}{\Delta t} = -k_s f^2 \quad \text{ergs/sec} \quad [12]$$

For the energy loss given by Eq. 12, it can be easily shown that there is a resulting torque acting on the satellite which is given by

$$T_s = \frac{1}{2\pi f} \frac{dE_s}{dt} \quad \text{dyne-cm} \quad [13]$$

The torque is related to the satellite's spin rate and moment of inertia by

$$T_s = I \frac{d\omega}{dt} = 2\pi I \frac{df}{dt} \quad \text{dyne-cm} \quad [14]$$

Equating the values of T_s from Eqs. 13 and 14 gives

$$2\pi I \frac{df}{dt} = \frac{1}{2\pi f} \frac{dE_s}{dt} \quad [15]$$

and substituting the value of $\Delta E_s/\Delta t$ from Eq. 12, in place of dE_s/dt in Eq. 15 (which is valid if we take T_s to be the average torque over a cycle), we then obtain

$$4\pi^2 I \frac{df}{dt} = -k_s f \quad [16]$$

Separating the variables, integrating and evaluating the constant of integration (using the initial condition that $f = f_0$ when $t = 0$), yields the result

$$f = f_0 \exp [-(k_s/4\pi^2 I)t] \quad \text{rps} \quad [17]$$

that is, the spin rate will decay exponentially with time.

Spin Removal by Means of Hysteresis Damping

Because heat is generated as a result of internal friction due to the motion of magnetic domains within the permeable rod, a permeable rod spinning in the Earth's magnetic field (as shown in Fig. 1) will also experience a hysteresis loss. For a single permeable rod, the hysteresis loss over one period of rotation is given by

$$\Delta E_h = \frac{V}{4\pi} \oint H dB \quad \text{ergs/cycle} \quad [18]$$

Letting $\Delta E_h/\Delta t$ represent the hysteresis energy loss per unit time, and averaging over a complete revolution of the rod we get that

$$\frac{\Delta E_h}{\Delta t} = -\frac{0.25f}{\pi} V \oint H dB \quad \text{ergs/sec} \quad [19]$$

where the negative sign is taken because the energy is decreasing with time.

Letting $\langle \oint H dB \rangle$ equal the average area of the hysteresis loop of a rod as the satellite traverses its orbit, we get that the energy loss per unit time due to hysteresis damping for n bars having a separation effect coefficient σ_h is given by

$$\frac{\Delta E_h}{\Delta t} = -\frac{0.25}{\pi} \sigma_h n V f \langle \oint H dB \rangle \quad \text{ergs/sec} \quad [20]$$

and defining a hysteresis damping coefficient

$$k_h = \frac{0.25}{\pi} \sigma_h n V \langle \oint H dB \rangle \quad \text{ergs} \quad [21]$$

we get for hysteresis damping that

$$\frac{\Delta E_h}{\Delta t} = -k_h f \quad \text{ergs/sec} \quad [22]$$

As with the case of eddy current damping, the torque due to hysteresis loss is given by

$$T_h = \frac{1}{2\pi f} \frac{\Delta E_h}{\Delta t} = -\frac{k_h}{2\pi} \quad \text{dyne-cm} \quad [23]$$

Eq. 23 shows that the average torque over a revolution of the satellite is independent of the spin rate. We now obtain the differential equation

$$4\pi^2 I \frac{df}{dt} = -k_h \quad [24]$$

Solving the differential equation and applying the initial condition that $f = f_0$ at $t = 0$ yields

$$f = f_0 - \frac{k_h}{4\pi^2 I} t \quad \text{rps} \quad [25]$$

The interesting result obtained here is that the spin rate of the satellite will decrease linearly with time, and will actually go to zero rps (with respect to the ambient magnetic field) in a finite time. This is distinctly different from the case of eddy current (or shorted coil) damping where the spin rate decreases exponentially, but never reaches zero. This method of damping is particularly important where it is desired to obtain fairly rapid decay of low spin rates.

To find the time required for the satellite to stop spinning (with respect to the ambient magnetic field) we set $f = 0$ in Eq. 25 and obtain the result

$$t_{f=0} = \frac{4\pi^2 I f_0}{k_h} \quad \text{sec} \quad [26]$$

Spin Removal by Means of Shorted Coil Damping

It is a well known fact that if the rotor of a dynamo is shorted, it will rapidly come to a stop. Similarly a satellite can be made to stop spinning by shorting a coil of wire that has been wound on a permeable core (in this case a cylindrical rod). The voltage generated across the winding as the bar spins in the Earth's magnetic field is given by

$$v = -N \frac{d\phi}{dt} \times 10^{-8} \quad \text{volts} \quad [27]$$

As with the eddy current damping it can easily be shown that the voltage across the coil is given by

$$v = -2\pi N A (B_m)_s f \cos \omega t \times 10^{-8} \quad \text{volts} \quad [28]$$

where $(B_m)_s$ is the peak value of the flux density averaged over the length of the coil. The power dissipated in the coil is

$$\frac{\Delta E_s}{\Delta t} = i^2 R \quad \text{watts} \quad [29]$$

and if the coil has an impedance Z then

$$\frac{\Delta E_s}{\Delta t} = \frac{v^2 R}{Z^2} \times 10^7 \quad \text{ergs/sec} \quad [30]$$

The impedance of the coil is given by

$$Z = \sqrt{R^2 + \omega^2 L_c^2} = \sqrt{R^2 + 4\pi^2 f^2 L_c^2} \quad \text{ohms} \quad [31]$$

If in Eq. 30 we substitute the value of v from Eq. 28 (setting $\cos^2 \omega t = 1/2$) and the value of Z from Eq. 31 we get

$$\frac{\Delta E_s}{\Delta t} = -\frac{2\pi^2 \sigma_s n R N^2 A^2 \langle B_m^2 \rangle_s f^2 \times 10^{-9}}{R^2 + 4\pi^2 f^2 L_c^2} \quad \text{ergs/sec} \quad [32]$$

where the negative sign is taken because the energy decreases with time. In Eq. 32 we also have gone to n bars, with separation coefficient σ_s . The symbol $\langle B_m^2 \rangle_s$ represents the average value in orbit of the square of the peak flux density for the flux linking the shorted coil. $\langle B_m^2 \rangle_s$ differs from $\langle B_m^2 \rangle$, in that, for eddy currents we consider the flux density over the entire length of the rod, where for the shorted coil only the flux linking the coil need be considered.

We shall now consider the damping that results from coils having $R^2 \gg 4\pi^2 f^2 L_c^2$; this is characteristic of coils

having reasonably high resistance and spinning at a slow rate. We now define a shorted coil damping coefficient

$$k_s = 2\pi^2 \sigma_s n R^{-1} N^2 A^2 \langle B_m^2 \rangle_s \times 10^{-9} \quad \text{erg-sec} \quad [33]$$

and for this approximation, the rate of loss of kinetic energy is given by

$$\frac{\Delta E_s}{\Delta t} = -k_s f^2 \quad \text{ergs/sec} \quad [34]$$

and the torque is

$$T_s = \frac{1}{2\pi f} \frac{dE_s}{dt} = -\frac{k_s}{2\pi} f \quad \text{dyne-cm} \quad [35]$$

To find the equation of spin rate as a function of time for shorted coil damping we follow the same procedure as for eddy current damping. We need only substitute k_s for k_e in Eq. 17 to obtain

$$f = f_0 \exp [-(k_s/4\pi^2 I)t] \quad \text{rps} \quad [36]$$

Spin Removal by Combined Magnetic Damping

For a particular satellite the combined effects of eddy current, hysteresis, and shorted coil damping may be employed for removing spin energy. For a combination of these three methods of damping, the kinetic energy loss by the satellite per unit time is given by

$$\frac{\Delta E}{\Delta t} = \frac{\Delta E_e}{\Delta t} + \frac{\Delta E_h}{\Delta t} + \frac{\Delta E_s}{\Delta t} \quad \text{ergs/sec} \quad [37]$$

Equating the resulting torques gives

$$2\pi I \frac{df}{dt} = -\frac{k_e}{2\pi} f - \frac{k_h}{2\pi} - \frac{k_s}{2\pi} f \quad [38]$$

separating the variables and integrating yields

$$\int \frac{df}{(k_e + k_s)f + k_h} = -\frac{1}{4\pi^2 I} \int dt \quad [39]$$

If as before we let $f = f_0$ when $t = 0$, we get the result

$$f = \left(\frac{k_h}{k_e + k_s} + f_0 \right) \exp \left[-\left(\frac{k_e + k_s}{4\pi^2 I} \right) t \right] - \frac{k_h}{k_e + k_s} \quad \text{rps} \quad [40]$$

The time required for f to go to zero is found by setting $f = 0$ in Eq. (40). This yields

$$t_{f=0} = \frac{4\pi^2 I}{k_e + k_s} \ln \left[1 + \frac{f_0(k_e + k_s)}{k_h} \right] \quad \text{sec} \quad [41]$$

A curve of spin rate as a function of time for combined magnetic damping (using arbitrary coefficients) is shown in Fig. 7.

Calculation of Despin Rate for an Orbiting Satellite

As previously stated, only the component of the Earth's magnetic field along the rod's longitudinal axis will have an effect in removing spin kinetic energy. Thus to be most effective, the rods must be mounted perpendicular to the satellite's spin axis, since as the satellite traverses its orbit, only the component of the Earth's magnetic field perpendicular to the satellite's spin axis will be effective. This normal component H_n is equivalent to the peak magnetizing field H_m given in Eq. 1. The value of H_n as a function of time for the orbit of the TRANSIT 2A satellite is shown in Fig. 8. Also shown in Fig. 8 is the hysteresis loop area as a function of time in orbit. The value of $\oint H dB$ is determined by integrating the curve of hysteresis loop area as a function of time in orbit. If we plotted $\langle B_m^2 \rangle_s$ and $\langle B_m^2 \rangle$ as a function

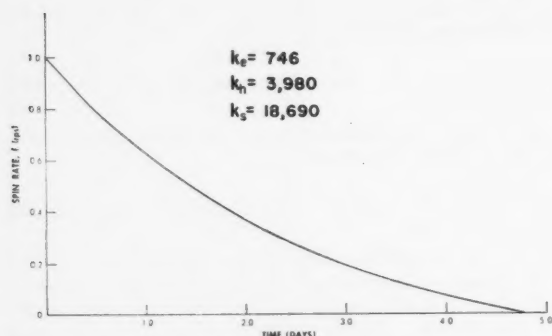


Fig. 7 Spin rate as a function of time for combined magnetic damping

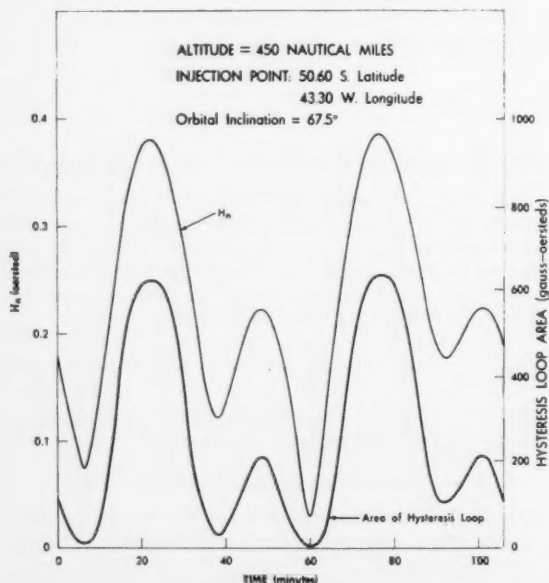


Fig. 8 Normal component of the Earth's magnetic field and the hysteresis loop area as a function of time in an orbital period

of time in orbit and then integrated, we obtain the values for $\langle B_m^2 \rangle$ and $\langle B_n^2 \rangle$, respectively. These values plus the bar dimensions and geometry are sufficient information to calculate the magnetic damping coefficients, k_a , k_b and k_s .

The shape of the curve of H_n in orbit is strongly dependent on the attitude of the satellite at injection. Tilting of the spin axis more parallel to the equator increases the values of H_n , and conversely, tilting of the spin axis toward the Earth's spin axis reduces the values of H_n . If the attitude of the satellite's spin axis at injection is controlled to within $\pm 10^\circ$ quite accurate values of H_n as a function of time can be obtained.

Damping of Oscillatory Motions

Although only spin damping theory has been discussed in detail, the same principles apply to the magnetic damping of oscillatory motions.

An orbiting satellite containing a strong dipole moment M (viz., TRANSIT 2A) will align itself along the local direction of the Earth's magnetic field. If we wish to damp out oscillations when the satellite is initially displaced an angle θ_0 from the local direction of the Earth's magnetic field, then it can be shown (4) that the time required to damp down to a maximum displacement angle θ_f is given approximately by

$$t \approx \frac{3.10\pi^2}{nV} \sqrt{I_s M} H_0^{-5/2} (\cos \theta_f - \cot \theta_0) \times 10^{-4} \text{ sec} \quad [42]$$

In this case the slow oscillations of the satellite about its equilibrium position cause the effect of eddy current and shorted coil damping to be negligible in comparison to the effect of hysteresis damping. For the TRANSIT 3B satellite, an initial displacement of 90° would damp down to less than 3° in one day.

Magnetic rods can also be used in damping oscillatory motions for other types of attitude control systems. The manner in which the rods are used depends entirely on the type of attitude control system that is being considered for a particular satellite.

Experimental Results From the TRANSIT 1B and 2A Satellites

Table 1 lists the pertinent details of the magnetic rods used in the TRANSIT 1B and 2A satellites. A photograph of the rods mounted on top of the TRANSIT 1B instrument

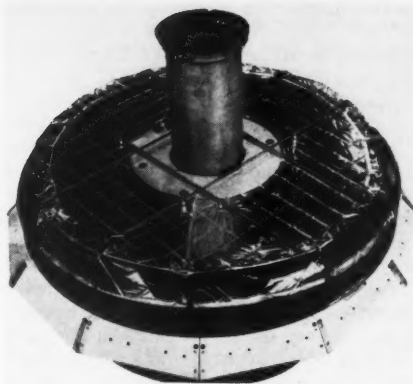


Fig. 9 Magnetic despin bars in the TRANSIT 1B satellite

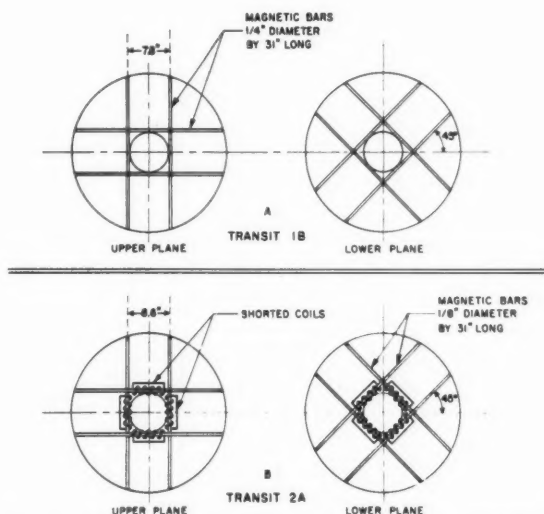


Fig. 10 Mounting of magnetic despin bars in the TRANSIT satellites. Within each satellite the upper and lower planes of the magnetic despin bars were mounted parallel to each other with a separation distance of 10 in.

Table 1 Magnetic despin systems of the TRANSIT 1B and 2A satellites

Item	Transit 1B	Transit 2B
Number of bars	8	8
Bar diameter	0.25 in.	0.125 in.
Bar length	31 in.	31 in.
Length to diameter ratio	124	248
Weight per bar	0.48 lb	0.12 lb
Bar material	AEM 4750	AEM 4750
Magnetic properties (for $H_m = 0.35$ oersted)		
Permeability	2710	7670
Maximum flux density	950 gauss	2680 gauss
Coercive force	0.035 oersted	0.074 oersted
Remanence	120 gauss	725 gauss
Hysteresis loop area	120 gauss-oersted	576 gauss-oersted
Bar resistivity	51.2 $\mu\text{ohm-cm}$	51.2 $\mu\text{ohm-cm}$
Number of shorted turns	0	173
Wire size	...	no. 18 AWG
Resistance of shorted coil	...	0.055 ohm
Spin moment of inertia	9.62 slug-ft ²	8.53 slug-ft ²

tray is shown in Fig. 9. Fig. 10 shows the configuration of rods for the TRANSIT 1B and 2A satellites. When two rods are perpendicular the separation effect is not apparent. For the separation distances shown in Fig. 10, the separation effect coefficient was greater than 0.95.

In Fig. 11 is shown the measured spin rate of the TRANSIT 1B satellite as a function of time. From this curve it can be seen that the satellite spin rate decreased linearly both before and immediately after the mechanical despin operation. This agrees with theoretical calculations which predicted that the dominant energy loss is due to hysteresis damping. The mechanical despin operation consisted of deploying two weights attached by cables around the satellite's equator. After seven days the weights were released, and thus removed a majority of the satellite spin energy. As the satellite spin rate decreased below 0.02 rps the permanent magnet installed in the satellite caused the spin axis of the satellite to align itself parallel to the Earth's magnetic field. As a result the rate of spin energy removal was decreased. The last measurement of spin rate (approximately 13 days after launching) showed that the satellite was spinning at 0.004 rps. The eventual spin rate of the satellite will be two revolutions per orbital period (0.00036 rps) which is

due to the tumbling action caused by the strong permanent magnet (3).

The despin curve of the TRANSIT 2A satellite is shown in Fig. 12. As with the case of TRANSIT 1B the predominant mechanism for energy dissipation was the hysteresis damping, since the mechanical despin weights on this satellite failed to deploy. However, the actuation of devices internal to the satellite at the time when the weights should have deployed apparently caused a change in the satellite's attitude. Hence the change in the slope of the despin curve after the mechanical despin timer operated. The changing of the slope at low angular rates is undoubtedly a result of the interaction of the satellite's strong permanent magnet with the Earth's magnetic field. Because a considerably weaker magnet was employed on the 2A satellite, this effect of decreasing slope at low angular rates was not as great with the 1B satellite. The last measurement of spin rate was made

26.5 days after the launching. At that time no detectable spin was observed during a 10-min observation. This means that, at that time, the spin rate must have been considerably below 0.00167 rps.

The telemeter records also indicated that the satellite was aligned along the direction of the Earth's magnetic field with no detectable oscillations about that direction.

Conclusions

Magnetic materials can be utilized to damp the spinning and oscillatory motions of an Earth satellite. The amount of damping obtainable is strongly dependent on the geometry of the magnetic materials. The spin of the TRANSIT 1B and 2A satellites was stopped by magnetic damping; there was no detectable oscillatory motion.

The fact that spinning magnetic rods will cause a torque to act upon a satellite can also be used to actively control the satellite's orientation in orbit. That is, if we spin magnetic rods inside the satellite, we can create torques that could be used for controlling attitude. This interesting possibility warrants further investigation.

Acknowledgments

The author wishes to express his appreciation to L. Parsons, E. Adams, H. Helms and D. I. Gordon of the U. S. Naval Ordnance Laboratory, White Oak, Maryland, for their invaluable assistance in providing magnetic materials, magnetic testing facilities and technical consultation. The author also wishes to acknowledge the assistance of J. L. Vanderslice and W. E. Allen of The Johns Hopkins University, Applied Physics Laboratory, for their assistance in consultation, and for performing computations.

Nomenclature

A	= cross-sectional area of a rod, sq cm
B	= flux density, gauss
B_m	= peak flux density averaged along length of rod, gauss
D	= rod diameter, cm
f	= spin rate, rps
f_0	= initial spin rate of the satellite, rps
H	= magnetic field intensity, oersted
H_0	= Earth's (local) magnetic field intensity, oersted
i	= RMS current in the shorted coil, amp
I	= satellite spin moment of inertia, gm-cm ²
I_x	= satellite moment of inertia about the axis of oscillation, gm-cm ²
k_e	= eddy current damping coefficient, erg-sec
k_h	= hysteresis damping coefficient, ergs
k_s	= shorted coil damping coefficient, erg-sec
L	= length of the permeable rod, cm
L_s	= inductance of the shorted coil, henries
M	= magnetic dipole moment of the satellite, pole-cm
M_e	= magnetic dipole moment of the Earth, pole-cm
n	= number of bars
N	= number of turns
r	= radius of a cylindrical element in the rod, cm
R	= resistance, ohms
t	= time, sec
$t_{f=0}$	= time required for satellite to stop spinning, sec
T	= period of revolution of a spinning rod, sec
T_e	= torque acting on satellite due to eddy currents, dyne-cm
T_h	= torque acting on satellite due to hysteresis loss, dyne-cm
T_s	= torque acting on satellite due to the shorted coil dyne-cm
v	= rms voltage induced from changing flux, volts
V	= volume of a permeable rod, cu cm
ρ	= resistivity of the rod, ohm-cm
σ_e	= separation effect coefficient for eddy current damping

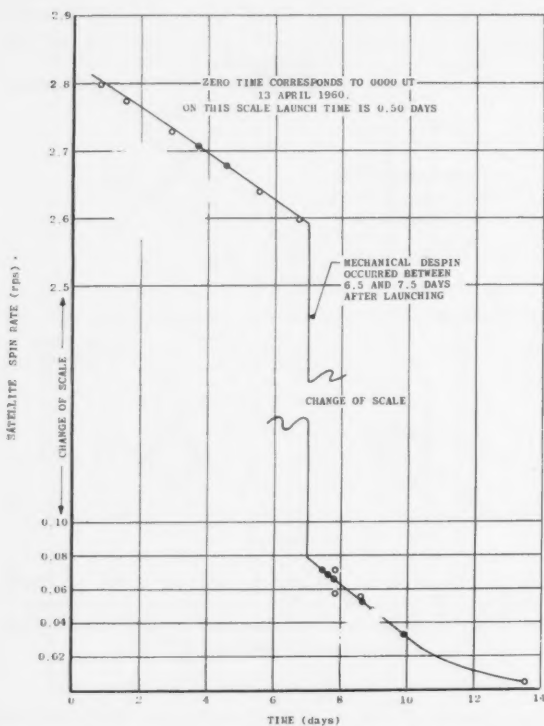


Fig. 11 Spin rate as a function of time for the TRANSIT 1B satellite

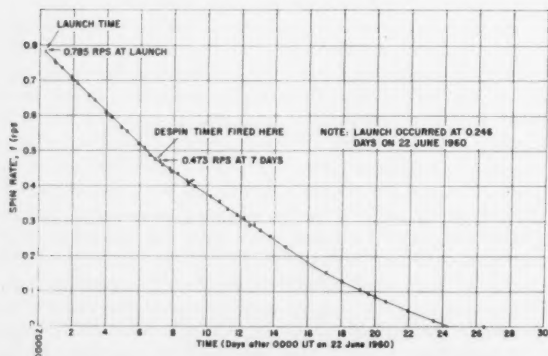


Fig. 12 Spin rate as a function of time for the TRANSIT 2A satellite

σ_h	= separation effect coefficient for hysteresis damping
σ_s	= separation effect coefficient for shorted coil damping
θ_i	= initial angular displacement of the satellite dipole axis from the direction of the Earth's magnetic field, deg
θ_f	= final angular displacement of the satellite dipole axis from the direction of the Earth's magnetic field
φ	= flux encircled by a closed path, Maxwells
ω	= angular spin rate, radians/sec
$\frac{\Delta E}{\Delta t}$	= rate of total energy loss, ergs/sec
$\frac{\Delta E_s}{\Delta t}$	= rate of energy loss (averaged over a complete revolution of the rod) due to eddy current, ergs/sec
$\frac{\Delta E_h}{\Delta t}$	= rate of energy loss (averaged over a complete revolution of the rod) due to hysteresis damping, ergs/sec

$\frac{\Delta E_s}{\Delta t}$	= rate of energy loss (averaged over a complete revolution of the rod) due to the shorted coil, ergs/sec
$\langle B_m^2 \rangle_s$	= average over an orbital period of the square of the peak flux density causing eddy currents, gauss ²
$\langle B_m^2 \rangle_s$	= average over an orbital period of the square of the peak flux density linking the shorted coil, gauss ²
$\langle \oint H dB \rangle$	= average over an orbital period of the hysteresis loop area, gauss-oersted

References

- 1 Bozorth, R. D. and Chapin, D. M., "Demagnetizing Factors of Rods," *J. Appl. Phys.*, vol. 13, May 1942, pp. 320-326.
- 2 Wilson, R. H., Jr., "Magnetic Damping of Rotation of the Vanguard I Satellite," *Sci.*, Feb. 13, 1960, pp. 355-357.
- 3 Fischell, R. E., "Control of Earth Satellite Motions by Magnetic Devices," Johns Hopkins Univ., Appl. Phys. Lab., TG 60-31, 1960.
- 4 Fischell, R. E., "Magnetic and Gravity Attitude Stabilization of Earth Satellites," Rep. CM-996, Johns Hopkins Univ., Appl. Phys. Lab., June 1961.

Hodograph Analysis of the Orbital Transfer Problem for Coplanar Nonaligned Elliptical Orbits

SAMUEL P. ALTMAN¹ and
JOSEF S. PISTINER²

The Martin Co.
Denver, Colo.

The orbital transfer between two arbitrarily selected points on an initial and a final orbit is analyzed by use of hodographs. The transfer analysis is applicable to all coplanar elliptical orbits, with either coincident or noncoincident apsidal lines, that result from the central force field of one spherical celestial body. An orbit is represented by a hodograph of radial velocity vs. normal velocity components. The geometric conditions for a transfer orbit hodograph are defined by three orbital parameters. However, the orbit is determined by one independent and two dependent variables. The hodograph analysis provides several forms of graphical construction and the equations for the resultant transfer orbit solutions. The solutions provide complete transfer orbit characteristics directly and uniquely. These characteristics include the flight path angles between velocity vectors at the transfer points and the required velocity increments.

THE THREE-DIMENSIONAL transfer between an initial and a final closed orbit about one spherical celestial body has been discussed and formulated in (1),³ and the corresponding energy relations have been presented in (2).

Presented at the ARS 15th Annual Meeting, Washington, D. C., Dec. 5-8, 1960.

¹ Presently Supervisor Systems Design, Missiles and Space Systems Dept., Hamilton Standard Div. of United Aircraft Corp., Windsor Locks, Conn. Member ARS.

² Presently Senior Engineer Control Systems, Missiles and Space Systems Dept., Hamilton Standard Div. of United Aircraft Corp., Windsor Locks, Conn. Member ARS.

³ Numbers in parentheses indicate References at end of paper.

In general, it is convenient and desirable to express the ballistic trajectory about the celestial body in terms of orbital parameters. The complete transfer problem has been shown to be presentable as a combination of orbital plane reorientation and orbital plane reshaping with epoch selection. If the orbital planes need not be reorientated (i.e., the incidence angles and the lines of nodes are equal), then the transfer problem can be solved in the plane of the initial and final orbits. This paper presents a graphical technique for coplanar transfer by a transfer orbit developed by use of the hodograph parameters (1) that describe the geometric figure of the closed orbit.

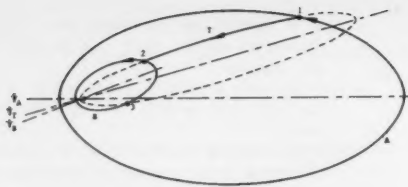


Fig. 1 Geometry of the orbital transfer problem

In general, the transfer will be between an initial orbit *A* and a final orbit *B*, as shown in Fig. 1. When the orbital vehicle reaches point 1 in its orbit, an instantaneous change of the velocity vector is assumed, which places the vehicle in its transfer orbit *T*. Since this change results from a propulsive thrust applied to the vehicle structure for a finite interval of time, the velocity change cannot be instantaneous in reality, but this idealization can be considered valid as a first-order approximation to the physically realizable system. When the orbital vehicle arrives at point 2 or 3, a second velocity change will be made so that the vehicle trajectory will be described by the final orbit *B*.

An elliptical orbit is described here by a pair of hodograph parameters instead of conic parameters. Consequently, the orbital velocity is presented graphically so that transfer by instantaneous velocity changes can be simply developed by graphical construction. Also, analytic relations for various transfer characteristics of interest can be defined from the transfer geometry.

Development of the Transfer Hodograph

As shown in Fig. 2, the position of the center of mass of the orbital vehicle relative to the center of the attracting celestial sphere is defined by the position vector \vec{r} . This position vector \vec{r} can also be described by a directed line Φ and a scalar distance r along the line. The directed line Φ is defined by the angle between the radial line and a reference line in space through the center of the celestial sphere.

Two geometric conditions must be fulfilled for transfer from one orbit to a second orbit at a given point. Consequently

$$r_{A1} = r_{T1} \quad [1]$$

$$\Phi_{A1} = \Phi_{T1} \quad [2]$$

and

$$r_{T2} = r_{B2} \quad [3]$$

$$\Phi_{T2} = \Phi_{B2} \quad [4]$$

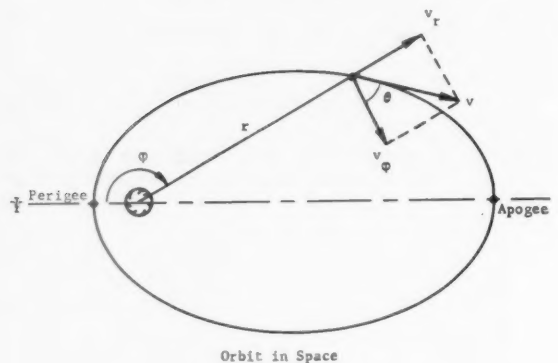
where the subscripts define the quantities in terms of the orbital parameters for the respective orbits (Fig. 1).

An orbit can be uniquely defined by the radial and normal velocity components, as developed in (1) and shown schematically in Fig. 3. The analytical transformations between the elliptical orbit in space and its hodograph are listed in Table 1. Note that the hodograph shown in Fig. 3 presents the true magnitude of the velocity vector, although the direction of this scalar magnitude is not that of the velocity vector, i.e., it is displaced from the ordinate axis by the flight path angle $\theta = \beta$. However, for ease of graphical construction, the vector direction on a hodograph should be related to that in space. Consequently, further study of the hodograph relations results in the development described below.

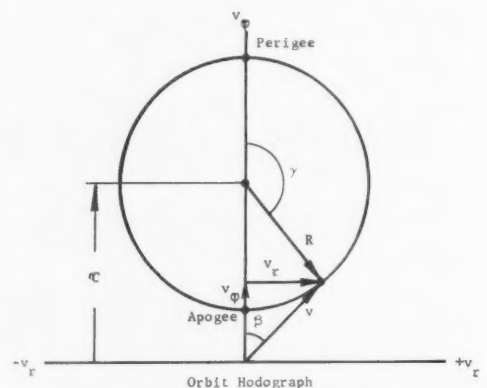
Since hodograph vector direction in space should be established, it is quite reasonable to first define the relations between rectilinear and polar velocity coordinates. The following relations are obtained on consideration of Fig. 4:



Fig. 2 Vector relations for an orbiting vehicle



Orbit in Space



Orbit Hodograph

Fig. 3 Planar orbit and its hodograph

$$\dot{x} = v_{\phi} \sin \phi - v_r \cos \phi \quad [16]$$

$$\dot{y} = v_{\phi} \cos \phi + v_r \sin \phi \quad [17]$$

Since

$$v_{\phi} = C + R \cos \phi$$

$$v_r = R \sin \phi$$

then

$$\dot{x} = C \sin \phi \quad [16a]$$

$$\dot{y} = R + C \cos \phi \quad [17a]$$

Consequently, the modified hodograph which retains velocity vector direction in space will appear as shown in Fig. 5. This modified hodograph can be identified as an alternative form of the classical hodograph (3) developed by Hamilton. The equation for this classical hodograph is

$$\dot{x}^2 + \left(\dot{y} - \frac{ke}{\sqrt{p}} \right)^2 = \frac{k^2}{p} \quad [18]$$

Table 1 Hodograph transformations for the elliptical orbit

$$\varphi = \gamma \quad [5]$$

$$\theta = \beta \quad [6]$$

$$v_r = R \sin \varphi \quad [7]$$

$$v_\varphi = C + R \cos \varphi \quad [8]$$

$$v^2 = C^2 + R^2 + 2CR \cos \varphi \quad [9]$$

where

$$C = \frac{\mu}{rv_\varphi} \quad [10]$$

$$R = \sqrt{\frac{2E}{m} + C^2} \quad [11]$$

E = orbital energy of the vehicle

$$e = \frac{R}{C} \quad [12]$$

$$a = \frac{\mu}{C^2 - R^2} \quad [13]$$

$$n = \frac{(C^2 - R^2)^{3/2}}{\mu} \quad [14]$$

$$a(1 - e^2) = \frac{\mu}{C^2} \quad [15]$$

where

\dot{x} = linear velocity component of the vehicle along a rectilinear axis parallel to the apsidal line of the orbit

\dot{y} = linear velocity component of the vehicle along a rectilinear axis normal to the apsidal line of the orbit

k^2 = gravitational constant

p = semilatus rectum of the elliptical figure of the orbit

e = eccentricity of the elliptical figure of the orbit

This equation defines a circle of radius $\sqrt{k^2/p}$ with its center displaced by ke/\sqrt{p} parallel to the y -axis.

However

$$p = a(1 - e^2) = \frac{\mu}{C^2}$$

$$e = \frac{R}{C}$$

$$k^2 = \mu$$

so that

$$\sqrt{\frac{k^2}{p}} = C$$

and

$$\frac{ke}{\sqrt{p}} = R$$

Consequently, the classical hodograph is identical with the modified hodograph represented by

$$\dot{x}^2 + (\dot{y} - R)^2 = C^2 \quad [19]$$

Referring to Fig. 5, we see that the hodograph point corresponding to the orbital point in space leads the orbital point by 90° , as expected. It is apparent that the hodograph

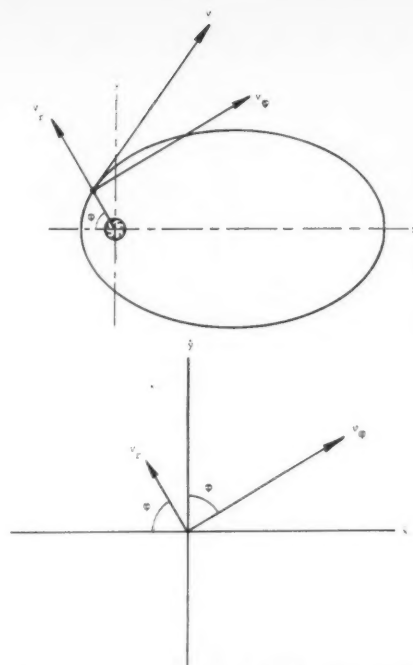


Fig. 4 Polar and rectilinear velocity coordinates for the planar orbit

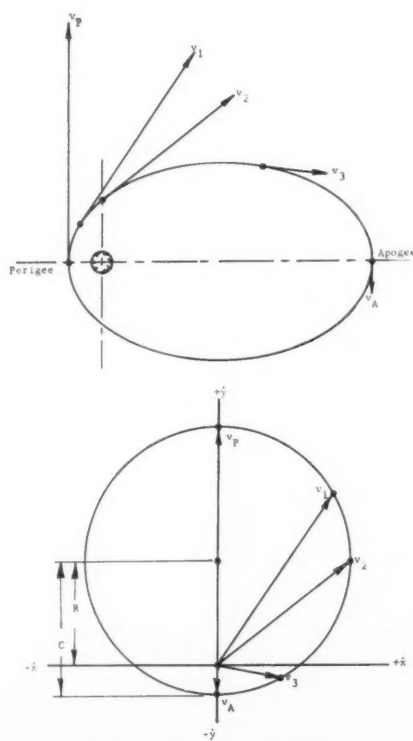


Fig. 5 Orbital hodograph in rectilinear coordinates

presentation (Fig. 3) of v_φ as an ordinate axis provides the proper directional relation between R and v_φ , except that R would appear to rotate in the opposite sense to the rotation of the vehicle in actual orbit.

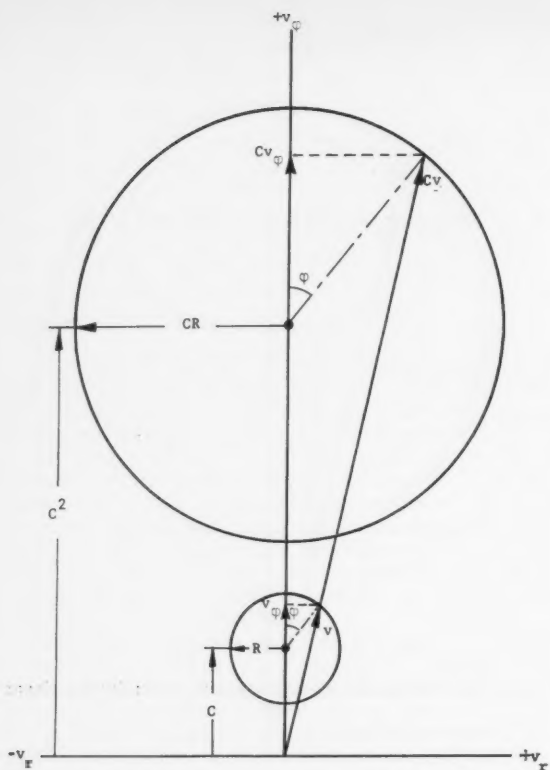
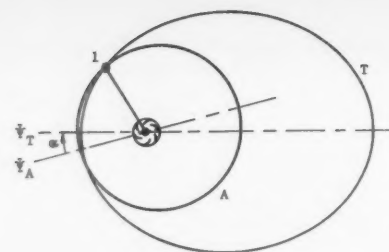
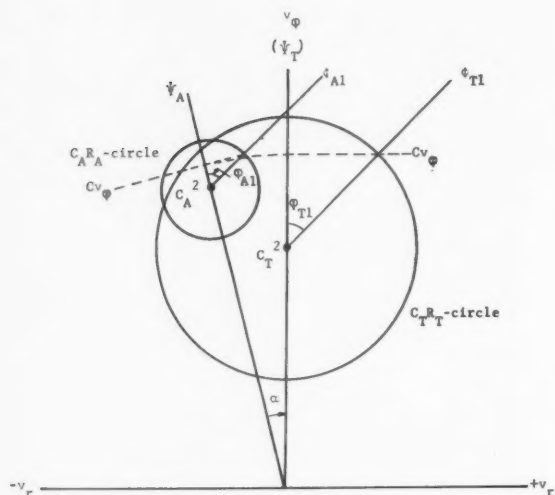


Fig. 6 Modified hodograph retaining spatial direction of the velocity vector



Orbits in Space



Orbit Hodographs

Fig. 8 Hodograph construction for two orbits with noncoincident apsidal lines

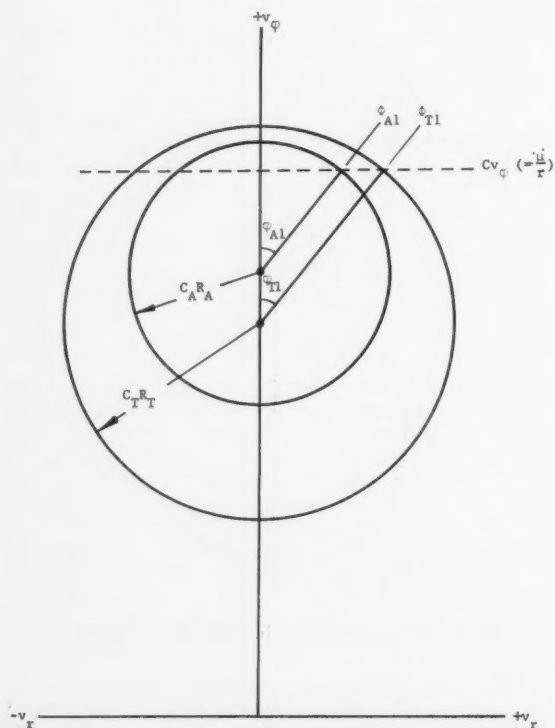


Fig. 7 Modified hodographs for two orbits with coincident apsidal lines

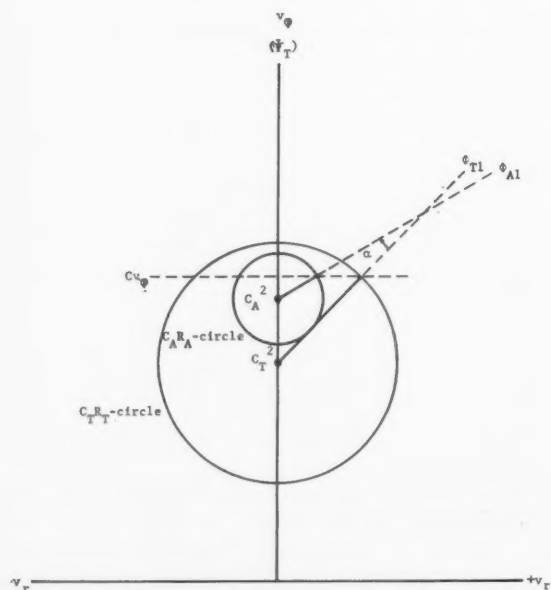


Fig. 9 Final hodograph representation for two orbits with noncoincident apsidal lines

$$(Cv_\varphi)_{A1} = (Cv_\varphi)_{T1} = \frac{\mu}{r_1} \quad [20]$$
$$\tan \varphi = \frac{Cv_r}{Cv_\varphi - C^2} = \frac{v_r}{v_\varphi - C} \quad [21]$$
$$Cv_r = CR \sin \varphi \quad [22]$$

$$Cv_s = C^2 + CR \cos \varphi \quad [23]$$

Now the intersection of an initial orbit A with a transfer orbit T at a point 1 is provided by use of a $C_A R_A$ circle and $C_T R_T$ circle, so that Eqs. 1 and 2 are satisfied. These equations are satisfied by the construction shown in Fig. 7 for initial and transfer orbits with coinciding apsidal lines. Since

$$\varphi = \Phi - \Psi \quad [24]$$

$$\Psi_A = \Psi_T$$

$$\varphi_{A1} = \varphi_{T1}$$

Now consider the case in which the apsidal lines of the initial and final orbits differ in angular position in space by $\alpha = \Psi_T - \Psi_A$ as shown in Fig. 8. Intersection of these orbits is also shown in Fig. 8 by use of $C_A R_A$ and $C_T R_T$ circles with v_φ -axes oriented to the apsidal line directions in space. The apsidal lines have relative orientation $\alpha = \Psi_T - \Psi_A$ as shown for the orbits in space. The Φ lines must be parallel, while the Cv_φ scalar measured from the hodograph origin must be the same for both hodographs. This graphical construction may be further simplified by rotating the $v_{\varphi A}$ -axis about the origin until it coincides with the $v_{\varphi T}$ -axis, as shown in Fig. 9. Now the respective Cv_φ lines coincide, while the Φ lines intersect at an angle equal to α .

While the values of R_T , C_T and Ψ_T may be selected arbitrarily within the region of required values for solution, the Φ line intersections must provide

$$\alpha + \eta = \Psi_B - \Psi_A \quad [25]$$

$$\eta = (\Psi_B - \Psi_A) - \alpha \quad [26]$$

Fig. 10 Hodograph representation of the complete point to point transfer problem

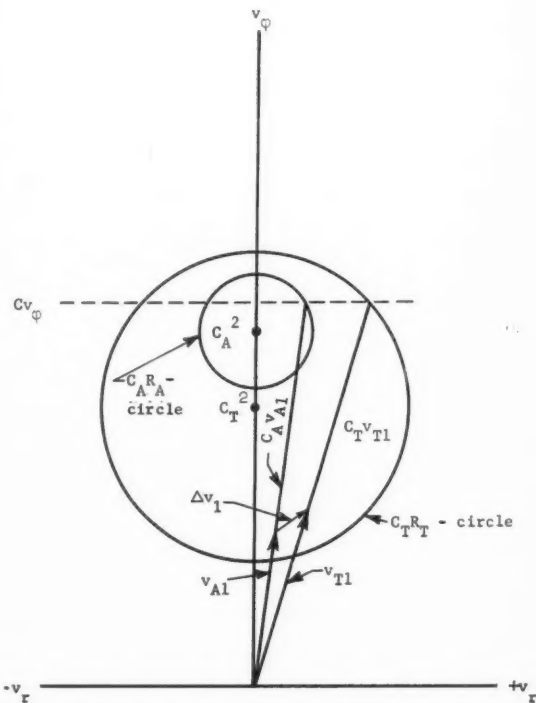


Fig. 11 Determination of the required velocity change at a point of transfer

Transfer Trajectories of Interest

For a proposed system or mission objectives, various transfer conditions may be imposed on a transfer orbit. The remainder of this paper describes possible trajectory design applications of the hodograph, and presents the analytic functions defining the most significant transfer conditions for present and future trajectory applications. The following transfer cases are presented:

- 1 Point to point transfer.
- 2 Arbitrary flight path angle at transfer.
- 3 Hohmann transfer.

Point to point transfer provides departure from and termination at arbitrarily selected points in space on the initial

and final orbits. In this case, the position and velocity coordinates of the initial and final points of transfer are specified as boundary conditions. Such arbitrary selection of the end points of transfer may result from mission requirements, or guidance design criteria. Also, the analytic relations for this point to point transfer between coplanar orbits can enable optimization of the transfer orbit, such as for minimum fuel consumption of transfer.

Transfer with a flight path angle arbitrarily specified at a given transfer point will provide a given difference between initial and final velocity vectors. For example, tangential transfer at a point of intersection between orbits is a special case of an arbitrary flight path angle in which the initial and terminal velocity vectors have the same direction at a given point of coincidence of two orbits. Certain missions, such as

Table 2 Analytic relations for point to point transfer

$$v_A^2 = \left(\frac{v_{c1}^2}{C_A}\right)^2 + \left(\frac{v_{c1}^2}{C_A} - C_A\right)^2 \tan^2 \varphi_A \quad [27]$$

$$v_{T1}^2 = \left(\frac{v_{c1}^2}{C_T}\right)^2 + \left(\frac{v_{c1}^2}{C_T} - C_T\right)^2 \tan^2 \varphi_{T1} \quad [28]$$

$$v_{T2}^2 = \left(\frac{v_{c2}^2}{C_T}\right)^2 + \left(\frac{v_{c2}^2}{C_T} - C_T\right)^2 \tan^2 \varphi_{T2} \quad [29]$$

$$v_B^2 = \left(\frac{v_{c2}^2}{C_B}\right)^2 + \left(\frac{v_{c2}^2}{C_B} - C_B\right)^2 \tan^2 \varphi_B \quad [30]$$

$$\Delta v_T = |\Delta v_1| + |\Delta v_2| \quad [31]$$

$$\Delta v_1^2 = \frac{1}{C_A^2 C_T^2 \sin^2 \sigma} [a_1(C_A - C_T)^2 + (b_1 C_T^2 + c_1 C_T + d_1)^2] \quad [32]$$

$$\Delta v_2^2 = \frac{1}{C_B^2 C_T^2 \sin^2 \sigma} [a_2(C_B - C_T)^2 + (b_2 C_T^2 + c_2 C_T + d_2)^2] \quad [33]$$

where

$$\sigma = (\varphi_B - \varphi_A) + (\Psi_B - \Psi_A) = (\varphi_B - \varphi_A) + (\alpha + \eta)$$

$$a_1 = v_{c1}^4 \sin^2 \sigma \quad [34]$$

$$b_1 = C_A(1 - \cos \sigma) \quad [35]$$

$$c_1 = (C_A^2 - v_{c1}^2) \tan \varphi_A \sin \sigma \quad [36]$$

$$d_1 = C_A(v_{c1}^2 \cos \sigma - v_{c2}^2) \quad [37]$$

$$a_2 = v_{c2}^4 \sin^2 \sigma \quad [38]$$

$$b_2 = C_B(\cos \sigma - 1) \quad [39]$$

$$c_2 = (C_B^2 - v_{c2}^2) \tan \varphi_B \sin \sigma \quad [40]$$

$$d_2 = C_B(v_{c1}^2 - v_{c2}^2 \cos \sigma) \quad [41]$$

and

$$v_{c1}^2 = (Cv_\varphi)_1 = \frac{\mu}{r_1} \quad [42]$$

$$v_{c2}^2 = (Cv_\varphi)_2 = \frac{\mu}{r_2} \quad [43]$$

$$\varphi_{T1} = \varphi_A - \alpha = \arctan \left[\frac{1}{\sin \sigma} \left(\cos \sigma - \frac{C_T^2 - v_{c2}^2}{C_T^2 - v_{c1}^2} \right) \right] \quad [44]$$

$$\varphi_{T2} = \varphi_B + \eta = \arctan \left[\frac{1}{\sin \sigma} \left(\frac{C_T^2 - v_{c1}^2}{C_T^2 - v_{c2}^2} - \cos \sigma \right) \right] \quad [45]$$

$$C_T R_T = \frac{v_{c1}^2 - C_T^2}{\cos \varphi_{T1}} = \frac{v_{c2}^2 - C_T^2}{\cos \varphi_{T2}} \quad [46]$$

or

$$C_T R_T = \frac{v_{c2}^2 - v_{c1}^2}{\cos \varphi_{T2} - \cos \varphi_{T1}} \quad [46a]$$

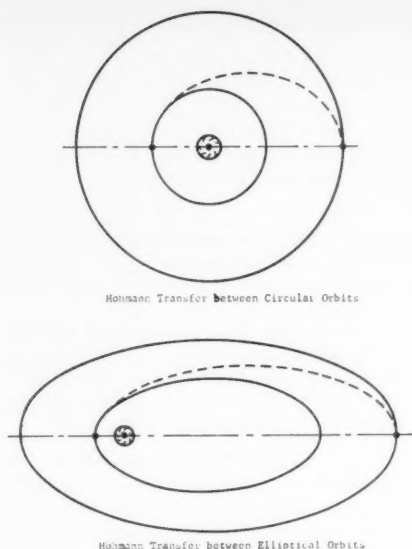


Fig. 12 Hohmann transfer orbits

rendezvous of a ferry vehicle with a target satellite, may require the tangential relation for orbital transfer in order to obtain desirable initial conditions for the terminal phase of the rendezvous.

Hohmann transfer is provided by a transfer orbit with initial and final transfer points providing tangential contact with the initial and final orbits respectively. If both the initial and final orbits are circular, Hohmann transfer is always possible. If the initial and final orbits are elliptic, the apsidal lines must coincide so that the initial transfer point occurs at one apsidal point on the initial orbit and the final transfer point occurs at the opposing apsidal point on the final orbit. Hohmann transfer may be desirable (assuming it is physically realizable with a given orbital vehicle system) if minimal fuel consumption is a critical design factor. However, other mission and design considerations may become dominant in the transfer problem, so that a flight path angle change other than zero (i.e., tangential transfer) may be required.

Point to Point Transfer

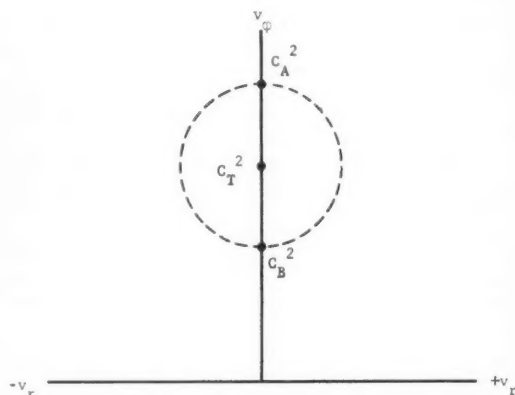
In this case, an initial and a final orbit are given, and the point of departure from the initial orbit and point of arrival at the final orbit are arbitrarily specified. The transfer orbit is defined by three parameters: C_T , R_T and Ψ_T . A transfer orbit may be obtained by assigning an acceptable value to one of these parameters, i.e., considering that parameter as an independent variable. Then the other two parameters are dependent variables with unique values that must lie within the realizable regions of solution defined by the conditions of dependency. In general, three bases for selection of a transfer orbit appear possible:

- 1 To control the transfer time.
- 2 To control the crossing angles of the orbits at the transfer points.
- 3 To control the total velocity change required to achieve transfer.

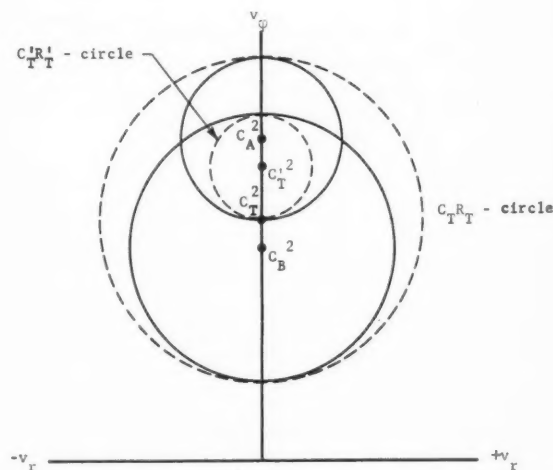
As noted in Table 1, the mean orbital velocity n is a function of C and R . Consequently, primary concern for transfer time would dictate selection of C_T and R_T on this basis, with secondary concern for selection of Ψ_T . On the other hand, variation of Ψ_T would appear to exert the greatest influence

on the orbital crossing angles. In this case, primary concern for the orbital crossing angles would dictate selection of Ψ_T on this basis, with secondary concern for selection of C_T and R_T . Finally, achievement of transfer with minimum total velocity change is a most obvious objective for design purposes. Although the conditions that must be imposed on the transfer parameters to obtain this optimization are not immediately obvious until further analysis is completed, the geometric construction and the resulting analytic relations indicate promising results from further analysis.

The procedures for graphical construction of the transfer orbit hodograph are presented in (4). Three alternative procedures have been developed, each for arbitrary selection of Ψ_T , C_T^2 , or $C_T R_T$ respectively. Since solutions can be obtained by geometric construction, analytic relations for such solutions must necessarily exist. Although many alternative forms of equations for solution are available, the relations listed in Table 2 are considered most suitable for analysis. Those terms which are not defined in the table are identified in Fig. 10. Three variables are used: Ψ_T , C_T and R_T . In these equations, C_T is the independent variable; thus the required velocity increments are functions of the given constants and C_T only, as shown in Table 2. The variables Ψ_T and R_T are dependent only, as shown in Eqs. 44, 45 and 46. Eqs. 32 and 33 for the required velocity increments are dependent on Ψ_T and R_T implicitly.



Hodograph for Hohmann Transfer between Circular Orbits



Hodograph for Hohmann Transfer between Elliptical Orbits

Fig. 13 Hodographs for Hohmann transfer

Arbitrary Flight Path Angle at Transfer

In this case, an initial and a final orbit are given, and the change in the increment of the flight path angle at a transfer point is arbitrarily specified. This trajectory design requirement may be necessary due to subsystem limitations of vehicle attitude control for direction of either the propulsion thrust, or of the guidance system field of view. Then the direction of the velocity vector at one of the end points of the transfer orbit is defined, and the transfer orbit is thereby determined.

The procedure for graphical construction of the transfer orbit hodograph is fully presented in (4). The general analytic relations developed for point to point transfer are valid for arbitrary flight path angles. However, for the special case of tangential transfer at a point, the following simpler forms can be used

$$\Delta v_1 = \frac{C_A - C_T}{C_A C_T} [v_{c1}^4 + (v_{c1}^2 - C_A^2) \tan^2 \varphi_A]^{1/2} \quad [47]$$

$$\Delta v_2 = \frac{C_T - C_B}{C_B C_T} [v_{c2}^4 + (C_B^2 - v_{c2}^2) \tan^2 \varphi_B]^{1/2} \quad [48]$$

Eq. 47 represents the velocity increment required for tangential transfer at point 1, whereas Eq. 48 applies to tangential transfer at point 2.

Hohmann Transfer

Hohmann transfer between circular or elliptical orbits is defined by departure from the initial orbit at a point on a line with, but in phase opposition to, the arrival point on the final orbit, as shown in Fig. 12. Hohmann transfer between elliptical orbits is only possible when the apsidal lines coincide.

The hodographs for Hohmann transfer are shown in Fig. 13. Note that two Hohmann ellipses are possible for transfer between elliptical orbits. The transfer hodograph is tangent to the initial and final orbit hodographs, with circle radius and center defined by the geometry.

Although the general analytic relations developed for point to point transfer are valid for the Hohmann transfer, the simpler forms of equations shown in Table 3 appear more useful.

Table 3 Analytic relations for Hohmann transfer

$$C_T^2 = 0.5 [(C_A^2 + C_A R_A) + (C_B^2 - C_B R_B)] \quad [49]$$

$$C_T R_T = 0.5 [(C_A^2 + C_A R_A) - (C_B^2 - C_B R_B)] \quad [50]$$

$$\Delta v_T = |\Delta v_1| + |\Delta v_2|$$

$$\Delta v_1 = (C_A + R_A) \left(\frac{C_A}{C_T} - 1 \right) \quad [51]$$

$$\Delta v_2 = (C_B - R_B) \left(1 - \frac{C_B}{C_T} \right) \quad [52]$$

or

$$C_T'^2 = 0.5 [(C_A^2 - C_A R_A) + (C_B^2 + C_B R_B)] \quad [53]$$

$$C_T' R_T' = 0.5 [(C_A^2 - C_A R_A) - (C_B^2 + C_B R_B)] \quad [54]$$

$$\Delta v_T' = |\Delta v_1'| + |\Delta v_2'|$$

$$\Delta v_1' = (C_A - R_A) \left(\frac{C_A}{C_T'} - 1 \right) \quad [55]$$

$$\Delta v_2' = (C_B + R_B) \left(1 - \frac{C_B}{C_T'} \right) \quad [56]$$

Summary and Conclusions

A geometric method for determining a required transfer orbit is developed by use of a modified hodograph. The initial and final elliptical orbit figures that lie in one plane are given, and the transfer orbit parameters and velocities at the transfer points can be obtained so that various desired transfer conditions are fulfilled. The solutions will consist of the following data:

- 1 The transfer orbit parameters C_T , R_T , Ψ_T .
- 2 The transfer orbit anomalies at the transfer points.
- 3 All velocity vectors at the transfer points, referred to the local horizon.
- 4 As a consequence of 3, the required relative velocity vectors for transfer at the points of orbital intersection.
- 5 Although not discussed in this paper, the time for transit between the initial and final points may be obtained by the integration procedure indicated in (2).

The analytic relations for the geometric solution are tabulated for use in obtaining added accuracy of solution and subsequent optimization. Realizable solutions for any point to point transfer problem in which σ is specified, either explicitly or implicitly, exist only when the angle $\varphi_{T2} - \varphi_{T1}$ is equal to σ .

The developments of this paper are concerned principally with point to point transfer. If these points are not selected a priori, then those transfer orbits providing minimum velocity change or minimum time for transfer between two orbital figures may be desired. The equations derived in this paper can be used in subsequent optimization of the required velocity change. However, the geometric construction does not provide time solutions for possible optimization of the required transfer time. Although variation of the transfer time as a function of the transfer orbit parameters C_T , R_T and the anomalies at the transfer points may be obtained separately in parametric form, analytic relations suitable for time optimization are not yet available.

Finally, it is suggested that the geometric analysis of orbital plane reorientation may be accomplished with comparable ease. Then complete three-dimensional transfer by use of a transfer orbit would be directly solvable for complete space orbit shaping.

Nomenclature

- a = semi-major axis of the ellipse, ℓ
 C = velocity parameter of the orbit, ℓ^{-1}
 e = eccentricity of the ellipse
 E = total potential and kinetic energy of the orbital body, $m\ell^2\ell^{-2}$
 k^2 = acceleration of the orbiting body at unit distance from the attracting body = μm , ℓ^{-2}
 n = mean angular velocity of the body in orbit, ℓ^{-1}
 m = mass of the orbital body, m
 p = semilatus rectum of the ellipse, ℓ
 r = radial distance between the gravitational centers of the orbital and celestial bodies, ℓ
 R = velocity parameter of the orbit, ℓ^{-1}
 v = linear velocity, $\ell\ell^{-1}$
 Δv = magnitude of the vector difference between two linear velocities, $\ell\ell^{-1}$
 \hat{x} = component of the total velocity vector, resolved along apsidal line
 \hat{y} = component of the total velocity vector, resolved along an axis normal to the apsidal line
 α = angular difference between the apsidal lines of the initial orbit and the transfer orbit at perigee, with sense established by that order
 β = angle between the hodograph v_φ -axis and the hodograph total velocity
 γ = angle between the hodograph v_φ -axis and the hodograph radius R to the orbital body on the hodograph
 η = angular difference between the apsidal lines of the transfer

orbit and the final orbit at perigee, with sense established by that order

- θ = angle between the total velocity vector and the local horizon in the orbital plane
- $\Delta\theta$ = angular difference between two total velocity vectors at a transfer point in space
- μ = gravitational constant for the given celestial body, $\ell^2 t^{-2}$
- σ = angular difference between the transfer orbit phases for the two transfer points
- φ = true anomaly of the body in orbit
- Φ = radial line between centers of the orbital and celestial bodies
- Ψ = apsidal line of the orbit at perigee

Subscripts

- a = apogee
- A = initial orbit
- B = final orbit

- p = perigee
- r = radial
- T = transfer orbit
- 1 = point of transfer from the initial orbit to the transfer orbit
- 2 = point of transfer from the transfer orbit to the final orbit
- φ = normal

References

- 1 Altman, S. P., "Orbital Transfer for Satellites," *Proc. Fourth BMD Symposium on Ballistic Missiles and Space Technology*, Pergamon Press, 1961.
- 2 Pistiner, J. S., "Some Characteristics of the Planar Satellite Orbit," *ARS JOURNAL*, vol. 30, no. 3, March 1960, pp. 275-277.
- 3 MacMillan, W. D., *Statics and the Dynamics of a Particle*, Dover Publications, N. Y., 1958.
- 4 Altman, S. P. and Pistiner, J. S., "Hodograph Analysis of the Orbital Transfer Problem for Coplanar, Nonaligned Elliptical Orbits," presented at the ARS 15th Annual Meeting, Washington, D. C., Dec. 5-8, 1960 (ARS preprint 1447-60).

Planar Motions About an Oblate Planet

MAURICE L. ANTHONY¹ and
GEORGE E. FOSDICK²

The Martin Co.
Denver, Colo.

Two cases of plane motion (equatorial and polar) of a vehicle about an oblate planet are discussed. Further, the results of these drag free plane motion studies may be applied to the determination of radial position, speed, and angular momentum for a motion whose initial velocity vector is inclined at an arbitrary angle to the equatorial plane. Approximate analytic results are found by expanding the solution of the system of nonlinear differential equations of the path in powers of the oblateness parameter J . Although only the first power is retained in this solution, no restriction is placed on eccentricity. Thus, for example, the results for an eccentricity of 0.5 may be found from the analysis. In fact, results for speeds in excess of escape speed (e.g., $e = 1.1$) may be found. Comparison with results obtained by numerically integrating the equations of motion indicates excellent agreement with the analysis.

IN THE past few months, intensified interest in artificial Earth satellites has resulted in considerable papers in the technical literature that are concerned with certain aspects of satellite motion. Generally speaking, these papers fall into two categories. One type provides approximate analytic solutions, but places fairly severe restrictions on either the eccentricity, or the inclination angle, or both. This class is exemplified by the work of Blitzer (1,2,3),³ Weisfield (1), and

Wheelon (1,2); Brouwer (4); Hall and Gawlowicz (5); Moulton (6); Orlov (7); and Roberson (8). The other type of paper treats the problem numerically, and involves the use of high speed computers. Typical of this type are the works of Fosdick and Hewitt (9), who numerically integrated the equations of motion to obtain the coordinates; and Nielsen, Goodwin, and Mersman (10), who integrated the variational equations to obtain the elements.

This paper presents the results of analytic investigation of the motion of a particle that is acted upon solely by the gravitational attraction of a spheroid. The two possible plane motions (equatorial and polar) are studied, with the particle initially at an apse (horizontal velocity vector). No restrictions are placed on the eccentricity.

Presented at the ARS Semi-Annual Meeting, Los Angeles, Calif., May 9-12, 1960.

¹ Manager, Space Flight Lab. Member ARS.

² Assistant Research Scientist, Astrodynamics Section. Member ARS.

³ Numbers in parentheses indicate References at end of paper.

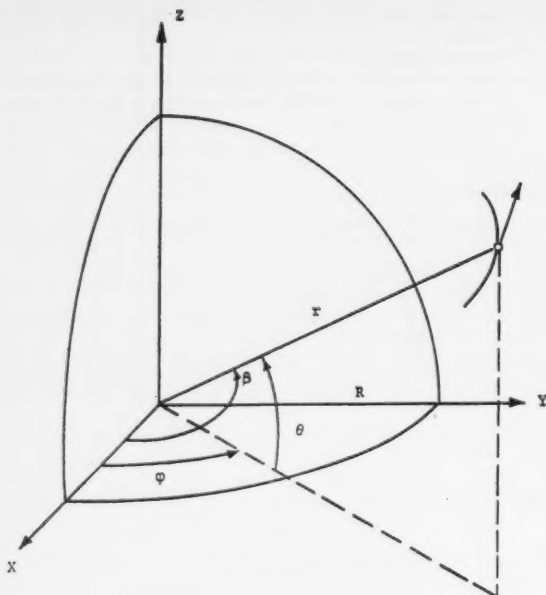


Fig. 1 Notations used in the analysis

The analysis is conducted in terms of polar coordinates; the notations used are shown in Fig. 1, where the z -axis represents the axis of rotational symmetry. The potential function for an oblate planet is given by Jeffreys (11) as

$$U = -\frac{\mu}{R} \left[\left(\frac{R}{r} \right) + J \left(\frac{1}{3} - \sin^2 \theta \right) \left(\frac{R}{r} \right)^3 + \frac{D}{35} (35 \sin^4 \theta - 30 \sin^2 \theta + 3) \left(\frac{R}{r} \right)^5 \right] \quad [1]$$

where J and D are dimensionless constants, which are empirically determined. For Earth, they are given approximately by $J = 1.638 \times 10^{-3}$ and $D = 1.06 \times 10^{-5}$.

The following analysis yields an approximate solution to the equations of the particle path. The method utilizes power series expansions in terms of the small parameter J and neglects terms of the order J^2 and above. Consistent with this order of approximation is the omission of the influence of D in the potential, as well as the pear shaped term of O'Keefe, et al. (12). Hence, the equations of motion become

$$\ddot{r} - r\dot{\theta}^2 - r \cos^2 \theta \dot{\phi}^2 = -\mu \left[\frac{1}{r^2} + \frac{JR^2}{r^4} (1 - 3 \sin^2 \theta) \right] \quad [2a]$$

$$\frac{1}{r} \frac{d}{dt} (r^2 \dot{\theta}) + r \dot{\phi}^2 \sin \theta \cos \theta = -\frac{\mu JR^2}{r^4} \sin 2\theta \quad [2b]$$

$$\frac{1}{r \cos \theta} \frac{d}{dt} (r^2 \cos^2 \theta \dot{\phi}) = 0 \quad [2c]$$

Solutions are determined for two special cases: the equatorial plane, and the polar plane. In these cases the equations of motion become

Motion in Equatorial Plane

$$r^2 \dot{\phi} = r_0 V_0 \quad [3a]$$

$$\ddot{r} - r\dot{\phi}^2 = -\frac{\mu}{r^2} \left[1 + J \left(\frac{R}{r} \right)^2 \right] \quad [3b]$$

Motion in Polar Plane

$$\frac{d}{dt} (r^2 \dot{\theta}) = -\frac{\mu JR^2}{r^3} \sin 2\theta \quad [4a]$$

$$\ddot{r} - r\dot{\theta}^2 = -\frac{\mu}{r^2} \left[1 + J \left(\frac{R}{r} \right)^2 (1 - 3 \sin^2 \theta) \right] \quad [4b]$$

Following are an illustration of the method of solution, general results of the analysis, and detailed discussions of the polar and equatorial plane cases. The final discussion indicates how radial position, speed, and angular momentum of a particle in an orbit inclined arbitrarily to the equatorial plane may be determined by superposition of the solutions for the two plane cases.

Method of Solution and General Results

The method of solution is illustrated by applying it to the determination of the particle path in the polar plane. Although results for a launch at an arbitrary latitude are presented in this paper, the method of solution is illustrated for launch from the equatorial plane. The equatorial plane may be treated in the same way, and is essentially a simpler case than the polar one since the angular momentum is conserved.

Specifically, the radial position r , the speed V , and the angular momentum P are determined as functions of the central space angle. The governing differential equations are Eqs. 4a and b; the initial conditions are, at $t = 0$

$$r = r_0 \quad [5a]$$

$$\dot{r} = 0 \quad [5b]$$

$$\theta = 0 \quad [5c]$$

$$r^2 \dot{\theta} = r_0 V_0 \quad [5d]$$

which imply that the particle is initially moving horizontally in the polar plane from a launch in the equatorial plane.

The equations of the path are determined by eliminating the time and using the substitutions

$$u = \frac{1}{r} \quad [6a]$$

$$P = r^2 \dot{\theta} \quad [6b]$$

$$v = \frac{du}{d\theta} \quad [6c]$$

in Eqs. 4a and b. The nonlinear first-order system of differential equations below results

$$0 = P^2 \frac{dv}{d\theta} + P_v \frac{dP}{d\theta} + P^2 u - \mu [1 + J(Ru)^2 (1 - 3 \sin^2 \theta)] \quad [7a]$$

$$0 = P \frac{dP}{d\theta} + 2\mu JR^2 u \sin \theta \cos \theta \quad [7b]$$

$$0 = \frac{du}{d\theta} - v \quad [7c]$$

The method of approximate solution of these equations, essentially due to Lindstedt (13), is to expand the unknowns u , v , and P into power series in the parameter J . In addition, secular terms in the solution may be eliminated by a simple change of independent variable. Thus, in Eqs. 7a, b and c the following substitutions are made

$$u(\xi) = u_0(\xi) + J u_1(\xi) + \dots \quad [8a]$$

$$v(\xi) = v_0(\xi) + J v_1(\xi) + \dots \quad [8b]$$

$$P(\xi) = P_0(\xi) + J P_1(\xi) + \dots \quad [8c]$$

$$\theta(\xi) = \xi [1 + J \theta_1 + \dots] \quad [8d]$$

where θ_1 is a constant to be determined later. After this

substitution, Eqs. 7a, b and c become three power series in J which vanish identically. Thus, the coefficients of each power of J in each series must be zero. Since, in this study, terms of second order and higher in J are neglected, the remaining terms in the identities lead to the following six equations, where the prime notation indicates differentiation with respect to ξ

$$0 = P_0' \quad [9a]$$

$$0 = u_0' - v_0 \quad [9b]$$

$$0 = P_0(v_0' + u_0) + P_0'v_0 - \frac{\mu}{P_0} \quad [9c]$$

$$0 = P_0P_1' + \mu R^2u_0 \sin 2\xi \quad [9d]$$

$$0 = u_1' - v_1 - v_0\theta_1 \quad [9e]$$

$$0 = P_0(v_1' + u_1 + u_0\theta_1) + P_1(v_0' + u_0) + P_0'v_1 + P_1'v_0 - \frac{\mu}{P_0} \left[-\frac{P_1}{P_0} + \theta_1 + R^2u_0^2(1 - 3 \sin^2 \xi) \right] \quad [9f]$$

These equations may be solved successively. Since the initial conditions must be satisfied identically for all values of J , they may be expressed, at $\xi = 0$ as

$$u_0 = 1/r_0 \quad [10a]$$

$$P_0 = r_0V_0 = c \sqrt{\mu r_0} \quad [10b]$$

$$u_1 = u_1' = u_0' = v_0 = v_1 = P_1 = 0 \quad [10c]$$

By eliminating the v terms and using the functions u_0 , P_0 , and P_1 , the equation for u_1 may be written as follows

$$u_1'' + u_1 = A(\xi) + B(\xi) \quad [15]$$

where

$$A(\xi) = \frac{-\eta}{r_0c^2} \left[2\theta_1 + \frac{1}{c^4} \left(\frac{R}{r_0} \right)^2 \right] \cos \xi \quad [16a]$$

$$B(\xi) = \frac{1}{r_0c^6} \left(\frac{R}{r_0} \right)^2 \left[\left(\frac{1}{2} + \frac{4}{3} \eta - \frac{1}{8} \eta^2 \right) + \frac{(1 + \eta^2)}{2} \cos 2\xi + \frac{5}{3} \eta \cos 3\xi + \frac{5}{8} \eta^2 \cos 4\xi \right] \quad [16b]$$

and the constant θ_1 is still open to choice.

The particular solutions that arise from $B(\xi)$ are periodic in ξ . In order to assure that for all values of η no secular terms occur in the solution, the quantity θ_1 is chosen so that $A(\xi) = 0$.

Thus

$$\theta_1 = -\frac{1}{2c^4} \left(\frac{R}{r_0} \right)^2 \quad [17]$$

and

$$\theta = \xi \left[1 - \frac{J}{2c^4} \left(\frac{R}{r_0} \right)^2 \right] \quad [18]$$

With $A(\xi) = 0$, the solution of Eq. 15, subject to the initial conditions ($u_1 = u_1' = 0$ for $\xi = 0$), is

$$u_1 = \frac{1}{r_0c^6} \left(\frac{R}{r_0} \right)^2 \left[\left(\frac{1}{2} + \frac{4}{3} \eta - \frac{1}{8} \eta^2 \right) + \left(-\frac{1}{3} - \frac{9}{8} \eta + \frac{1}{3} \eta^2 \right) \cos \xi - \left(\frac{1}{6} + \frac{\eta^2}{6} \right) \cos 2\xi - \frac{5}{24} \eta \cos 3\xi - \frac{1}{24} \eta^2 \cos 4\xi \right] \quad [19]$$

where

$$\theta = \xi \left[1 - \frac{J}{2c^4} \left(\frac{R}{r_0} \right)^2 \right] \quad [20]$$

The solution for u ($= u_0 + Ju_1$) is thus

$$u = \frac{1}{r_0c^4} \left\{ 1 + \eta \cos \xi + \frac{J}{c^4} \left(\frac{R}{r_0} \right)^2 \left[\left(\frac{1}{2} + \frac{4}{3} \eta - \frac{1}{8} \eta^2 \right) + \left(-\frac{1}{3} - \frac{9}{8} \eta + \frac{1}{3} \eta^2 \right) \cos \xi - \left(\frac{1}{6} + \frac{\eta^2}{6} \right) \cos 2\xi - \frac{5}{24} \eta \cos 3\xi - \frac{1}{24} \eta^2 \cos 4\xi \right] \right\} \quad [21]$$

Integrating Eqs. 9a through 9f subject to Eqs. 10a through c yields

$$P_0 = r_0V_0 \quad [11]$$

$$u_0 = (1/r_0c^2) [1 + \eta \cos \xi] \quad [12]$$

$$P_1 = -\frac{r_0V_0}{c^4} \left(\frac{R}{r_0} \right)^2 \left[\left(\frac{1}{2} + \frac{2}{3} \eta \right) - \frac{\eta}{2} \cos \xi - \frac{1}{2} \cos 2\xi - \frac{\eta}{6} \cos 3\xi \right] \quad [13]$$

Thus, to first order in J , the angular momentum per unit mass may be expressed as

$$\begin{aligned} r^2\dot{\theta} &= P = P_0 + JP_1 \\ &= r_0V_0 \left\{ 1 - \frac{J}{c^4} \left(\frac{R}{r_0} \right)^2 \left[\left(\frac{1}{2} + \frac{2}{3} \eta \right) - \frac{\eta}{2} \cos \xi - \frac{1}{2} \cos 2\xi - \frac{\eta}{6} \cos 3\xi \right] \right\} \quad [14] \end{aligned}$$

The speed of the satellite may be found from the expression

$$V^2 = P^2 \left[u^2 + \left(\frac{du}{d\theta} \right)^2 \right] \quad [22]$$

The result of this expression, and other results pertinent to a particle path in the polar plane, launched from the equatorial plane are shown in Table 1. For a launch at an arbitrary latitude, the initial conditions are the same as those given in Eqs. 5a through 5d except that $\theta = \theta_0$. The results for this case are presented in Table 2.

Although the results found in this way are approximate in that terms of the order of J^2 and above have been neglected, no restriction has been placed on η , the analog of eccentricity. Thus, solutions have been determined that are valid not only for nearly circular paths, but also for highly eccentric paths, including escape paths.

Since for nonescape paths the functions r , P , and V have the period 2π in the variable ξ , Eq. 20 indicates that they have the period $2\pi[1 - (J/2c^4)(R/r_0)^2]$ in the space angle θ . Therefore, r , P , and V go through an entire period before the

Table 1 Summary of polar plane results (launched from equatorial plane)

$$r = r_0 \left\{ \frac{1 + \eta}{1 + \eta \cos \xi} - \frac{J}{24} \left(\frac{R}{r_0} \right)^2 \frac{L(\xi)}{(1 + \eta)[1 + \eta \cos \xi]^2} \right\} \quad [23]$$

$$V = \frac{V_0 \sqrt{1 + \eta^2 + 2\eta \cos \xi}}{1 + \eta} \left\{ 1 + \frac{J}{48} \left(\frac{R}{r_0} \right)^2 \frac{M(\xi)}{(1 + \eta)^2 [1 + \eta^2 + 2\eta \cos \xi]} \right\} \quad [24]$$

$$P = r_0 V_0 \left\{ 1 - \frac{J}{6c^4} \left(\frac{R}{r_0} \right)^2 [3 + 4\eta - 3\eta \cos \xi - 3 \cos 2\xi - \eta \cos 3\xi] \right\} \quad [25]$$

where

$$L(\xi) = (12 + 32\eta - 3\eta^2) + (-8 - 27\eta + 8\eta^2) \cos \xi - 4(1 + \eta^2) \cos 2\xi - 5\eta \cos 3\xi - \eta^2 \cos 4\xi \quad [26]$$

$$M(\xi) = 16(\eta - 3\eta^2 - \eta^3) + 2(-8 - 21\eta + 8\eta^2 + 3\eta^3) \cos \xi + 16(1 + \eta^2) \cos 2\xi + (26\eta + 7\eta^3) \cos 3\xi + 16\eta^2 \cos 4\xi + 3\eta^3 \cos 5\xi \quad [27]$$

$$\theta = \xi \left[1 - \frac{J}{2c^4} \left(\frac{R}{r_0} \right)^2 \right] \quad [28]$$

Table 2 Summary of polar plane results (launched from arbitrary latitude)

$$r = r_0 \left\{ \frac{1 + \eta}{1 + \eta \cos(\xi - \xi_0)} - \frac{J}{24} \left(\frac{R}{r_0} \right)^2 \frac{L_1(\xi)}{(1 + \eta)[1 + \eta \cos(\xi - \xi_0)]^2} \right\} \quad [29]$$

$$V = \frac{V_0}{(1 + \eta)} [1 + \eta^2 + 2\eta \cos(\xi - \xi_0)]^{1/2} \left\{ 1 + \frac{J}{48} \left(\frac{R}{r_0} \right)^2 \frac{M_1(\xi)}{(1 + \eta)^2 [1 + \eta^2 + 2\eta \cos(\xi - \xi_0)]} \right\} \quad [30]$$

$$P = r_0 V_0 \left\{ 1 + \frac{J}{6c^4} \left(\frac{R}{r_0} \right)^2 [- (3 + 4\eta) \cos 2\xi_0 + 3\eta \cos 2\xi_0 \cos(\xi - \xi_0) - 3\eta \sin 2\xi_0 \sin(\xi - \xi_0) + 3 \cos 2\xi_0 \cos 2(\xi - \xi_0) - 3 \sin 2\xi_0 \sin 2(\xi - \xi_0) + \eta \cos 2\xi_0 \cos 3(\xi - \xi_0) - \eta \sin 2\xi_0 \sin 3(\xi - \xi_0)] \right\} \quad [31]$$

where

$$L_1(\xi) = \{ [-12 - 6\eta^2 + (24 + 32\eta + 3\eta^2) \cos 2\xi_0] + [12 + 4\eta^2 + (-20 - 27\eta + 4\eta^2) \cos 2\xi_0] \cos(\xi - \xi_0) - (8 + 15\eta + 16\eta^2) \sin 2\xi_0 \sin(\xi - \xi_0) + [2\eta^2 - (4 + 6\eta^2) \cos 2\xi_0] \cos 2(\xi - \xi_0) + (4 + 6\eta^2) \sin 2\xi_0 \sin 2(\xi - \xi_0) - 5\eta \cos 2\xi_0 \cos 3(\xi - \xi_0) + 5\eta \sin 2\xi_0 \sin 3(\xi - \xi_0) - \eta^2 \cos 2\xi_0 \cos 4(\xi - \xi_0) + \eta^2 \sin 2\xi_0 \sin 4(\xi - \xi_0) \} \quad [32]$$

$$M_1(\xi) = \{ [-24 + 24\eta + 8\eta^2 + (24 - 8\eta - 48\eta^2 - 24\eta^3) \cos 2\xi_0] + [24 - 24\eta + 8\eta^2 - 6\eta^3 + (-40 - 18\eta + 8\eta^2 + 12\eta^3) \cos 2\xi_0] \cos(\xi - \xi_0) - (16 + 66\eta + 32\eta^2 + 6\eta^3) \sin 2\xi_0 \sin(\xi - \xi_0) + [-8\eta^2 + (16 + 24\eta^2) \cos 2\xi_0] \cos 2(\xi - \xi_0) - (16 + 24\eta^2) \sin 2\xi_0 \sin 2(\xi - \xi_0) + [-2\eta^3 + (26\eta + 9\eta^3) \cos 2\xi_0] \cos 3(\xi - \xi_0) - (26\eta + 9\eta^3) \sin 2\xi_0 \sin 3(\xi - \xi_0) + 16\eta^2 \cos 2\xi_0 \cos 4(\xi - \xi_0) - 16\eta^2 \sin 2\xi_0 \sin 4(\xi - \xi_0) + 3\eta^3 \cos 2\xi_0 \cos 5(\xi - \xi_0) - 3\eta^3 \sin 2\xi_0 \sin 5(\xi - \xi_0) \} \quad [33]$$

$$\theta = \xi \left[1 - \frac{J}{2c^4} \left(\frac{R}{r_0} \right)^2 \right]; \theta = \theta_0 \text{ at } \xi = \xi_0 \quad [34]$$

Table 3 Summary of equatorial plane results

$$r = r_0 \left\{ \frac{1 + \eta}{1 + \eta \cos \xi} - \frac{J}{6} \left(\frac{R}{r_0} \right)^2 \frac{[6(1 - \cos \xi) + \eta^2(3 - 2 \cos \xi - \cos 2\xi)]}{(1 + \eta)(1 + \eta \cos \xi)^2} \right\} \quad [35]$$

$$V = \frac{V_0 \sqrt{1 + \eta^2 + 2\eta \cos \xi}}{1 + \eta} \left\{ 1 + \frac{J}{12} \left(\frac{R}{r_0} \right)^2 \frac{N(\xi)}{(1 + \eta)^2 (1 + \eta^2 + 2\eta \cos \xi)} \right\} \quad [36]$$

$$P = r_0 V_0 \quad [37]$$

where

$$N(\xi) = 4(3 - 3\eta - \eta^3) + (-12 + 12\eta - 4\eta^2 + 3\eta^3) \cos \xi + 4\eta^2 \cos 2\xi + \eta^3 \cos 3\xi \quad [38]$$

$$\varphi = \xi \left[1 + \frac{J}{c^4} \left(\frac{R}{r_0} \right)^2 \right] \quad [39]$$

space angle has made one complete circuit, so that, for example, the apses regress (move in the opposite direction to the satellite motion) at the rate of $(\pi J/c^4)(R/r_0)^2$ radians per revolution.

Results for motion in the equatorial plane may be found using the same method, and are presented in Table 3. In this case, the angular momentum is constant, and the functions r and V have the period $2\pi[1 + (J/c^4)(R/r_0)^2]$ in the space angle φ , so that the apses advance at the rate of $(2\pi J/c^4)(R/r_0)^2$ radians per revolution. Thus, the apsidal advance in the equatorial plane is twice the apsidal regression in the polar plane.

Both apsidal distances and the apsidal angle have been shown to vary with a long term period, equal to one half the period of revolution of the apses (9). Thus, over a long term period the first-order result is inaccurate. A numerical check was made on a near circular orbit at a 300-miles altitude indicating that, even with the "breathing" of apogee and perigee, the differences between numerical and first-order results in radius and speed were less than 1000 ft and 1 fps respectively for the first five days in orbit (about 80 revolutions).

Motion in the Polar Plane, Launched From the Equatorial Plane

Table 1 summarizes the equations for polar plane motion launched from the equatorial plane. Eq. 25 shows that the angular momentum is not constant. Orbital radius and speed in a polar orbit are given by Eqs. 23 and 24. Details for this case are presented below. Similar results for launch from an arbitrary latitude may be inferred from Table 2.

Differences Between First-Order Oblateness Results and Classical Inverse-Square Results

The classical inverse-square results are obtained from Eqs. 23 to 25 and 28, by setting $J = 0$. Then $|\eta|$ is equal to the eccentricity. Thus the differences between first-order oblateness results and the classical inverse-square results are

$$\theta - \theta_s = -\frac{J}{2c^4} \left(\frac{R}{r_0}\right)^2 \xi \quad [40]$$

$$\frac{P - P_s}{r_0 V_0} = -\frac{J}{6c^4} \left(\frac{R}{r_0}\right)^2 \times [3 + 4\eta - 3\eta \cos \xi - 3 \cos 2\xi - \eta \cos 3\xi] \quad [41]$$

$$\frac{r - r_s}{r_0} = -\frac{J}{24} \left(\frac{R}{r_0}\right)^2 \frac{L(\xi)}{(1 + \eta)(1 + \eta \cos \xi)^2} \quad [42]$$

$$\frac{V - V_s}{V_0} = \frac{J}{48} \left(\frac{R}{r_0}\right)^2 \frac{M(\xi)}{(1 + \eta)^2 \sqrt{1 + \eta^2 + 2\eta \cos \xi}} \quad [43]$$

where $L(\xi)$ and $M(\xi)$ are defined by Eqs. 26 and 27 respectively. Eq. 42 is presented in Fig. 2 in the following non-dimensional form

$$f_{190} = \frac{r - r_s}{\frac{J R^2}{6 r_0}} = -\frac{1}{4} \frac{L(\xi)}{(1 + \eta)(1 + \eta \cos \xi)^2} \quad [44]$$

As shown in Fig. 2, in the polar plane, oblateness can either increase or decrease orbital radius depending on η and ξ . Maximum effects on radius generally increase as η increases.

For the special case $\eta = 0$ corresponding to initial speed equal to circular speed, the maximum effect of oblateness on radius occurs at $\xi = 120^\circ$, and is given by $f_{190} = -4.5$.

The effects of oblateness on the polar orbit of Discoverer I (perigee altitude 176 statute miles, apogee altitude 519 statute miles) have been studied (14). The maximum effects on radius and speed ($r - r_s$ and $V - V_s$) for this case are -5.15 statute miles and 24.8 fps respectively.

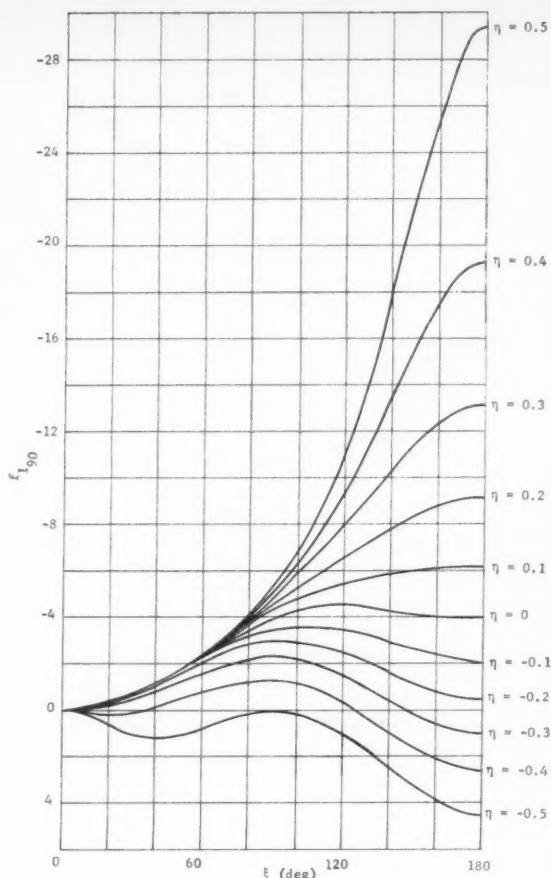


Fig. 2 Oblateness effects on polar orbital radius

Nearly Circular Orbits

Of particular interest is the motion with a nearly constant radius both because of the possibility of circular orbits and because of the possibility of additional apses. Since η is nearly zero for such motions, the terms of order η^2 , $J\eta$, and higher are neglected. Eqs. 23 to 28 then become

$$\theta = \left[1 - \frac{J}{2} \left(\frac{R}{r_0}\right)^2\right] \xi \quad [45]$$

$$P = r_0 V_0 \left[1 - \frac{J}{2} \left(\frac{R}{r_0}\right)^2 (1 - \cos 2\xi)\right] \quad [46]$$

$$u = \frac{1}{r_0} \left\{ 1 - \eta(1 - \cos \xi) + \frac{J}{6} \left(\frac{R}{r_0}\right)^2 [3 - 2 \cos \xi - \cos 2\xi] \right\} \quad [47]$$

$$r = r_0 \left\{ 1 + \eta(1 - \cos \xi) - \frac{J}{6} \left(\frac{R}{r_0}\right)^2 [3 - 2 \cos \xi - \cos 2\xi] \right\} \quad [48]$$

$$V = V_0 \left\{ 1 - \eta(1 - \cos \xi) + \frac{J}{3} \left(\frac{R}{r_0}\right)^2 [-\cos \xi + \cos 2\xi] \right\} \quad [49]$$

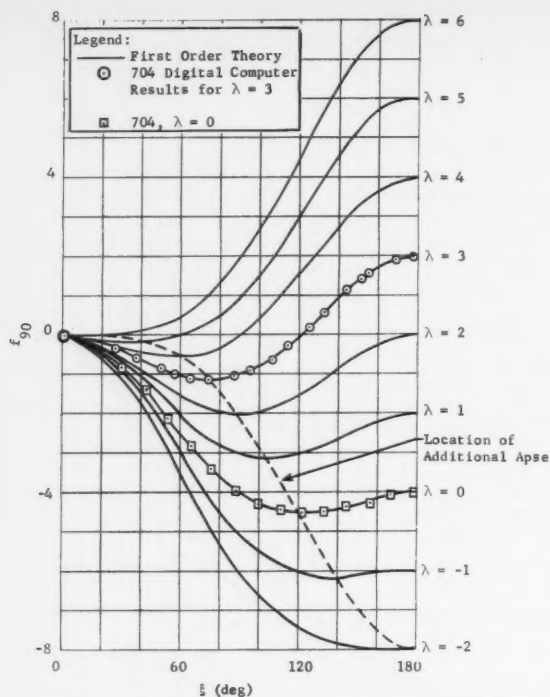


Fig. 3 Radius variations in nearly circular polar orbits

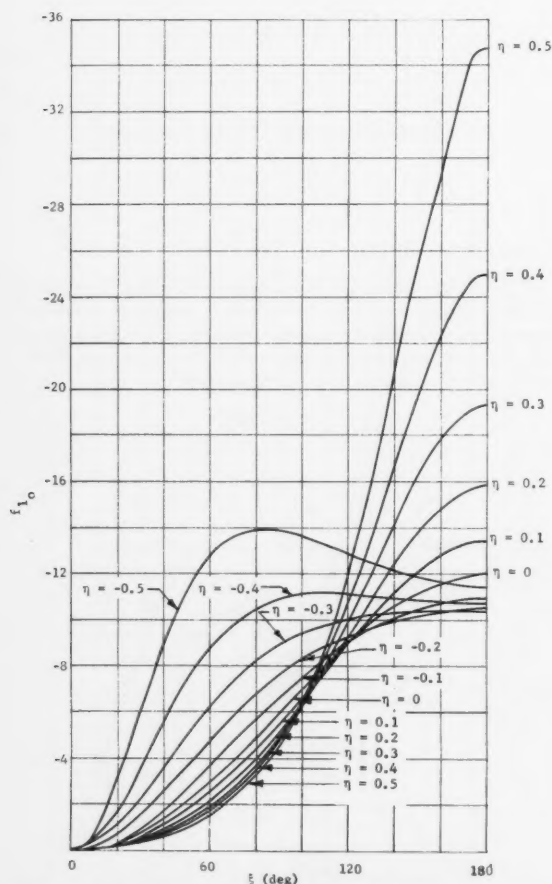


Fig. 4 Oblateness effects on equatorial orbital radius

Eq. 48 indicates that r cannot be made a constant by any choice of η , since the coefficients of both η and $J(R/r_0)^2$ are linearly independent.

An apse is a point on a trajectory where $\dot{r} = 0$. The radius at which the apse occurs is called the apsidal distance, and the angle subtended between two successive apses is called the apsidal angle. For the case of a particle in a central force field, the path has at most two apsidal distances and one apsidal angle. In general, apses may occur with or without symmetry for a noncentral force field. Angles at which the apses occur are determined by setting $du/d\xi = 0$, since this is equivalent to $\dot{r} = 0$. The result is an equation of the form $du/d\xi = \sin \xi [f(\xi, \eta, \epsilon)] = 0$. Thus at $\xi = m\pi$ apses always occur independent of the values of η or ϵ . In addition to these apses, others will be provided where the second factor is equal to zero, resulting in

$$\eta = c^2 - 1 = (\epsilon/3)(1 + 2 \cos \xi^*) \quad [50]$$

where $\xi = \xi^*$ is the location of an additional apse for the prescribed η and ϵ . The allowable range on η for occurrence of additional apses in the polar plane is

$$-\epsilon/3 < \eta < \epsilon$$

The radius at the additional apse is denoted by r^* and is found by substituting η from Eq. 50 in the expression for radius (Eq. 48) evaluated at $\xi = \xi^*$, which yields

$$r^* = r_0 \left[1 - \frac{4\epsilon}{3} \sin^4 \frac{\xi^*}{2} \right] \quad [51]$$

which may be stated alternately in terms of η as

$$r^* = r_0 \left[1 - \frac{3\epsilon}{4} \left(1 - \frac{\eta}{\epsilon} \right)^2 \right] \quad [52]$$

Eqs. 51 and 52 show that for any additional apse, r^* is less than r_0 .

Radius variations in near circular polar orbits are presented in Fig. 3 in the following nondimensional form

$$f_{\infty 0} = \frac{r - r_0}{\frac{J R^2}{6 r_0}} = (3 - 4 \cos \xi + \cos 2\xi) + (\lambda - 6)(1 - \cos \xi) \quad [53]$$

To verify the methods of this discussion, the equations of motion were integrated numerically on the IBM 704 digital computer (including the J term but not the D term) for two cases, $\lambda = 0$ and $\lambda = 3$. Fig. 3 shows that the agreement between numerical and analytical results is excellent.

The special case, $\lambda = 0$, corresponds to initial speed equal to circular speed (for the spherical case). At $\xi = 180^\circ$, the value for f is -4 indicating that the radius is less than initial radius.

Motion in the Equatorial Plane

A summary of the equations for equatorial plane motion is given in Table 3. Eqs. 35 and 37 indicate that the motion is planar and conserves angular momentum. These results follow from the fact that the force field is central, which in turn is due to the assumed symmetry of the force field. Eqs. 35 and 36 show the dependence of radius and speed on ξ , η , and ϵ .

Differences Between First-Order Oblateness Results and Classical Inverse-Square Results

Classical inverse-square results are obtained from Eqs. 35 to 37 by setting $J = 0$. Subtracting the inverse-square results from Eqs. 35 to 37 then yields the differences due to

oblateness

$$\varphi - \varphi_s = \frac{J}{c^4} \left(\frac{R}{r_0} \right)^2 \xi \quad [54]$$

$$P - P_s = 0 \quad [55]$$

$$\frac{r - r_s}{r_0} = -J \left(\frac{R}{r_0} \right)^2 \times \frac{\left[1 - \cos \xi + \frac{\eta^2}{6} (3 - 2 \cos \xi - \cos 2\xi) \right]}{(1 + \eta)(1 + \eta \cos \xi)^2} \quad [56]$$

$$\frac{V - V_s}{V_0} = \frac{J}{12} \left(\frac{R}{r_0} \right)^2 \frac{N(\xi)}{(1 + \eta)^3 (1 + \eta^2 + 2\eta \cos \xi)^{1/2}} \quad [57]$$

The difference in radial position is presented in Fig. 4. For all values of η and ξ , oblateness acts to pull the particle closer to the earth. At $\xi = 180^\circ$ the influence of oblateness for any orbit is at least as large as $f_1 = -10.4$, which for a 300 n miles altitude orbit of Earth corresponds to $r - r_s = -8.96$ n miles. For the case $\eta = 0$, f_1 at $\xi = 180^\circ$ is -12 , three times the polar value. Again for a 300 n miles orbit, this corresponds to -10.3 n miles.

Accuracy of the first-order results has been numerically checked at $\eta = 1.1$ for the following conditions:

- 1 Values of J , R , μ for Earth.
- 2 $r_0 = 2.153401 \times 10^7$ ft (corresponding to a 100 n miles altitude).
- 3 $V_0 = 37050.688$ fps.

After 12,000 sec flight time, the differences between IBM 704 results and the analytical results are

	IBM 704	Analytical	Difference (704 - Analytical)
$r = 209,784,760$ ft	209,784,760 ft	209,784,470 ft	+290 ft
$V = 14,103.056$ fps	14,103.056 fps	14,102.984 fps	+0.072 fps

This excellent agreement between analytical and numerical results indicates that the analytical results are very accurate, even for escape trajectories.

Nearly Circular Orbits in the Equatorial Plane

Results for nearly circular equatorial orbits are obtained from the equations of Table 3 by neglecting terms containing $J\eta$ and η^2 since η is of the order of J in this case. Eqs. 35 to 39 reduce to

$$\varphi = \left[1 + J \left(\frac{R}{r_0} \right)^2 \right] \xi \quad [58]$$

$$P = r_0 V_0 \quad [59]$$

$$r = r_0 \left\{ 1 + \left[\eta - J \left(\frac{R}{r_0} \right)^2 \right] [1 - \cos \xi] \right\} \quad [60]$$

$$V = V_0 \left\{ 1 - \left[\eta - J \left(\frac{R}{r_0} \right)^2 \right] [1 - \cos \xi] \right\} \quad [61]$$

The monotonic nature of r , as given by Eq. 60 indicates the absence of apsides other than at $\xi = m\pi$. Furthermore, a circular path is possible in the equatorial plane if

$$\eta = J \left(\frac{R}{r_0} \right)^2 = \epsilon \quad [62]$$

(hence $\lambda = 6$), or equivalently

$$V_0 = V_c \left[1 + \frac{J}{2} \left(\frac{R}{r_0} \right)^2 \right] \quad [63]$$

Radius variations in near circular orbits are presented in Fig. 5. Symmetry about $\lambda = 6$ exists so that, for example, results for $\lambda = 7$ are obtainable from $\lambda = 5$ by reflection.

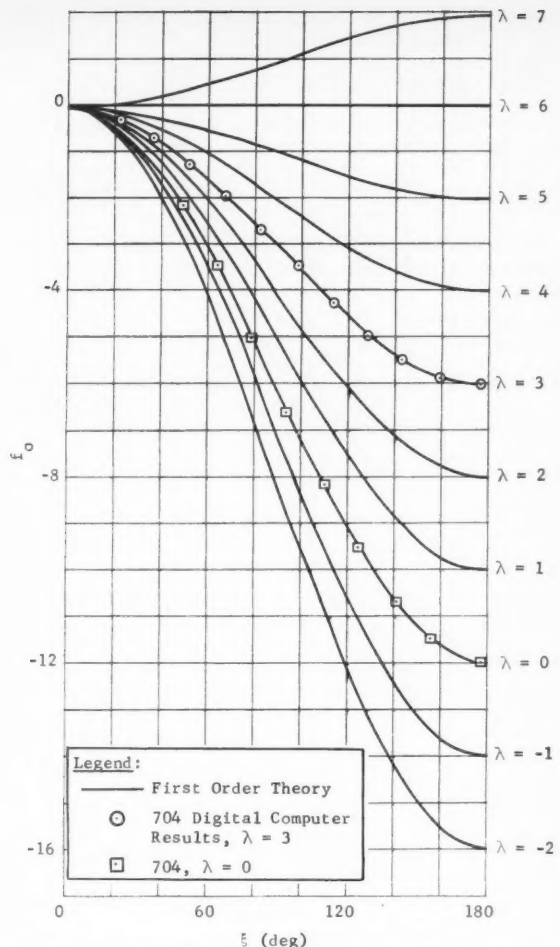


Fig. 5 Radius variations in nearly circular equatorial orbits

Superposition Principle

For fixed η , r_0 , R , J , ξ_0 and ξ , any of the quantities—radius, angular momentum, speed, and space angle—may be determined by forming a linear combination of these same quantities which are solutions for the equatorial plane and the polar plane (14). For example, the radial position $r(i)$ of a particle initially launched in an orbit inclined by an arbitrary angle i to the equatorial plane may be found from

$$r(i) = r(0) \cos^2 i + r(\pi/2) \sin^2 i \quad [64]$$

where $r(0)$ and $r(\pi/2)$ are the radial positions in the equatorial and polar planes, respectively. Similarly, the central angle in the inclined plane as measured from the x -axis is given by

$$\beta = \xi \left[1 + \frac{J}{c^4} \left(\frac{R}{r_0} \right)^2 \left(1 - \frac{3}{2} \sin^2 i \right) \right] \quad [65]$$

Given the angle β_0 , between the x -axis and the radius vector to the initial position, ξ_0 may be found from Eq. 65. Thus the motion of a particle initially inclined to the equator is intimately connected to the motion in the equatorial and polar planes.

An accuracy check on the superposition principle was performed for the following case

$$i = 60^\circ \quad \xi_0 = 0$$

$r_0 = 22,510,010$ ft (corresponding to a 300-miles altitude above the Earth's equator)

$\eta = 0.5$

$\varphi = 120.1239^\circ$ (a tabulated IBM 704 data point)

The differences between the IBM 704 numerical integration of the equations of motion and the first-order theory are

$$\begin{aligned} r_{\text{CALC}} - r_{704} &= -90 \text{ ft} \\ V_{\text{CALC}} - V_{704} &= 0.012 \text{ fps} \end{aligned}$$

The superposition principle, therefore, appears to yield accurate numerical results even for large values of η .

Nomenclature

c	$= V_0/V_c$
D	$=$ coefficient of fourth harmonic in the gravitational potential function for an oblate spheroid (1.060×10^{-5} for Earth)
f	$= \frac{r - r_0}{\frac{J R^2}{6 r_0}}$
f_0	$= f$ at $i = 0^\circ$
f_{90}	$= f$ at $i = 90^\circ$
f_1	$= \frac{r - r_s}{\frac{J R^2}{6 r_0}}$
f_{10}	$= f_1$ at $i = 0^\circ$
f_{190}	$= f_1$ at $i = 90^\circ$
G	$=$ Newton's constant of universal gravitation
i	$=$ orbital inclination to the Equator
J	$=$ coefficient of the second harmonic in the gravitational potential function for the oblate spheroid (1.638×10^{-3} for Earth)
$L(\xi)$	$=$ defined by Eq. 26
$L_1(\xi)$	$=$ defined by Eq. 32
M	$=$ mass of the Earth
$M(\xi)$	$=$ defined by Eq. 27
$M_1(\xi)$	$=$ defined by Eq. 33
$N(\xi)$	$=$ defined by Eq. 38
P	$=$ angular momentum per unit mass to first order in J
P_s	$=$ angular momentum per unit mass about a spherical Earth
	$= P_0 = r_0 V_0$
r	$\left. \begin{array}{l} r \\ \theta \\ \varphi \end{array} \right\} = \text{spherical coordinate system as defined in Fig. 1}$
θ	
φ	
r_0	
r_s	$=$ radius vector over a spherical central body
r^*	$= r$ at an additional apse between $\xi = 0$ and π
R	$=$ equatorial radius of the oblate spheroid (2.092601×10^7 ft $= 3441.7779$ n miles for Earth)
t	$=$ time
u	$= 1/r (= u_0 + J u_1, \text{ to first order in } J)$
U	$=$ gravitational potential function, Eq. 1
V	$=$ orbital speed (over oblate spheroid)
V_c	$= \sqrt{\mu/r_0}$, circular speed for a spherical body at $r = r_0$
V_s	$=$ orbital speed for spherical central body
V_0	$=$ initial speed at radius r_0 at apse

$$\Delta V_0 = V_s - V_c$$

$$v = du/d\theta$$

β $=$ the angle between the x -axis and a radius vector to the projection of the particle onto the initial plane of motion (for the polar plane $\beta = \theta$; for the equatorial plane $\beta = \varphi$)

$$e = J(R/r_0)^2$$

$$n = c^2 - 1$$

$$\theta_0 = \text{initial value of } \theta$$

$$\theta_1 = \text{a constant determined to eliminate secular terms}$$

$$\lambda = \frac{6n}{e} \simeq \frac{2\Delta V_0}{V_c} \frac{J}{6} \left(\frac{R}{r_0} \right)^2$$

$$\mu = \text{gravitational constant} = GM = 1.4076613 \times 10^{16} \text{ ft}^2/\text{sec}^2 \text{ for Earth}$$

$$\xi = \text{independent variable chosen to make the analytical results periodic to first order in } J$$

$$\xi_0 = \text{initial value of } \xi$$

$$\xi^* = \text{value of } \xi \text{ at which an additional apse } r^* \text{ occurs}$$

$$\varphi_0 = \text{initial value of } \varphi$$

A prime superscript indicates differentiation with respect to ξ . A dot over a variable indicates differentiation with respect to t .

References

- 1 Blitzer, L., Weisfeld, M. and Wheelon, A. D., "Perturbations of a Satellite's Orbit due to Earth's Oblateness," *J. Appl. Phys.*, vol. 27, no. 10, October 1956.
- 2 Blitzer, L. and Wheelon, A. D., "Oblateness Perturbation of Elliptical Satellite Orbits," *J. Appl. Phys.*, February 1957.
- 3 Blitzer, L., "Apsidal Motion of an IGY Satellite Orbit," *J. Appl. Phys.*, November 1957.
- 4 Brouwer, D., "The Motion of a Particle with Negligible Mass Under the Gravitational Attraction of a Spheroid," *Astronom. J.*, vol. 51, no. 1156, 1946, pp. 223-231.
- 5 Hall, N. S. and Gawlowicz, H. F., "The Oblatory Perturbations of Satellite Orbits," presented at the 6th National Annual Meeting of the Amer. Astronaut. Soc., January 1960.
- 6 Moulton, F. R., *Periodic Orbits*, Carnegie Inst., Washington, D. C., 1920, pp. 99-150.
- 7 Orlov, A. A., "Almost Circular Periodic Motions of a Particle of Matter Under the Gravitational Attraction of a Spheroid," *NRL Translation* no. 519.
- 8 Roberson, R. E., "Orbital Behavior of Earth Satellites," *J. Franklin Inst.*, vol. 264, no. 4, October 1957, pp. 269-285.
- 9 Fosdick, G. E. and Hewitt, M., "Effects of the Earth's Oblateness and Atmosphere on a Satellite Orbit," Engng. Rep. no. 8344, Martin Co., Baltimore, Md., June 1956.
- 10 Nielsen, J. N., Goodwin, F. K. and Mersman, W. A., "Three Dimensional Orbits of Earth Satellites, Including Effects of Earth Oblateness and Atmospheric Rotation," NASA Memo 12-4-58 A, December 1958.
- 11 Jeffreys, H., *The Earth, Its Origin, History, and Physical Constitution*, 3rd ed., Cambridge Univ. Press, 1952.
- 12 O'Keefe, J. A., Eckels, A. and Squires, R. K., "Earth's Shape," *IGY Bull.*, April 1959.
- 13 Cesari, L., *Asymptotic Behavior and Stability Problems in Ordinary Differential Equations*, p. 116, Springer-Verlag, Berlin, 1959.
- 14 Anthony, M. L. and Fosdick, G. E., "An Analytical Study of the Effects of Oblateness on Satellite Orbits," Research Rep. R-60-2, Martin Co., Denver, Colorado, March, 1960.
- 15 Anthony, M. L. and Fosdick, G. E., "Planar Motions about an Oblate Planet," Research Rep. R-60-45, Martin Co., Denver, Colorado, May 1960.
- 16 Anthony, M. L. and Fosdick, G. E., "Escape in the Equatorial Plane of an Oblate Planet," *ARS JOURNAL*, September 1960, pp. 898-901.
- 17 Anthony, M. L. and Fosdick, G. E., "Satellite Motions about an Oblate Planet," *J. Aero/Space Sci.*, August, 1961.
- 18 Anthony, M. L., Fosdick, G. E. and Perko, L. M., "Escape from an Oblate Planet," *Advances in Astronaut. Sci.*, vol. 6, 1961.
- 19 Anthony, M. L. and Perko, L. M., "A Second Order Analysis of Particle Motion in the Equatorial Plane of an Oblate Planet," Research Rep. R-60-17, Martin Co., Denver, Colo., June 1960.

Interplanetary Maneuvers Using Radial Thrust

C. M. PETTY¹

Lockheed Missile and Space Div.
Sunnyvale, Calif.

Basic interplanetary maneuvers are considered, with emphasis placed on simplicity in instrumentation. First, a general theory of radial thrust is developed geometrically, where the primary tool is a plot of the square of the eccentricity vs. radial distance, since it reveals a proper perspective of the opportunities and limitations of the theory. The special case of constant radial thrust acceleration is treated in detail. Finally, an example of a Martian capture maneuver is given where the initial portion of the maneuver has constant radial thrust acceleration, and in the terminal portion the thrust acceleration varies to maintain constant radial speed. The associated characteristic velocity and other parameters are computed.

THERE are three basic maneuvers which are natural to consider in conjunction with interplanetary flight: escape from a satellite orbit about a planet to attain a given hyperbolic excess departure speed in a specified direction; capture of an approaching vehicle by a planet (reduction to a satellite orbit), given the hyperbolic excess arrival speed; a maneuver around a planet with prescribed change in direction and given hyperbolic excess arrival and departure speeds.

Approach to these problems will place emphasis on simplicity in instrumentation. It will be assumed that the thrust of the engine always lies along the radial direction from the planet and that the magnitude of the thrust acceleration is either constant or controlled to maintain a constant Doppler frequency shift with respect to the planet. However, it is instructive in the analysis to consider the more general case where the magnitude of the acceleration due to the thrust is a prescribed function of radial distance, i.e., to pretend that the vehicle can measure its distance from the planet by some device, so that whenever the engine is running, the acceleration is controlled to follow a preset function of radial distance regardless of the direction of travel. It is further assumed that we are so close to the planet that only its gravitational attraction is important.

The use of geometrical diagrams are instructive in studies of this type. Rodriguez (1)² uses an energy-angular momentum diagram and Paiewonsky (2) uses a plot of equivalent one-dimensional potentials vs. radial distance. Here, we will use a plot of the square of the eccentricity of the osculating conic vs. radial distance.

General Case

The conditions imposed above imply that the angular momentum per unit mass is a constant during either a coasting or a powered phase. Consequently, the semi-latus rectum p of the osculating conic remains constant, and it will be assumed that its value is known. Parameters, represented in notation by capitals, are to be measured in the system of units such that p is unit distance, and the circular velocity at distance p has unit magnitude. The corresponding notation in lower case will represent the same parameters in some convenient laboratory units.

Let R and $A(R)$ denote the radial distance and the acceleration supplied by the engine, respectively. We will assume that $A(R)$ is a continuous function of R for all values of $R > 0$. We have then

$$\ddot{R} = A(R) - [(R - 1)/(R^3)] \quad [1]$$

during a powered phase. If ϵ is the eccentricity of the osculating conic, then

$$\epsilon^2 = (\dot{R})^2 + (1 - 1/R)^2 \quad [2]$$

The qualitative features of radial thrust are contained in Eqs. 1 and 2. From these equations we conclude that whenever $\dot{R} \neq 0$ we have

$$\frac{d(\epsilon^2)}{dR} = 2A(R) \quad [3]$$

Integrating Eq. 3 we obtain

$$\epsilon^2 = \epsilon_0^2 + 2 \int_{R_0}^R A(R) dR \quad [4]$$

If we plot ϵ^2 as a function of R , then by Eq. 2, the integral curves of Eq. 4 must remain on or above the boundary curve given by

$$\epsilon^2 = (1 - 1/R)^2 \quad [5]$$

as shown in Fig. 1.

The following graphical procedure establishes all the essential features (except for the time scale) of what may be accomplished for a given value of $A(R)$. First, a template may be prepared of $\int_1^R 2A(R) dR$ vs. R for $R > 0$ which covers the range of interest. By translating this parallel to the ϵ^2 -axis, the family of curves of Eq. 4 may be drawn where each curve is omitted when it passes below the boundary curve given by Eq. 5. Through each interior point of the permissible region there will pass one and only one such curve. If the engine of the hypothetical vehicle is running at this point, one follows the curve to the right if $\dot{R} > 0$ and to the left if $\dot{R} < 0$. By Eqs. 2 and 5, the radial speed \dot{R} is zero if and only if the point is on the boundary curve. If the curve of Eq. 4 through a point on the boundary curve shares a common tangent with the curve of Eq. 5, such as P in Fig. 1, then this point is an equilibrium point of Eq. 1, i.e., the vehicle travels in a circular orbit about the planet while the

Received Jan. 20, 1961.

¹ Staff Scientist.

² Numbers in parentheses indicate References at end of paper.

engine is running. However, if the curve is followed toward the equilibrium point from the interior, it cannot be reached in finite time; instead the vehicle spirals inward ($\dot{R} < 0$) or outward ($\dot{R} > 0$) approaching a circle asymptotically. If the curve of Eq. 4 cuts the boundary curve at an angle in some point (such as Q in Fig. 1), then starting at this point one may follow the path of Eq. 4 into the interior of the permissible region. Also if such a point on the curve of Eq. 5 is approached from the interior, then it is reached in finite time and the path is hence retraced.

Let T denote the time and let ϵ_0, R_0 correspond to T_0 . By Eq. 2 we have

$$T - T_0 = \pm \int_{R_0}^R \frac{dR}{|\dot{R}|} = \pm \int_{R_0}^R \frac{dR}{\sqrt{\epsilon^2 - \left(1 - \frac{1}{R}\right)^2}} \quad [6]$$

where the plus or minus sign before the integral is chosen according to whether \dot{R}_0 is positive or negative. If $\dot{R}_0 = 0$ and $A(R_0) \neq (R_0 - 1)/R_0^3$, then the positive sign is chosen if $A(R_0) > (R_0 - 1)/R_0^3$ and the negative sign if $A(R_0) < (R_0 - 1)/R_0^3$. In the latter case the integrand has a singularity at the initial point, but the integral is convergent.

The characteristic velocity V_c is defined for any portion of a maneuver by

$$V_c = \int_{T_0}^T A(R) dT \quad [7]$$

We will calculate this number only over portions of the powered flight when $\dot{R} \neq 0$ and $A(R)$ is always positive or always negative, except possibly at the end points. Consequently, by Eq. 4 and the implicit function theorem we may solve for R as a function of ϵ^2 . We then have by Eqs. 7 and 3

$$V_c = \frac{1}{2} \int_{\epsilon_0^2}^{\epsilon^2} \frac{d(\epsilon^2)}{\dot{R}} = \pm \frac{1}{2} \int_{\epsilon_0^2}^{\epsilon^2} \frac{d(\epsilon^2)}{\sqrt{\epsilon^2 - \left(1 - \frac{1}{R}\right)^2}} \quad [8]$$

where the plus or minus sign is chosen in agreement with the sign of \dot{R} during the interval. From Eq. 8 we obtain the lower bound

$$|V_c| > |\epsilon - \epsilon_0| \quad \epsilon \neq \epsilon_0 \quad [9]$$

By Eq. 2, it is seen that this lower bound corresponds to an impulse applied when $R_0 = 1$, where all acceleration is concentrated in a single impulse at an end point of the semilatus rectum.

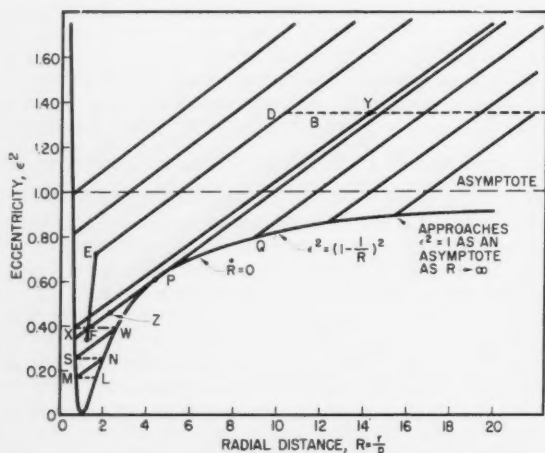


Fig. 1 Maneuvers using constant radial thrust acceleration

Constant Radial Thrust Acceleration

If A is a constant, then the curves of Eq. 4 are straight lines and we have

$$\epsilon^2 = \epsilon_0^2 + 2A(R - R_0) \quad [10]$$

Suppose the vehicle is initially in an elliptic orbit, say ML in Fig. 1, and the engine is started at the periplanet M , then if A is sufficiently small the vehicle will travel back and forth on MN and cannot escape from the planet. However, if the engine is turned off at N and the maneuver repeated after the vehicle coasts back to the periplanet at S , it is clear that escape from the planet can be effected in this way with a finite number of thrust arcs regardless of how small A may be.

The time consuming coast arcs may be avoided by the method suggested by Paiewonsky (2), i.e., reversing the direction of the radial thrust (A is alternatively positive and negative) at suitable locations. For any of these schemes one may graphically compute, using Fig. 1, the number of thrust arcs necessary to escape from the planet.

The ability to alternate coast and powered arcs when the osculating conics are ellipses enables one to transfer a given elliptic orbit into another by a finite number of thrust arcs such that the total characteristic velocity is arbitrarily close to the lower bound given by Eq. 9 no matter how small $|A|$ ($\neq 0$) may be. To illustrate, suppose $A > 0$ and $0 < \epsilon_0 < \epsilon \leq 1$. Divide the interval from ϵ_0 to ϵ into equal subintervals $\Delta\epsilon < A^2$ by intermediary ϵ_i . In transferring from ϵ_i to ϵ_{i+1} , we start the hypothetical engine at $R = 1$, $\dot{R} = \epsilon_i$. The inequality $\Delta\epsilon < A^2$ insures that \dot{R} is monotonically increasing during the transfer, and consequently

$$(\Delta V_c)_i = \frac{1}{2} \int_{\epsilon_i^2}^{\epsilon_{i+1}^2} \frac{d(\epsilon^2)}{\dot{R}} < \frac{1}{2} \left(2 + \frac{\Delta\epsilon}{\epsilon_i} \right) \Delta\epsilon \leq \Delta\epsilon + \frac{1}{2} \frac{(\Delta\epsilon)^2}{\epsilon_0}$$

and therefore

$$V_c = \sum (\Delta V_c)_i < (\epsilon - \epsilon_0) + \frac{1}{2} (\epsilon - \epsilon_0) \frac{\Delta\epsilon}{\epsilon_0}$$

In order to escape from the planet with a single positive ($A > 0$) thrust arc from an initial point (R_0, ϵ_0^2) where $\epsilon_0 < 1$, it is clear that A must exceed a certain lower bound which depends on ϵ_0 and R_0 . This value may be obtained graphically from Fig. 1 where, say, Z is the initial point and ZP corresponds to the lower bound on the slope $2A$. Let $(1/(1 - \epsilon), \epsilon^2)$ be the point of tangency on the boundary curve given by Eq. 5; we then obtain

$$A = \epsilon(1 - \epsilon)^2 \quad [11]$$

where

$$2R_0\epsilon^3 + (3 - 4R_0)\epsilon^2 + 2(R_0 - 1)\epsilon - \epsilon_0^2 = 0 \quad [12]$$

The cubic equation in ϵ , Eq. 12, has one or three roots in the interval $0 \leq \epsilon < 1$ counting possible multiple roots; however, these roots correspond to tangents through (R_0, ϵ_0^2) to that part of the boundary curve corresponding to $R \geq 1$, and consequently it is clear that it is always the maximum of these roots which we seek. If the initial point is at the periplanet, i.e., $R_0 = 1/(1 + \epsilon_0)$, then $\epsilon = (1 + \epsilon_0)/2$ and $A = 1/8(1 - \epsilon_0)(1 - \epsilon_0^2)$. This latter result has been obtained by Paiewonsky (2), Appendix I, where he expresses the acceleration in terms of the initial periplanet distance (in the preprint, there is a misprint in the numerical coefficient which should be $1/2$ instead of 2).

It is interesting to note that, by Eq. 11, if $A > 4/27$, then escape is possible in a single thrust arc starting from any point on any initial ellipse [compare (2) Appendix II].

The solution to the equations of motion in terms of elliptic integrals has already been treated in detail. See Dobrowolski (3) for the case $0 < A < 1/8$ and Copeland (4), with some minor corrections by Karrenberg (5) and Au (6), for the com-

plete solution. Also (7) provides simple approximations to the above solutions over a limited time period.

The above discussion relating to constant radial thrust acceleration can now be related to the problem of capture. The first and third maneuvers mentioned in sentence one of this paper may be approached by similar procedures. Initially the vehicle will be traveling to the left on a horizontal line in Fig. 1 corresponding to some $\epsilon_0 > 1$. We wish then to transfer this orbit to some $\epsilon < 1$. It is clear, however, that if $A > 0$ is quite small, a modest value of ϵ cannot be obtained without a "zigzagging" procedure, comprising alternation of powered and coasting arcs. Furthermore, if the powered arc, say \overline{YX} , passes close to an equilibrium point (P), then considerable fuel would be expended since the vehicle would remain for some time in the vicinity of P , where it is slowly spiraling in before breaking away and reaching X .

Because of Eq. 8, a procedure which maneuvers the vehicle in the region of Fig. 1, where the radial speed is relatively large, is always desirable. We will limit the investigation here to maneuvers which effect capture by use of a single continuous thrust arc. As a consequence of the latter condition, vehicles with low thrust acceleration must be provided with higher thrust during the terminal stage; for instance, the design may lead to a path DEF in Fig. 1, where the low thrust is initiated at D , and perhaps a capsule with a high thrust retro-engine ejected in the radial direction at E . However, the terminal maneuver which follows the curves of constant radial speed will be considered, since this condition keeps the path away from the boundary curve and appears to offer an advantage in instrumentation. Also, it requires in general only a small acceleration, as shown in Fig. 3.

Maneuvers With Constant Radial Speed

If

$$A(R) = \frac{R-1}{R^3} \quad [13]$$

then the curves of Eq. 4 are translates parallel to the ϵ^2 -axis of the boundary curve represented by Eq. 5, and the radial speed is constant along each curve. The maximum positive acceleration, by Eq. 13, is attained at $R = 3/2$ when $A = 4/27$. This value corresponds to the inflection point in the boundary curve of Eq. 5 at $R = 3/2$. We also have the relations

$$R - R_1 = \dot{R}_1(T - T_1) \quad [14]$$

$$\epsilon^2 = \epsilon_1^2 + \left(\frac{1}{R_1} - \frac{1}{R}\right)\left(2 - \frac{1}{R} - \frac{1}{R_1}\right) \quad [15]$$

$$V_c = \frac{1}{2R_1}(\epsilon^2 - \epsilon_1^2) \quad [16]$$

and if φ is the angle in radians swept out by the radius vector during the maneuver, then

$$\varphi = \frac{1}{R_1} \left(\frac{1}{R_1} - \frac{1}{R} \right) \text{ radians} \quad [17]$$

By Eq. 2, one may find \dot{R}_1 from R_1 and ϵ_1 .

The procedure for capture to be considered here is indicated in Fig. 2. The maneuver terminates at $R = 1$, and for $1 \leq R \leq R_1$ (where $R_1 \geq 3/2$) the curves of Eq. 4 are contours of constant radial speed. For $R \geq R_1$ the radial acceleration A_1 is constant and given by

$$A_1 = \frac{R_1 - 1}{R_1^3} \quad [18]$$

so that these straight lines are tangent to the contours of constant radial speed. The instrumentation does not require

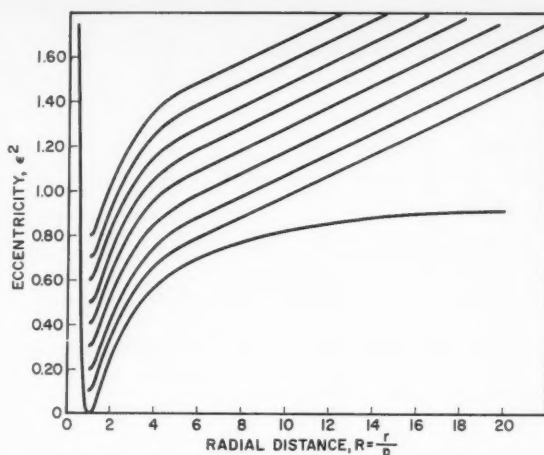


Fig. 2 Terminal capture maneuver keeping the radial speed constant

the radial distance after the engine is started but only Doppler shift as a comparative measure of the radial speed. Suppose the approach hyperbola has eccentricity ϵ_0 and the low thrust constant radial acceleration is initiated at R_0 ; then the magnitude of the radial speed will decrease until a minimum value is attained at R_1 . The engine then accelerates to maintain this frequency difference until the engine shuts itself off, by Eq. 13, at $R = 1$, thus terminating the maneuver.

If v_∞ is the hyperbolic excess arrival speed, then

$$\epsilon_0^2 = \frac{p}{\mu} v_\infty^2 + 1 \quad [19]$$

where μ is the product of the universal gravitational constant and the mass of the planet. Also the low thrust acceleration α_1 corresponding to A_1 in laboratory units is

$$\alpha_1 = \frac{A_1 \mu}{p^2} \quad [20]$$

By Eqs. 15, 10, 19 and 20 the expression is obtained for the final eccentricity ϵ at $R = 1$ ($r = p$) in terms of p , v_∞ and r_0

$$\epsilon^2 = 1 + \frac{p}{\mu} v_\infty^2 - 2 \frac{p}{\mu} \alpha_1 (r_0 - r_1) - \left(\frac{r_1 - p}{r_1} \right)^2 \quad [21]$$

where r_1 is determined by

$$\alpha_1 = \mu \frac{(r_1 - p)}{r_1^3} \quad [22]$$

Example of a Martian Capture

The hyperbolic excess arrival speed at Mars for departure dates from Earth during 1960 [see (8)] may be as small as 7700 fps. However, a somewhat more typical value of $v_\infty = 8730$ fps will be used in the following calculations. Upon arrival in the vicinity of Mars and prior to the capture maneuver a final guidance correction is needed to establish the nominal value of p . This maneuver is economically performed by thrust perpendicular to the radial direction and at least approximately in the plane of motion relative to Mars. Since it is performed at a relatively large distance from Mars, say 250,000 miles, the velocity vector will be nearly aligned with the radial direction, and consequently this correction will have only a small effect on the parameter v_∞ .

For the nominal capture orbit investigated, the semi-parameter p is 3 times the radius of Mars and has an eccen-

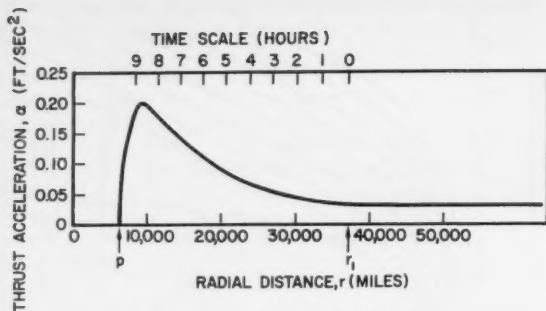


Fig. 3 Thrust acceleration history for a Martian capture

tricity $\epsilon = 0.707$ ($\epsilon^2 = 1/2$). This selection yields a nominal elliptic orbit with an altitude of 1600 miles at its closest point to the surface of Mars and an altitude of 19,500 miles at its greatest distance. Also we will assume that the design of the engine yields an acceleration $\alpha_1 = 0.0322 \text{ ft/sec}^2$ ($= 10^{-3}g$) for its long period, low thrust, constant acceleration. Summarizing, the input parameters are

$$\begin{aligned} \mu &= 1.4989 \times 10^{15} \text{ ft}^3/\text{sec}^2 \\ p &= 3.339 \times 10^7 \text{ ft} \\ v_\infty &= 8730 \text{ fps} \\ \epsilon &= 0.707 \\ \alpha_1 &= 0.0322 \text{ ft/sec}^2 \end{aligned} \quad [23]$$

By Eqs. 19, 22, 21, 20 and 10 the nominal values for ϵ_0 , r_0 , ϵ_1 , r_1 , may be calculated.

The nominal approach hyperbola has eccentricity $\epsilon_0 = 1.64$. When the distance from Mars is $r_0 = 237,000$ miles ($R_0 = 37.45$), the constant acceleration (first phase) portion of the capture maneuver should begin. When α_1 is small, the final eccentricity ϵ_1 by Eq. 21, is not sensitive to an error in r_0 . Consequently a device which measures the image size of Mars should be adequate to start this maneuver. During the first phase the magnitude of the radial speed will decrease until r reaches $r_1 = 37,270$ miles ($R_1 = 5.89$) with the corresponding eccentricity $\epsilon_1 = 1.09$. From Eq. 6, the time elapsed during the first phase is 44.8 hr and the corresponding characteristic velocity is 5190 fps. After reaching r_1 , the radial speed is maintained at a constant value (second phase) until the engine is automatically shut off when $r = p = 6320$ miles ($R = 1$) and $\epsilon = 0.707$. By Eqs. 14 and 16 the time elapsed is 9.6 hr and the characteristic velocity for the second phase is 3270 fps.

The acceleration history for the nominal capture maneuver is given in Fig. 3, where the maximum acceleration is obtained when $r = (3/2)p = 9480$ miles and $\alpha = 4/27 (\mu/p^2) = 0.2 \text{ ft/sec}^2$ ($= 6.2 \times 10^{-3}g$).

The angle swept out by the radius vector during the first phase is given by the elliptic integral

$$\varphi = \int_{R_1}^{R_0} \frac{dR}{R^2 \sqrt{\epsilon^2 - \left(1 - \frac{1}{R}\right)^2}} \text{ radians} \quad [24]$$

where $\epsilon^2 = \epsilon_0^2 + 2A_1(R - R_0)$. For the nominal first phase of the capture maneuver $\varphi = 13.7^\circ$. During the second phase, by Eq. 17, this angle is 67.3° ; and therefore the total angle swept out by the radius vector during the capture maneuver is about a quarter of a revolution.

If it is assumed that the main engine and the associated Doppler equipment perform as indicated, the distribution of

the final eccentricity ϵ may be found by Eq. 21 with independent variables v_∞ , p and r_0 . It is seen that a fairly liberal error may be made in these variables and still attain a reasonable capture orbit. There are, however, certain side effects. If p is quite small, there is danger of collision with Mars; but as long as p is greater than twice the radius of Mars, collision is impossible for any final elliptic orbit. Also, the acceleration α in Fig. 3 for the second phase will be higher or lower than indicated as p is less or greater than its nominal value.

Let us use the criterion

$$r^* = d \left(\frac{M_\odot}{M_\oplus} \right)^{2/5} \quad [25]$$

for the effective radius r^* of Mars with respect to the sun [See (9), p. 194], where d is the distance between Mars and the sun and M_\odot/M_\oplus is the mass ratio. Evaluated at the mean distance of Mars from the sun we obtain $r^* = 360,000$ miles. For our example the perturbative influence of the sun during the capture maneuver should be small.

Conclusions

Radial thrust does not appear to its best advantage when the eccentricity of the osculating ellipse is small. In this case, when the thrust acceleration is small, a sizeable change in the eccentricity requires either coasting periods or thrust reversal. Circumferential or tangential acceleration avoids this problem and is, of course, more economical. See Lawden (10,11) and Moeckel (12) on optimization of escape from a circular orbit.

When the radial direction is more nearly aligned with the tangential direction, as in our example, then radial thrust is more attractive. The total characteristic velocity of our example is 8460 fps compared to 6300 fps obtained for a radial impulse at $R = 1$. Other steering programs may be alternated with radial thrust [see Rodriguez (1)], but in the case of our example we cannot better 3700 fps which is the tangential velocity increment needed at the periplanet to transfer an approach hyperbola having a hyperbolic excess arrival speed of 8730 fps into our nominal capture ellipse.

References

1. Rodrigues, E., "Method for Determining Steering Programs for Low Thrust Interplanetary Vehicles," *ARS JOURNAL*, vol. 29, October 1959, pp. 783-788.
2. Paiewonsky, B., "The Motion of an Orbiting Vehicle Subjected to Continuous Radial Thrust, Including a Study of Planetary Encounters," presented at the 10th International Astronautical Congress, London, 1959.
3. Dobrowolski, A., "Satellite Orbit Perturbations Under a Continuous Radial Thrust of Small Magnitude," *JET PROPULSION*, vol. 28, October 1958, pp. 687-689.
4. Copeland, J., "Interplanetary Trajectories Under Low Thrust Radial Acceleration," *ARS JOURNAL*, vol. 29, April 1959, pp. 267-271.
5. Karrenberg, H. K., "Note on Interplanetary Trajectories Under Low Thrust Radial Acceleration," *ARS JOURNAL*, vol. 30, January 1960, pp. 130-131.
6. Au, G., "Corrections for Interplanetary Trajectories Under Low Thrust Radial Acceleration," *ARS JOURNAL*, vol. 30, July 1960, p. 708.
7. Arthur, P. D., Karrenberg, H. K. and Stark, H. M., "Simple Method for Approximating the Characteristics of Low Thrust Trajectories," *ARS JOURNAL*, vol. 30, July 1960, pp. 649-652.
8. Breakwell, J. V., Gillespie, R. W. and Ross, S., "Researches in Interplanetary Transfer," *ARS 14th Annual Meeting*, Washington, D. C., November 16-20, 1959 (ARS preprint 954-59).
9. Subbotin, M. F., *Course in Celestial Mechanics*, Vol. 2, United Scientific and Technical Press, 1937, p. 194, as quoted in *The Russian Literature of Satellites*, Part I, International Physical Index, Inc., N. Y., 1958, p. 118.
10. Lawden, D. F., "Optimal Programming of Thrust Direction," *Astronautica Acta*, vol. 1, 1955, pp. 41-56.
11. Lawden, D. F., "Optimal Escape from a Circular Orbit," *Astronautica Acta*, vol. 4, 1958, pp. 218-233.
12. Moeckel, W. E., "Trajectories with Constant Tangential Thrust in Central Gravitational Fields," *NASA Tech. Rep.*, R-53, 1960.

Satellite Orbit Sustaining Techniques

RICHARD W. BRUCE¹

Space Technology Laboratories,
Inc., Los Angeles, Calif.

Techniques for sustaining circular orbits, which decay because of atmospheric drag, are examined. In particular, studies are made of the requirements for propulsion devices aboard the satellite to counteract the drag forces. Two sustaining schemes are considered, namely, a thrust device that operates continuously with the thrust magnitude equal to the drag, and a thrust device that provides discrete impulsive velocity corrections spaced throughout the desired sustaining period. Single stage propulsive systems with continuous thrust capability over long periods are assumed for the former scheme, whereas single stage propulsive systems with multiple restart capability are assumed for the latter. For both schemes it is found that there is a linear dependence between the required propellant mass fraction and the sustained lifetime. It is shown that the longest lifetime per pound of propellant is obtained by using the continuous thrusting criterion. It is of particular significance that use of a sustaining device requiring only moderate expenditure of propellant substantially increases the lifetime of the satellite.

IN SATELLITE systems designed to perform various missions, for example, reconnaissance, surveillance, navigation, communications, or defense, it is desirable and sometimes even necessary to build an orbit sustaining device into the system. This counteracts the non-Keplerian forces which, dissipating energy from the satellites that make up the system, would otherwise prevent the satisfactory fulfillment of the mission.

While there exist non-Keplerian forces acting on a satellite that do not dissipate its energy, such as the higher order forces due to the Earth's oblateness, or the interaction of the Earth's magnetic field on a statically charged satellite, they do not detract from the satellite lifetime regardless of how else they might affect the orbital elements.

On the other hand, forces due to atmospheric and cosmic drag, ion sweep-up, or meteoritic collision, dissipate the energy of a satellite, and their effect, however large or small, will in time make the satellite incapable of sustaining its orbit. Techniques may be envisioned, for example, corrective propulsion devices aboard the satellite, that will counteract these dissipative forces and increase the lifetime of a satellite system.

It is with these dissipative forces, in particular atmospheric drag, and the methods used to nullify them, that this study is concerned. Some pertinent references (1-6)² are listed.

System Description

Though the particular mission assigned to a satellite system will dictate orbital conditions, such as altitude and eccentricity, some general conclusions may be drawn as to the probable operating altitudes and eccentricities of satellite systems.

Certain limitations on the altitude range of the missions under consideration will be imposed by optical, infrared, or other detection and tracking devices that are necessary to the satellite systems. On the other hand, the higher the design altitude of a particular system, the less the necessity for incorporating a sustaining device. For these reasons an arbitrary upper limit of 30 n miles was chosen as the example for this study.

Presented at the ARS Annual Meeting, Washington, D. C., Dec. 5-8, 1960; revision received, July 5, 1961.

¹ Formerly Member of the Technical Staff; presently Member of the Technical Staff, Aerospace Corp., Los Angeles, Calif.

² Numbers in parentheses indicate References at end of paper.

Circular orbits are desirable in that noncircular or eccentric orbits offer few, if any, advantages for reconnaissance, surveillance, or defense. Also, any detection or tracking devices in the satellite which would depend on precise orientation with respect to the Earth would encounter undesirable geometrical problems associated with an eccentric orbit. In this light, circularity was assumed to be one of the general required conditions for the satellite systems, and associated missions, under consideration.

Orbital Sustaining Schemes

Corrective propulsion needed to sustain an orbit may be divided into two categories, namely, use of a thrust device that operates continuously with the thrust magnitude just equal to the drag force; and a thrust device that provides the required velocity addition during each maneuver to return the satellite to its original orbit.

Continuous Thrust Sustaining System

In the continuous thrust sustaining system the thrust must be equal to the drag. Under such conditions the satellite would not *feel* the drag force and would continue in orbit unaffected by drag until the available propellant was exhausted. The total time over which the propellant was expended would constitute the sustained lifetime of a satellite utilizing this system. Remaining at its initial altitude, the satellite would encounter a constant drag force, and a constant thrust, hence a constant mass flow of propellant would be required to sustain it. For this application some means would have to be available within the satellite to maintain the orientation of the thrust vector along the velocity vector for the duration of the sustaining period. However, for the satellite missions under consideration, the desirability of maintaining a fixed orientation capability would in all probability be evident in lieu of the sustaining system and would not, therefore, add any complexity to the overall system.

Discrete Velocity Addition Sustaining System

Another sustaining system to be considered is one in which the satellite is allowed to decay some increment in altitude or for some increment of time at which point an impulsive velocity addition is imparted to the satellite by the sustaining device. The magnitude of this velocity addition would ef-

fect a Hohmann transfer back to the desired altitude. Upon reaching the desired altitude—apogee of the transfer orbit—a second increment of velocity would be added to the satellite to circularize the orbit.

Given that two impulsive velocity additions are required for a single corrective maneuver, what is left to be determined is the manner in which these corrective maneuvers would be spaced throughout the orbital sustaining period. Two criteria for the spacing of these maneuvers are: the application of the corrective maneuvers at equal time intervals during the orbital sustaining period; and the application of the maneuvers after the satellite orbit has decayed a specified and predetermined increment in altitude.

Consider first the equal time criterion. Some time after the establishment of the initial orbit, the satellite has lost a certain amount of its altitude. Assuming, then, that proper velocity corrections are made and the satellite is re-established in its desired orbit, the decay begins again. The propellant used for the first corrective maneuver has now decreased the initial ballistic coefficient W_0/C_{DA} , and since the rate of orbital decay is proportional to this same coefficient (shown in a later section), the increment in altitude to be lost in the next equal time interval will be greater than that lost in the previous interval. This would require a second corrective maneuver made up of impulsive velocity additions *different in magnitude* from the first. Some means would have to be available within the satellite to provide these corrective velocity additions of differing magnitude, i.e., either a computer in the loop with the thrust termination device, or engines of various thrust levels, or both.

In considering the second spacing criterion, namely, the application of the corrective maneuver after the satellite has decayed some specified increment in altitude, it can be reasoned that the magnitude of the total required velocity addition would be equivalent for each correction. From this standpoint there are inherent advantages in this system of spacing the maneuvers, and it will be the method considered for use in the discrete velocity addition sustaining system.

Analysis

Continuous Thrust Sustaining System

For

$$F = D \quad [1]$$

where

$$F = I_{sp}\dot{W} \quad [2]$$

$$\dot{W} = W_p T_s = \text{const} \quad [3]$$

$$D = (1/2)\rho V^2 C_{DA} = q C_{DA} \quad [4]$$

we have the relation

$$T_s / \frac{W_0}{C_{DA}} = \frac{W_p}{W_0} / \frac{q}{I_{sp}} \quad [5]$$

At a given altitude, the dynamic pressure q may be determined with a knowledge of the density ρ , which in this case was obtained from the ARDC Model Atmosphere 1959, and the circular velocity

$$V = \sqrt{\frac{GM}{R + h_0}} \quad [6]$$

For a given initial altitude h_0 and ballistic coefficient W_0/C_{DA} , there is a linear dependence of the required propellant mass fraction W_p/W_0 on the sustained lifetime T_s . This, then, will be compared with the lifetimes realizable with the discrete velocity addition sustaining system, and particularly with the lifetimes of satellites using no sustaining systems.

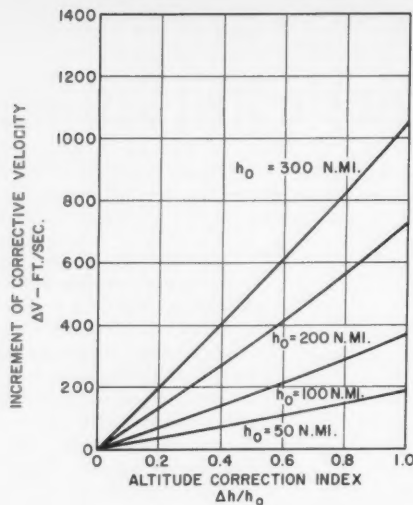


Fig. 1 Total velocity required per maneuver

Discrete Velocity Addition Sustaining System

Since the total velocity required for each correction is constant, attention will be given to the determination of the magnitude of the total velocity correction as a function of the initial orbit parameters and the incremental loss in altitude between corrections.

The total required velocity ΔV is the sum of the separate velocity additions ΔV_1 and ΔV_2 , where ΔV_1 refers to the velocity addition necessary to obtain a Hohmann transfer back to the desired altitude, and where ΔV_2 is the velocity addition necessary to circularize the orbit having once reached the desired altitude. ΔV , then, is the total required velocity for a single two impulse correction maneuver.

The separate velocity additions, ΔV_1 and ΔV_2 , may be determined from the vis-viva energy relation, namely

$$\Delta V_1 = \sqrt{GM \left[\frac{2}{R + h_0 - \Delta h} - \frac{1}{R + h_0 - \Delta h/2} \right]} - \sqrt{GM \left[\frac{1}{R + h_0 - \Delta h} \right]} \quad [7]$$

$$\Delta V_2 = \sqrt{GM \left[\frac{1}{R + h_0} \right]} - \sqrt{GM \left[\frac{2}{R + h_0} - \frac{1}{R + h_0 - \Delta h/2} \right]} \quad [8]$$

It is the sum, $\Delta V = \Delta V_1 + \Delta V_2$, that must be provided by the propulsive device aboard the satellite for each corrective maneuver. Shown in Fig. 1 is ΔV as a function of $\Delta h/h_0$ and the initial altitude.

The velocity addition available from a given engine is related to the propellant mass fraction W_p/W_0 by the familiar rocket equation

$$\Delta V_i = I_{sp} g \ln \left[\frac{1}{1 - W_{pi}/W_{oi}} \right] \quad [9]$$

or

$$W_{pi}/W_{oi} = 1 - \exp(-\Delta V_i/I_{sp}g) \quad [10]$$

where ΔV_i is the i th total velocity addition, and W_{pi} is the amount of propellant required for that particular velocity addition.

Since all the ΔV requirements are the same for each maneuver, it follows that

$$\frac{W_{p1}}{W_0} = \frac{W_{p2}}{W_0 - W_{p1}} = \frac{W_{p3}}{W_0 - W_{p1} - W_{p2}} = \dots = \frac{1}{1 - \exp(-\Delta V/I_{sp}g)} \quad [11]$$

where the subscripts 1, 2, 3, etc., denote successive corrective maneuvers. The total amount of propellant used after n maneuvers is then

$$W_p = \sum_{i=1}^n W_{pi} \quad [12]$$

where

$$W_{p1} = W_0[1 - \exp(-\Delta V/I_{sp}g)] \quad [13]$$

$$W_{p2} = (W_0 - W_{p1})[1 - \exp(-\Delta V/I_{sp}g)] \quad [14]$$

$$W_{pn} = (W_0 - W_{p1} - W_{p2} - \dots - W_{p(n-1)}) \times [1 - \exp(-\Delta V/I_{sp}g)] \quad [15]$$

It is now desirable to relate the total amount of propellant expended after n maneuvers, as shown by Eq. 12, to the total time elapsed after n maneuvers. Then, given an amount of propellant available, the corresponding elapsed time would constitute the sustained lifetime of satellites utilizing the discrete velocity addition sustaining system.

The total time elapsed after n maneuvers is the summation of the increments of time between successive maneuvers, where Δh is the loss in altitude from one maneuver to the next.

A classical approach to the determination of the time ΔT it takes a satellite in an initially circular orbit to decay a specified Δh in altitude is shown below. From the energy equation we have

$$dE = -\frac{GMm}{2(R+h)^2} dh \quad [16]$$

where E is the total energy of a satellite of mass m in a circular orbit at an altitude h .

A drag force D acting on the satellite will dissipate its energy by an amount

$$dE = DV dt = (1/2)\rho V^3 C_D A dt \quad [17]$$

By combining Eqs. 16 and 17 with the expression for circular velocity Eq. 6, and approximating the atmospheric density by

$$\rho = \rho_0 \exp(-\beta h) \quad [18]$$

we have, for $h \ll R$

$$\frac{(W/C_D A)}{g\rho_0 \sqrt{GMR}} \int_{h_0}^{h_0 - \Delta h} \exp(\beta h) dh = - \int_0^{\Delta T} dt \quad [19]$$

After integrating and rearranging

$$\Delta T = \frac{(W/C_D A)}{\beta g\rho_0 \sqrt{GMR}} \exp(\beta h_0) [1 - \exp(-\beta \Delta h)] \quad [20]$$

Again denoting successive maneuvers by the subscripts 1, 2, 3, n , it follows that

$$\Delta T_1 = W_0 \left[\frac{\exp(\beta h_0) [1 - \exp(-\beta \Delta h)]}{\beta C_D A g\rho_0 \sqrt{GMR}} \right] \quad [21]$$

$$\Delta T_2 = (W_0 - W_{p1}) \left[\frac{\exp(\beta h_0) [1 - \exp(-\beta \Delta h)]}{\beta C_D A g\rho_0 \sqrt{GMR}} \right] \quad [22]$$

$$\Delta T_n = (W_0 - W_{p1} - W_{p2} - \dots - W_{p(n-1)}) \times \left[\frac{\exp(\beta h_0) [1 - \exp(-\beta \Delta h)]}{\beta C_D A g\rho_0 \sqrt{GMR}} \right] \quad [23]$$

The total time elapsed after n maneuvers is then

$$T_s = \sum_{i=1}^n \Delta T_i \quad [24]$$

Dividing the above by the total amount of propellant used after n maneuvers, Eq. 12, we may eliminate the series common to both

$$W_0 + (W_0 - W_{p1}) + \dots + (W_0 - W_{p1} - W_{p2} - \dots - W_{p(n-1)}) \quad [25]$$

arriving at the desired expression

$$T_s / \frac{W_0}{C_D A} = \frac{W_p}{W_0} \left[\frac{\exp(\beta h_0) [1 - \exp(-\beta \Delta h)]}{\beta g\rho_0 \sqrt{GMR} [1 - \exp(-\Delta V/I_{sp}g)]} \right] \quad [26]$$

The above relation between the propellant mass fraction required to sustain a satellite a specified lifetime and the ballistic coefficient is explicitly independent of the number of impulse corrections, and like the continuous thrust system, shows a linear dependence of the propellant mass fraction W_p/W_0 on the sustained lifetime T_s for a given set of initial conditions. Fig. 2 shows the linear relationship, as predicted by Eq. 26, as a function of the ballistic coefficient for various $\Delta h/h_0$ at an initial altitude of 200 n miles. The continuous thrust case of Eq. 5 is shown for comparison. A value of 300 sec was assumed for the vacuum specific impulse of the engines. The exponential form of atmospheric density, Eq. 18, was assumed in order to allow closed form integrations in the lifetime analysis.

The compatibility between the analysis of the two sustaining schemes may be established by showing that the expression for the discrete velocity addition sustaining system, Eq. 26, reduces to that of the continuous thrust system, Eq. 5, by taking the limit as $\Delta h \rightarrow 0$ in the former expression.

For small Δh , the quantity $[1 - \exp(-\beta \Delta h)]$ approaches the value $\beta \Delta h$. Similarly, since small Δh implies small ΔV , the quantity

$$[1 - \exp(-\Delta V/I_{sp}g)]$$

approaches the value $\Delta V/I_{sp}g$. Then

$$T_s / \frac{W_0}{C_D A} = \frac{W_p}{W_0} \left[\frac{I_{sp} \exp(\beta h_0)}{\rho_0 \sqrt{GMR}} \frac{\Delta V}{\Delta h} \right] \quad [27]$$

The quantity $\Delta V/\Delta h$ may be obtained by differentiating the expression for circular velocity, Eq. 6, such that

$$\frac{\Delta V}{\Delta h} = -\frac{GM}{2V(R+h)^2} \quad [28]$$

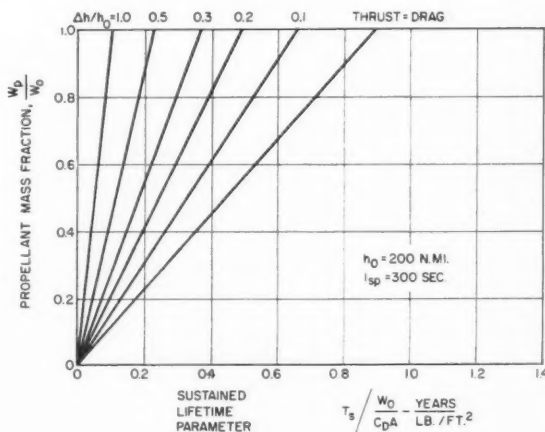


Fig. 2 Discrete velocity addition sustaining system

Making the consistent assumption that $h \ll R$, and recalling that the term $\rho_0 \exp(-\beta h_0)$, appearing in Eq. 27 is the true density ρ we have indeed

$$T_s / \frac{W_0}{C_D A} = - \frac{W_p}{W_0} \left[\frac{I_{sp}}{\rho \sqrt{GMR}} / \frac{2VR^2}{GM} \right] \quad [29]$$

$$= - \frac{W_p}{W_0} / \frac{q}{I_{sp}} \quad [5]$$

The minus sign states that propellant is being used up, or decreased, with time. By convention, however, the negative sign is not shown since it is understood that an increasingly larger proportion of propellant is required as the sustained lifetime T_s increases.

Unsustained Satellite Orbits

Having developed the propellant requirements for the continuous thrust and discrete velocity addition sustaining system as shown in Eqs. 5 and 26 respectively, it is of interest to compare these resulting sustained lifetimes with those of satellites using no sustaining devices. Referring to

the previous analysis made to determine the time it takes a satellite in an initially circular orbit to decay a specified amount in altitude, we have

$$\frac{(W_0/C_D A)}{g \rho_0 \sqrt{GMR}} \int_{h_0}^0 \exp(\beta h) dh = - \int_0^{T_u} dt \quad [30]$$

and upon integrating

$$T_u / \frac{W_0}{C_D A} = \frac{\exp(\beta h_0) - 1}{\beta g \rho_0 \sqrt{GMR}} \quad [31]$$

Fig. 3 shows the unsustained lifetimes, as predicted by the above equation, for a representative range of initial altitudes. See (1-6) for comparison with Eq. 31.

Lifetimes of satellites utilizing the orbital sustaining systems considered may now be compared to the unsustained lifetimes by the following expressions, which result from dividing Eqs. 5 and 26 by Eq. 31 above.

Continuous Thrust Sustaining System

$$\frac{T_s}{T_u} = \frac{W_p}{W_0} \left[\frac{I_{sp} \beta g \rho_0 \sqrt{GMR}}{\exp(\beta h_0) - 1} \right] \quad [32]$$

Discrete Velocity Addition Sustaining System

$$\frac{T_s}{T_u} = \frac{W_p}{W_0} \left[\frac{[1 - \exp(-\beta \Delta h)]}{[1 - \exp(-\beta h_0)][1 - \exp(-\Delta V/I_{sp} g)]} \right] \quad [33]$$

Shown, then, in Fig. 4 is the parameter $[(T_s/T_u)/(W_p/W_0)]$ evaluated for both systems for pertinent initial conditions.

Conclusions

The comparisons between sustained and unsustained lifetimes in Fig. 4 show that substantial increases in lifetime are obtained with moderate propellant expenditure. Another interesting fact that is also evident from Fig. 4 is that the advantages of a sustained satellite over an unsustained satellite are greatest at the lower altitudes, where they are needed most. It can be concluded that for the discrete velocity addition sustaining system, longer lifetimes are realized for a given mass fraction as the increment in altitude Δh is decreased, whereas the maximum lifetime per pound of propellant is obtained from the continuous thrust sustaining system.

Some consideration should be given to the effects that result from the drag forces that act on the satellite during the Hohmann transfer and during the burning periods of the velocity additions themselves. If the time taken to decay the increment in altitude Δh is of the same order of magnitude as the Hohmann transfer time, the drag impulse is not negligible compared to the drag impulse that caused the decay. This analysis has assumed that most applications of the results will pertain to systems that take many orders of magnitude of time longer to decay the specified and predetermined Δh than the transfer time back to the desired orbit; hence drag effects during transfer are negligible.

In the finite burning periods of the propulsive devices that provide the discrete velocity additions, there will result some drag losses that have not been accounted for in this study. Thus, the actual required velocity additions necessary to accomplish the desired corrective maneuver will be greater than the theoretical values predicted by the vis-viva energy relation. The lower the altitudes at which the corrective maneuvers are allowed to occur, the greater will be these unaccounted drag losses. For this reason, the results of this study tend to be less valid in the region of $\Delta h/h_0$ equal to unity, where the drag losses that occur during the finite burning periods of the corrective maneuvers are most severe.

It should be remembered that in so far as the physical realities of either system are concerned, the drag force en-

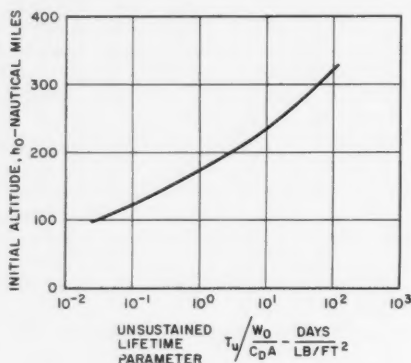


Fig. 3 Lifetimes of unsustained satellites

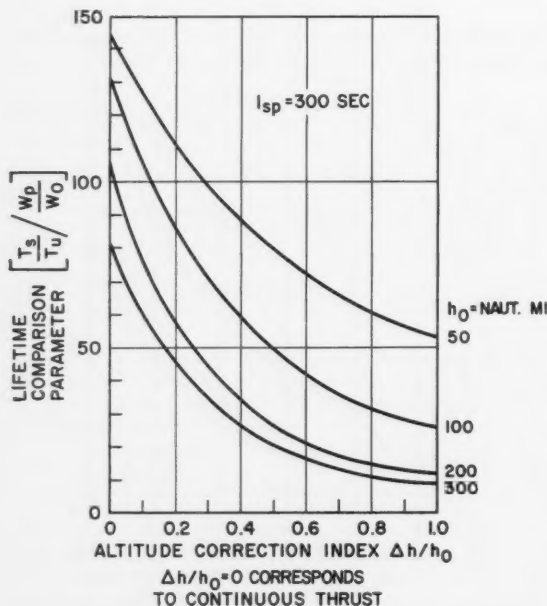


Fig. 4 Comparison of lifetimes of sustained and unsustained satellites

countered by a real satellite is not constant for any given altitude, but varies with latitude, diurnal effects, solar activity, etc. The continuously thrusting vehicle would, in the real atmosphere and in the absence of corrections, wander from its desired altitude possibly resulting in sustained lifetimes shorter than those predicted here. Similarly, satellites utilizing discrete velocity additions would decay Δh in altitude in a time increment different from that predicted in this analysis.

However, it is felt that the comparison of the two sustaining systems described remains valid in the real world, and for most applications involving the question of sustained orbits, the simple closed form of the expressions derived in this study will serve as a useful tool to the orbit analyst.

Nomenclature

A	= reference area, sq ft
C_D	= drag coefficient
D	= drag force, lb
E	= total energy of satellite orbit, ft-lb
F	= thrust, lb
G	= universal gravitational constant = 3.45×10^{-8} ft ³ /slug-sec ²
g	= conversion factor = 32.174 (lbm/lbf)(ft/sec ²)
h	= altitude, ft
h_0	= sustaining altitude, ft
Δh	= increment of altitude decay, ft
I_{sp}	= specific impulse, (lbf/lbm) sec

M	= mass of Earth = 4.09×10^{23} slug
q	= dynamic pressure, psf
R	= radius of Earth = 2.09×10^7 ft
T_s	= sustained lifetime, sec
T_u	= unsustained lifetime, sec
ΔT	= elapsed time between maneuvers, sec
V	= velocity, fps
ΔV	= increment of corrective velocity, fps
W_0	= initial weight, lb
W_p	= propellant weight, lb
\dot{W}	= propellant weight flow, lb/sec
W_p/W_0	= propellant mass fraction
W_0/C_{DA}	= initial ballistic coefficient, psf
β	= atmospheric density matching coefficient, ft ⁻¹
ρ	= atmospheric density, slug/ft ³
ρ_0	= atmospheric density matching coefficient, slug/ft ³

Subscripts

1, 2, 3, ..., n denote successive maneuvers

References

- 1 Petersen, N. V., "Lifetimes of Satellites in Near-Circular and Elliptic Orbits," *JET PROPULSION*, vol. 26, no. 368, 1956, pp. 341-351.
- 2 Henry I. G., "Lifetimes of Artificial Satellites of the Earth," *JET PROPULSION*, vol. 27, 1957, p. 21.
- 3 Roberson, R. E., "Effect of Air Drag on Elliptic Satellite Orbits," *JET PROPULSION*, vol. 28, 1958, pp. 90-97.
- 4 Nonweiler, T. R. F., "Perturbations of Elliptic Orbits by Atmospheric Contact," *J. Brit. Interplanetary Soc.*, vol. 16, 1958, pp. 368-379.
- 5 Newton, R. R., "Lifetimes of Artificial Satellites," *JET PROPULSION*, vol. 28, 1958, pp. 331-333.
- 6 Billik, B. H., "Survey of Current Literature on Satellite Lifetimes," Aerospace Corp. Rep. no. TDR-594(1560-01)TN-1, April 1961.

1961-62 ARS Meeting Schedule

Date	Meeting	Location	Abstract Deadline
1961			
Oct. 2-7	XIIth International Astronautical Congress	Washington, D.C.	Past
Oct 9-15	ARS SPACE FLIGHT REPORT TO THE NATION	New York, N.Y.	Past
1962			
Jan. 23-26	Solid Propellant Rocket Conference	Waco, Tex.	Oct. 20
March 14-16	Electric Propulsion Conference	Monterey, Calif.	Nov. 20
April 3-5	Launch Vehicles Structures and Materials Conference	Phoenix, Ariz.	Sept. 15

Recording of Pressure Step Functions of Low Amplitude by Means of Composite-Dielectric Capacitance Transducer Placed in Parallel-T Network

K. POSEL¹

University of Witwatersrand
Johannesburg, South Africa

This paper describes in detail the theory of operation and design procedure of a pressure measuring system to record pressure step functions as generated by a shock tube via the amplitude modulation process of a 500-keps carrier signal by the capacitance change of a composite-dielectric capacitance transducer housed in a three-terminal electrical bridge configuration known as the parallel-T network. An input voltage of 3.5 v to this network has enabled a pressure step of amplitude only 20 psi to be recorded as the full scale deflection on an oscilloscope having a sensitivity of 5 mv/cm when the measured transducer natural frequency is 33 keps. The damping factor of the transducer is sufficiently high to permit meaningful oscillograms to be obtained at sweep speeds as rapid as 5 microsec/cm without the use of electronic techniques to correct for transducer deficiencies. The published literature would appear to indicate that this is a considerable improvement over what has previously been achieved with the capacitance transducer in shock tube instrumentation.

A CURRENT topic of postgraduate research in the laboratory of the Department of Mechanical Engineering is concerned with gas flow phenomena occurring in the operation of a shock tube. With the completion of construction of the shock tube and calibration of the resulting wave velocity,² attention was turned to the measurement of transient pressures at various points along the tube.

The aim of this paper is to indicate, in detail, the theory of operation, design procedure and experimental results of such a pressure measuring system based on the amplitude modulation process of a 500-keps carrier signal by the capacitance change of a composite-dielectric capacitance transducer housed in a simple electrical bridge configuration known as the parallel-T network.

A perusal of the literature published recently indicates that the electronic instrumentation of pressure waveforms of extremely rapid rise-time, such as are generated by a shock tube, is a subject of continual investigation. It would appear from this published literature that the three most popular transducers used to accomplish such shock tube pressure measurements are the piezoelectric, the strain gauge and the capacitance types. Each of these possesses its own peculiar advantages and disadvantages when compared with the remaining two, and herein lies the cause of the continual work in this field. Although the above transducers have not been placed in order of popularity, it appears that the capacitance type is possibly the least popular of the three for this particular application.

Received Jan. 16, 1961.

¹ Dept. of Electrical Engineering.

² This portion of the work is contained in a thesis submitted by Mr. B. W. Skews of the Mechanical Engineering Dept. for the degree of Master of Science in Engineering and entitled: "The Construction and Calibration of a Shock Tube."

It can be said of the papers which have appeared on this subject that two categories exist. In the first only one type of transducer is used, the author concerned indicating its particular merits and demerits together with possible remedies of any errors that may have arisen. No comparison is attempted, however, between the transducer used and the remaining types. The papers of second category not only extoll the virtues of the transducer favored, but also attempt to point out the shortcomings of the other types.

The former class of publication may be regarded as an addition to the prevailing "state of the art" as it points out the capabilities of a particular transducer in the hands of a particular individual or group of individuals. If these results are subsequently bettered by another author using the same type of transducer, no really valid criticism can be leveled at the first, since what has been achieved is merely an improvement in standard.

The second category of paper, however, must be viewed rather differently. It is one matter to show that a certain method works, but it is quite a different proposition to show simultaneously that the particular method chosen is *better* than other alternative procedures. The author of a paper of this type has to be particularly careful that his comments are fair and impartial. The normal implication is that the pressure instrumentation has been attempted using not only the method finally adopted, but also other methods which are stated to be inferior. The published literature would appear to indicate, however, that this is only seldom done; as a result the comparisons made are accurate in some cases, but it appears, more often than not, that the transducers not favored are subjected to unduly harsh criticism.

The published literature indicates also that there is a second trap into which an author of this second category of

paper may unwittingly fall. In those cases where the choice of transducer has been based upon personal experience of all the methods compared, it may be found that it was made on the basis of ability to accomplish the required pressure measurement under one specific set of circumstances. Thereafter, unfortunately, the advantages of the chosen type are propounded to include more generalized fields of application. Upon careful investigation it is often found that whereas the choice made for the particular task in mind was correct, it needs to be revised when other cases of pressure instrumentation are considered.

In preparing this paper, the present author has attempted to avoid the pitfalls of the second category and has tried, to the best of his ability, to direct it into the former class. The aim is therefore not to establish the virtues of the capacitance transducer under all circumstances, but to point out some favorable properties that have been overlooked (or even incorrectly stated as being distinct disadvantages) by other workers in this field when the specific problem of recording pressure step functions as generated by a shock tube is being considered. These favorable properties have emerged as the result of original analyses firstly of the composite-dielectric type of capacitance transducer (1)³, and secondly of the use of the parallel-T network as a transfer bridge for the transducer (2).

The parallel-T network (3) is a three terminal electrical bridge configuration consisting only of resistors and capacitors. This property allows the amplitude modulation of a carrier frequency as high as 500 kcps to be performed without any special shielding considerations. Using a carrier of this frequency and an rms voltage only of 3.5 v, a pressure step of amplitude 20 psi has been recorded as the full scale deflection on an oscilloscope having a sensitivity of 5 mv/cm when the measured natural frequency of the capacitance transducer was 33 kcps. Using this simple apparatus, meaningful oscillograms have been obtained at a sweep speed of 5 micro-sec/cm. It should be pointed out that in order to use these fast sweep speeds Liu and Berwin (4) have found it necessary to resort to a rather complex analog computer technique to correct for transducer deficiencies which occurred as the result of inadequate damping.

Review of the Literature

A convenient starting point in this review of literature is the 1949 paper of Draper and Li (5). Although this paper considered the capacitance transducer specifically from the viewpoint of recording pressures during an engine cycle, it nevertheless contains some severe attacks on its general principle of operation. In view of the uncomplimentary remarks made therein and the severity of the allegations against the capacitance transducer, the present author is somewhat surprised that he has to date been unable to find any refutation of these allegations in the published work on the subject.

The error made by Draper and Li in their criticism of the capacitance transducer arises in their section entitled, somewhat uncomplimentarily, "Performance Limiting Characteristics of Flat-Diaphragm Pressure Receivers"; this error has occurred as the somewhat natural consequence of an analysis which has attempted too generalized a treatment. It would appear that the validity and accuracy of generalized analyses are often open to doubt when the detailed treatment of specific cases, supposedly falling within the boundaries of the generalized case, are considered.

In an attempt to include both the electromagnetic and the electrostatic pressure transducers in their discussion, Draper and Li have stated that "the pressure-displacement sensitivity of a flat-diaphragm pressure receiver is equal to the ratio of the displacement of the diaphragm center to the pressure applied to the diaphragm." As the result of this definition,

certain graphs are derived relating to the support acceleration and temperature difference across the diaphragm of such a flat-diaphragm pressure transducer. When the time comes to state the overall transfer sensitivity of the capacitance transducer, in picofarads (pf) of capacitance change per applied pressure in psi, the authors unfortunately still retain this "pressure-displacement sensitivity" as defined above in unmodified form and as determined by the equation

$$S = y_{\max}/P = (3/16)(1 - \sigma^2)R_d^4/ET^3$$

where

- y_{\max} = deflection at diaphragm center
- P = applied pressure
- σ = Poisson's ratio for the diaphragm material
- R_d = diaphragm radius
- T = diaphragm thickness
- E = elastic modulus

As has been shown elsewhere (1), the transfer sensitivity of a composite-dielectric-type of capacitance transducer is actually given by

$$\begin{aligned} \Delta C/P &= 0.235R_d^2y_{\max}/(a + t/\epsilon_r)^2 \\ &= 0.235(3/16)(1 - \sigma^2)R_d^6/(a + t/\epsilon_r)^2ET^3 \end{aligned}$$

which is a different equation for what should be the same quantity when compared with the expression used by Draper and Li. In this equation a denotes the airgap dimension, t the mica thickness and ϵ_r the relative permittivity of mica.

Therefore, to summarize, although the arguments put forward by Draper and Li concerning the defects of the capacitance transducer are basically correct, the quantitative evaluation of the characteristics as used in the comparison with their catenary diaphragm strain gage pickup is in error. In fairness it must be added that these authors are not alone in committing this error, as Bleakney and Arons (6) have committed essentially the same mistake by discussing the transfer sensitivity of the capacitance transducer with reference solely to the deflection at the diaphragm center.

In a survey paper of high standard, Eckenrode and Kirshner (7) stated in 1954 that the frequency response of the capacitance transducer "is a serious drawback in very high frequency measurements. In addition condenser gauge sensitivity for a given pickup is usually increased at the expense of linearity of pressure response."

In 1955 Dimeff, Carson and Charters (8) stated their dislike of the capacitance transducer as: "The capacitance pickup, however, requires electronic equipment of special design, and requires frequent adjustment by the user," and gave as one of their reasons for favoring the strain gage pressure pickup: "The equipment required is not specialized, consisting of common laboratory power supplies, amplifiers and oscilloscopes."

In a subsequent paper in 1958 Dimeff (9) discusses "survey probe transducers," which are transducers "used in pressure surveys of a short-duration impulse flow such as is characteristic of shock tube tunnels" and states:

"For installations of this general type, the Ames laboratory has considered capacitance transducers desirable. Two advantages are afforded by these transducers: (a) The simplicity of the basic mechanical construction of the transducer is greater than that of either the reactive or resistive transducer. (b) The electrical heat generated within the transducer is considerably smaller than that generated in either of the other types. These characteristics allow the design of a transducer that provides smaller size, wider frequency response and smaller thermal instabilities.

"The capacitance type dynamic pressure cell in use at Ames is a conventional deflecting diaphragm transducer used with a 100-kilocycle carrier system. Problems in obtaining zero stability and factors affecting linearity of this type of transducer are conventional problems in mechanical design and have been described adequately in the literature. The

³ Numbers in parentheses indicate References at end of paper.

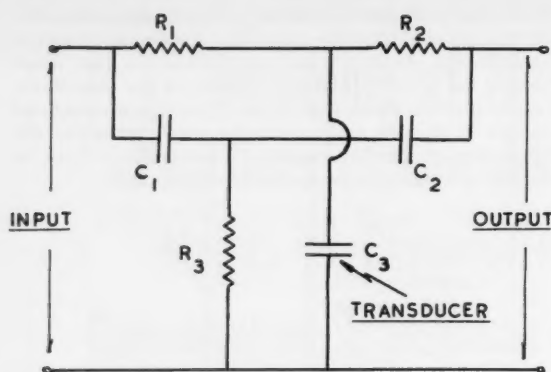


Fig. 1 The unsymmetrical parallel-T as a transfer network for the capacitance transducer

major development problem with this type of transducer involves the selection of materials and methods which will allow the construction of usable cells with a higher sensitivity or a smaller size."

To be able to use this 100-keps carrier, Dimeff emphasizes the extremely careful shielding arrangements which had to be adopted when using the bridge circuit he has indicated.

In an excellent paper, which incidentally typifies the first category of publication mentioned in the introduction, Willmarth (16) describes the application of a barium titanate transducer of diameter 0.162 in. to the recording of shock waves. With a transducer resonant frequency of 80 keps, oscillograms of a high standard are shown of a pressure step of amplitude 0.45 atm at a sweep speed of 10 microsec/division. These oscillograms indicate an overshoot and a rise-time of the order of 20% and 10 microsec, respectively. Willmarth also describes in considerable detail the dynamic calibration procedure required for this type of transducer.

In one of the most recent papers in this field, entitled "Piezoelectric Pressure Gauges for Use in a Shock Tube," Gerrard (10) states: "It is generally accepted that the measurement of pressure changes which take place in a few microseconds requires a piezoelectric transducer. A review of the literature shows this acceptance to be well founded." He continues: "Pressure gauges for use in a shock tube are limited to those types which depend for their action upon the compression of a solid." As a result of this latter statement it is of interest to point out that in his survey of shock tube instrumentation the use of a capacitance transducer of the type to be described here is not even hinted at by Gerrard.

In one of the few papers that has used a capacitance transducer for shock tube work, Tallman (11) shows an oscillogram of duration 500 microsec indicating the considerably under damped system response with a capacitance transducer having a measured natural frequency of 55 keps. It should be noted that this transducer was designed for a 2000 psi maximum pressure and was recording a step of amplitude 350 psi.

Although out of place chronologically, there is a definite reason for discussing the two 1958 papers by Liu and Berwin (4,12) at this juncture. In this instance the transducers were recognized as suffering from inadequate damping, but they were nevertheless used to record the pressure step generated by a shock tube. An analog computer technique was then used to correct this transducer deficiency, and thereby meaningful oscillograms were obtained. This is the first occasion, as far as the author is aware, that resort has been made to electronic compensation for transducer errors.

The relevant observation may be made at this stage that if such a correcting procedure exists there is then no point in discussing further methods of improving transducer response. It should be pointed out, however, that such a compensatory technique is relatively complex, and in addition there arises the very debatable principle as to whether effort should rather be spent on designing an instrumentation procedure which of its own accord falls within the accuracy of the required measurement as opposed to the idea of spending relatively little effort on the measuring apparatus, but thereafter devising a means of correcting for any deficiencies which do arise. The ultimate choice appears to be a matter of opinion into which it is not intended to venture here. However it would appear that the electronic compensatory technique might emerge as the more expensive means of achieving the same end.

Transfer Sensitivity of Loaded Parallel-T Network

Choice of Carrier Frequency

The recording of pressure step functions as set up in a shock tube is to be achieved in this paper by the amplitude-modulation of a carrier signal. To record faithfully the leading edge of such a step, this carrier frequency should therefore have the highest possible value consistent with complications which arise in the associated apparatus as the result of the frequency being increased. To indicate a few of these complications, there is firstly the consideration of the input capacitance of the oscilloscope which, being of the order of 20 to 50 picofarads, presents a relatively low input impedance in the frequency range of hundreds of kilocycles. Secondly, the maximum permissible sensitivity of oscilloscopes decreases as frequency increases, and thirdly the components used in the parallel-T network itself become of smaller and smaller magnitude as the carrier frequency is increased in value.

As far as the author is aware, the previously highest value of carrier frequency that was used in such an amplitude modulation system is 100 keps (9). Employing the parallel-T network as the transfer bridge, however, it has here been found possible to advance up to 500 keps.

A discussion of the demodulation process is relevant here. The best state of affairs results when the amplitude modulated carrier is fed directly into the oscilloscope. As the resulting modulated pattern on the screen is symmetrical, "visual" demodulation can quite easily be performed by taking the envelope of one half of the pattern about a horizontal axis. The insertion of a diode demodulator between the parallel-T and the oscilloscope is a procedure which offers basically no advantages, and only possible disadvantages, as the situation may easily arise where an extremely rapid change in the modulated waveform is not faithfully followed by the diode circuit.

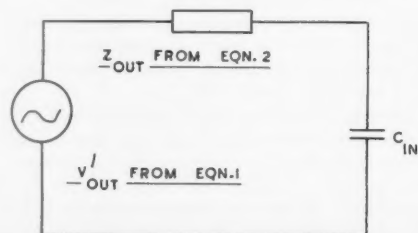


Fig. 2 Analysis of the loaded parallel-T network

Analysis of Loaded Parallel-T Network

As has been shown above, the input capacitance of the oscilloscope results in an input impedance low enough at the carrier frequency used to warrant inclusion in the analysis of the parallel-T network transfer sensitivity.

When the input impedance of the oscilloscope is assumed infinite, it has been shown (2) that the open circuit transfer sensitivity of the parallel-T network is

$$\frac{V_{out}}{V_{in}} = \frac{-\Delta}{[1 + R_1/R_2 + 1/(w_0 C_1 R_3)^2 (1 + C_2/C_1)] \cdot [1 + jw_0 C_1 R_3 (1 + C_2/C_1)]} \quad [1]$$

where Δ is the proportional change in the shunt capacitor C_3 , w_0 is the angular carrier frequency and the remaining quantities can be identified with reference to Fig. 1.

The transfer sensitivity is obtained at an output impedance, at balance, given by (2)

$$Z_{out} = \frac{-j(R_1 + R_2)[1 + jw_0 C_1 R_3 (1 + C_2/C_1)]}{w_0 C_1 R_3 (1 + C_2/C_1)(1 + R_1/R_2) + 1/w_0 C_1 R_3} \quad [2]$$

Denoting the oscilloscope input capacitance by C_{in} , the required circuit to be analysed, taking into account the loading effect of C_{in} , is then shown in Fig. 2 if it is assumed that the parallel-T output impedance at balance remains relatively unchanged in the very near vicinity of balance. It can be shown (3) that this is in fact a valid assumption.

Using the circuit of Fig. 2 together with Eqs. 1 and 2 the required transfer sensitivity follows immediately as

$$V_{out} = V_{out}' \cdot Z_{in}/(Z_{out} + Z_{in}) = V_{out}'/(1 + Z_{out}/Z_{in}) \quad [3]$$

After suitable manipulation, Appendix I shows that Eq. 3 may be stated in the form

$$V_{out} = \Delta \cdot V_{in}/f(d) \quad [4]$$

where

$$[f(d)]^2 = [1 + d(1 + C_2/C_1)] \cdot \{[1 + R_1/R_2 + (1 + C_{in}/C_2)/d]^2 + (4C_{in}/C_{30})^2(1 + C_2/C_1)d\} \quad [5]$$

and

$$d = (w_0 C_1 R_3)^2 (1 + C_2/C_1) \quad [6]$$

C_{30} = the capacitance of the shunt capacitor C_3 of the parallel-T network under balance conditions

Δ = the proportional change in this capacitance value due to the applied pressure to the transducer diaphragm

Eq. 4 is then the required expression for the transfer sensitivity of the loaded parallel-T network, as it gives the output voltage, which is fed to the oscilloscope for a given change in the transducer capacitance for a known (and constant) input carrier voltage to the network, taking into account the oscilloscope input capacitance. Although there are other alternative forms of expressing the function $f(d)$, Eq. 5 will be found the most convenient for design purposes.

Comparison Between the Symmetrical and Unsymmetrical Forms of the Parallel-T.

The symmetrical form of the parallel-T network is that in which $R_1 = R_2 = 2R_3$ and $C_1 = C_2 = C_{30}/2$. The relation between the carrier frequency and the network components can then be shown (3) to be $w_0 = 1/C_1 R_1$. Under these conditions the value of d as given by Eq. 6 becomes 0.5 and the transfer sensitivity of the symmetrical parallel-T becomes, from Eqs. 4 and 5

$$V_{out} = \Delta \cdot V_{in}/2.83[(2 + C_{in}/C_2)^2 + (C_{in}/C_2)^2]^{0.5} \quad [7]$$

which is in a particularly suitable form for design purposes, as the value of C_2 is definitely known before the design procedure

commences (for reasons to be seen later), and the value of C_{in} is determined once the oscilloscope to be used has been chosen.

As a quantitative example of the magnitudes involved, consider the practical case where $C_{in} = 50$ pf and where C_{30} is also equal to 50 pf. For a 1 pf change in C_{30} , $\Delta = 2 \times 10^{-2}$, and therefore for a 1v input to the parallel-T network the output voltage is given by

$$V_{out}/\text{pf change/volt input} = 2 \times 10^{-2} \times 10^3/12.65 \text{ mv} = 1.58 \text{ mv}$$

It must be pointed out at this stage that this value of the parallel-T transfer sensitivity was derived on the assumption of completely lossless capacitors. It is extremely difficult to fulfill this condition at the carrier frequency of 500 kcps; therefore the sensitivity as derived above will be found to be optimistic, the actual degree of optimism depending upon the dissipation factors of the capacitors used in the parallel-T network.

Considering now the unsymmetrical form, it has been shown (2) that the analysis of the transient response is a procedure which becomes unduly complicated unless the ratio of the resistors R_1 and R_2 is made unity. Under these conditions it follows (2) that the relation between C_2 and C_{30} is given by

$$C_2 = C_{30}/4d \quad [8]$$

and therefore in this case Eq. 5 becomes

$$[f(d)]^2 = [1 + d(1 + C_2/C_1)] \cdot \{[2 + (1 + C_{in}4d/C_{30})/d]^2 + (4C_{in}/C_{30})^2 d(1 + C_2/C_1)\} \quad [9]$$

As an illustrative example of the magnitudes involved, consider again the case where $C_{in} = C_{30}$ and let d have the value unity. If C_2 is made very much less than C_1 the value of $f(d)$ is reduced, making for a higher value of the transfer sensitivity. Under these conditions the value of $f(d)$ follows as being 11.4, as compared with the value of 12.65, which was calculated for the symmetrical form of the network for similar magnitudes of C_{in} and C_{30} .

The unsymmetrical parallel-T network can therefore be made to result in a transfer sensitivity slightly larger than that of the symmetrical. As this difference is only of the order of 10%, and as it will invariably be found that the component conditions are far easier to fulfill in the symmetrical case, this latter form of the parallel-T will be used henceforth.

It should be pointed out that if in any specific instance the transfer sensitivity of the unsymmetrical parallel-T can be made markedly larger than that of the symmetrical, and if the resulting component values are feasible, there is only advantage to be gained in using the former configuration without any attendant disadvantages.

Consideration of the Capacitance Transducer

System Design Procedure.

Once it has been decided to use the symmetrical parallel-T network, and the oscilloscope has been chosen, the only quantity still required in order to calculate the transfer sensitivity, by Eq. 7, is the capacitance C_2 . Since in the symmetrical network C_2 is equal to $C_{30}/2$, the information fundamentally required is the standing capacitance of the transducer. Therefore, at this stage attention must be paid to the principles governing the choice of the transducer diaphragm thickness and gap dimensions.

These considerations are considerably simplified once the basic principle has been established that the electronic circuitry must be made to operate at its most sensitive condition consistent with the difficulties of hum, noise and the like. This idea is of sufficient importance to warrant further elaboration.

As is shown in the following section, the faithfulness with

which the diaphragm displacement represents the applied pressure waveform depends firstly on the degree of the diaphragm damping and, secondly, on its natural frequency. For any degree of damping the higher the natural frequency the better, and this latter requirement is achieved by suitably thickening the diaphragm for a given radius. As is shown in the section Transducer Design Considerations, the transducer conversion sensitivity, as measured in picofarads change per applied psi, varies inversely as the cube of diaphragm thickness, so that to make the diaphragm natural frequency as high as possible, the conversion sensitivity will be at its lowest permissible value. Therefore to compensate for this the electronic circuitry must be at its most sensitive. Once this principle has been established, the transducer design proceeds in a logical sequence.

Transient Response of the Transducer to Suddenly Applied Ramp Function of Finite Rise-Time

The problem of the transducer response has in the past normally been evaluated with respect to a suddenly applied step function; that is the rise-time of the pressure waveform has been taken as zero. Although this procedure leads to a considerable simplification in the resulting analysis of the transducer transient response, it is nevertheless of importance to consider the effect of finite rise-time of the pressure waveform. The topic to be considered is therefore the sudden application of the waveform shown in Fig. 3 to a single degree of freedom circuit consisting of mass m , stiffness constant k and damping coefficient c .

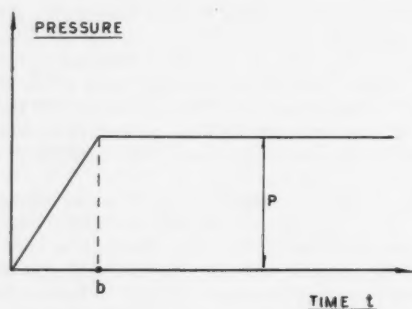


Fig. 3 Applied pressure waveform to be considered

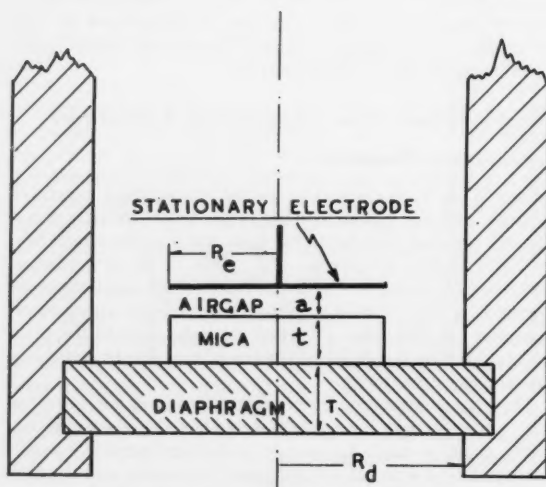


Fig. 4 Concerning the composite-dielectric capacitance transducer

It can then be shown that the relation between the displacement x of such a single degree of freedom system and the peak value P of the applied pressure is given at any instant of time t by the expression

$$x(t) = (P/k) \{ [1 + (T_n/b) \{ (\exp - \alpha t') \sin(t'/T_n + 2\beta) - (\exp - \alpha t) \sin(t/T_n + 2\beta) \}] \} \quad [10]$$

where

- T_n = the natural period of the system
- b = the time interval indicated in Fig. 3
- α = the system damping factor = $c/2m$
- $t' = t - b$

The more difficult interpretation of Eq. 10 as compared with the equation emerging from the response of the system to a perfect (zero rise-time) step function is then only too apparent.

It follows, however, that whatever else may be said about Eq. 10, the following statements are correct for an applied pressure waveform of given rise-time:

- 1 The smaller the value of T_n , that is the higher the value of the natural frequency, the less will be the overshoot.
- 2 For a given value of T_n , the overshoot decreases as the value of the damping factor α increases.

It should be pointed out that an oversimplification very often used by other workers (4) in this field is: "When the rise-time of the driving function becomes shorter than one fourth of the natural period of the transducer, ringing or resonance of the transducer's moving element will take place." Eq. 10 shows that there is no sudden transition from the underdamped to the overdamped case as the value of the quantity b passes through that given by $T_n/4$.

Transducer Design Considerations

As has been shown (1) the expression for the capacitance change of the transducer caused by the application of a pressure of P psi to the diaphragm is given by

$$\Delta C/C_0 = [(1 + 2s)y_{\max}/3(a + t/\epsilon_r) \cdot [1 + 0.6y_{\max}/(a + t/\epsilon_r) + \dots]] \quad [11]$$

where

- ΔC = capacitance change in picofarads
- C_0 = transducer standing capacitance in picofarads
- y_{\max} = deflection at center of diaphragm
- a = airgap thickness (see Fig. 4)
- t = mica thickness (see Fig. 4)
- ϵ_r = relative permittivity of mica
- $(1 + s) = R_d/R_e$
- R_d = diaphragm radius (see Fig. 4)
- R_e = stationary electrode radius (see Fig. 4)

Eq. 11 may be divided into two components, the sensitivity component, which is the first factor appearing on the right-hand side of the equation, and a linearity component. For a transducer which is made adequately linear (i.e., $0.6y_{\max}/(a + t/\epsilon_r) \ll 1$) it follows that

$$\Delta C/C_0 = (1 + 2s) \cdot y_{\max}/3(a + t/\epsilon_r) \quad [12]$$

In terms of the applied pressure, diaphragm radius and thickness, the quantity y_{\max} has been shown (1) to be given, for a steel diaphragm, by the equation

$$y_{\max} = 55.5 \times 10^{-10} PR_d^4/T^3 \quad [13]$$

where

- P = applied pressure in psi
- T = diaphragm thickness in in. (see Fig. 4)

It has also been shown (1) that the fundamental resonant

frequency of such a steel diaphragm is given by

$$f_0 = 9.82 \times 10^4 T/R_d^2 \quad \text{cps} \quad [14]$$

Eqs. 11 to 14 permit of a simple design procedure for the transducer quantities, as follows.

The most sensitive arrangement results when no additional capacitance is placed in parallel with C_0 , so that C_0 is then the quantity C_{30} used in Eq. 5. Under these circumstances the ratio $\Delta C/C_0$ is the quantity Δ which has been used in this equation. An additional important piece of information is that in this case the nonlinearity factor is equal to $1.8(1 + 2s)$ times the sensitivity factor.

The crux of the transducer design process is to allot to the airgap dimension a the smallest practicable value. For the smallest feasible value of a , Eq. 12 shows that for a given t and a stipulated value of Δ , y_{\max} will have its least value. For y_{\max} at its least value, Eq. 13 indicates that, for given R_d and a stipulated pressure which is to be measured, the dimension T will have its largest permissible value. For largest permissible T and fixed R_d , Eq. 14 shows that the resonant frequency of the diaphragm will be at highest allowable value, which is precisely what is required of a successful design.

In addition to resulting in the highest feasible resonant frequency, use of the smallest practicable value of a also introduces a considerable damping factor into the diaphragm motion. This important advantageous feature⁴ may be regarded pictorially as being due to the inability of the air trapped in the space above the mica dielectric to escape rapidly enough when the diaphragm is displaced inwards.

It is important to note that for a stipulated value of Δ and chosen value of a , Eq. 13 indicates that the diaphragm thickness T increases as the value of the pressure which is to be measured increases. Therefore for fixed R_d , Eq. 14 indicates that f_0 increases as the applied pressure increases. Therefore, finally, it is seen that design conditions are most stringent when the amplitude of the pressure waveform possessing a fast rise-time is low.

The lowest value that the airspace dimension a can be allowed to assume depends almost entirely on considerations of mechanical stability. In this determination of mechanical stability it will invariably be found that temperature plays the major role. It is therefore seen that the value allotted to a depends upon the actual application for which the transducer is to be used. For example, other things being equal, the value of a to be used when engine pressures are to be recorded should normally be far greater than that used for shock tube instrumentation.

The value of the diaphragm radius R_d is normally determined by two considerations. Firstly, it may be designed to result in a certain required value of the transducer standing capacitance C_0 or, secondly, it may follow as the result of considerations of the pressure variation with distance of the waveform being recorded.

Once the design procedure as indicated above has been completed, the final check on the standard of the resulting transducer is that the capacitance change be sufficiently linear, that is, that the quantity $0.6 \cdot y_{\max}/(a + t/\epsilon_r)$ be sufficiently small compared with unity.

Design of Apparatus

It has been shown under the heading Considerations of the Capacitance Transducer that the design conditions become more stringent as the peak value of the pressure step is reduced in magnitude. In order to pose a severe test for this method of instrumentation, the design is attempted here for a pressure step of only 20 psi amplitude. As stated under

subheading Choice of Carrier Frequency, a carrier frequency of 500 kcps is to be used.

As it was anticipated that the role played by temperature in this instance would be relatively small, the value of a was chosen to be 0.2×10^{-3} in. A working diameter of 3/8 in. was chosen for the diaphragm, and on this basis the diameter of the stationary electrode was made 0.355 in. In addition it was decided that a transducer standing capacitance of the order of 50 pf would result in a reasonable parallel-T design at the frequency of 500 kcps. This latter condition was achieved by the use of a mica thickness of approximately 1.2×10^{-3} in.

The oscilloscope available was a Tektronix Model 545 with a type D preamplifier which has an input capacitance of 45 pf and permitted a maximum sensitivity of 5 mv/cm at a frequency of 500 kcps. The full scale deflection on this oscilloscope is 2 cm, and therefore a voltage of 10 mv peak value, that is of rms value 7.07 mv, is required at the oscilloscope input terminals for a 20 psi applied pressure to the transducer diaphragm.

At this stage a guess must be hazarded at the available input voltage to the parallel-T network. It is shown in the following section that the actual value of the input voltage used involves considerations of its harmonic distortion, but for the time being a value of 2v rms seems reasonable. For a symmetrical parallel-T $C_2 = C_{30}/2 = 25$ pf and therefore, from Eq. 7, the required value of Δ to enable a 7.07 mv output to be obtained with a 2v input is given by

$$7.07 \times 10^{-3} = \Delta \times 2/2.83[(2 + 45/25)^2 + (45/25)^2]^{0.5} \\ \text{i.e., } \Delta = 4.21 \times 10^{-3}$$

Neglecting s , this enables the nonlinearity factor to be immediately stated as $1.8 \times 4.21\%$, that is 7.6%. The required value of y_{\max} to give this value of Δ is then, from Eq. 12, and assuming a relative permittivity of 7 for mica, given by

$$\Delta = 4.21 \times 10^{-3} = y_{\max}/3(0.2 + 1.2/7) \times 10^{-3} \\ \text{i.e., } y_{\max} = 0.0471 \times 10^{-3} \text{ in.}$$

The diaphragm thickness to permit this value of y_{\max} to be obtained is, from Eq. 13, given by

$$T^3 = 55.5 \times 10^{-10} \cdot P \cdot R_d^4 / y_{\max} = 55.5 \times 10^{-10} \times 20 \times \\ (0.375/2)^4 / 4.71 \times 10^{-5} = 2.89 \times 10^{-6} \text{ in.}^3 \\ \text{i.e., } T = 14.2 \times 10^{-3} \text{ in.}$$

The diaphragm natural frequency is then, from Eq. 14, given by

$$f_0 = 9.82 \times 10^4 \times 14.2 \times 10^{-3} / (0.375/2)^2 = 39.6 \text{ kcps}$$

The nonlinearity figure of 7.6% calculated above may at first sight seem somewhat excessive. There are, however, two features which will reduce this nonlinearity rather substantially in the final output voltage vs. applied pressure graph. Firstly it must be remembered that the value of 7.6% expresses the nonlinearity at the applied pressure of 20 psi with respect to zero psi. On the actual graph of capacitance change vs. applied pressure it will be found that a mean straight line approximation can be drawn to show a far lower nonlinearity value. Secondly, it has been shown (1,2) that, whereas the capacitance change graph becomes concave downwards as the applied pressure is increased, the parallel-T characteristic of output voltage vs. the capacitance change ΔC_{30} becomes concave upwards. The overall system transfer characteristic of parallel-T output voltage vs. applied pressure to the transducer diaphragm, which after all is the transfer characteristic of real importance, then tends to be accurately linear when each of the other two graphs mentioned above is decidedly nonlinear.

In any event the transducer and its associated apparatus are subjected to a calibratory test before use, and if the re-

⁴ This was pointed out to the author by C. J. Rallis, Senior Lecturer in the Mechanical Engineering Dept.

sulting graph is unacceptable, the design process as indicated above can be redone to achieve a more linear response.

As mentioned in the section Comparison Between the Symmetrical and Unsymmetrical Forms of the Parallel-T, the use of Eq. 7 presupposes the use of perfectly loss-free capacitors in the network. As this is an extremely difficult condition to fulfill at 500 kcps, it must be expected that the input voltage assumed above of 2v must be increased somewhat, the actual increase depending upon the dissipation factors, at 500 kcps, of the capacitors used.

As regards the parallel-T design, as $C_{30} = 50$ pf, $C_1 = C_2 = 25$ pf and from equation $w_0 = 1/C_1 R_1$, it follows that

$$R_1 = 1/2\pi \times 500 \times 10^3 \times 25 \times 10^{-12} = 12.7 \text{ kohm}$$

Therefore $R_3 = R_1/2 = 6.35 \text{ kohm}$. It must again be pointed out that this value of R_3 has been shown (13) to be less than $R_1/2$ when capacitor loss is present, the actual reduction again depending on the specific loss occurring.

Additional Practical Requirements

For zero applied pressure to the transducer diaphragm, the parallel-T network is brought into the balanced condition by suitable variation of both R_3 and a small trimmer capacitor which is placed in parallel with the transducer itself. Under these circumstances zero output voltage results, and there is then no deflection on the oscilloscope screen.

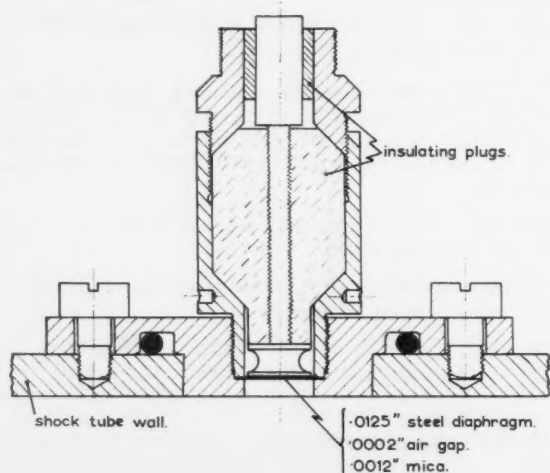


Fig. 5a Details of the pressure transducer

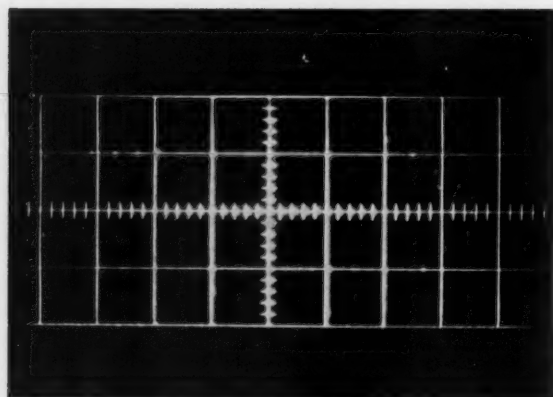


Fig. 5b Amplitude-modulated carrier of 500 kcps recording pressure step. Sweep speed: 5 microsec/cm

The above statement is completely accurate when applied to the fundamental component of the input voltage. The parallel-T, however, is a single frequency rejection network, and therefore any other frequency component present in the input voltage waveform is passed, partially or completely, depending upon its proximity to the fundamental.

As a quantitative example, consider the design calculated under heading Design of Apparatus. On a vertical scale of 2 cm, an initial zero trace of thickness 1 mm is easily discernible. Using a sensitivity of 5 mv/cm this latter trace then represents 0.5 mv peak value, and therefore this voltage, for an input voltage of 2v to the parallel-T, represents a distortion content of the order of $0.5 \times 10^{-3} \times 10^3/2\sqrt{2}\%$, that is 0.017%.

It can be safely said that oscillators of such low distortion content are seldom, if ever, encountered in normal laboratory equipment, and therefore a filter tuned to accept the fundamental component of the oscillator voltage has to be inserted between the oscillator and the input terminals of the parallel-T network.

The author has attempted in a previous paper (2) to predict the rejection characteristic required of such a tuned filter. It appears however that a far more satisfactory procedure is initially to try out a tuned filter in situ and then to modify its characteristics accordingly. This procedure is particularly recommended at frequencies of the order of 500 kcps, where filters of variable selectivity are pieces of apparatus easily devised.

In obtaining the experimental results indicated in the following section, the tuned filter used was the I.F. stage of an ordinary radio receiver, the diode demodulator having been removed as discussed later. Under these circumstances the zero trace thickness was slightly under 1 mm in thickness when using an oscillator of specified distortion content of the order of 0.5%.

It has been seen that one method of increasing the transfer sensitivity of the system is merely to increase the input voltage. In so doing, however, the requirements on the tuned filter become progressively more stringent. This feature results since the maximum thickness of trace under balance conditions remains at the figure of 1 mm mentioned above and does not increase in proportion to the input voltage increase. For a fixed percentage distortion content, the harmonic voltages in the input voltage waveform obviously increase as the fundamental component is increased in voltage; the filter has then to be more sharply tuned to result in the same thickness of initial trace as before. It will in fact be found that, for an oscillator of given harmonic content, the required rejection characteristic of the tuned filter provide the upper limit to the value of the transfer sensitivity that is obtainable from this method of pressure instrumentation.

Experimental Results

The parallel-T network and transducer were constructed using the design values calculated in a previous section with the one exception that, as a 14.2×10^{-3} in. diaphragm was not available, the nearest thickness of 12.5×10^{-3} in. was substituted in its place. A drawing of the transducer is given in Fig. 5a.

With this change the calculated new value of y_{max} is 0.0688×10^{-3} in., that of Δ is 6.15×10^{-2} and that of the new input voltage to cause the required output voltage of 7 mv for a 20 psi applied pressure is 1.37 v rms. The calculated diaphragm resonant frequency in this instance becomes 34.8 kcps.

For the system as constructed it was found that an input voltage of 3.5 v was required as opposed to the predicted value of 1.37 v. As has been stated earlier, the derivation of Eq. 7 has used the value $R_1/2$ for R_3 , and has thereby neglected the presence of capacitor loss and also capacitance between the input and output terminals of the parallel-T network.

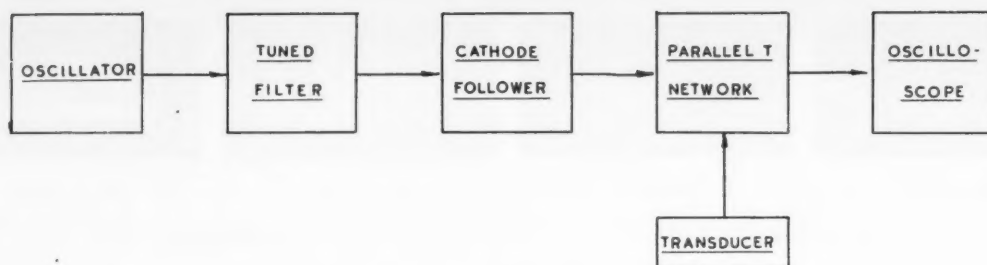


Fig. 6 Block diagram of the electronic circuitry

When these effects are present it can be shown (13) that the value of R_3 becomes appreciably lower than $R_1/2$, especially if C_1 and C_2 are each small in magnitude, as is the case here. The derivation of Eq. 7 then shows that this causes the transfer sensitivity to be reduced, that is, a larger input voltage is required for a given output voltage and a given applied pressure.

A block diagram of the electronic circuitry is shown in Fig. 6.

The response of the transducer and its associated equipment was obtained by recording the pressure step as generated by a shock tube, a well-known procedure (11,14) in the transducer field. The shock tube used was constructed as part of a postgraduate research program (15) in the departmental laboratory, and possessed the following characteristics:

- 1 Chamber and channel built of aluminium and of cross section 1.75 sq in.
- 2 Length of chamber 25 in.; length of channel 143 in.
- 3 Diaphragms used were of cellulose acetate 10×10^{-3} in. thick; conventional methods of diaphragm rupturing were employed.
- 4 When 80 psi (gage) was used in the chamber and atmospheric pressure in the channel, the resulting shock wave velocity was Mach 1.5.

Since the displacement of the diaphragm center was to be of the order of only 0.07×10^{-3} in., concern might be expressed about the standard of the reproducibility of the pressure records. With this in mind all records were taken for the same initial conditions (within experimental setting accuracy) for at least two consecutive occasions. The high standard of reproducibility achieved is shown in the oscillograms obtained.

Another issue which arises out of the high value of the transfer sensitivity of the apparatus, as well as the small displacement of the diaphragm center, concerns the amount and frequency of possible rebalancing required of the parallel-T network after each pressure record has been taken. It was found that absolutely no rebalancing at all of the parallel-T was required until some twenty records had been taken, and after the time interval involved, the slight variation of the balancing controls that was called for could possibly have been attributed either to a small frequency change in the oscillator or to the small change of the transducer standing capacitance caused by the diaphragm not returning precisely to its previous neutral position.

The transducer was mounted in a manner which enabled the diaphragm to be within 0.09 in. from the inner surface of the shock tube wall. The resonant frequency of the entrance canal so formed was then not expected to influence the records obtained.

The records obtained are shown in Fig. 7. The first important point is to compare the predicted resonant frequency of 34.8 kcps with the experimentally obtained value of 33

kcps for the natural frequency. The second feature to emerge from these oscillograms is the high damping factor of the system. These two properties then enabled the fast sweep speeds indicated to be successfully used, without any recourse to a compensatory technique to correct for transducer deficiencies.

The oscillograms shown consist of a modulated carrier waveform which is symmetrical about a horizontal axis. It must be pointed out that in most instances this axis has not coincided with the horizontal axis of symmetry of the oscilloscope graticule; this merely means that the oscilloscope trace under parallel-T balance conditions was not situated in mid-screen. This characteristic, which was caused initially by the viewing system of the camera used, of course introduces no additional error into the resulting oscillograms. The required pressure vs. time records are obtained by taking the envelope of the upper half of the modulated pattern in each case.

Figs. 7 a and b show that the overall measuring apparatus possesses a rise-time and an overshoot of the order of 10 microsec and 50%, respectively. The remaining oscillograms show the application of the pressure measuring system as described in this paper to the recording of transient pressures occurring in the operation of a shock tube.

It is of interest in this connection to point out the slight rise in pressure which occurs once the shock wavefront has passed, as shown in Figs. 7i and j. This pressure rise was also noticed by Shunk, Dranetz and Budenstein (17) who state:

"This gauge suffers, in common with all piezoelectric gauges, the disadvantage that it cannot be calibrated statically. This and three other types of pressure gauge have confirmed a continuing rise in pressure of the gas in the shock tube after the shock passes. Thus even though the pressure jump across the shock is known from shock velocity measurements, so that the initial rise can be calibrated, it is not possible to calibrate the long-time characteristic of the gauge in the shock tube by assuming constant pressure in the flow following the shock."

As this shock tube procedure is the normal manner of dynamically calibrating a piezoelectric type of transducer, it would appear that this pressure rise after the shock introduces complications into the calibration process.

It is the intention to deal with the interpretation of the pressure waveforms resulting from the application of the parallel-T method of instrumentation to shock tube operation in a separate paper in the near future. For the moment, attention is being focussed on both oscillator and tuned filter design in an attempt to produce an input voltage waveform to the parallel-T network of even greater purity. This will enable the conversion sensitivity of the apparatus to be increased further, which will then lead to an increased natural frequency of the transducer diaphragm.

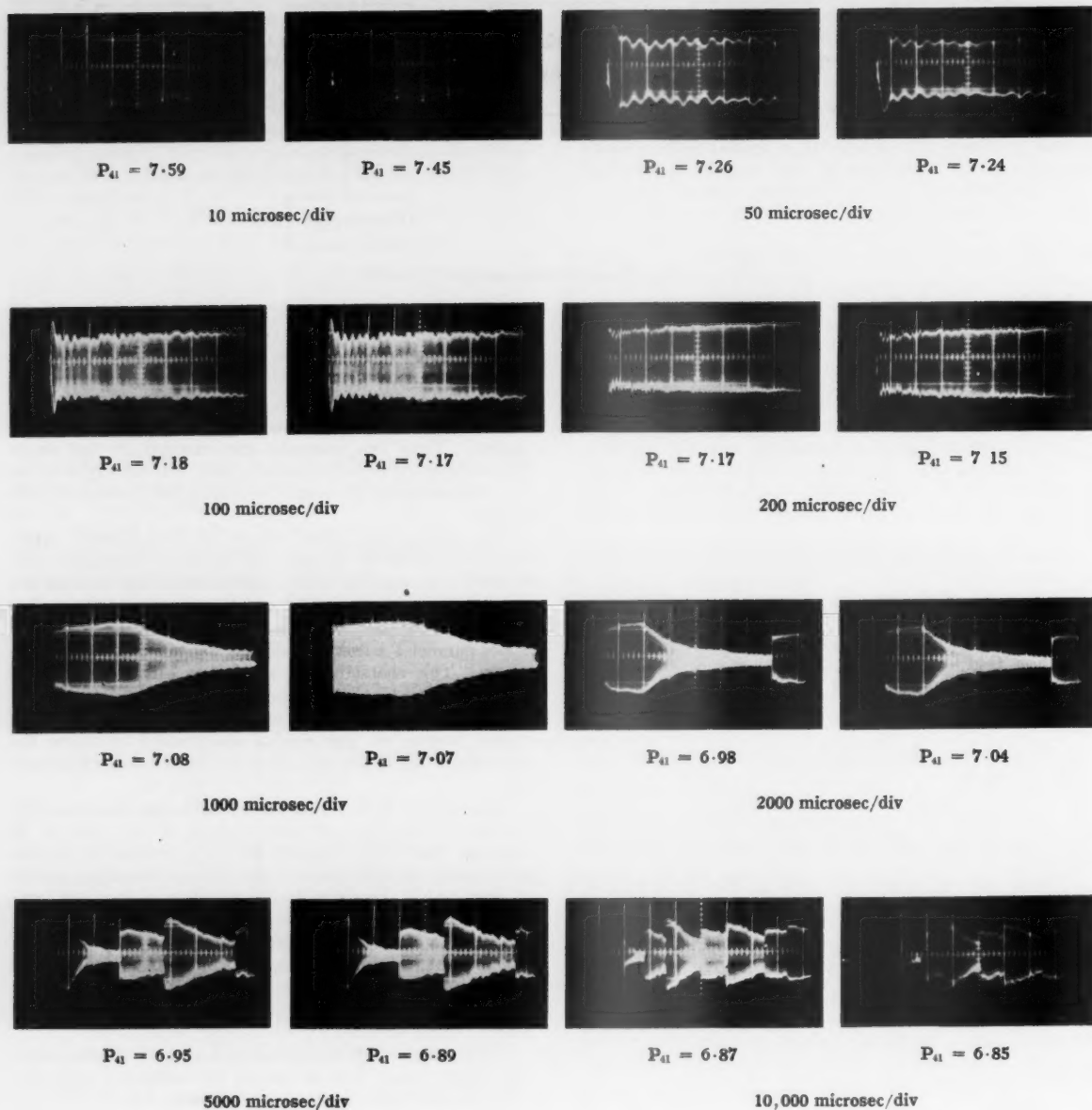


Fig. 7 The pressure records obtained. Each of the above oscillograms is an amplitude-modulated wave

Conclusions

Possibly the severest criticisms of the capacitance type pressure transducer are contained in the remarks of Eckenrode and Kirshner (7) and of Dimeff, Carson and Charters (8) which are quoted in a previous section that deals with the review of the literature.

The aim of this paper has been an attempt to repudiate these allegations by indicating a capacitance transducer design procedure which results in a product which does not "require frequent adjustment by user (8)," and by the introduction of the parallel-T network as a transfer bridge, to show that the "equipment required is not specialised, consisting of common laboratory power supplies, amplifiers and oscilloscopes (8)."

The use of this pressure measuring system has enabled meaningful oscillograms to be recorded at sweep speeds which have previously been obtained only, as far as the author is aware, by the use of an analog computer technique to correct for capacitance transducer deficiencies.

Acknowledgments

The author wishes to indicate his sincere appreciation to B. W. Skews of the Mechanical Engineering Dept. for operating the shock tube when the pressure records indicated above were taken and for photographic assistance.

Thanks are also due to S. Smolenec and to C. J. Rallis of the department for their continual encouragement and discussions.

Appendix I: Derivation of Eq. 4

The term Z_{out}/Z_{in} which appears in Eq. 3 may be written, using Eq. 2, as

$$\begin{aligned} Z_{out}/Z_{in} &= \frac{-j(R_1 + R_2) \cdot [1 + jw_0 C_1 R_3 (1 + C_2/C_1)]}{[w_0 C_1 R_3 (1 + C_2/C_1) (1 + R_1/R_2) + 1/w_0 C_1 R_3]} \cdot (jw_0 C_{in}) \\ &= \frac{-j(R_1 + R_2) \cdot [1 + jw_0 C_1 R_3 (1 + C_2/C_1)] \cdot jw_0 C_{in}}{(1 + C_2/C_1) w_0 C_1 R_3 [1 + R_1/R_2 + 1/(w_0 C_1 R_3)^2 (1 + C_2/C_1)]} \end{aligned}$$

and substituting the above expression for Z_{out}/Z_{in} and Eq. 1 for the term V_{out}' into Eq. 3 there results

$$\begin{aligned} V_{out} &= \frac{-\Delta V_{in}/[1 + jw_0 C_1 R_3 (1 + C_2/C_1)]}{[1 + R_1/R_2 + 1/(w_0 C_1 R_3)^2 (1 + C_2/C_1)] - \frac{j(R_1 + R_2) [1 + jw_0 C_1 R_3 (1 + C_2/C_1)]}{w_0 C_1 R_3 (1 + C_2/C_1) / jw_0 C_{in}}} \\ &= \frac{-\Delta V_{in}/[1 + jw_0 C_1 R_3 (1 + C_2/C_1)]}{1 + R_1/R_2 + 1/d + w_0 C_{in} (R_1 + R_2) [j + 1/w_0 C_1 R_3 (1 + C_2/C_1)]} \end{aligned}$$

where the term d is given by Eq. 6.

$$\begin{aligned} \text{i.e., } V_{out} &= \frac{-\Delta V_{in}/[1 + jw_0 C_1 R_3 (1 + C_2/C_1)]}{1 + R_1/R_2 + 1/d + jw_0 C_{in} (R_1 + R_2) + C_{in}/C_2 d} \\ \text{i.e., } |V_{out}| &= \frac{\Delta V_{in}/[1 + (w_0 C_1 R_3)^2 (1 + C_2/C_1)^2]^{0.5}}{[1 + R_1/R_2 + (1 + C_{in}/C_2)/d]^2 + [w_0 C_{in} (R_1 + R_2)]^2]^{0.5}} \\ &= \frac{\Delta \cdot V_{in}/[1 + d(1 + C_2/C_1)]^{0.5}}{[1 + R_1/R_2 + (1 + C_{in}/C_2)d]^2 + (4C_{in}/C_2)^2 d(1 + C_2/C_1)]^{0.5}} \end{aligned}$$

which then leads directly to Eqs. 4 and 5 in the text.

References

- 1 Posel, K., "The Theory and Design of a Clamped-Diaphragm, Composite Dielectric, Variable-Capacitance Transducer," *J. S. African Inst. of Mech. Engrs.*, October 1960, pp. 54-69.
- 2 Posel, K., "The Steady-State and Transient Response of the Unsymmetrical Parallel-T Network as a Transfer Bridge for Use in Conjunction with Variable-Capacitance Transducers," *Transactions of the S. African Inst. of Elec. Engrs.*, May 1960, pp. 106-123.
- 3 Posel, K., "The Parallel-T Network and Applications," Thesis for the degree of Ph.D., Univ. of the Witwatersrand, 1959.
- 4 Liu and Berwin, "Extending Transducer Transient Response by Electronic Compensation for High-Speed Physical Measurements," *Rev. Scient. Instr.*, January 1958, pp. 14-22.
- 5 Draper and Li, "A New High-Performance Engine Indicator of the Strain-Gauge Type," *J. Aeronaut. Sci.*, October 1949, p. 593.
- 6 Bleakney and Arons, "Pressure Measuring Manometers and Gauges," Article B, 2 of High Speed Aerodynamics and Jet Propulsion "Physical Measurements in Gas Dynamics and Combustion," Vol. 9, pp. 124-135.
- 7 Eckenrode and Kirshner, "Measurement of Pressure Transients," *Rev. of Scient. Instr.*, January 1954, pp. 33-40.
- 8 Dimeff, Carson and Charters, "Piston-Type Strain Gauge for Measuring Pressures in Interior Ballistics Research," *Rev. Scient. Instr.*, September 1955, pp. 879-883.
- 9 Dimeff, "A Survey of New Developments in Pressure Measuring Techniques in the NACA," NATO, AGARD, Rep. 106, March 1958.
- 10 Gerrard, "Piezoelectric Pressure Gauges for Use in a Shock Tube," *Acustica*, vol. 9, 1959, pp. 17-23.
- 11 Tallman, "Transducer Frequency Response Evaluation for Rocket Instability Research," *JET PROPULSION*, February 1959, pp. 119-122.
- 12 Liu and Berwin, "Recent Advances in Dynamic Pressure Measurement Techniques," *JET PROPULSION*, February 1958, p. 83.
- 13 Posel, K., "The Unbalanced Symmetrical Parallel-T Network Taking Account of Capacitor Loss," *Transactions of the S. African Inst. Elec. Engrs.*, July 1957.
- 14 Bowersox, "Calibration of High-Frequency-Response Pressure Transducers," *J. Instrument Soc. of America*, November 1958, pp. 98-103.
- 15 Skews, "The Construction and Calibration of a Shock Tube," Thesis for the degree of M.Sc. (Eng), Univ. Witwatersrand, 1961.
- 16 Willmarth, "Small Barium Titanate Transducer for Aerodynamic or Acoustic Pressure Measurements," *Rev. Scient. Instr.*, March 1958, pp. 218-222.
- 17 Shunk, Dranetz and Budenstein, "Ring-Shaped Piezoelectric Gauge for Shock Tube," *Rev. Scient. Instr.*, 1953, pp. 1069-1070.

The Traveling-Wave Pump¹

EUGENE E. COVERT² and
CHARLES W. HALDEMAN³

Aerophysics Laboratory
Massachusetts Institute of
Technology
Cambridge, Mass.

An ionized gas can be accelerated by a moving magnetic field. This principle has been used to produce an electrodeless a-c accelerator called a "traveling-wave pump." Since high gas velocities are obtainable in this way, the device may be used directly for propulsion or for simulating re-entry flow conditions. The operating principle of the "traveling-wave pump" is discussed. A prototype experimental facility of this type is described. The possible application to electrodeless power generation is also briefly mentioned.

THE PURPOSE of this discussion is to present one form of the alternating current analog to the magnetohydrodynamic pump. The direct current machine, which has been successfully applied to pumping of liquid metals, requires electrodes that are wetted by the conducting fluid. When the conducting fluid is a hot gas, the electrode design becomes difficult. The problems associated with the electrodes can be eliminated by use of alternating current electrodeless discharges. This kind of discharge has been used as a propulsion scheme for shock tubes with success. The discussion that follows illustrates the application of the electrodeless discharge to problems of continuous pumping. The pumping problem in this discussion differs from that used in the Stellarator (1)⁴ where the field is stationary and the purpose of the "pumping" is to add heat, and corresponds more nearly to that situation described in (2). Experiments are described in (2) in which kinetic energy is added to an ionized gas, and in which a direct current discharge was used to amplify a radio frequency signal. In the author's application to wind tunnel propulsion, the primary purpose of the pumping is to add a maximum directed velocity, i.e., kinetic energy with minimum heating.

The remaining portion of this paper is separated into three major parts. In the first, a qualitative discussion of the traveling-wave pump is presented. The second contains a description of the apparatus that has been constructed to test these ideas. The third presents some preliminary data taken from the apparatus. The possible application of this device to wind tunnel propulsion, rocketry, or, conversely, power conversion, is briefly mentioned.

Discussion of the Traveling-Wave Pump

In its simplest form, the traveling-wave pump consists of a tube that fits inside a long solenoid (Fig. 1). The upstream end of the solenoid is connected electrically to an alternating

current oscillator. The downstream end of the solenoid is terminated in its characteristic impedance. Each time that a current pulse is admitted to the coil it travels to the downstream end of the coil. This current pulse sets up a radial magnetic field and a longitudinal magnetic field. As these magnetic fields move down the tube they induce or, more precisely, they are accompanied by an azimuthal electric field. If the magnetic Reynolds number is small, as it is in the type of machine we are discussing, then an azimuthal current distribution is formed in the conducting gas in response to the electric field. The current is larger when the electrical conductivity is larger. This current distribution interacts with the radial magnetic field and causes a volume force that tends to push the gas in the direction of the traveling current pulse. Each current pulse that travels down the coil tends to push the fluid in the same way. Consequently directed energy is added to the gas. As predicted by the second law of thermodynamics, this process is not fully efficient because entropy is generated by the so-called I^2R losses in the gas. Thus, the gas comes out at a higher temperature than it had when it entered. While part of this added enthalpy might in some cases be recovered, less directed energy is added to the stream than would be added in a more perfect situation.

The statement that the operation is being carried out at low magnetic Reynolds number warrants additional discussion. It has been shown that the ability of a magnetic field to diffuse into a medium of any kind is dependent upon its electrical conductivity and its magnetic permeability (3). The rate of diffusion of magnetic field lines is inversely proportional to the product of the conductivity and the permeability. That is, the magnetic field enters a poor conductor more readily than a good conductor when their permeability is the same. Since the magnetic Reynolds number is proportional to the product of electrical conductivity and permeability, it follows that in magnetohydrodynamic processes that are characterized by a low magnetic Reynolds number, it is quite easy to get the exciting magnetic fields into the gas. The electric fields that are set up in these plasmas can be calculated by Maxwell's laws. The internal current distribution follows from the conductivity and the electric field. Thus, the process is similar, conceptually, to dragging a screen of variable solidity down the tube. The viscous forces that accompany the motion of the screen correspond to the body force resulting from interaction of the current

¹ Presented at the ARS 15th Annual Meeting, Washington, D. C., Dec. 5-8, 1960.

² The authors would like to acknowledge the financial assistance that enabled these experiments to be conducted. In addition to the internal sponsorship, the Plasma Research Group of MIT (National Science Foundation sponsored) and the MITRE Corp. have made funds available for this work.

³ Assistant Chief Scientist. Member ARS.

⁴ Research Engineer. Member ARS.

⁵ Numbers in parentheses indicate References at end of paper.

density and the magnetic field. In the case of high magnetic Reynolds number the plasma resists the magnetic field. It tends to be deformed, and in the process being discussed the plasma would become sausage shaped. The high magnetic Reynolds number process tends to be more nearly the systaltic process that is similar to milking a cow.

Now if the gas has some directed velocity, a second electromotive force is induced that tends to oppose the driving force. Consequently the average net force is proportional to the difference between the wave velocity and the gas velocity.

The solenoid feels three losses of energy. In addition to the pumping, energy is extracted by ohmic heating, and also is stored in radial motion. The latter is not used in the process.

In the application to either wind tunnel propulsion or thrust generation it is desirable that the gas velocity be a large fractional part of the line speed. Hence, it would be desirable to make the wave speed increase along the length of the tube.

The effectiveness of the coupling between the electromagnetic process and the gas can be described in terms of several dimensionless parameters. Consider first the ratio of the magnetic pressure $B^2/2\mu$ to the dynamic pressure $\frac{1}{2}\rho v^2$. For a primary magnetic field strength of 100 gauss the magnetic pressure is 40 newtons per square meter or 0.0058 psia. If the pump is running at a static pressure of 0.05 psia and at sonic speed, then the dynamic pressure is approximately 0.042 psia for helium. Consequently the ratio of magnetic pressure to the dynamic pressure indicates that a weak interaction is possible.

A second parameter is the magnetic Reynolds number $R_m = \mu\sigma v l$. This parameter also is a measure of the size of the induced fields, and consequently the "back emf," to use the terminology of the electric motor engineers. At large R_m the forces are large with very little slip; at small values of R_m the actual force is small even if the slip is large. In the latter case it is very difficult to build up any currents in the gas. For a tube two meters long the magnetic Reynolds number (in MKS units) is $R_m \cong 25 \times 10^{-7} \sigma v$. The electrical conductivity σ can vary from 0.1 to 100 mhos per meter depending upon the temperature and pressure. When $\sigma \sim 10$ mhos per meter and v is 6000 m/sec, i.e., sonic speed, the value of R_m is about 0.3. If the velocity is 90% of the line speed (for the line to be discussed below) or 27×10^3 m/sec, then at the conductivity used before, R_m is 1.35. In this midrange of R_m it is difficult to find any good approximate analytical solutions. If it is assumed that the magnetic field propagates at a speed c , then an elementary calculation gives the applied body force components (c.f. the Appendix), namely:

Radial Body Force F_r

$$F_r = \sigma(\mu NI)^2 \{ I_0(kr) I_1(kr) (c - v_z) \cos k(z - ct) \sin k(z - ct) + I_0^2(kr) v_r \cos^2 k(z - ct) \}$$

Longitudinal Body Force F_z

$$F_z = \sigma(\mu NI)^2 \{ I_1^2(kr) (c - v_z) \sin^2 k(z - ct) + I_1(kr) I_0(kr) v_r \sin k(z - ct) \cos k(z - ct) \}$$

The average accelerating force

$$\frac{1}{\pi r^2} \int_0^r F_z r dr$$

divided by $\sigma(\mu NI)^2$ is given in Fig. 2. It illustrates the desirability of increasing the outer radius R using an annular configuration. Since the axial force is proportional to the square of $I_1(kr)$, it is clear that an annular configuration is more practical than a hollow cylindrical tube. This concentric configuration is not a handicap for thrust generators, but does not seem practical for wind tunnel propulsion. Alternately, it is possible to use a polyphase system which is

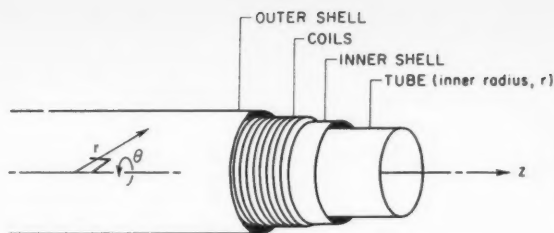


Fig. 1 Analytical model of traveling-wave pump

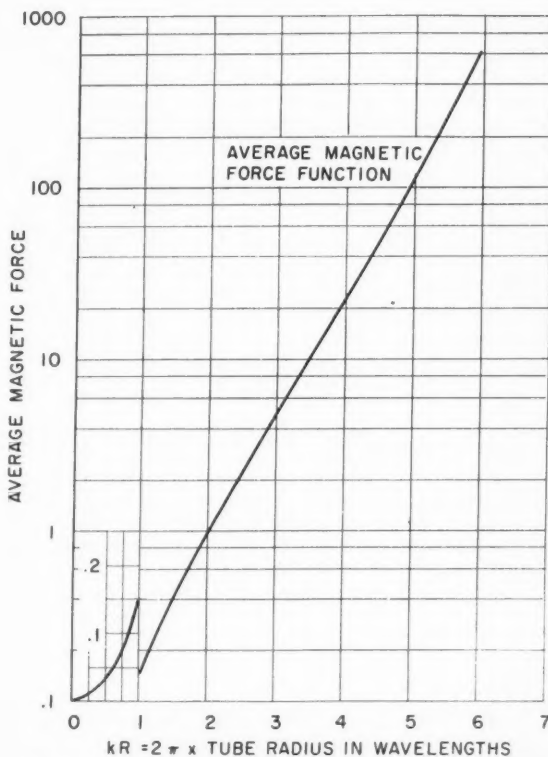


Fig. 2 Average accelerating function as a function of kR

simpler externally, but its interaction with the flow is quite complicated.

The relative effectiveness by which the power is fed into the gas may be approximated from a simple energy balance, and by use of the imaginary part of the propagation constant calculated in the Appendix. After use of the small R approximation and integration over the area, the rate of power attenuation from the driving coil is, if Z_0 is the coil impedance, approximately

$$1 - e^{-\beta z}$$

where

$$\beta = \frac{1}{16} \sigma R^4 (\mu N)^2 \frac{c^2 k^2 \pi}{Z_0} \left(1 - \frac{v_z}{c} \right)$$

Prototype Apparatus

A system has been constructed (Fig. 3) and consists of three units: the plasma source, the nozzle, and the traveling-

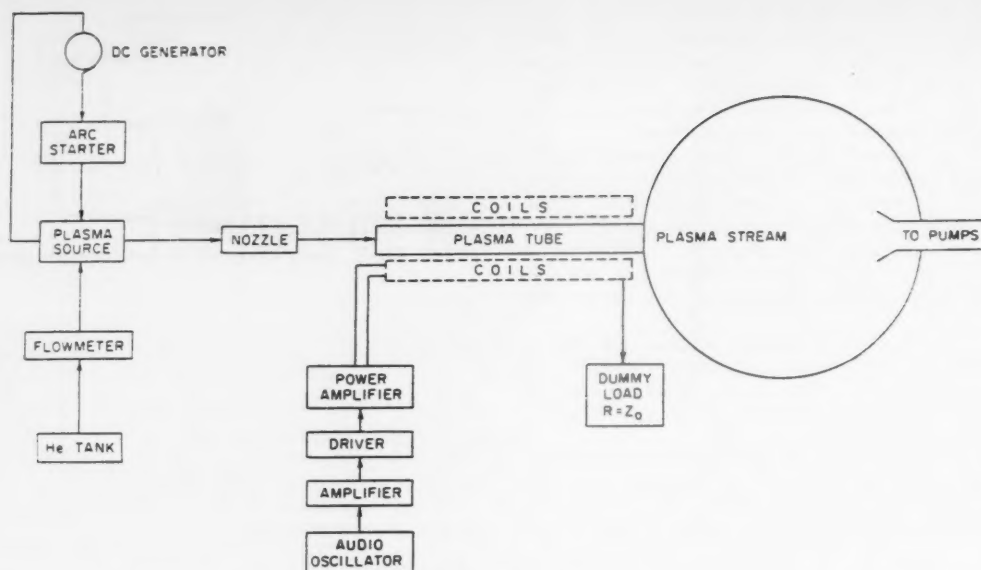


Fig. 3 Sketch of plasma pump

wave pump TWP that are connected with the vacuum system. The development of each of these components is discussed in turn.

Applying the first law to the energy addition in the traveling-wave pump, the power added by the pump must equal the increase in kinetic energy of the stream plus the heating of the stream.

Considering first the pumping only, if h denotes enthalpy

$$h_0 = h + \frac{v^2}{2g_0}$$

Assuming inlet velocity negligible

$$\Delta h_{\text{pump}} = \frac{\Delta v^2}{2g_0}$$

For $v = 10^5$ fps and $m = 10^{-4}$ lbm/sec

$$P_{\text{pump}} = 22 \text{ kw}$$

If a pumping efficiency of 50% could be maintained, 44 kw of RF power would be required. A velocity of 10^4 fps would require about 7 kw at 50% efficiency, or 21 kw at 15% efficiency.

The design conditions for the coil were

Number of layers ^a	$c(\text{fps} \times 10^{-4})$	Z_0, ohm	$f(\lambda = 2 \text{ ft}) \text{ kc}$
2	16.4	1500	82
6	7.35	688	36.7
8	6.2	581	31
10	5.46	513	27.6

The tests on the components of the pilot facility indicated that the individual parts tended to perform well although the line speed was several times higher than expected.

Plasma Source

The basic plasma source (4) was modified to ensure satisfactory operation at high current levels. The anode was designed with a replaceable copper nozzle insert and a water

^a Alternate layers in parallel.

jacket which utilized a vortex to create uniform high tangential velocity, and a 180° turn in the radial velocity to provide a pressure gradient at the wall of the nozzle throat favorable to nucleate boiling heat transfer. It was found that nozzle life could be increased greatly by placing a five-turn coil of $\frac{3}{16}$ copper tubing around the plasma source to supply an axial magnetic field as described by Shepard and Boldman (5) of Lewis Laboratory. The axial field interacts with the radial component of the arc current at the anode spot on the nozzle surface to produce a rotation of the spot about the nozzle axis, thus spreading the heat transfer over a wider area and creating uniform wear.

Arc Starter

In order to break down the initial gap between the electrodes and start the d-c arc, a high frequency high voltage generating device was constructed. The high frequency arc starter utilizes an 861 power tetrode in a Hartley oscillator circuit with a high L/C ratio self-resonant coil and auto-transformer to match the high impedance starting load (6).

The auto-transformer configuration in the output circuit was found to be best suited for the changing load conditions. The tank-coil auto-transformer unit was wound of half inch copper tubing and was water cooled. Teflon tape was used to provide low loss turn to turn insulation.

Supersonic Nozzle

Efficient pumping (high ratio of pumping power to heating power) requires a gas velocity comparable to the traveling-wave speed. The wave speed of the line was measured and found to be 10^5 fps. Hence, supersonic velocity would be desirable at the entrance to the traveling-wave pump. The converging copper nozzle of the plasma source was therefore mounted to a separate diverging section. A quartz nozzle and cooling jacket were designed and purchased. The performance of the quartz nozzle has been satisfactory. Replaceable throat inserts of boron nitride and tungsten have been incorporated in the nozzle design to permit area ratio changes.

Traveling-Wave Coils

The traveling-wave coils were wound with ten layers around an ID of $4\frac{3}{16}$ in.

Consider a line composed of two layers wound in opposite directions as shown in Fig. 4. The advantages of this type of line are: the losses are low because the inductance and capacitance are truly distributed—inductance, capacitance, and resistance per unit length can be chosen independently; the oppositely wound construction permits use of twice as many turns as with a single layer coil while maintaining low losses, thus making possible low values for c ; the spacings b and a can be varied easily with length to obtain higher c while maintaining Z_0 constant, thus permitting the construction of an accelerating line; the increased number of turns makes possible greater traveling B fields from given current in the line.

For any transmission line (7)

$$Z_0 = \frac{L}{C} \times \sqrt{\frac{1 - jR_c/\omega L}{1 - jG/\omega C}}$$

c = propagation velocity = $f\lambda$

$$c = \omega \left\{ \frac{\omega C}{2} \times \left[\sqrt{(R_c + \omega^2 L^2) \left\{ \left(\frac{G}{\omega C} \right)^2 + 1 \right\}} - R_c \frac{G}{\omega C} + \omega L \right] \right\}^{-1/2}$$

The inductance per unit length is $\mu(\pi/4)D^2N^2$ (henries/m) if the two windings are driven 180° out of phase; i.e., the two windings form a balanced line.

The capacitance per unit length can be estimated by considering the turns in adjacent layers as parallel connected, parallel wire capacitors of length πD so

$$C(\text{farads/m}) = \frac{\epsilon\pi^2 D}{(d+b) \cosh^{-1} \frac{a+d}{d}}$$

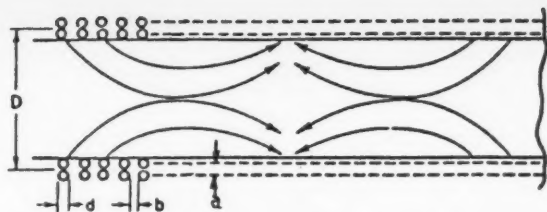


Fig. 4 Line composed of two layers wound in opposite directions

where ϵ is the constant of the dielectric separating the layers.

The cooling water requirement for the total winding length of 6 ft was satisfied by making six 1-ft coils which had an average tube length per layer of 285 ft. The coils were wound with 0.063×0.041 copper tubing which had been insulated with teflon tape 0.001 in. thick. The final coated tubing was coiled at 186 turns per one-foot layer. The insulation between layers consisted of 0.020 in. teflon tape with 1 in. overlap, and the ends of the coils were potted with paraffin wax to suppress arcing across the ends of this tape. Assembly of three coils is shown in Fig. 5.

The heat transfer and pressure gradient along capillary tubes can be calculated from the laminar flow equation given by McAdams (8).

At 700 psi the capability is 890 w per layer with 160° rise, thus permitting operation at a Q of over 50.

Measurement of Coil Characteristics

The line speed was measured originally by applying a periodic pulse input to a terminated section of coil and observing the resulting "echo" with an oscilloscope. By varying the terminating resistance, the characteristic impedance could be determined as the resistance for most rapid damping.

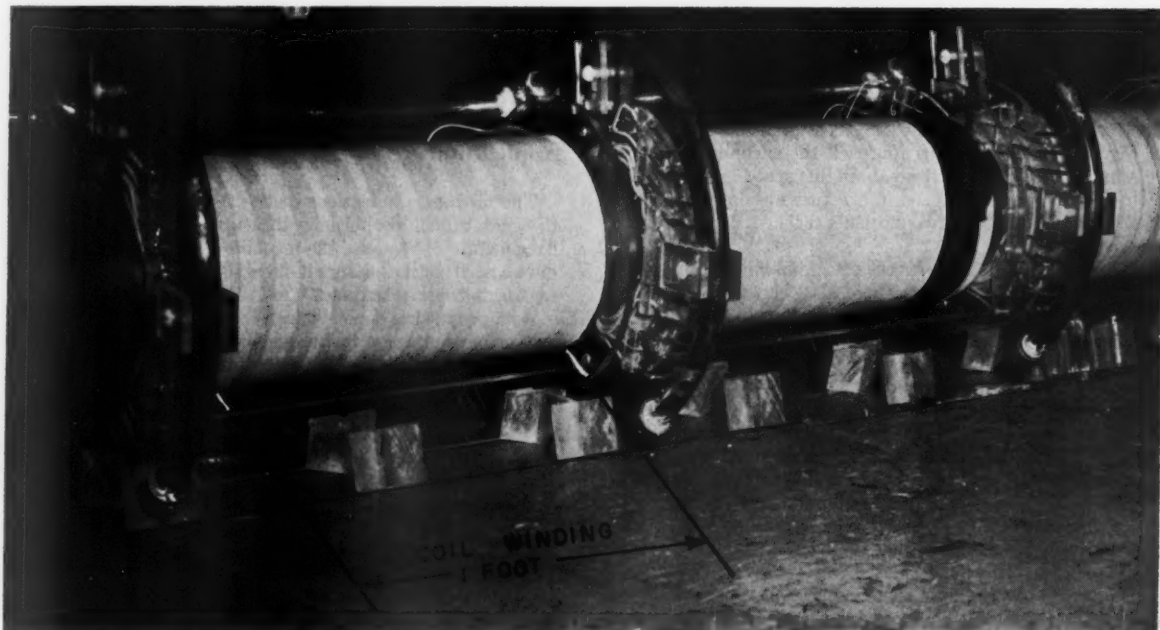


Fig. 5 Three coil assembly

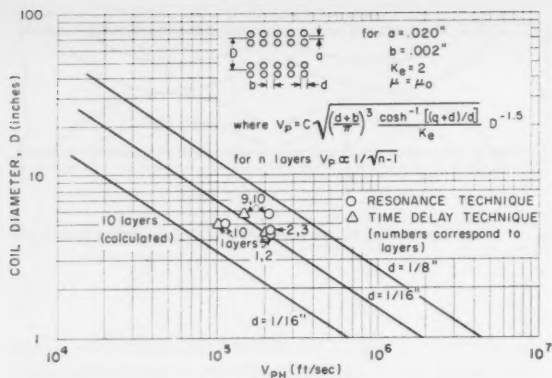


Fig. 6 Phase velocity vs. coil diameter, two layer line

The results of these measurements are plotted in Fig. 6 as circles. The characteristic impedance was observed to be $500 \text{ ohm} \pm 100 \text{ ohm}$, the minimum echo point being very broad. The above measurements were considered to be only qualitative because of the indeterminate effects of the circuit elements in the pulse generator upon the ringing frequency of the line segment.

Also, at low signal levels it was suspected that the observed reflections were being carried by the fastest two layers (layers 1 and 2) through interlayer coupling. This coupling gave the effect of all the layers being as fast as the fastest layer and greatly decreased the speed change as more layers were added in parallel.

In order to refine the above measurements, a 2-ft length of coil was terminated in a 500 ohm resistive load (carbon resistors), and about 20 w of 25-kc power was fed into the line. The voltages at the line input and at the terminating load were displayed on a dual beam oscilloscope, and the time delay across the line was thus measured. The frequency spectrum was swept from 100 cps up to 50 kc to determine if the phase shift was more than one cycle. The time delay was 10 microsec/ft at 25 kc with slight increase with frequency; a maximum to about 12 microsec/ft being found at about 40 kc. These measurements seem much more reliable because the line was actually transmitting power, more nearly simulating operating conditions. The termination load also insured that reflected signals be very much smaller than the transmitted wave. These results are plotted as triangles in Fig. 6 and more closely approach the theoretical values. It is to be noted that the decrease in line speed by paralleling many layers was not realized in practice, although the speed of a double layer counterwound helix reached the theoretical line speed exactly.

The characteristic impedances of a four-coil section of line and six-coil section were measured at 25 kc with a Z angle meter. For four coils, Z_0 was found to be 430 ohm at -1° and for six coils to be 480 ohm at -2.5° . When terminated by 400-ohm resistive load, the four-coil line measured 450 ohm at $\pm 1^\circ$, and when terminated by 525 ohm, the six-coil line measured 450 ohms $\pm 1^\circ$. These results seem in good agreement with the theoretical value of 500 ohm in view of the difficulties inherent in standing wave and impedance measurements.

For the 525-ohm load, two radio frequency amperes at 25 kc were loaded into the line. The standing wave ratio on the line was measured with a dual beam oscilloscope and found to be less than 1.1.

The field strength inside the tube has been measured by a small coil. The results indicate that the magnetic field within the tube, except near the ends of the tube, agrees with the calculated field strengths.

Radio Frequency Supply

The RF supply for the traveling-wave pump was constructed by modifying a Thermionic induction heater to operate over a frequency range well below its design frequency of 400 kc. A resonant plate circuit was designed for frequencies from 25 to 85 kc. The design conditions were found by the approximate method for Class C amplifiers (9).

Probes and Measurement of Properties

Aside from measurement of mass flow and electrical power to the plasma jet and static pressures at various points in the system, measurements of properties are very difficult.

A total pressure probe was constructed having a large inlet size to ensure that thermal creep (10) was unimportant.

Presently, Mach number is determined from the Rayleigh pitot formula, and temperatures from the estimated enthalpy. The value of the speed of sound can then be found, and hence the velocity. In making the calculations it is assumed that the static pressure is constant across the jet and equal to the tank pressure.

The properties of the plasma jet have been measured by means of an enthalpy balance and by a Langmuir probe. There is a qualitative agreement; i.e., the electron temperature is compatible with the estimated enthalpy of the gas. The Langmuir probe is very difficult to use near the arc due to fluctuation. At lower pressures the electron temperature tends to exceed the gas temperature. This observation is in accordance with other data (11,12).

For the experimental conditions the pressure is not low enough so that the electrons can have much more than twice the gas energy; hence the departures from equilibrium are not beneficial.

A typical set of measurements of the system is given in Table 1.

If the flow is subsonic, the velocity is about one sixth the line speed. Consequently, the gas tends to be heated more than pumped (Table 1). The experimental results indicate the exit Mach number is decreased by about 0.1 due to heat addition. The results indicate that the reduction in total head that would be expected in heating is not measured. Consequently it is inferred that some kinetic energy is added.

The heating of the gas also indicates a coupling. The high line speed causes inefficient pumping due to excessive slip between wave velocity and gas velocity.

Applications

The obvious applications of the traveling-wave pump are to wind tunnel propulsion, thrust generation, and energy conversion. The use of the machine as an energy conversion device is attractive because it offers the possibilities of generating an alternating current.

As a propulsion device, it can be shown that if the flow is fully expanded, then the increase in thrust due to pumping is just equal to the increase in thrust due to addition of energy. That is, if the chemical energy is $\Delta\epsilon_a$, the thrust due to this energy addition (M slug/sec of gas)

$$F = M\sqrt{2\Delta\epsilon_a}$$

and if an energy $\Delta\epsilon_p$ is added by pumping

$$F = M\sqrt{2(\Delta\epsilon_a + \Delta\epsilon_p)}$$

The amount of thrust that can be obtained is large. However, the weight of the equipment required to generate this power is of the order of the thrust, if one talks in thousands of pounds.

Table 1 Experimental Data

Run	d-c stage		RF stage			Gas	Gas properties			Mach number
	Volts	Amps	Volts	Amps	Frequency		p_0 , psia	p_s , psia	\dot{m} lbm $\times 10^{-3}$	
10/20-1	150	100	helium	0.11	0.05	0.074	1.05
10/20-2	120	130	helium	0.17	0.07	0.130	1.15
10/20-3	155	125	helium	0.16	0.08	0.120	0.945
10/20-4	150	120	760	3.1	44 kc	helium	0.15	0.08	0.116	0.90
10/20-5	150	120	helium	0.15	0.07	0.116	1.05

Conclusions

It may be concluded that a weak interaction can give rise to a measureable coupling between the gas and the magnetic field. While data on this device are very sparse, the results indicate that the application is not impractical, even though good performance lies in the future.

Appendix: Analysis

As a first approximation consider a circular tube that is infinitely long. The magnetic field results from a coil symmetric with the tube. The following primary assumptions were made: (a) approximate electrical neutrality; (b) the magnetic Reynolds number $\sigma\mu v l$ will be small; (c) material properties are constant; and (d) polarization, displacement currents, and Lorentz currents will be neglected.

The electrodynamic equations, in the magnetohydrodynamic approximation are

$$\text{curl } \vec{E} = -\frac{\partial \vec{B}}{\partial t} \quad [\text{A-1}]$$

$$\text{curl } \vec{H} = \vec{j} \quad [\text{A-2}]$$

$$\text{div } \vec{B} = 0 \quad [\text{A-3}]$$

$$\text{div } \vec{j} = 0 \quad [\text{A-4}]$$

The boundary conditions will be set forth below.

Eq. A-3 can be satisfied identically if \vec{B} is derived from a vector potential \vec{A} ; i.e.

$$\vec{B} = \text{curl } \vec{A} \quad [\text{A-5}]$$

By substitution of Eq. A-5 into Eq. A-1 and integrating the curl it can be shown that

$$\vec{E} = -\frac{\partial \vec{A}}{\partial t} - \nabla \phi \quad [\text{A-6}]$$

The last term on the right-hand side is the emf due to a potential which is externally applied, or is the consequence of Eq. A-4, or results from the boundary conditions.

The Ohm law in the fluid takes the form

$$\vec{j} = \sigma[\vec{E} + \vec{v} \times \vec{B}] \quad [\text{A-7}]$$

Eqs. A-5, A-6, and A-7 may be substituted into Eq. A-2 and after using the constitutive equation $\vec{B} = \mu\vec{H}$, the basic equation for \vec{A} takes the form for the fluid

$$\text{curl curl } \vec{A} = \sigma\mu \left[-\frac{\partial \vec{A}}{\partial t} - \nabla \phi + \vec{v} \times \text{curl } \vec{A} \right] \quad [\text{A-8}]$$

and outside the fluid and tube the governing equation is

$$\text{curl curl } \vec{A} = 0 \quad [\text{A-9}]$$

The solutions inside and outside the coil are related by

$$\hat{a}_r \cdot [\vec{B}_0 - \vec{B}_i] = 0 \quad [\text{A-10a}]$$

and, assuming a traveling current sheet, $J_0 \exp[i(kz - \omega t)]\hat{a}_\theta$ of thickness δ acting in the coil

$$\hat{a}_r \times [\vec{B}_0 - \vec{B}_i] = \mu\delta J_0 \exp[i(kz - \omega t)]\hat{a}_\theta \quad [\text{A-10b}]$$

The first condition is that the normal component of \vec{B} is continuous across the boundary, and the second condition relates the change in tangential \vec{B} to the current flux in the sheet. Since the walls are assumed to be nonconducting, the boundary condition is, neglecting space charge

$$\hat{a}_r \cdot [\vec{E}_0 - \vec{E}_i] = 0 \quad [\text{A-11a}]$$

$$\hat{a}_r \times [\vec{E}_0 - \vec{E}_i] = 0 \quad [\text{A-11b}]$$

and

$$\vec{E}_0 \equiv 0$$

It is assumed that a traveling wave is excited in the tube; hence the time part of \vec{A} has the form $\exp[i(kz - \omega t)]$. Here ω is the applied frequency and k is the propagation constant. If the \vec{B} field has azimuthal symmetry, which is common at low frequencies, the vector potential takes the form, if \hat{a}_θ is a unit azimuthal vector

$$\vec{A} = A_\theta(r) \exp[i(kz - \omega t)]\hat{a}_\theta \quad [\text{A-12}]$$

and so

$$\text{curl } \vec{A} = \left(-ikA_\theta \hat{a}_r + \frac{1}{r} \frac{\partial}{\partial r} rA_\theta \hat{a}_z \right) \exp[i(kz - \omega t)] \quad [\text{A-13}]$$

As long as the velocity is primarily axial, i.e., $\vec{v} = v(r,z)\hat{a}_z$, the $\vec{v} \times \vec{B}$ term in Eq. A-8 is $-ikvA_\theta \exp[i(kz - \omega t)]\hat{a}_\theta$. Further it will be noted that the left-hand side of Eq. A-8 can be written as $(-\nabla^2 + (1/2))\vec{A}$. This suggests that inside the tube A_θ has the form $I_1(\kappa r)$, where κ is a complex constant, and I_1 is the Bessel function of the first kind with an imaginary argument. These comments and Eq. A-13 lead to the form

$$(-\kappa^2 + k^2)C_1 I_1(\kappa r) \exp[i(kz - \omega t)] = \sigma\mu \left\{ i\omega - \frac{\nabla \phi_0 \hat{a}_\theta}{C_1 I_1(\kappa r) \exp[i(kz - \omega t)]} - ikv \right\} C_1 I_1(\kappa r) \exp[i(kz - \omega t)] \quad [\text{A-14}]$$

Outside the coil the solution takes the form

$$(-\kappa^2 + k^2)C_2 K_1(\kappa r) \exp[i(kz - \omega t)] = 0 \quad [\text{A-15}]$$

Here the solution requires that $\kappa = k$; the function K_1 is the Bessel function of the second kind with imaginary argument. This function satisfies the conditions that the wave vanish as $r \rightarrow \infty$ and shows that outside the tube $\kappa = k =$

ω/c . The parameter c is the propagation speed of the wave along the line. This solution is a "quasi-steady" approximation and is valid whenever $(c^2/\epsilon_0\mu) \ll 1$, ϵ_0 being the permittivity of free space.

The propagation constant κ in the tube can be computed from Eq. A-14 after the value of $\nabla\phi$ is computed. By use of Eqs. A-4, A-6 and A-7

$$\text{div } \vec{j} = \text{div } [\vec{E} + \vec{v} \times \vec{B}] = \text{div} \left[-\frac{\partial \vec{A}}{\partial t} - \nabla\phi + \vec{v} \times \vec{B} \right] \quad [\text{A-16}]$$

Hence ϕ is the solution of

$$\nabla^2\phi = -\frac{\partial}{\partial t} \text{div } \vec{A} + \vec{B} \cdot \text{curl } \vec{v} - \vec{v} \cdot \text{curl } \vec{A} \quad [\text{A-17}]$$

or since $\vec{B} \cdot \text{curl } \vec{v} \equiv 0$

$$\nabla^2\phi = \left(i\omega A_\theta + \frac{v}{r} \frac{\partial}{\partial r} r A_\theta \right) \exp [i(kz - \omega t)] \quad [\text{A-18}]$$

so $\nabla\phi$ has only radial and axial components; thus $\vec{\nabla}\phi \cdot \hat{a}_\theta = 0$. So the equation for κ is the solution of, if v is a slowly varying function of r

$$k^2 + \sigma\mu\{ikv\} - \kappa^2 - i\sigma\mu\omega = 0 \quad [\text{A-19}]$$

or^a

$$\kappa = \pm \sqrt{k^2 + i\sigma\mu k(v - c)} \quad [\text{A-20a}]$$

and if $\sigma\mu v$ is small

$$\kappa \sim \pm \left[k + i\frac{\sigma\mu}{2}(v - c) \right] \quad [\text{A-20b}]$$

where $k = \omega/c$ as before. The approximation

$$\kappa = \frac{\omega}{c} + i\frac{\sigma\mu}{2}(v - c) \quad [\text{A-21}]$$

corresponds to the wave propagating in the z direction. The imaginary part of κ represents the power taken from the magnetic field and fed into the gas at the point where the velocity is v .

The boundary conditions allow the values of the constants C_1 and C_2 to be calculated. Finally, then, inside the tube of radius R

$$\vec{A}_1 = \frac{\mu NI}{\kappa(R)} \frac{K_1(\kappa R) I_1(\kappa r) \exp [i(kz - \omega t) \hat{a}_\theta]}{[I_0(\kappa R) K_1(\kappa R) - K_0(\kappa R) I_1(\kappa R)] \left(1 + i\frac{\sigma\mu R}{2} \right)} \quad [\text{A-22a}]$$

$$\vec{A}_0 = \frac{\mu NI}{\kappa(R)} \frac{I_1(\kappa R) K_1(\kappa r) \exp [i(kz - \omega t) \hat{a}_\theta]}{[I_0(\kappa R) K_1(\kappa R) - K_0(\kappa R) I_1(\kappa R)] \left(1 + i\frac{\sigma\mu R}{2\kappa(R)} \frac{\partial v}{\partial r} \right)_{r=R}} \quad [\text{A-22b}]$$

where NI is the rms ampere turns per unit length.

The next step is to calculate the impedance. It is assumed, the coil alone has a known impedance Z_0 , which can be calculated from its geometry. The induced emf, inside the tube is

$$\vec{E}_{\text{ind}} = -\text{real part } \frac{\partial \vec{A}}{\partial t} \quad [\text{A-23}]$$

^a A better approximation to κ is $\kappa = \pm \int_0^r \sqrt{k^2 + i\sigma\mu k(v - c)} dr$.

$$\vec{E}_{\text{ind}} = \frac{\mu NI}{\kappa(R)} \frac{K_1(\kappa R) I_1(\kappa r) \omega \sin (kz - \omega t)}{[I_0(\kappa R) K_1(\kappa R) - K_0(\kappa R) I_1(\kappa R)] \left(1 + i\frac{\sigma\mu R}{2} \right)} \quad [\text{A-24}]$$

The impedance of the tube and plasma

$$Z = Z_0 - c\mu N \frac{2\pi K_1(\kappa R) \int_0^R I_1(\kappa r) r dr}{[I_0(\kappa R) K_1(\kappa R) - K_0(\kappa R) I_1(\kappa R)] \left(1 + i\frac{\sigma\mu R}{2} \right)} \quad [\text{A-25}]$$

The second complex term in the right-hand side is the change in the impedance due to the plasma in the tube. The impedance of the tube and plasma can be approximated easily in two cases

Case 1

$$Z \rightarrow Z_0 - \frac{\pi\mu c N \kappa R^2}{\left(1 + i\frac{\sigma\mu R}{2} \right) (2 - (\kappa R)^2 \ln \kappa R)} \quad \kappa R \ll 1 \quad [\text{A-26}]$$

Case 2

$$Z \rightarrow Z_0 + \frac{2\pi\mu\kappa c N}{1 + i\frac{\sigma\mu R}{2}} \quad \kappa R \gg 1 \quad [\text{A-27}]$$

where

$$\kappa \simeq \frac{\omega}{c} + i\frac{\sigma\mu}{2}(u - c) \quad [\text{A-28}]$$

The factor $u \sim$ average velocity can be included to show its effect on κ . Note in case 1 the effect of the plasma is to increase the inductive load. As the size of the tube is increased, the plasma begins to act in a more complicated way and for large tubes (case 2) the behavior is definitely capacitive.

The force acting in the plasma is given by $\vec{j} \times \vec{B}$. Note that in carrying out the calculation, one must use the real part of \vec{j} and \vec{B} . The axial force is calculated from the axial part of $\text{Re}(\vec{j}) \times \text{Re}(\vec{B})$ in terms of a characteristic constant C_3

$$C_3 = \left[\frac{\mu N I K_1(\kappa R)}{[I_0(\kappa R) K_1(\kappa R) - I_1(\kappa R) K_0(\kappa R)] \left(1 + i\frac{\sigma\mu R}{2} \right)} \right] \quad [\text{A-29}]$$

When

$$\frac{\sigma\mu}{2k}(c - v) \ll 1 \quad [\text{A-30}]$$

$$C_3(\kappa R) \simeq C_3(kR) \quad [\text{A-31}]$$

and the axial force is

$$\sigma\mu C_3^2 I_1^2(\kappa r) (c - v) \sin^2 (kz - \omega t) \quad [\text{A-32}]$$

The longitudinal momentum equation is

$$\rho \left(\frac{\partial v}{\partial t} + v \frac{\partial v}{\partial z} \right) = -\frac{\partial p}{\partial z} + \eta \left(\frac{\partial^2 v}{\partial r^2} + \frac{1}{r} \frac{\partial v}{\partial r} + \frac{\partial^2 v}{\partial z^2} \right) + \sigma\mu C_3^2 I_1^2(\kappa r) (c - v) \sin^2 (kz - \omega t) \quad [\text{A-33}]$$

For a relative performance calculation denote the average magnetic field speed as v_m and the field weighted average gas speed as \bar{v} , then the fraction of energy absorbed by the gas that is used for pumping is \bar{v}/v_m and the rest goes into heating the gas; this is just $(1 - \bar{v}/v_m)$. Further, the ability

of the gas to absorb energy, per unit length, is given in terms of a parameter β that is defined as

$$\beta = \frac{\sigma R^4 (\mu N)^2 \omega^2 \pi}{16 Z_0} \left(1 - \frac{\bar{v}}{v_m}\right) = \kappa_0 \left(1 - \frac{\bar{v}}{v_m}\right) \quad [\text{A-34}]$$

The fraction of the power in the traveling-wave line that goes into the gas is $[1 - \exp(-\beta z)]$. The pumping power is

$$P_P = P_T \cdot \left(\frac{\bar{v}}{v_m}\right) \cdot (1 - \exp[-\kappa_0(1 - \bar{v}/v_m)z]) \quad [\text{A-35}]$$

It is clear that some sort of optimum exists, for the power input factor approaches zero when there is no slip. If the pumping power is considered as a function of \bar{v}/v_m , then there is an optimum value of κ for each value of \bar{v}/v_m . In general \bar{v}/v_m satisfies the equation

$$1 + \kappa_0 \frac{\bar{v}}{v_m} = \exp[\kappa_0(1 - \bar{v}/v_m)] \quad [\text{A-36}]$$

This equation has a root of $\bar{v}/v_m = 0.57$ when κ_0 is unity and has the limiting forms for the roots

$$\frac{\bar{v}}{v_m} \sim \frac{1}{2} + \frac{\kappa_0}{8} \quad [\text{A-37}]$$

as $\kappa_0 \rightarrow 0$ and

$$\bar{v}/v_m \sim 1 - \frac{\ln \kappa_0}{\kappa_0}$$

as $\kappa \rightarrow \infty$. This function is plotted in Fig. 7.

The simple analysis indicates that for the most pumping the parameter β should be large, the optimum value of β being $\ln \kappa_0$. An examination of the terms that make up κ_0 leads one to conclude that for fixed geometry it is desirable to have the highest possible electrical conductivity. Alternately the product $(N\omega)^2/Z_0$ may be maximized. These terms are related to a particular geometry. In considering any particular geometry the ratio of the ohmic power losses in the gas to those in the coil becomes important, and if κ_0 is made large by increasing σ , the ohmic losses in the gas approach the losses in the line. It should be noted that it is not always desirable to have the value of κ_0 too large because a very large κ_0 implies that the magnetic field cannot penetrate too deeply into the plasma, but rather the plasma is mostly shoved out of the way; at the end of the pumping coil the part of the plasma which the field has penetrated experiences difficulties in escaping from the field.

Nomenclature

\vec{A}	= vector potential
a	= layer to layer separation
\vec{B}	= magnetic flux density (induction) vector
b	= turn to turn axial separation
C	= capacitance or capacitance per unit length
C_1, C_2, C_3	= constants defined in the text
c	= wave speed = phase velocity of transmission line
D	= mean coil diameter
d	= conductor outside diameter
\vec{E}	= electric field
\vec{F}	= force per unit volume
f	= frequency
G	= conductance per unit length of pumping coil (transmission line)
g_0	= acceleration due to gravity
\vec{H}	= magnetic field intensity
h	= enthalpy
h_0	= stagnation enthalpy
I	= electric current in coil
I_n	= Bessel function of first kind of n th order with imaginary argument
i	= $\sqrt{-1}$
\vec{j}	= current density

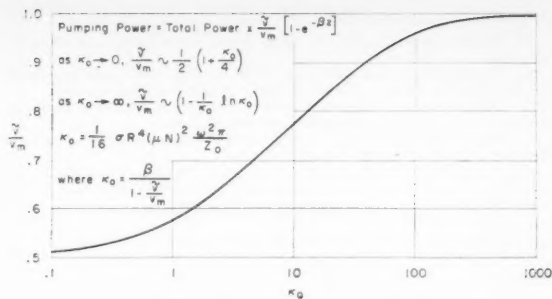


Fig. 7 Curve of best $\frac{\bar{v}}{v_m}$ for pumping at fixed κ_0

K_n	= Bessel function of the second kind of n th order with imaginary argument
k	= real propagation constant in the coil = $\omega/c = 2\pi/\lambda$ (k is assumed z only, wave propagating in z direction)
L	= inductance or inductance per unit length
\dot{m}	= mass flow rate
N	= coil winding turns per unit length
P	= power
P_P	= pumping power per unit volume ($\vec{F} \cdot \vec{v}$)
P_T	= total power per unit volume (pumping and heating, $\vec{F} \cdot \vec{v} + (j^2/\sigma)$)
p	= fluid pressure
p_0	= total pressure
p_s	= static pressure
Q	= resonant system quality factor = $\frac{2\pi \text{ energy stored per cycle}}{\text{energy dissipated (per cycle)}}$
R	= outer radius of anulus or pipe radius or electrical resistance
R_c	= resistance per unit length of coil
R_m	= magnetic Reynolds number = $\mu \sigma l v$
\vec{v}	= velocity vector
\bar{v}	= field weighted average fluid velocity
v_m	= average magnetic field speed; for coil only $v_m = c$
Z_0	= characteristic impedance of pumping coil (transmission line)
β	= attenuation constant of pumping coil; transmission line = $\kappa_0(1 - (\bar{v}/v_m))$
ϵ	= permittivity
ϵ_0	= permittivity of vacuum
η	= fluid viscosity
κ	= complex propagation constant in the plasma defined in text
κ_0	= $\frac{\sigma R^4 (\mu N)^2 \omega^2 \pi}{16 Z_0}$
λ	= wavelength
μ	= magnetic permeability
μ_0	= magnetic permeability of vacuum
ρ	= fluid density
σ	= electrical conductivity
ϕ	= scalar electric potential
ϕ_0	= potential outside coil
ϕ_i	= potential inside coil
ω	= angular frequency

Vectors and Coordinates

r, θ, z	= cylindrical coordinates (z distance along tube axis)
$\hat{a}_r, \hat{a}_\theta, \hat{a}_z$	= unit vectors
\vec{X}	= vector quantity X
X	= magnitude of $\vec{X} = \sqrt{X_r^2 + X_\theta^2 + X_z^2}$

References

- 1 Bishop, A. S., *Project Sherwood—The U. S. Program in Controlled Fusion*, Addison-Wesley, 1958, p. 46.
- 2 Thonemann, P. C., Cowhig, W. T. and Davenport, P. A., "Interaction of Traveling-Magnetic Fields with Ionized Gases," *Nature*, vol. 169, 1952, pp. 34-35.

3 Cowling, T. G., *Magnetohydrodynamics*, Interscience Publishers, N. Y., 1957.
 4 Whittenbury, C., The Douglas Aircraft Company, private communication.
 5 Shepard, C. E. and Boldman, D. R., "Preliminary Development of Electrodes for an Electric Arc Wind Tunnel," NASA Memo 4-14-59E.
 6 Radio Corp. of America, *Radiotron Designer's Handbook*, Commercial Engng. Div., RCA, Harrison, New Jersey, 1954.
 7 International Telephone and Telegraph Corp. *Reference Data for Engineers* 4th ed., Stratford Press, N. Y., 1957.

8 McAdams, W. H., *Heat Transmission*, McGraw-Hill, N. Y., 1954.
 9 Editors and Engineers Ltd., *The Radio Handbook*, 14th ed., Summerland, Calif., 1956.
 10 Howard, W. M., "The Effect of Temperature on Pressures Measured in a Hypersonic Wind Tunnel," *JAS*, vol. 26, no. 11, November 1959.
 11 Brown, S. C., *Basic Data of Plasma Physics*, The Technology Press (Massachusetts Institute of Technology) and John Wiley, N. Y. 1959, p. 319.
 12 Delcroix, J. L., *Introduction a la Theorie des Gaz Ionisés*, Dunod, Paris, 1959.

Effect of Glass Fiber Geometry on Composite Material Strength

JAMES E. BELL¹

Boeing Airplane Co.
Seattle, Wash.

This paper reports the results of a study to determine the effect of glass fiber geometry on composite material strength. Equations are derived for the load distribution in a composite material and also for the stress distribution. To determine the effect of fiber geometry, epoxy resin composites are analyzed for composite efficiency. These same composites are analyzed for glass fiber efficiency. The highest composite efficiency determined was 58% for filament wound fibers; and the highest fiber efficiency was 68% for cross laminated fibers. In general, this type of analysis may be useful in evaluating fiber geometries in other composites. No attempt was made here to analyze other systems.

FIBER geometry of a composite material is here defined to include the length and cross-sectional area of the fiber as well as the orientation of the fiber in the matrix. Practically all the fibers presently used have a circular cross section, although there is some interest in drawing more complex shapes such as diamond, cross and star shapes (16).² A preliminary analysis to determine the minimum fiber length required to develop full fiber strength indicated that for current fiber diameters (0.0004 in.) and matrix shear strengths (1000 psi), minimum fiber length is approximately one-quarter inch. The additional peripheral area provided by other cross sections does not appear to be required. Therefore, the analysis of the influence of glass fiber geometry on composite material strength will be confined to a study of the effect of continuous or discontinuous fibers and their orientation in the matrix.

Derivation of Equations

In order to analyze the effect of fiber geometry on composite strength, the fundamental mechanics of composite theory need to be reviewed. Therefore, a relationship will be de-

rived for the load distribution in a composite and the properties of the individual materials. Also a relationship will be derived for the stress in the fiber and the stress in the composite. Outwater (1) and Swica (2) have made similar derivations. The derivations will be based on the following assumptions:

- 1 Stress is proportional to the strain in both materials.
- 2 Both materials are securely bonded together so they are strained an equal amount under load.
- 3 The fibers are straight, continuous and aligned with the axis of the applied load.
- 4 The materials are homogeneous and isotropic.

From assumption 1

$$\sigma = E\epsilon \quad [1]$$

From assumption 2

$$\epsilon_c = \epsilon_f = \epsilon_m \quad [2]$$

Since load is equal to unit stress times area, the load on the fiber is

$$P_f = \sigma_f A_f = E_f \epsilon_c A_f \quad [3]$$

and the load on the matrix is

$$P_m = \sigma_m A_m = E_m \epsilon_c A_m \quad [4]$$

Presented at the ARS 15th Annual Meeting, Washington, D. C., Dec. 5-8, 1960; revision received July 6, 1961.

¹ Structural Development Research Engineer, Aero-Space Div.

² Numbers in parentheses indicate References at end of paper,

The ratio of the load carried by the fibers to the applied load is

$$\frac{P_f}{P_c} = \frac{P_f}{P_f + P_m} \quad [5]$$

Eq. 5 can be written as

$$\frac{P_f}{P_c} = \frac{1}{1 + E_m/E_f (1/A_f - 1)} \quad [6]$$

The ratio of the fiber stress to composite stress can be determined by dividing the fiber and composite loads by their respective areas, thus

$$\frac{\sigma_f}{\sigma_c} = \frac{P_f/A_f}{P_c/A_c} = \frac{1}{A_f + E_m/E_f (1 - A_f)} \quad [7]$$

Therefore, it can be concluded from Eq. 6 that the percentage of the applied load carried by the fiber is a function of the relative moduli of the matrix and fiber, and also a function of the area of fiber resisting the applied load. The same statement is true for the ratio of the stress in the fibers to the stress in the composite. Fig. 1, a plot of Eq. 6, shows the load distribution in the fiber and matrix for different E_m/E_f values and the effect of A_f on composite strength. Fig. 2, a plot of Eq. 7, shows how the stress in the fiber increases as the E_m/E_f decreases and A_f decreases. These plots will be referred to again later in this discussion.

Effects of Fiber Discontinuity and Orientation

The theoretical load distribution between the fiber and the matrix has been shown (Fig. 1) to be a function of modulus and area of the materials. The ability of the matrix and the fiber to transmit an applied load is dependent upon the shear strength, area of the matrix, the bond between the matrix and the fiber, and fiber continuity parallel to the applied load.

Continuous fibers, such as in filament winding, cross laminates and cloth laminates, can transmit the applied load or stress from the point of application to the reaction via a continuous load path. If the fibers are not continuous between the load and the reaction, the matrix must transfer the load from one fiber to the next fiber at the points of discontinuity as shown in Fig. 3. Fiber continuity also affects the type of failure of the composite. With continuous fibers, it can be assumed that failure will ultimately occur by fracture of the fibers. Discontinuous fibers, on the other hand, can have three other types of failure: fracture of the resin at a weak net section; shear failure in the matrix at the points of discontinuity of the fiber; and failure of the bond between the fibers and the matrix.

Fiber orientation can be categorized either as alignment of the fiber with the axis of the load, or as random orientation. Where the fibers are aligned with the load axis, the fibers have the full fiber area both to resist the load and to provide a direct load path from the load to the reaction. Where the fibers are randomly oriented, less than the full fiber area resists the load and there is not a direct load path.

Analysis of Reinforced Plastics

Using the equations derived earlier, the five types of reinforcement in reinforced plastics can be analyzed to determine the effect of glass fiber geometry on composite material strength. The theoretical composite strength is defined as the sum of the strengths of the fiber and matrix materials. This can be written as

$$P_c = A_f F_f + A_m F_m \quad [8]$$

or when the composite is assumed to have a unit area

$$F_c = A_f F_f + A_m F_m$$

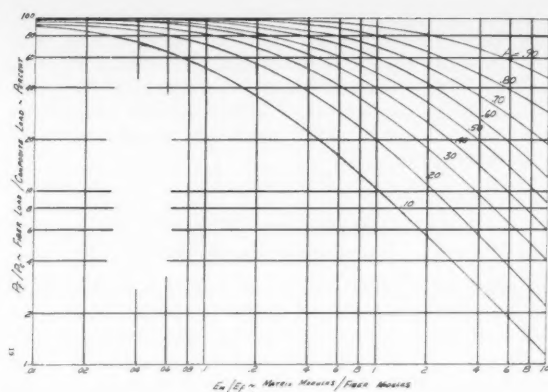


Fig. 1 Plot of the ratio of fiber load to composite load as a function of modulus ratio and fiber area

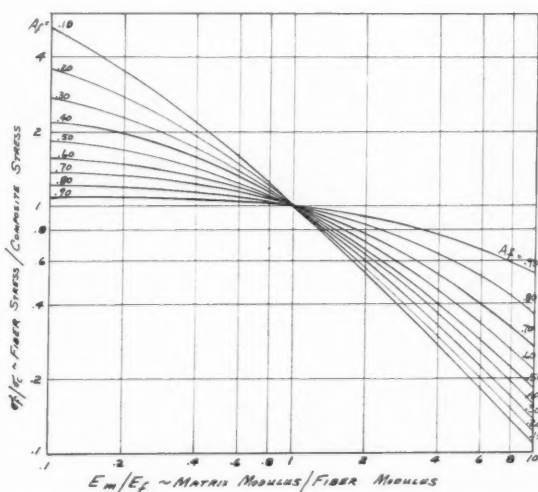


Fig. 2 Plot of the ratio of fiber stress to composite stress as a function of modulus ratio and fiber area

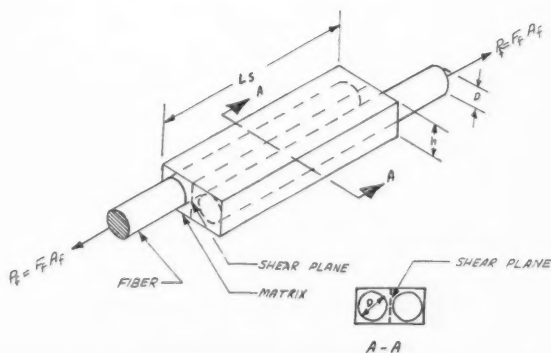


Fig. 3 Load transfer in discontinuous fibers

As shown in Figs. 4a and 4b, the maximum elongation of glass fibers and epoxy resins are about equal, and Eq. 8 is valid for epoxy glass fiber composites. Also, from Figs. 4a and 4b, it can be assumed that $F_m = 10,000$ psi. The composite efficiency is the ratio of the composite strength as tested to the simple composite theoretical strength expressed in per cent. Thus

Composite efficiency =

$$\frac{\text{Test strength of the composite}}{\text{Theoretical composite strength}} \times 100 \quad [9]$$

The effective fiber stress can be determined from the load in the fiber and the fiber area. The percentage of the applied load which is carried by the fiber is dependent upon E_m/E_f and A_f . This can be determined from Fig. 1. This load divided by the fiber area is the effective fiber stress. Thus

$$\sigma_f(\text{effective}) = \frac{P_f}{P_c} \times \frac{\text{Test strength of composite}}{A_f} \quad [10]$$

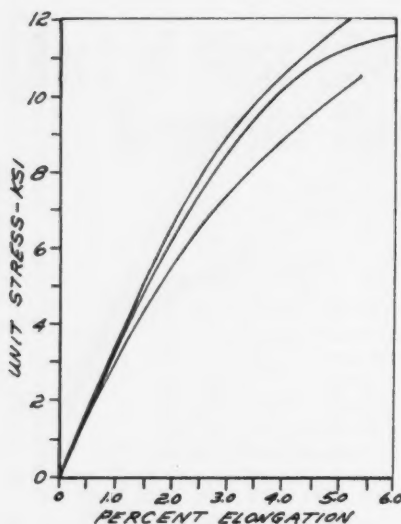


Fig. 4a Typical stress-strain curves, epoxy resin (17)

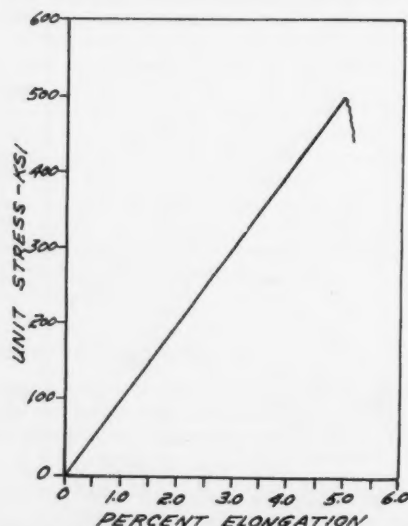


Fig. 4b Typical stress-strain curves, glass fiber (3,4)

Fiber efficiency can now be defined as the ratio of the developed fiber stress to the base strength of the fibers. Thus

$$\text{Fiber efficiency} = \frac{\text{Developed fiber stress}}{\text{Base fiber strength}} \times 100 \quad [11]$$

Composite efficiency is based upon the total glass content plus the total matrix content, whereas fiber efficiency is based on the glass area oriented in the load direction.

The average strengths of glass fibers in its several common forms are approximately

Single filament: 500,000 psi
Single glass roving: 400,000 psi
Glass strands: 250,000 psi
(as woven into cloth)

For the basis of comparing fiber geometries, the base glass strength will be assumed as 400,000 psi for glass roving. Single glass filaments are not practical to handle, and glass strands as used in cloth have undergone the first phase of fabrication.

Based on this, the results are tabulated in Tables 1 and 2, and are determined as follows: First, the typical composite strength is changed to load on a unit cube of the composite as shown in Fig. 5. Next the load (lb) is distributed to the fiber and the matrix by the relationship of E_m/E_f and A_f resisting this load. Finally, the composite efficiency and the fiber efficiency are determined by Eqs. 9 and 11.

As an example, the filament wound composite is analyzed as follows:

For filament wound fibers in tension the theoretical compos-

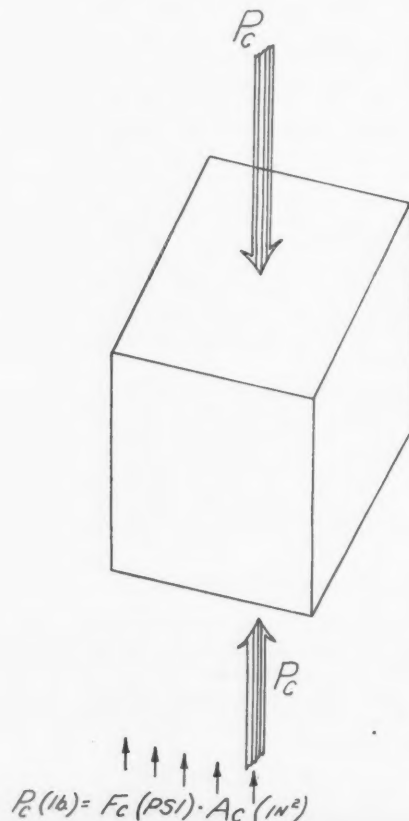








Fig. 5 Sketch of fiber load and fiber stress relationship

Table 1 Composite efficiency of reinforced plastics

Types of fibers and flake composites	Fiber orientation	Fiber-length ^a	A_f	A_m	F_{theo}^b psi	F_{test}^c psi	Com- posite ^d effi- ciency, % (see Eq. 18)
Filament wound		Con	0.77	0.23	310,000	180,000 (5)	58.0
Cross laminated		Con	0.48	0.52	197,000	72,500 (6)	36.8
Cloth laminated		Con	0.48	0.52	197,000	43,000 (7)	21.8
Mat laminated		Con	0.48	0.52	197,000	57,200 (6)	29.0
Chopped fiber systems		N.Con	0.13	0.87	60,700	15,000 (8)	24.7
Glass flake composites		N.Con	0.70	0.30	165,500	20,000 (9)	12.1







^a Con = continuous. N.Con = noncontinuous.

^b $F_{theoretical} = A_f F_f + A_m F_m$, $F_f = 400,000$ psi, $F_m = 10,000$ psi.

^c Typical test data; numbers in parentheses indicate to References at end of paper.

^d Composite efficiency = test strength of composite/simple theoretical composite strength.

Table 2 Fiber efficiency of reinforced plastics

Item	Fiber orientation	Fiber ^a length	A_f	P_f/P_c	F_{test}^b	Effective fiber stress ^c	Fiber ^d efficiency
Filament wound fibers		Con	0.77	1.00	180,000 (5)	234,000	58.5
Cross laminated fibers		Con	0.24	0.90	72,500 (6)	272,000	68.0
Cloth laminated fibers		Con	0.24	0.90	43,000 (7)	161,000	40.5
Mat laminated fibers		Con	0.20	0.88	57,200 (6)	252,000	63.0
Chopped fiber systems		N.Con	0.043	0.38	15,000 (8)	132,000	33.0
Glass flake composites		N.Con	0.70	1.00	20,000 (9)	28,300	7.0

^a Con = continuous. N.Con = noncontinuous.

^b Typical test data; numbers in parentheses indicate to References at end of paper.

^c Effective fiber stress = $P_f/P_c \times$ test strength of composite/ A_f .

^d Fiber efficiency = effective fiber stress/base fiber strength.

ite strength is

$$A_f F_f + A_m F_m = 0.77 (400,000) + 0.23 (10,000) = 310,000 \text{ psi}$$

The developed fiber stress is

$$\sigma_f (\text{effective}) = \frac{P_f}{P_c} \times \frac{\text{Test strength of composite}}{A_f}$$

$$\sigma_f (\text{effective}) = \frac{1.00 (180,000)}{0.77} = 234,000 \text{ psi}$$

Therefore, the composite efficiency is

$$\text{Composite efficiency} = \frac{180,000}{310,000} \times 100 = 58.0\%$$

and the fiber efficiency is

$$\text{Fiber efficiency} = \frac{\text{Developed fiber stress}}{\text{Base fiber strength}}$$

$$\text{Fiber efficiency} = \frac{234,000}{400,000} \times 100 = 58.5\%$$

Results

Table 1 shows that filament wound fibers form the most efficient composite, and that composite efficiency goes down as fiber orientation is changed from unidirectional to random orientation. It appears that bending the fibers by weaving them into cloth imposes the most severe reduction in efficiency.

The maximum glass fiber efficiency in tension is approximately 65%; about the same fiber efficiency is developed by filament winding, cross laminates, and mat laminates. This can be expected on the basis of straight continuous fibers. When the straight, continuous fibers are deformed or bent, such as when woven into a cloth laminate, the fiber efficiency goes down. Due to the discontinuous fibers and random orientation, the glass fiber efficiency of chopped fiber systems is extremely low. It could be concluded that since only 33% of the glass strength is developed, 67% of the base glass strength is wasted.

This analysis could be improved by increasing the amount of data used to determine efficiencies. However, increasing the amount of data would complicate the analysis without increasing the accuracy by a large margin, and so the assumption that the data is typical seems a valid one. Qualitatively, the results seem to bear out the arguments presented earlier on the effect of fiber geometry on composite strength.

Effect of Fiber Geometry on Other Composites

Five parameters are used in Eqs. 9 and 11 to determine the composite efficiency and the fiber efficiency of reinforced plastics. These are modulus ratio E_m/E_f , total area of fiber A_f , area of fiber in the load direction A_f , base fiber strength F_f , and base matrix strength F_m .

In addition to these explicit parameters used in the analysis, there are some implicit parameters which will affect the composite and fiber efficiency of other composites.

The three main implicit parameters are the bond stress between the fiber and the matrix, the matrix shear stress, and the length of fiber overlap. These are not considered parameters for reinforced plastics where fiber lengths exceed one half inch. In other composites employing larger diameter fibers and lower strength materials, these parameters may affect the composite and fiber efficiency.

The remaining implicit parameters are the sensitivity of glass fibers to handling during fabrication and the brittleness

of glass fibers. These two parameters influence the magnitude of the composite efficiency and the fiber efficiency of Tables 1 and 2. Increased handling of the fibers and twisting or bending the fibers reduce both the composite efficiency and the fiber efficiency.

Ceramic fibers, whisker materials, and metal filaments are three groups of fiber materials. Ceramic fibers have the same general characteristics of glass fibers in that the fibers are brittle, they are sensitive to handling which cause abrasion and with increased handling they decrease in strength. Therefore, assuming the fiber matrix relationship of ceramic fibers in a matrix are the same as that of glass fiber plastic resin composites, it is probable that about the same composite and fiber efficiencies would be achieved. Ductile ceramic fibers, on the other hand, would probably result in higher composite and fiber efficiencies.

The typical properties of three whisker materials are listed in Table 3. Whisker materials in general are supersensitive to handling which contaminates the single crystals of the material. In addition, the short fiber lengths of whiskers confine their use to chopped fiber systems. These two points indicate that both the composite and fiber efficiency of whisker materials may be extremely low. It seems probable that methods will be developed to control the handling sensitivity of whiskers, but an increase in available lengths is necessary to utilize the full fiber strength. Increased fiber strength requires more fiber overlap to develop both bond strength and matrix shear strength.

The typical properties of several finely drawn metal wires are listed in Table 3. Of these five metals, steel and molybdenum are the most ductile, whereas tungsten is very brittle. It seems probable that using very brittle tungsten filaments in a composite may result in composite and fiber efficiencies comparable to those of glass fibers. These filaments would probably be sensitive to handling much the same as glass filaments. On the other hand, the use of ductile metal filaments may yield composite and fiber efficiencies higher than those of glass filaments since they would be neither as sensitive to handling nor exhibit brittle behavior.

In general, the effect of fiber geometry on composites other than glass fibers and plastic resin should be about the same except that the magnitude, depending on the handling sensitivity and the brittleness of the fibers, will be changed. Both composite efficiency and fiber efficiency should be higher for ductile fibers than for brittle fibers.

Summary

The effect of glass fiber geometry on composite material strength has been investigated by a rational analysis of five fiber geometries used in reinforced plastics. Fiber geometry has been briefly scrutinized by considering the fundamental mechanics of composite materials and the manner in which the fibers transmit load through the matrix. To some extent, the magnitude of the effect of glass fiber geometry on composite strength has been determined by calculating typical composite and fiber efficiencies for the five fiber geometries. Typical composite efficiencies are as follows: filament wound fibers, 58%; cross laminated fibers, 37%; cloth laminated fibers, 22%; mat laminated fibers, 29%; and chopped fibers, 25%. Straight, continuous fibers develop the highest composite and fiber efficiencies while discontinuous, randomly oriented fibers develop the lowest efficiencies.

The effect of fiber geometry on composite strength for other composites will depend to some extent on ductility of the fibers. Brittle fiber materials should exhibit about the same efficiencies as reinforced plastics, whereas ductile fibers will probably exhibit higher efficiencies.

Nomenclature

A_c = area of composite, sq in.
 A_f = total fiber area, sq in.

Table 3 Potential fiber materials

Material	Tensile strength, psi	Mod. of elasticity, psi	Ref.
Wires			
molybdenum	225,000	42×10^6	(10)
tungsten	300,000	58×10^6	(11)
tantalum	180,000	27×10^6	(12)
columbium	100,000	16.5×10^6	(13)
steel	450,000	29.0×10^6	(14)
Whisker materials			
iron whiskers	1,900,000	29.0×10^6	(15)
aluminum oxide	1,800,000	42.0×10^6	(15)
sapphire whiskers	1,700,000	74.0×10^6	(15)

A_f = area of fiber in load direction, sq in.
 A_m = area of matrix, sq in.
 D = fiber diameter, in.
 E_c = modulus of elasticity of composite, psi (tension)
 E_f = modulus of elasticity of fiber, psi (tension)
 E_m = modulus of elasticity of matrix, psi (tension)
 F_f = base strength of the fiber, psi
 F_m = base strength of the matrix, psi
 F_c = theoretical composite strength, psi
 h = height of shear plane, in.
 L_s = length of shear plane and required overlap of fibers
 P_c = load on composite, lb
 P_f = load on fiber, lb
 P_m = load on matrix, lb
 σ_c = unit stress in composite, psi
 σ_f = unit stress in fiber, psi
 σ_m = unit stress in matrix, psi
 ϵ_c = unit strain of composite, in./in.
 ϵ_f = unit strain of fiber, in./in.
 ϵ_m = unit strain of matrix, in./in.

References

1 Outwater, J. O., Jr., "The Mechanics of Plastic's Reinforcement in Tension," *Modern Plastics*, vol. 33, no. 155, 1956.

- 2 Swics, J. J. and others, "Metal Fiber Reinforced Ceramics," WADC Tech. Rep. 58-452, January 1960.
- 3 Sonneborn, R. H., *Fiber Glass Reinforced Plastics*, Reinhold Publishing Corp., N. Y., 1st ed., 1954.
- 4 "Materials Selection," *Materials in Design Engng.*, vol. 50, no. 5, Mid October 1959.
- 5 Boeing Airplane Co., "Allowable Design Stress," unpublished data.
- 6 Donaldson, A. L. and Velleu, R. B., "Directionally Reinforced Plastics," *Modern Plastics*, vol. 35, no. 2, October 1957.
- 7 Bowditch, W. R. and Johnson, E. L., "Investigation of the Effect of Glass Fabric Geometry on the Strength Properties of Low Pressure Glass Fabric Base Structural Laminates," WADC Tech. Rep. 56-270, May 1957.
- 8 Plastics Properties Chart, *Modern Plastics*, Encyclopedia Issue 1961, September 1960.
- 9 Rugger, G., "Glass Flake Laminates," *SPE J.*, vol. 13, 1957, p. 35-70.
- 10 Tungsten, Metallwerk Plansec, Reutte, Tyrol Austria, also, see (11).
- 11 Defense Metals Information Center (DMIC) Rep. no. 127, March 15, 1960.
- 12 "The Metal Tantalum," Fansteel Metallurgical Corp., 1953.
- 13 Yntema, L. F., "Columbium," *Metals Handbook*, Amer. Soc. for Metals, 1948 ed.
- 14 Boeing Airplane Co., Test Data.
- 15 Hoffman, G. A., "The Exploitation of the Strength of Whiskers," Rep. P-1294, 1958, Rand Corp., Santa Monica, Calif.
- 16 "New Shape for New Fibers," anonymous, *Product Engng.*, September, 1960, p. 9.
- 17 Kyte, R. M. and Pollman, D., "The Effect of Resin Systems on the Strength of Filament Wound Glass Fiber Composites," presented at the ARS 15th Annual Meeting, Washington, D. C., Dec. 5-8, 1960, (ARS preprint 1581-60).

Use of Binary Light Metal Mixtures and Alloys as Additives for Solid Propellants

A. W. BLACKMAN¹
and D. K. KUEHL²

Research Laboratories
United Aircraft Corp.
East Hartford, Conn.

Studies are described of the use of binary light metal mixtures and alloys, rather than pure metals, as additives for solid propellant formulations to increase performance and burning rates. It is shown that appreciable increases in theoretical performance can be obtained through the use of binary metal additives rather than single metal additives with a dual oxidizer system, such as NH_4ClO_4 . For example, the theoretical specific impulse of a system composed of 15% hydrocarbon binder, 70% ammonium perchlorate, and 15% metal additive is increased by approximately 6 sec when a bimetal additive of lithium-beryllium is used rather than a pure beryllium additive. The maximum theoretical specific impulse for each metal system is obtained in an oxygen-halogen oxidizer system when the amount of the metal having an affinity for halogens (e.g., lithium) and the amount of the metal having an affinity for oxygen (e.g., beryllium) are present in approximately stoichiometric proportions with the available halogen and oxygen in the oxidizer and binder. The results of the specific impulse calculations are evaluated in terms of payload delivery capability for a representative rocket powered missile as a function of both the specific impulse and the propellant density. The payload delivery capability for a number of propellant systems employing bimetal additives are found to be superior to those of the systems employing the pure metals even though the density of the bimetal system is less than that of a system containing an equal weight of the denser metal constituent in a pure form. Experimental studies of the combustion characteristics of pure metals (Al, Mg, B, Si) and metal alloys (Al-Mg, Al-Si, Al-Li) burning in air are described, and data on burning times are included. Theoretical considerations are also discussed to explain variations in burning times with alloy composition.

Presented at the ARS Solid Propellant Rocket Conf., Salt Lake City, Utah, Feb. 1-3, 1961.

¹ Supervisor, Chemical Kinetics Group, Propulsion Sect. Member ARS.

² Research Engineer, Chemical Kinetics Group, Propulsion Sect. Member ARS.

LIGHT metals, such as aluminum, have found extensive use as additives for solid propellant formulations used to increase specific impulse and combustion stability (1).³ In solid propellant formulations using dual oxidizers, (e.g., ammonium perchlorate, which produces both oxygen and chlorine upon decomposition), it might be expected that performance increases could be achieved if two light metals were added to the formulation: one which preferentially combines with one oxidizer, and a second which preferentially combines with the other. Those metals having low atomic weights and high heats of formation when combined with the oxidizer under consideration would produce the greatest specific impulse improvement.

The investigations described herein were conducted to establish the specific impulse and density characteristics of a representative solid propellant formulation containing various binary metal additives, and to obtain experimental data regarding the burning characteristics of typical alloys.

Theoretical Performance

Various binary light metal additives were screened on the basis of the following factors: (a) atomic weight and molar heat of formation with the oxidizers under consideration, i.e., heat of formation per gram; (b) oxidation preference of the metals; and (c) relative proportions of the binder, oxidizer, and metal additives in the formulation from considerations of stoichiometry. Detailed specific impulse calculations were then performed for those systems which appeared promising from the initial screening.

Fig. 1 presents the heats of formation per gram of various metal oxides and chlorides. From such a plot, the metal combinations which would be expected to produce high performance can be ascertained. For example, the heats of formation obtained when beryllium is reacted with oxygen and chlorine to form BeO and BeCl₂ indicate that a higher heat of formation could be obtained from a binary mixture of beryllium and any of the metals above the BeCl₂ line in Fig. 1 if the beryllium preferentially reacts with the oxygen rather than the chlorine. Lithium and beryllium appear to be the most attractive combination from the standpoint of energy content. Fig. 1 indicates that with an ammonium perchlorate oxidizer, the highest performance would be obtained with the lithium-beryllium combination if the beryllium could be made to combine with the available oxygen, and the lithium could be made to combine with the available

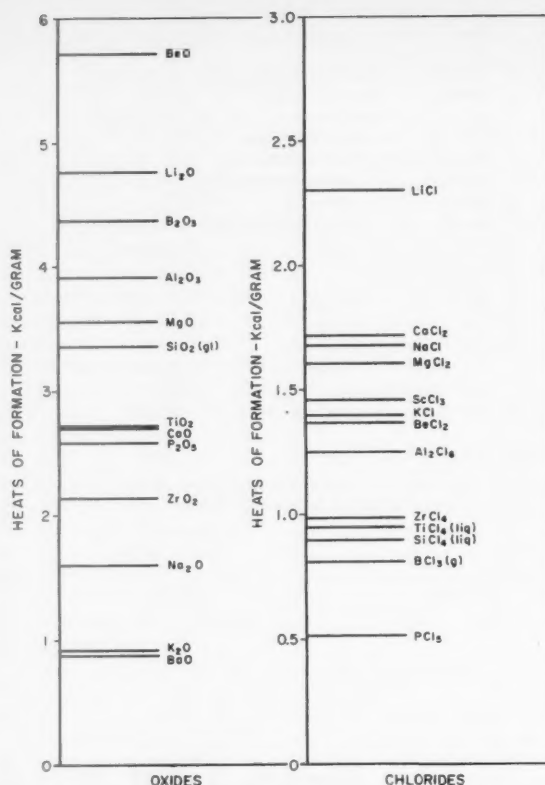


Fig. 1 Heats of formation at 298 °K

chlorine, because BeO has a higher heat of formation than Li₂O, and LiCl has a higher heat of formation than BeCl₂. A similar argument could be prepared for any dual oxidizer system, such as F-O or N-O, irrespective of whether both oxidizers occur in the same molecule or in separate molecules.

The energy liberated in systems comprised of ammonium perchlorate and binary metals varies, depending upon which of the metal additives combines with the available oxygen and which combines with the available chlorine. The oxide

³ Numbers in parentheses indicate References at end of paper.

Table 1 Heats of reaction and average molecular weights of products for simplified stoichiometry

Reactants at 298 °K, products at 1600 °K (assumed gaseous unless indicated otherwise)

Binary metal additive	Simplified reaction stoichiometry neglecting binder and dissociation	Heat of reaction, Kcal/gm mol	Avg. molecular weight of products	Heat of reaction, Kcal/gm of product
Be-Li	NH ₄ ClO ₄ + 4Be + Li → 1/2N ₂ + 2H ₂ + 4BeO(s) + LiCl(l)	-495.81	21.40	-3.09
Be-Mg	NH ₄ ClO ₄ + 4Be + 1/2 Mg → 1/2N ₂ + 2H ₂ + 4BeO(s) + 1/2MgCl ₂ (l)	-497.60	23.66	-2.90
Be-Al	NH ₄ ClO ₄ + 4Be + 1/3 Al → 1/2N ₂ + 2H ₂ + 4BeO(s) + 1/6Al ₂ Cl ₆	-471.14	24.40	-2.90
Be-Ca	NH ₄ ClO ₄ + 4Be + 1/2 Ca → 1/2N ₂ + 2H ₂ + 4BeO(s) + 1/2CaCl ₂ (l)	-501.90	24.78	-2.89
Be	NH ₄ ClO ₄ + 9/2 Be → 1/2N ₂ + 2H ₂ + 4BeO(s) + 1/2 BeCl ₂	-452.58	22.58	-2.86
Be-B	NH ₄ ClO ₄ + 4Be + 1/3B → 1/2N ₂ + 2H ₂ + 4BeO(s) + 1/3BCl ₃	-445.77	23.00	-2.84
Be-Si	NH ₄ ClO ₄ + 4Be + 1/4 Si → 1/2N ₂ + 2H ₂ + 4BeO(s) + 1/4SiCl ₄	-450.32	23.78	-2.81
Be-Ti	NH ₄ ClO ₄ + 4Be + 1/4Ti → 1/2N ₂ + 2H ₂ + 4BeO(s) + 1/4TiCl ₄	-455.90	24.51	-2.76
Be-Na	NH ₄ ClO ₄ + 4Be + Na → 1/2N ₂ + 2H ₂ + 4BeO(s) + NaCl(l)	-484.84	23.53	-2.75
Be-Zr	NH ₄ ClO ₄ + 4Be + 1/4Zr → 1/2N ₂ + 2H ₂ + 4BeO(s) + 1/4ZrCl ₄	-464.68	26.12	-2.64
Li	NH ₄ ClO ₄ + 9Li → 1/2N ₂ + 2H ₂ + 4Li ₂ O(s) + LiCl(l)	-446.49	23.99	-2.48
Al-Li	NH ₄ ClO ₄ + 8/3Al + Li → 1/2N ₂ + 2H ₂ + 4/3Al ₂ O ₃ (s) + LiCl(l)	-465.56	40.64	-2.37

s = solid l = liquid

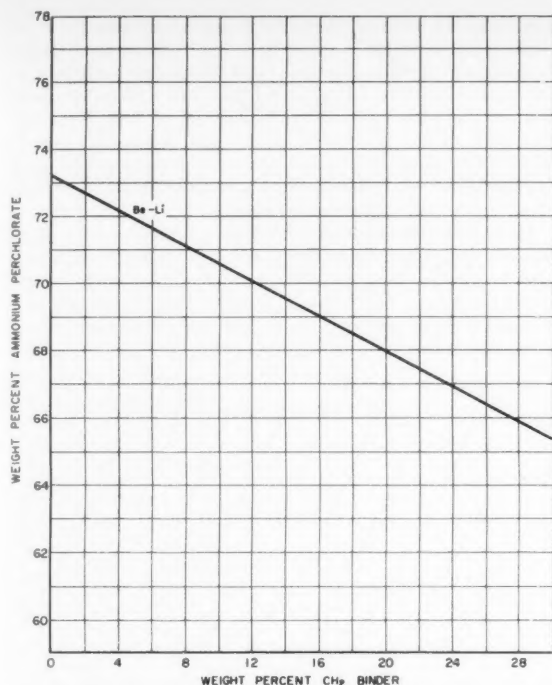


Fig. 2 Stoichiometric propellant compositions: % NH_4ClO_4 + % CH_2 + % alloy = 100

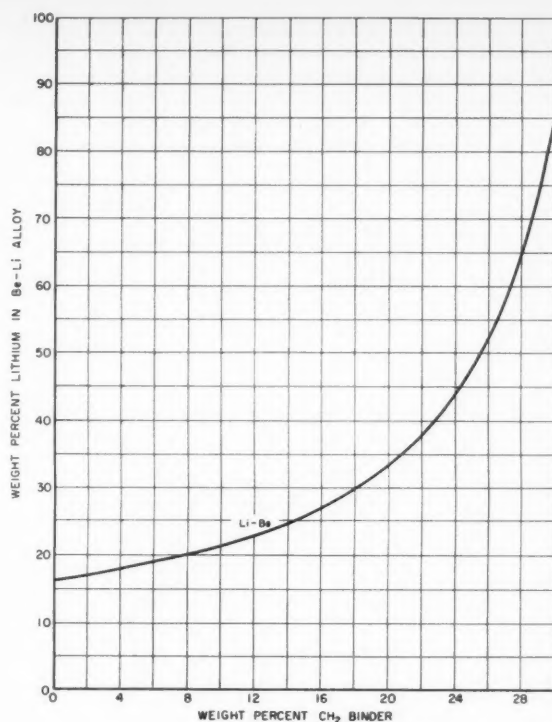


Fig. 3 Stoichiometric propellant compositions

states which will be produced can be indicated by considering the free energies of the reaction of a selected metal pair with oxygen and chlorine. The preferred oxidation state will be the state producing the highest negative free energy value. If the values are very close together, both products would exist simultaneously. Such free energy calculations were carried out for a number of metal pairs and the preferred oxidation states determined. By knowing the preferred oxidation states of the metals, neglecting dissociation and assuming a zero binder content, the simplified stoichiometry of the reactions was worked out. A further screening of the additives was obtained by computing the heat of the reaction and the average molecular weight of the products produced for the simplified stoichiometry. The results of such calculations are presented in Table 1. The heat of reaction represents the value obtained if the reaction follows the indicated stoichiometry, the reactants enter the reaction zone at 298 °K and the products leave at 1600 °K. Data for these calculations were obtained from (2 through 6). It can be seen that the Be-Li metal combination appears to have the best potential for producing high specific impulse in propellant formulations containing a dual oxidizer such as ammonium perchlorate. Figs. 2 and 3 present results of calculations for the stoichiometric proportions of an NH_4ClO_4 , Li-Be system which includes a CH_2 binder. These curves indicate the variation of the ammonium perchlorate and binary metal contents necessary to maintain stoichiometric proportions as the propellant binder content is varied.

The optimum compositions of binary metal additives for propellant formulations can only be determined on the basis of the propellant's payload delivery capability for specific missions. Rigorous calculations of the propellant specific impulse (considering dissociation, etc.) and propellant densities are necessary. Several systems were examined in detail by means of a calculation procedure (5) programmed for IBM 704 computers on the basis of isobaric combustion at

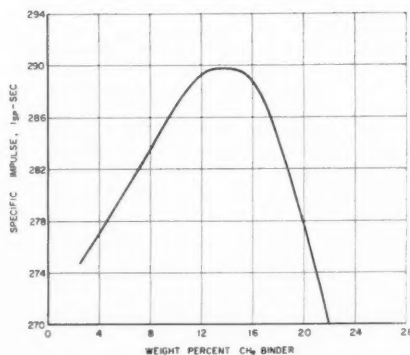


Fig. 4 Specific impulse vs. binder composition for stoichiometric propellant compositions of the Li-Be- CH_2 - NH_4ClO_4 system

1000 psia and isentropic nozzle expansion to 14.7 psia. Fig. 4 presents the variation of the specific impulse of the stoichiometric Li-Be- NH_4ClO_4 - CH_2 propellant system as a function of the binder content. A peak impulse of approximately 290 sec was obtained for a binder content of approximately 14%.

Fig. 5 illustrates the effect of varying the composition of binary metal additives on the payload delivery capability of propellant formulations having a constant per cent oxidizer for an arbitrary vehicle having a 2100-mile range and 18,000-lb gross weight. The superiority of some of the binary metal systems over the single metal additives is indicated. These systems are not optimized for binder contents or stoichiometry; however, the Li-Be and Al-Be systems are fairly close to optimum compositions at their maximum payload delivery points. The 15% binder content although not optimum

represents the order of the minimum allowable binder content from grain strength considerations. Fig. 6 presents a similar plot for selected metal additive systems having stoichiometric proportions between the additive, the CH_2 binder, and the NH_4ClO_4 oxidizer. A 15% binder content was assumed. The Be-Li additive gives the best performance, and the

WEIGHT %	—	---
NH_4ClO_4	70	70
CH_2 BINDER	10	15
METAL	20	15

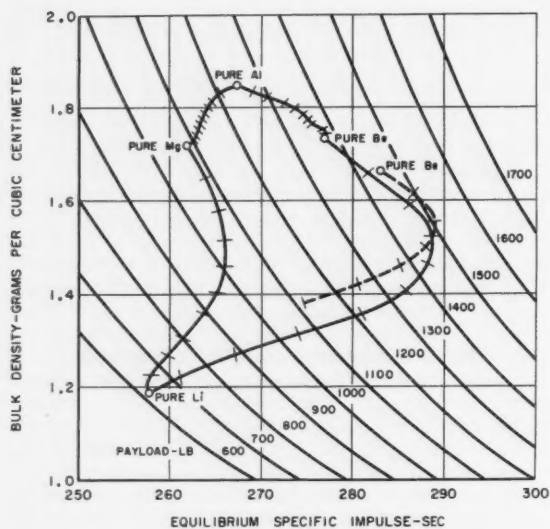


Fig. 5 Mission capability of solid propellants containing binary metal additives; Payloads based on an 18,000-lb gross weight vehicle having 2100-mile range; slashes on curves indicate a 10% change in alloy composition

superiority of some of the binary metal additives over the single metal additives is apparent. Fig. 7 shows the detailed variations in specific impulse, combustion temperature and molecular weight as a function of the binary metal composition for the propellant system consisting of 70% NH_4ClO_4 , 10% CH_2 binder, and 20% Li-Be metal additive. Due to the effect of molecular weights on specific impulse, the peak impulse does not coincide exactly with stoichiometric proportions, but the differences are small.

All of these calculations were made assuming a mixture of the two metals, or an ideal intermetallic solution with zero heat of alloying and partial specific volumes equal to the specific volumes of the pure metals. The inclusion of a nominal heat of alloying, which has not been measured for

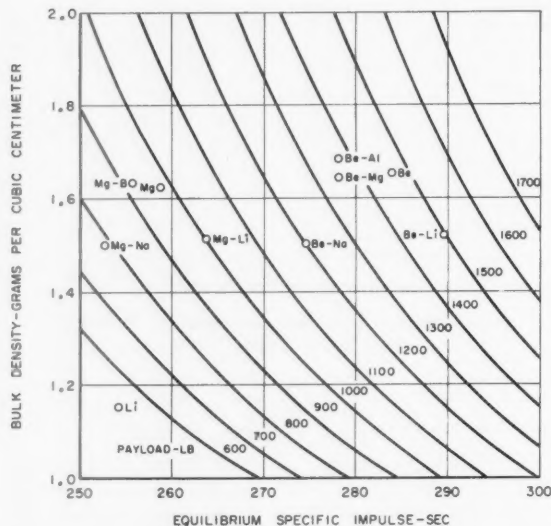


Fig. 6 Mission capability of solid propellants; payloads based on 18,000-lb gross weight vehicle having 2100-mile range; propellant consists of NH_4ClO_4 + CH_2 (binder) + light metal additive in stoichiometric proportions

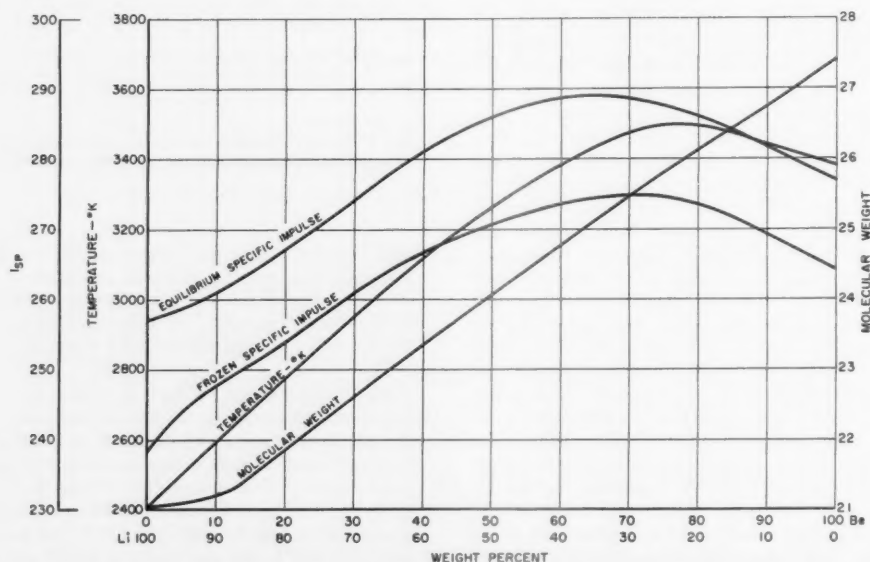


Fig. 7 Theoretical performance, 70% NH_4ClO_4 , 10% CH_2 , 20% Be-Li alloy. Chamber pressure = 1000 psia; exhaust pressure = 14.7 psia

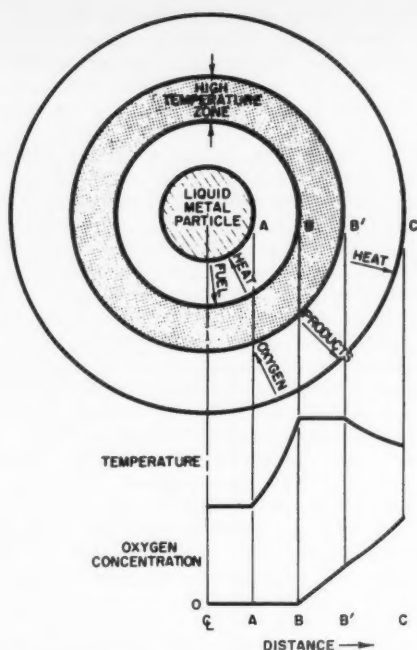


Fig. 8a Postulated model of burning metal showing qualitative temperature and concentration distribution around burning metal particle

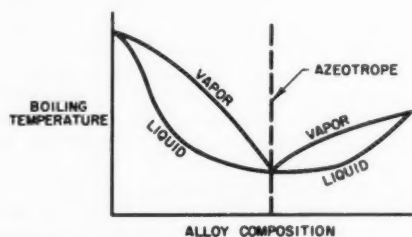


Fig. 8b Postulated azeotropic properties of alloys

most of the alloy systems considered here, would make only small changes in the performance parameters. For those alloys which have densities greater than the densities computed assuming the partial specific volumes equal to the specific volumes of the pure metals, the increase in performance would be relatively small. For volume limited systems where propellant densities assume a greater influence, the improvement in performance would be larger.

Burning Rate Characteristics

Basic Considerations of Metal Combustion

In addition to their effect on the specific impulse of solid propellant formulations, it is possible that binary metal alloy additives can also cause an increase in the burning rates of the metal additives. General discussions of metal combustion are presented in (1),⁴ (7), (8), and (9). In (1, 9), it has been postulated that the burning rates of metals are diffusionally controlled. For metals which produce oxides having vaporization temperatures greater than the vaporiza-

⁴ This reference contains an excellent bibliography of the literature covering the combustion of most of the metals of interest.

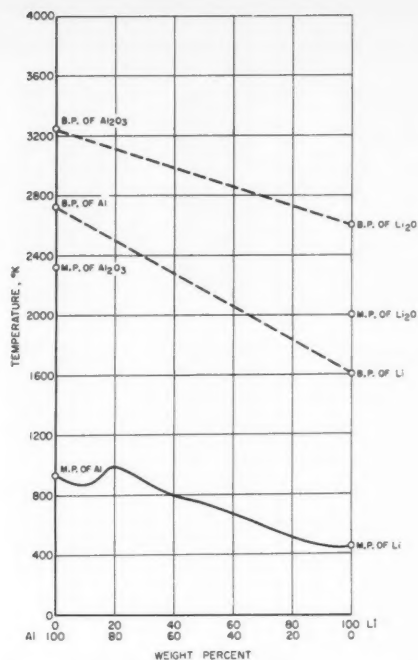


Fig. 9 Metal and metal oxide melting and boiling temperatures for Al-Li

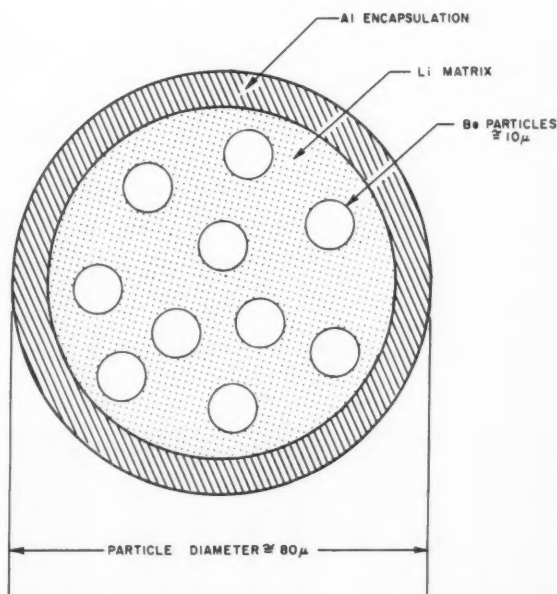


Fig. 10 Scheme for the preparation of Be-Li particles (not to scale)

tion temperatures of the metals, the burning model illustrated in Fig. 8a has been postulated (1). The metal particle at A is vaporized by heat transferred by radiation and conduction from a high temperature reaction zone B-B', which is at a constant temperature equal to the vaporization temperature (burning temperature) of the metal oxide. The vaporized metal then diffuses into zone B-B'; here it reacts with oxygen which diffuses into B-B' from zone C. It has been postulated

Table 2 Melting and boiling temperatures of various metals and metal oxides

Metal	Melting point, °K	Boiling point, °K	Metal oxide	Melting point, °K	Boiling point, °K
Mg	924 (2)	1380 (2)	MgO	3073 (2)	3350 (1)
Li	454 (10)	1600 (10)	Li ₂ O	2000 (1)	2600 (1)
Be	1551 (2)	3243 (2)	BeO	2803 (2)	4173 (2)
Al	933 (2)	2720 (1)	Al ₂ O ₃	2323 (1)	3800 (1)
Si	1693 (2)	2628 (2)	SiO ₂	1983 (2)	2500 (2)
B	2573 (2)	2823 (2)	B ₂ O ₃	723 (2)	2520 (1)
Na	371 (2)	1153 (2)	Na ₂ O	1193 (1)	1550 (1)

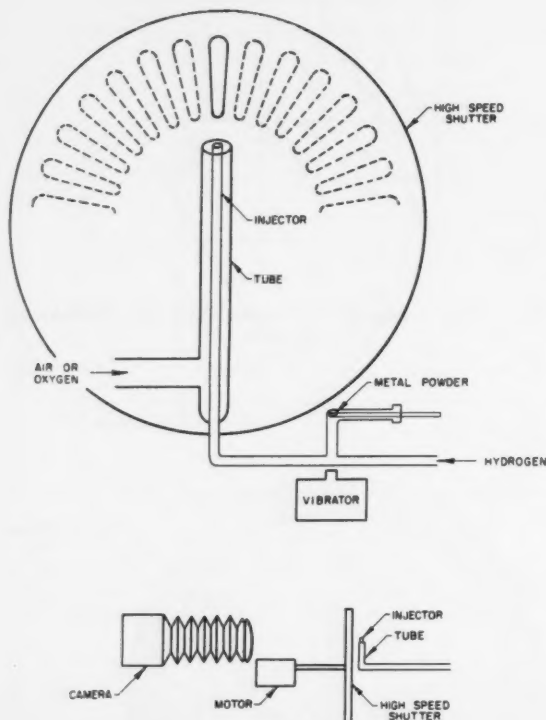


Fig. 11 Schematic drawing of metal powder combustion apparatus

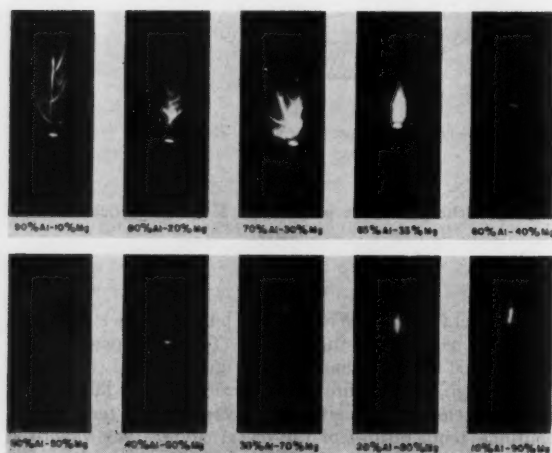


Fig. 12 Burning Mg-Al alloys in air

(9) that the distance between A and B increases as the difference between the vaporization temperature of the metal oxide and the vaporization temperature of the metal is increased. It would be expected that if the separation distance between A and B were increased, oxygen would diffuse into zone B-B' at a higher total rate because there would be a greater diffusional area. Hence the burning rate of the particle would be expected to increase as the difference between the vaporization temperature of the metal oxide and the vaporization temperature of the metal is increased. The temperature difference for a particular metal could possibly be increased if alloys of this metal could be found which would exhibit azeotropic properties at particular compositions; this is illustrated in Fig. 8b. At this time the existence of bimetallic azeotropic alloys has been postulated but not observed experimentally. Fig. 9 illustrates the relationships of metal and metal oxide melting and boiling points for the Al-Li bimetallic alloy system. The dashed lines represent estimated or probable melting or boiling points for alloys. For example, the addition of lithium to aluminum could decrease the boiling point of the alloy below that of pure aluminum. Assuming the high temperature reaction zone to remain at the vaporization temperature of aluminum oxide (at least for small percentages of lithium), the temperature difference between the reaction zone and the boiling metal should increase. This should increase the separation distance and increase the burning rate over that for pure aluminum. Similar data for other alloy systems are presented in Table 2, (1), (2) and (10).

Another possible technique for increasing the burning rate of metals is to use a pseudo alloy consisting of extremely small particles in a matrix of a low melting, low boiling metal. Analysis of the burning rates of particles (1) has shown that the rate varies inversely with the particle diameter. Sub-micron particles of many metals are reactive enough to be pyrophoric. By preparing a pseudo alloy of mutually non-soluble metals, in which the higher boiling metal is in the form of an extremely fine powder, the boiling of the low melting matrix in a reaction zone could release an extremely large number of sufficiently small particles to substantially increase the overall combustion rate. This technique is illustrated in Fig. 10 for a Li-Be system. Small beryllium particles (approximately 10 μ in diameter) could be hot pressed in a lithium matrix to form a larger particle of about 80 μ in diameter. This particle size would not be as reactive as the smaller sizes and would be easier to handle. In addition, the particle size of 80 μ is sufficiently large to allow aluminum encapsulation; this would further reduce the handling and storage problems. The boiling temperature of lithium is about the same as the melting temperature of beryllium (approximately 1600 °K). This characteristic would allow the small particles of beryllium to be liberated so they could burn discretely as the matrix is heated.

Exploratory Tests of Typical Alloys

The apparatus used in measuring burning times is shown schematically in Fig. 11. A uniformly sized metal powder was introduced to a carrier flow of hydrogen which burned as a pilot diffusion flame in an air stream. Photographs were obtained as the metal passed through the pilot flame, ignited, and burned. A high speed mechanical shutter interrupted the optical path at a rate of about 10,000 times per second, and the burning particle trajectories appeared as dotted tracks in the photographs. The number of dots divided by the repetition rate of the shutter gave the burning time directly with an accuracy of about ± 0.0001 sec. Examination of many particle tracks proved that the velocities of the burning particles were not uniform or constant; therefore, burning times calculated only from the length of the trace and an assumed average velocity would have been orders of magnitude less accurate than the method used.

In Fig. 12 photographs are presented of Al-Mg alloy particles burning in air. Photographs of pure aluminum, pure magnesium, pure boron, Al-Si and Al-Li alloys burning in air are shown in Fig. 13. Although lithium is normally highly reactive, no storage or handling difficulties were encountered with the 90% Al-10% Li alloy used in these tests. In each photograph the total exposure was about 40 millisecc. Except for the cases of pure aluminum and pure silicon, where a more intense pilot was required for ignition, particles of $49 \pm 5 \mu$ size were used with identical settings of pilot hydrogen flow, airflow, and air temperature (25°C) in each run.

For 90%, 80%, and 70% aluminum in Al-Mg alloys (Fig. 12), the tracks are in general sharp and well defined, with evidence of particle shattering early in the course of burning. For these aluminum rich alloys, it is postulated that the difference in the boiling points of the pure aluminum and the lower boiling component (possibly a eutectic) of the alloy is so large that the lower boiling component may boil explosively when the particle passes through the high heat flux zone of the pilot flame, resulting in fragmentation of the remaining aluminum. For magnesium concentrations greater than the 65%Al-35%Mg eutectic, any fragmentation that may have resulted is obscured by the fact that both the eutectic and the excess magnesium have burning times approaching the limits of accuracy of the high speed shutter employed. There was less fragmentation of the 90% Al-10% Li alloy (Fig. 13) than for the equivalent Al-Mg alloy, probably because the Al-Li alloy is approximately at a homogeneous eutectic composition. In the case of the Al-Si alloys, no fragmentation was observed, probably because the boiling points of aluminum and silicon (and, by interpolation, their alloys) are relatively close together (see Table 2).

It has been postulated by Fassel (11) and others that the lower melting metals (including aluminum and magnesium) melt prior to ignition. It is therefore logical to postulate that the formation of a eutectic alloy, melting at a lower temperature than the pure metal, could facilitate ignition. If this is the case, an alloy containing any significant amount of a eutectic phase might be ignited under conditions which would be insufficient to ignite the pure metal. Such was found to be the case. The pilot flame required to ignite the aluminum was more energetic than that required for all of the alloys containing aluminum, and the combustion of individual aluminum particles was not self-sustaining beyond the limits of the pilot flame. These results are similar to the results reported by Gordon (12). The photograph of aluminum in Fig. 13 shows limited combustion with an enlarged pilot flame. In addition, it was found impossible to ignite pure silicon in nonpreheated air without increasing the pilot flame beyond the field of view of the camera. Pure boron burned slowly, but ignited easily, and (as seen in Fig. 13) a glowing deposit of oxide built up at the tip of the hydrogen injector. It is possible that the relative ease of ignition for aluminum alloys containing magnesium or lithium might be attributed to the volatility of the lithium and magnesium being greater than that of aluminum. However, in the Al-Si alloy, the silicon has a much higher melting point and about the same boiling point as aluminum. The only factor common to all the alloy systems which can logically account for their improved ignition characteristics appears to be the formation of a eutectic phase which would have a melting temperature lower than the melting temperature of the pure aluminum.

The burning times of Al-Mg alloys in air, as shown in Fig. 14, decrease from pure aluminum to pure magnesium, as might be expected from the differences in the boiling points of the oxides and alloys. For the higher aluminum concentrations, the experimental burning times recorded below the curve were for fragmented particles. This fragmentation phenomenon presents the possibility of improved combustion efficiencies in solid propellants if ways of producing controlled

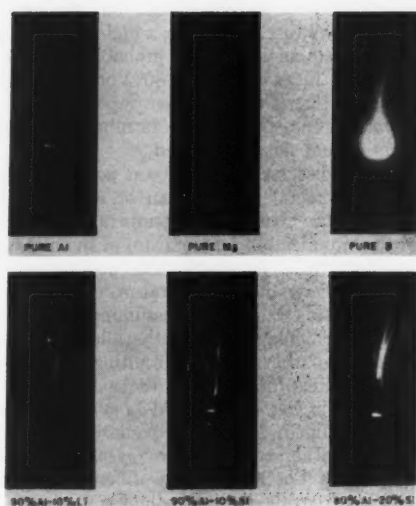


Fig. 13 Burning metal powders in air

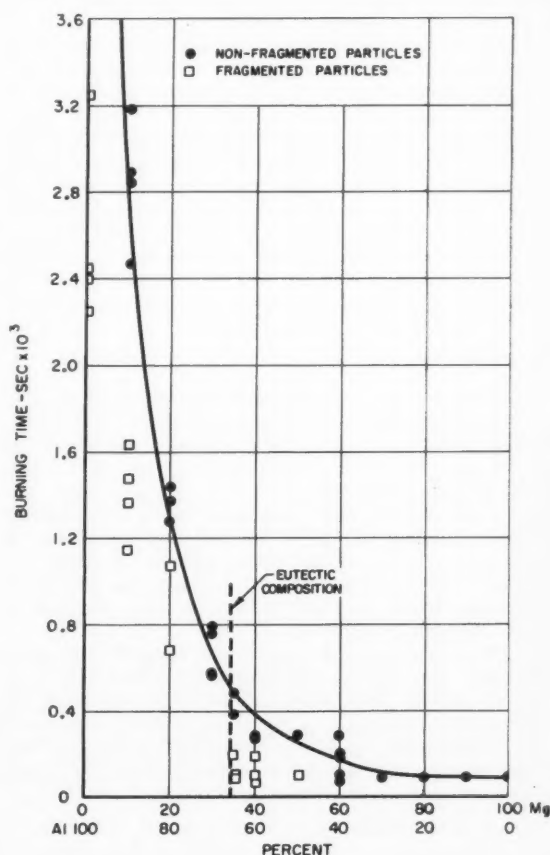


Fig. 14 Burning times of Al-Mg alloys in air; particle size $49 \pm 5 \mu$ burning time limits of accuracy ± 0.1 millisecc

fragmentation can be found. Qualitatively there was little change in the appearance of the combustion as the magnesium content was increased beyond the eutectic. In the entire range from the eutectic to pure magnesium, the metal flame was nebulous and diffuse, indicating a high degree of gaseous or vapor phase combustion. It is probable that the actual burning times for alloys containing 80% or more magnesium are actually less than the 0.0001 sec reported, because the limit of accuracy was equal to this burning time and faster burning times could not be resolved.

As previously discussed, it has been postulated that the burning times of metal particles can be related to the difference between the vaporization temperature of the metal oxide and the vaporization temperature of the metal particle ($T_v - T_A$ in Fig. 8a). To check this postulation, it was necessary to estimate these temperature differences for the various alloys. This was done by assuming a linear relationship between the boiling point of the alloy (or oxide) and the composition of the alloy (or resulting oxide) with end points at the values for pure metals as listed in Table 2. The dashed lines in Fig. 9 for the Al-Li system illustrate the relationships assumed. This approximation was necessary because the actual data for the alloy systems are not available. The log of the temperature difference between the flame (estimated oxide boiling point) and metal particle (estimated alloy boiling point) has been plotted against the log of the measured burning times for the Al-Mg alloy system and for selected points in the Al-Li and Al-Si systems in Fig. 15. Considering the assumptions made, the correlation is very good, and can be considered to provide a reasonable substantiation for the theory.

Within the limits of the experimental technique employed, it appears that particles which have a large temperature difference between the boiling points of the oxide and metal also have a higher burning rate (or shorter burning time). It is also apparent that combinations of a low boiling and a high boiling metal result in the shattering of alloy particles in a high heat flux zone, thus producing many small fragments. Therefore, the use of alloying to increase the combustion rate of metals appears to be of potential practical importance. It also appears that the presence of a eutectic phase in the alloy structure which will decrease the energy required for ignition, should increase combustion efficiency.

Conclusions

1 The theoretical specific impulses and payload delivery capabilities of propellant systems containing a dual oxidizer, such as NH_4ClO_4 , and a number of binary metal additives are superior to those of systems containing an equal weight of either metal in pure form.

2 The maximum specific impulse of binary metal-oxygen-halogen propellant systems is obtained when the amount of the metal having an affinity for oxygen and the amount of the metal having an affinity for halogens are present in approximately stoichiometric proportions with the available oxygen, halogen and binder.

3 When burned in air, the burning times of pure metal and metal alloy particles decrease as the difference between the vaporization temperature of the metal oxide and the vaporization temperature of the metal particle is increased.

4 The handling and storage problems associated with highly reactive lithium can be reduced by alloying lithium with a less reactive metal such as aluminum.

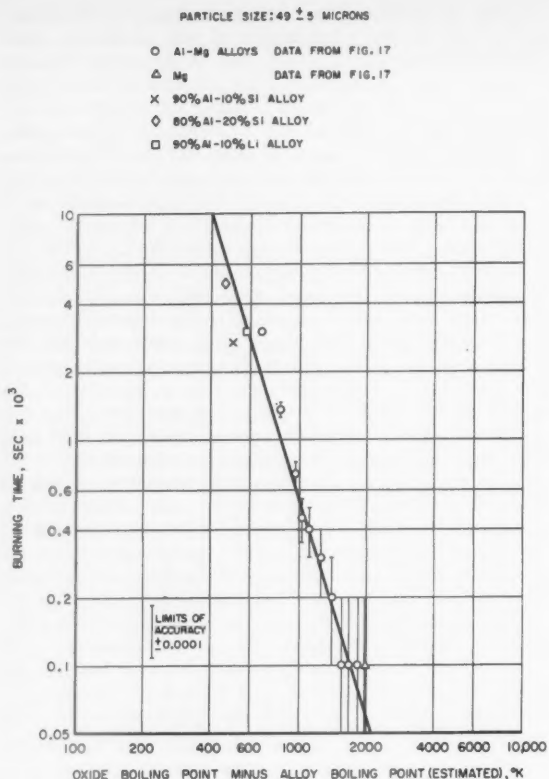


Fig. 15 Alloy burning times as a function of boiling point difference between oxide and alloy

References

- Glassman, I., "Metal Combustion Processes," presented at the ARS 14th Annual Meeting, Nov. 16-20, 1959 (ARS preprint 938-59).
- Handbook of Chemistry and Physics, 41st ed., Chemical Rubber Publishing Co., Cleveland, Ohio, 1959.
- Rossini, F. D., Wagman, D. D., Evans, W. H., Levine S., and Jaffe, I., "Selected Values of Chemical Thermodynamic Properties," circular of the NBS 500, Feb. 1, 1952.
- Sinke, G. C., "Thermal Properties of Combustion Products," Rep. no. AR-15-59, Dow Chemical Co., April 1, 1959.
- McMahon, D. G. and Roback, R., "Machine Computation of Chemical Equilibrium in Reacting Systems," Kinetics, Equilibria, and Performance of High Temperature Systems, Proc. First Conf., Western States Section of the Combustion Inst., Butterworths, Washington, 1960, p. 105.
- Kelley, K. K., "The Free Energies of Vaporization and Vapor Pressures of Inorganic Substances," U.S. Bureau of Mines, Bulletin 383, Contributions to the Data of Theoretical Metallurgy, vol. 3, 1935.
- Grosse, A. V. and Conway, J. B., "The Combustion of Metals," First Technical Rep., Office of Naval Research High Temperature Proj., Oct. 15, 1951.
- Grosse, A. V. and Conway, J. B., "Combustion of Metals in Oxygen," Ind. and Engng. Chem., vol. 50, no. 4, April 1958.
- Glassman, I., "Combustion of Metals-Physical Considerations," Solid Propellant Rocket Research, Academic Press, N.Y., 1960, p. 253.
- Douglas, T. B., Epstein, L. F., Dever, J. L. and Howland, W. H., JACS, vol. 77, 2144 (1955).
- Fassell, W. M., Papp, C. A., Hildenbrand, D. L. and Sernka, R. P., "The Experimental Nature of the Combustion of Metal Powders," Solid Propellant Rocket Research, Academic Press, N.Y., 1960, p. 259.
- Gordon, D. A., "Combustion Characteristics of Metal Particles," Solid Propellant Rocket Research, Academic Press, N.Y., 1960, p. 271.

Technical Notes

Low Thrust Orbit Penalty

PAUL D. ARTHUR¹

The Marquardt Corp., Van Nuys, Calif.

Low thrust orbit changes require more characteristic velocity than do minimum energy high thrust maneuvers. These penalties are approximated for tangential in-plane maneuvers and for orbit plane rotation.

In-Plane Maneuvers

BEGINNING from a circular orbit at unit radius, transfer characteristic velocity will be compared for low and high thrust. The total in-plane energy change

$$E = -1/2a + 1/2 \quad [1]$$

is taken as the independent variable, where a is the semi-major axis of the final orbit. Below escape energy, the comparison will be made between transfers to a final circular orbit at r , so that $a = r$ in Eq. 1. The extreme of high thrust transfer is the impulsive bitangential (Hohmann) orbit (1,2),² requiring a characteristic velocity

$$V_{CH} = \sqrt{\frac{2r}{r+1}} - 1 + \frac{1}{\sqrt{r}} - \sqrt{\frac{2}{r(r+1)}} \quad [2]$$

All velocities are expressed in units of circular velocity at unit radius V_{CO} .

The characteristic velocity for vanishing thrust is

$$V_{CH} = 1 - 1/\sqrt{r} \quad [3]$$

At final energy levels above escape, the final radius has receded to infinity, and the velocity at infinity (hyperbolic excess velocity) is the measure of energy change

$$E = \frac{1}{2}V_{\infty}^2 + \frac{1}{2} \quad [4]$$

The impulsive characteristic velocity is given by the energy equation evaluated at surface burnout

$$\frac{1}{2}(V_{CH} + 1)^2 - 1 = \frac{1}{2}V_{\infty}^2 \quad [5]$$

For vanishing thrust, the characteristic velocity to V_{∞} is $1 + V_{\infty}$. These characteristic velocities are plotted in Fig. 1 with results of intermediate values of α_r (tangential thrust to weight ratio) from numerical integrations (3, 4).

The ratio of low thrust to impulsive characteristic velocity for tangential in-plane maneuvers is given in Fig. 2. Starting with zero penalty for small increases in radius, the ratio increases to a value of 2.42 at escape and a maximum of 3.0

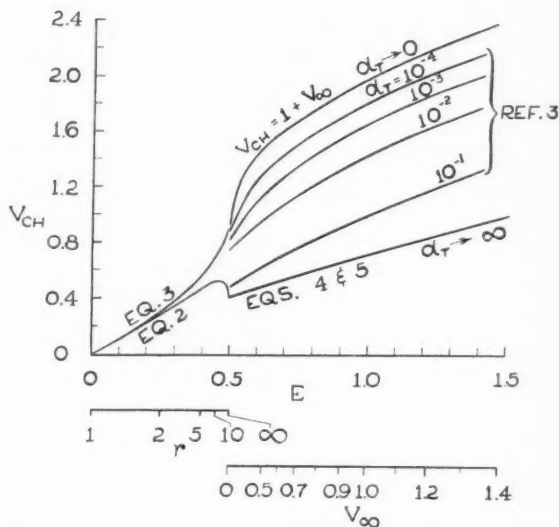


Fig. 1 Characteristic velocity for tangential circular orbit transfer

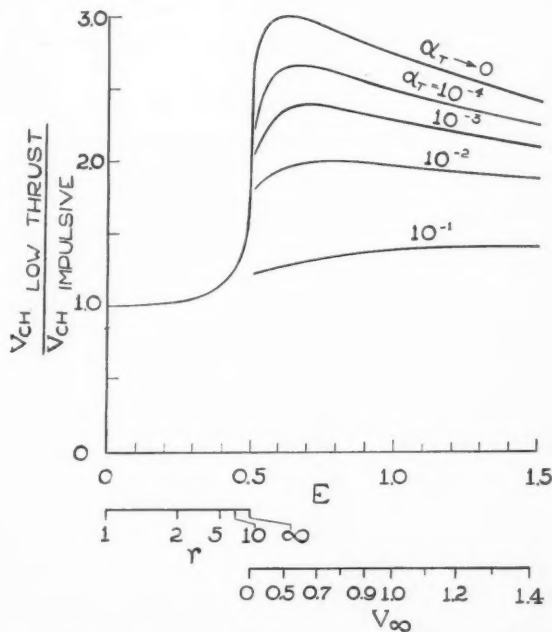


Fig. 2 Ratio of low thrust to impulsive characteristic velocities—in-plane

¹ Consultant, ASTRO. Member ARS.

² Numbers in parentheses indicate References at end of paper.

EDITOR'S NOTE: The Technical Notes and Technical Comments sections of ARS JOURNAL are open to short manuscripts describing new developments or offering comments on papers previously published. Such manuscripts are usually published without editorial review within a few months of the date of receipt. Requirements as to style are the same as for regular contributions (see masthead page).

at $V_\infty = 0.5$. As $V_\infty \rightarrow \infty$, the penalty again vanishes.

Low thrust maneuver time, in units of period at unit radius, is $V_{CH}/2\pi\alpha$, and may be inconveniently long.

This analysis considers constant vehicle mass and thrust with infinite exhaust velocity. Finite exhaust velocity implies decreasing vehicle mass and higher acceleration during the maneuver, thus decreasing the low thrust orbit penalty.

Orbit Plane Angle Changes

Using an impulse, the characteristic velocity to change

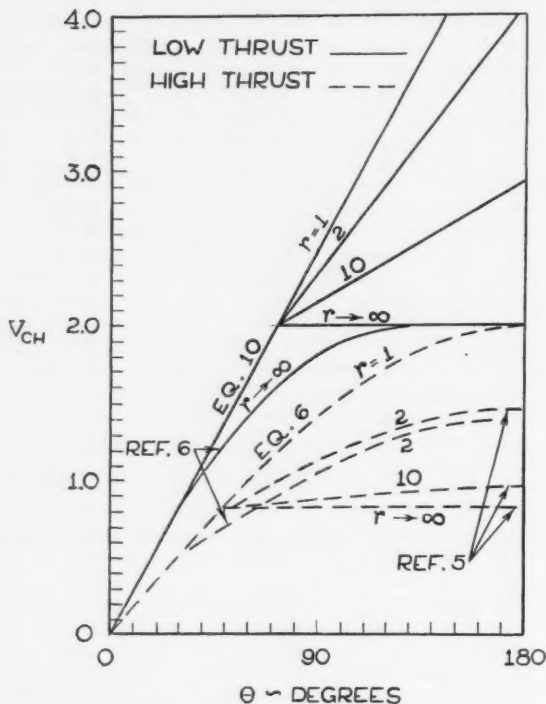


Fig. 3 Characteristic velocity for orbit plane angle change

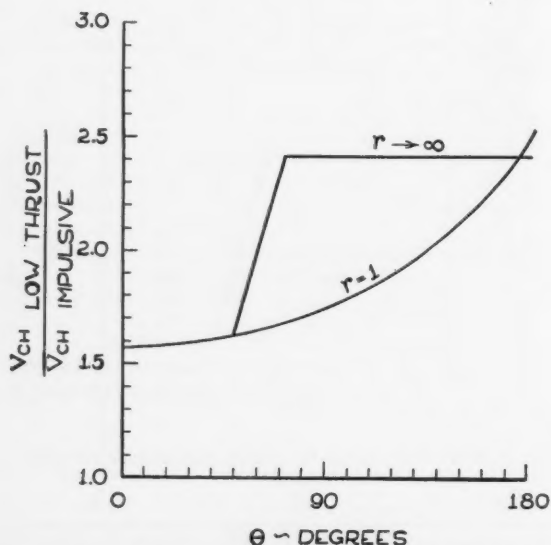


Fig. 4 Ratio of low thrust to impulse characteristic velocities—orbit plane angle change

the orbit plane angle of a circular orbit at unit radius is

$$V_{CH} = 2 \sin \frac{\theta}{2} \quad [6]$$

Rider (5) suggested first firing into an ellipse and then rotating the plane at the apofocus, where the speed is smallest. The three impulse maneuver uses less characteristic velocity for $\theta > 39^\circ$, although its transfer time increases rapidly from P_0 to infinity for $\theta = 49^\circ$. The minimum transfer time (for which the three impulse characteristic velocity equals the one impulse) of the three impulse maneuver can be shown to be given by

$$\sin \frac{\theta}{2} = \frac{2(T^{2/3} - 1)}{T^{1/3}\sqrt{2T^{2/3} - 1} - 1} - 1 \quad [7]$$

where T is in units of P_0 , the period at unit radius. Edelbaum (6) has further shown the benefit of a small out of plane component in the first and third impulses.

Considering only continuous low thrust, direction cycling every half period is required for secular changes of orbit plane angle. If the constant out of plane thrust is cycled at the nodes, the inclination is changed. Cycling at maximum latitudes changes the nodes. Following Levin (7), the secular change of a circular orbit per period is

$$\theta = 4r^2\alpha_w \quad [8]$$

where α_w is the ratio of vehicle thrust to vehicle weight at unit radius.

The characteristic velocity for plane rotation at unit radius is then

$$V_{CH} = \frac{\pi}{2} \theta \quad [9]$$

Analogous to the impulsive case, an in-plane spiral out to lower velocity at $r > 1$ followed by a plane change and spiral back gives a lower characteristic velocity for $\theta \geq 4/\pi = 73^\circ$

$$V_{CH} = 2 \left(1 - \frac{1}{\sqrt{r}} + \frac{\pi}{4} \frac{\theta}{\sqrt{r}} \right) \quad [10]$$

Edelbaum (6) shows an improvement by turning during the outward spiral.

These characteristic velocities are summarized in Fig. 3 and selected ratios presented in Fig. 4. For small orbit angle changes the penalty is 57%, increasing to a maximum of 141%. These penalties can be further reduced by applying thrust intermittently, but with an increase in total maneuver time.

Acknowledgment

Appreciation is expressed for the assistance given by C. R. Halbach of The Marquardt Corp. in the preparation of this paper.

Nomenclature

- a = semi-major axis in units of r_0
- E = energy change parameter—dimensionless
- P_0 = period for circular orbit at r_0
- r_0 = unit radius
- r = radius of final circular orbit for sub-escape case in units of r_0
- T = transfer time in units of P_0
- V_{CH} = characteristic velocity of maneuver in units of V_{CO}
- V_{CO} = circular velocity at r_0
- V_∞ = velocity at infinity in units of V_{CO}
- α_T = tangential thrust in units of vehicle weight at r_0
- α_w = out of plane thrust in units of vehicle weight at r_0
- θ = orbit plane angle change w.r.t. original plane

References

- 1 Vertregt, M., *Principles of Astronautics*, Elsevier, Amsterdam, and van Nostrand, N. Y., 1960.

- 2 Ehrlicke, K. A., "Interplanetary Operations," Chap. 8 of *Space Technology*, H. Seifert, ed., John Wiley & Sons, Inc., N. Y. 1959.
- 3 Moeckel, W. E., "Trajectories with Constant Tangential Thrust in Central Gravitational Fields," NASA TR R-53, 1959.
- 4 Hunter, M. W. and Tschirgi, J. M., "Advantages of High Thrust Space Vehicles," *ASTRONAUTICA*, vol. 5, no. 2, February 1960, p. 28.
- 5 Rider, L., "Characteristic Velocity for Changing the Inclination of a Circular Orbit to the Equator," *ARS JOURNAL*, vol. 29, no. 1, January 1959,

p. 48. Also see *ARS JOURNAL*, vol. 31, no. 3, March 1961, p. 345.

6 Edelbaum, T. N., "Propulsion Requirements for Controllable Satellites," presented at the ARS Semi-Annual Meeting, Los Angeles, Calif., May 9-12, 1960 (ARS preprint 1228-60)

7 Levin, E., "Low Acceleration Transfer Orbits," The RAND Corporation, P-2038, July 15, 1960. To be published in *Handbook of Astronautical Engineering*, McGraw-Hill Book Co., Inc., N. Y.

Rocket Nozzles as Temperature Indicators

Y. BASKIN¹ and D. C. SCHELL²

Armour Research Foundation of Illinois Institute of Technology, Chicago, Ill.

A DEFINITE need exists for accurately determining temperatures attained by sensitive missile components during operation. Such information is essential to insure effective use of materials at various critical sites in the rocket. Conventional measurement techniques generally give little more than a rough approximation of the temperatures reached by materials in the internal sections of a rocket. This is particularly true for solid propellant rocket nozzles, because the presence of the exhaust stream makes it virtually impossible to perform optical measurements on the critical throat surfaces. Furthermore, the use of thermocouples in the nozzle proper is not feasible because drilling of holes might weaken it and result in catastrophic failure of the nozzle assembly.

During the course of investigations on solid propellant materials certain phenomena were observed with Haynes LT-2 nozzles³ which provide a basis for determining maximum temperatures and heat fluxes to which various rocket components have been subjected. Experimental firings, conducted in the laboratory with unfired material, reproduced the phenomena observed in test nozzles and showed their relation to temperature and firing duration.

This paper describes the results of these investigations and suggests additional experiments for increasing the accuracy of thermal indicator devices employing Haynes LT-2. It is further suggested that still more refractory systems be investigated for the purpose of developing ultra-high temperature indicators.

The primary purpose of the study was the determination of failure mechanisms of a variety of nozzle materials tested in solid propellant rockets. Chemical, X-ray, microscopic and other relevant analytical techniques were employed in the investigation. Haynes LT-2 was one of the materials evaluated in the study. It is a cermet composed of alumina, chromium, and tungsten prepared by powder metallurgical methods. Prior to testing it consists of aluminum oxide interspersed in a metallic matrix consisting of two solid solution phases—one rich in chromium and the other in tungsten.

Haynes LT-2 nozzles exhibited only moderate resistance to erosion in these tests, primarily due to volatilization of chromium and susceptibility of thermal spalling. It was apparent that the severity of the current tests exceeded the capabilities of the material to maintain dimensional stability. Nevertheless, examination of the fired nozzles revealed some interesting facts which appear to have important ramifications. Metallographic analysis revealed the presence of a band paralleling the throat contour in nozzles subjected to severe firing treatment. Fig. 1 shows a photograph of such a nozzle fragment which had been electrolytically etched. The nozzle

contour is sketched in to show the original orientation of the fragment in the nozzle. It is evident that response of the polished surface to the etchant was not uniform. A narrow zone (about $\frac{1}{16}$ in. wide) paralleling the throat was unaffected by the etchant, while further back the surface was pitted.

Micro-hardness measurements also show a difference between the pitted and unpitted zones. The pitted areas have an average Vickers hardness of 730, while the unpitted zone exhibits micro-hardness values averaging over 1100 on the Vickers scale.

X-ray analysis of this sample revealed that the unpitted zone paralleling the throat consists of a single solid solution of chromium and tungsten, a result of being heated to temperatures exceeding those needed to produce complete solid solution of the two metals. Above 1500 °C chromium and tungsten are completely miscible, whereas limited solubility occurs below this temperature (1,2).⁴ For an alloy of the composition found in Haynes LT-2 (60 atomic per cent Cr and 40 atomic per cent W), the equilibrium temperature at which complete solubility occurs is also about 1500 °C, according to Kubaschewski and Schneider. Thus it is clear that temperatures at least of the order of 1500 °C must have existed at the throat region of nozzles exhibiting the band of solid solution. Rapid cooling of the nozzles did not permit any exsolution to occur.

⁴ Numbers in parentheses indicate References at end of paper.

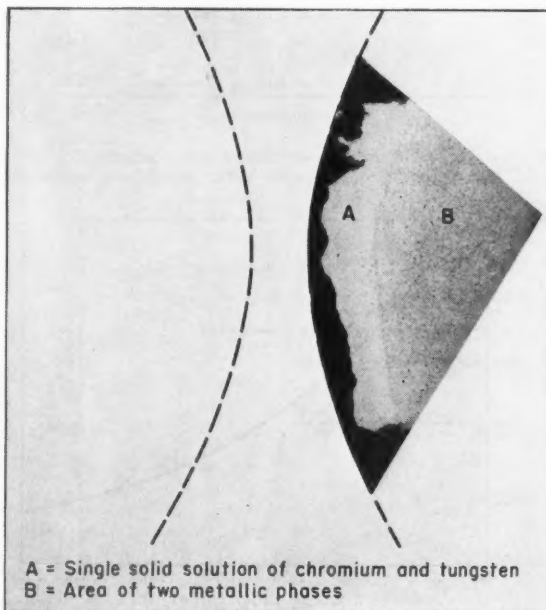


Fig. 1 Fragment of Haynes LT-2 nozzle showing band of single solid solution etched $\times 10$

Received May 8, 1961.

¹ Research Scientist.

² Associate Ceramic Engineer.

³ Manufactured by Haynes Stellite Co., Kokomo, Ind.

The pitted zone consists of two alloys, a chromium-rich phase and a tungsten-rich one. The chromium-rich phase is the one which is presumed to have been preferentially attacked by the etchant. Temperatures within this area during firing were apparently not sufficiently high to produce complete reaction of the two alloys within the firing period.

It is apparent that fired Haynes LT-2 nozzles contain a record of the heat treatment to which they were subjected. Temperatures at least of the order of 1500°C must have existed at the throat surface of the nozzles exhibiting bands of single solid solution. It is likely that considerably higher temperatures occurred to produce complete homogenization in this zone during the comparatively short firing durations employed in the tests. Knowledge of the effect of temperature and time on chromium-tungsten alloy compositions in Haynes LT-2 would help interpret the heat treatment record and possibly make this material useful as an indicator of temperature or "heat work."

Experimental firings were conducted using unfired Haynes LT-2 material to establish the effect of temperature and time

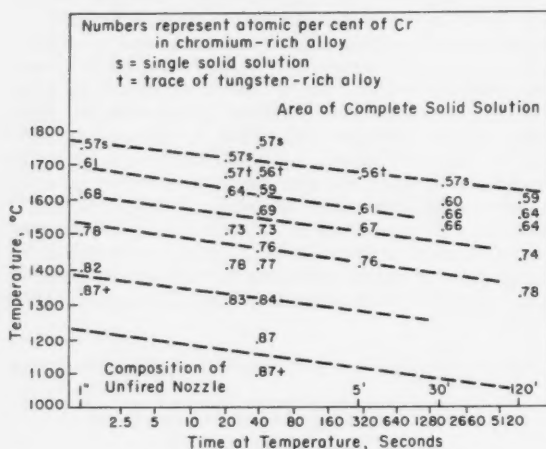


Fig. 2 Composition of chromium-tungsten alloys as a function of temperature and firing duration.

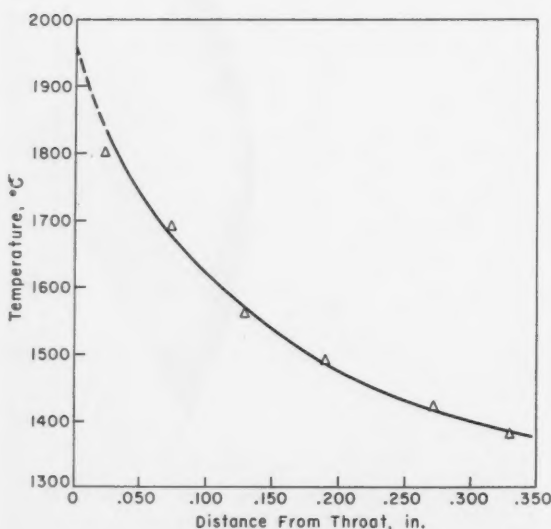


Fig. 3 Apparent temperature in fired Haynes LT-2 nozzle as a function of distance from throat

upon alloy compositions. Small samples were introduced into a heated inert atmosphere furnace and permitted to reach furnace temperatures. After specified time intervals at different temperature levels, samples were quenched in the cool zone of the furnace right above the cooling coils. Samples were then analyzed by X-ray diffraction, and alloy compositions were derived from the lattice constants. Results of the experiments are presented in Fig. 2. The numbers represent atomic percentages of chromium in the chromium-rich alloy; this alloy was found to be a much more sensitive indicator of heat treatments than the tungsten-rich alloy. The latter alloy exhibited very little compositional change with heating, but merely a diminution of intensity. Although the equilibrium temperature at which complete solid solution occurs is about 1540 °C, temperatures of about 1700°C are needed to produce complete homogenization during the short periods. Homogenization depends on the diffusion rates of the two metals, and the rate of change in the direction of a new equilibrium is primarily a function of temperature.

There are indications that the alloy compositions observed in fired nozzles reflect the highest temperatures attained by the nozzles, and that little or no unmixing of alloys occurs during cooling. Fully homogenized material showed only incipient unmixing after two hours at 1500 °C. One could expect significantly less unmixing to occur during the brief time it takes for a rocket nozzle to cool to 1200 °C. On the basis of the experimental data apparent maximum temperature attained at various sites in fired Haynes LT-2 nozzles can be estimated with greater accuracy than had been heretofore possible. Temperatures were derived assuming a duration of one half second at maximum temperature for short rocket firings, and a duration of two seconds at maximum temperature for the longer firings. An error of only 50 °C would result if the assumed duration (at maximum temperature) were off by a factor of ten. The apparent temperature values show excellent correlation with firing conditions and, as might be expected, also with degree of erosion. Higher chamber pressures and longer firing durations produce greater "heat work," which causes more profound compositional changes; concomitant with this is the occurrence of increased erosion and fracturing.

Fig. 3 shows a plot temperature as a function of distance from the throat for a nozzle which had been exposed to severe firing conditions. A surface temperature of about 1950°C is estimated for this nozzle by extrapolating the curve to zero depth. Although this value is substantially lower than the calculated flame temperature of about 2700°C, chromium vaporization, material spalling, and rapid heat conduction could account for the large difference. The leveling off of the curve at a moderate distance from the surface is either attributable to heat transfer characteristics or to equalization of temperature in the nozzle upon termination of the run. The latter could result in redistribution of temperature in the nozzle so that certain portions away from the throat could experience higher temperatures after the test than those attained during actual firing.

Although the experimental data permit one to make a fair estimate of the temperature reached by any site in a Haynes LT-2 nozzle, the accuracy of this estimate is somewhat impaired by the fact that comparatively little is known regarding the heating rates of the nozzles or the duration at maximum temperature. Additional experimental work is required to firmly establish the accuracy and reliability of Haynes LT-2 as a thermal indicator. Changes in composition must be related to time and temperature accurately determined. An experimental setup employing a gas torch could be used, and thermocouples inserted at various depths within a nozzle would give a continuous record of temperature. Optical pyrometric methods can be utilized at temperatures above those at which thermocouples can be employed. Thus the heating rates and maximum temperatures would be obtained, as well as the extent of thermal equalization after firing. Thermal

data would be correlated with alloy compositions derived from X-ray diffraction analysis.

The main limitation of Haynes LT-2 as a thermal indicator is that it may not be possible to transfer temperatures obtained to other materials because of its unique properties. Subjected to the same heat flux, Haynes LT-2 might exhibit a lower temperature than most other materials due to vaporization of chromium. The fact that it is only moderately refractory and susceptible to thermal spalling further restricts its usefulness. For these reasons more refractory materials should be investigated with the aim of developing ultra-high temperature indicator systems. Some of the binary carbide systems exhibit varying solubility with temperature. An example of this is the system ZrC-WC. Zirconium carbide dissolves about 10% WC at 1400°C, 30% at 2000°C and approximately 50% at 2700°C (3). It is conceivable that this behavior might be exploited for temperature indication purposes. Other promising phase systems that warrant investigation are HfC-WC and ZrC-Mo₂C.

Thus far discussions have centered around the use of Haynes LT-2 and other materials as post-firing thermal indicators. However, it is also possible that the device would be suitable for direct temperature determination. Electrical properties of the composites might be sufficiently sensitive to changes in solid solution to permit instrumentation of the device. This approach has interesting possibilities and bears investigation.

Acknowledgment

This study was supported in part by the Materials Laboratory at Wright Air Development Div. Wright-Patterson Air Force Base, Ohio.

References

- 1 Trzebiatowski, W., Polaszek, H. and Lobkowsky, J., *Anal. Chem.*, vol. 19, 1947, pp. 93-95.
- 2 Kubaschewski, O. and Schneider, A., *Zeit. Elektrochem.*, vol. 48, 1942, pp. 671-674.
- 3 Umanaki, J. S., *Ann. Sect. Anal. Phys-Chim. Inst. Chim. Gen.*, U.S.S.R. vol. 16, no. 1, 1943, p. 127.

Burning Rates of Composite Solid Propellants at Subatmospheric Pressure^{1,2}

HARRY SILLA³

AeroChem Research Laboratories, Inc., Princeton, N. J.

BURNING rates of solid propellants at subatmospheric pressure reported here, and re-examination of burning rates obtained by Webb (1,2)⁴ at subatmospheric pressure has shown that these rates do not agree with Summerfield's burning rate equation, but do agree with his model of the burning process. In addition, comparison of the solid propellant flame at atmospheric and subatmospheric pressure suggests that Summerfield's model of a diffusion flame is correct.

The propellant used for these experiments contained 80% ammonium perchlorate as the oxidizer and 20% polystyrene-polyester resin for the fuel binder. The only difference between this propellant and that employed by Webb was the oxidizer particle size and the lack of inhibitor⁵ in these experiments. In spite of the latter difference, tilting of the burning surface was slight. At some of the lowest pressures, it was difficult to ignite a solid propellant strand. This difficulty was overcome by igniting at a higher pressure and pumping down to the desired pressure. It was also found that a strand could be ignited and burned at pressures below the lower ignition point in the presence of oxygen.

The burning rate data are plotted in Fig. 1 as shown by the solid line. With some care, it was possible to measure a burning rate at 2.47 psia, which is lower than the 6.5 psia

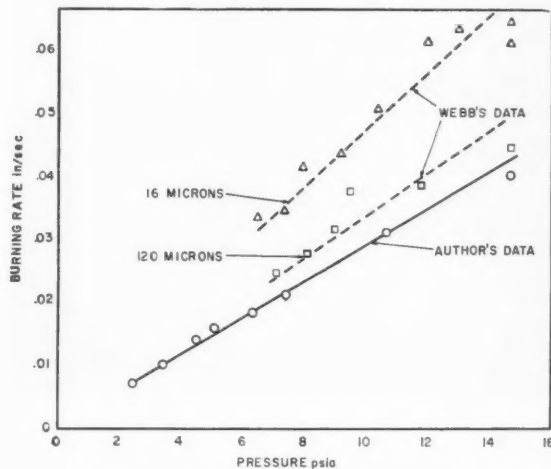


Fig. 1 Burning rates at subatmospheric pressure; 80% ammonium perchlorate, 20% polyester, polystyrene fuel binder

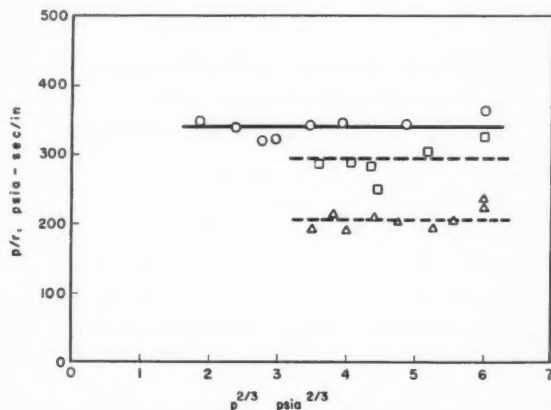


Fig. 2 Plot of burning rate equation $p/r = a + bp^{2/3}$

Received May 17, 1961.

¹ This research was supported by the Office of Naval Research under Contract Nonr 2806(00).

² The work reported here has been submitted by the author to Stevens Institute of Technology in partial fulfillment of the requirements for an M.S. degree.

³ Chemical Engineer.

⁴ Numbers in parentheses indicate References at end of paper.

⁵ A coating applied to solid propellant strands to maintain a flat burning surface.

burning rate obtained by Webb. This subatmospheric burning rate data was compared with Summerfield's burning rate equation (1). The Summerfield equation can be written in the form $p/r = a + b p^{2/3}$, where p is the pressure, r is the burning rate, and a and b are empirically determined con-

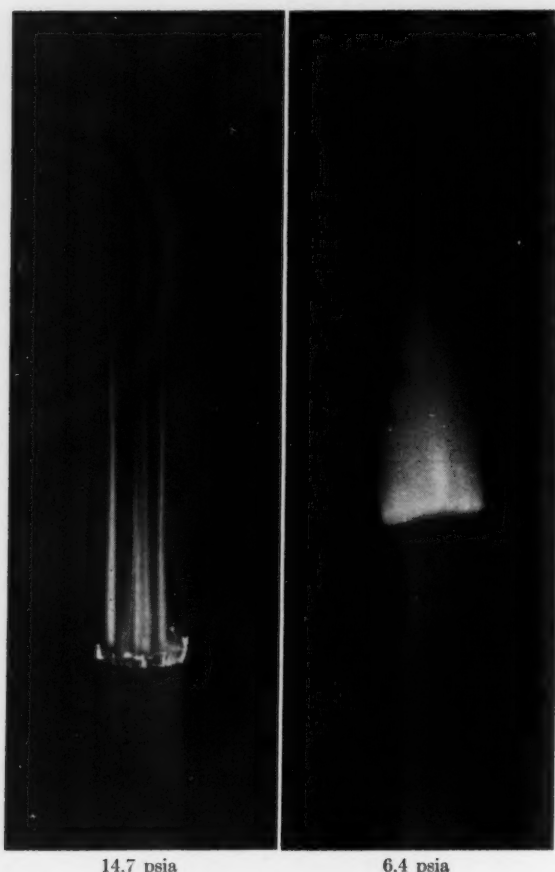


Fig. 3 Comparison of burning solid propellant strands at atmospheric and subatmospheric pressure

stants; a is related to a "reaction time," i.e., its magnitude is determined primarily by chemical reactions in the combustion zone; and b is related to a "diffusion time." If we plot p/r vs. $p^{2/3}$, we obtain a straight horizontal line as shown in Fig. 2. This shows that the slope b is zero and that $r \propto p$.

Webb's data (indicated by the dashed line) is also plotted in Figs. 1 and 2 and the same trends are evident. The average oxidizer particle size for Webb's data is indicated in Fig. 1. In the pressure range from subatmospheric to 2000 psia, Webb obtained values of $b = 27$ and 17 for average oxidizer particle sizes of 120 and 16 μ , respectively. Webb (2) reported that his data deviated from the Summerfield equation for the propellant containing the coarse oxidizer, but the deviation for the fine propellant went unnoticed. It appears that the relationship $p/r = a + b p^{2/3}$ does not hold at subatmospheric pressure and that $r \propto p$ is a more suitable relationship of the variation of burning rate with pressure. However, the relationship $r \propto p$ is consistent with Summerfield's model of second-order chemical reactions controlling the burning process at low pressures.

An interesting observation was made by comparing the flames of solid propellants at atmospheric and subatmospheric pressures (Fig. 3). The streaks in the flame at atmospheric pressure have been attributed by Sutherland (3) to soot particles originating from the propellant surface. However, it is difficult to see how reduced pressure could decrease the number of soot particles. It is suggested that these streaks are abnormally large zones of gaseous fuel or oxidizer and are the result of large particles of oxidizer or pockets of fuel in the propellant itself. Then, the almost total disappearance of the streaks at lower pressures would be attributed to more rapid diffusion and subsequent blending of these zones, which is consistent with Summerfield's model of a solid propellant diffusion flame.

Acknowledgment

The encouragement of E. J. Henley of Stevens Institute of Technology during this research is appreciated.

References

- 1 Summerfield, M., Sutherland, G. S., Webb, M. J., Taback, H. J. and Hall, K. P., "Burning Mechanism of Ammonium Perchlorate Propellants," ARS preprint 737-58, Nov. 1958.
- 2 Webb, M. J., "The Dependence of Linear Burning Rate upon Pressure for Ammonium Perchlorate-Polyester Resin Composite Solid Propellant," M.S. Thesis, Princeton Univ., 1958.
- 3 Sutherland, G. S., "The Mechanism of Combustion of an Ammonium Perchlorate-Polyester Resin Composite Solid Propellant," Ph.D. Thesis, Princeton Univ., 1958.

Direct Thrust and Efficiency Measurements of a Continuous Plasma Accelerator

STERGE T. DEMETRIADES¹

and

RICHARD W. ZIEMER²

Norair Div., Northrop Corp., Hawthorne, Calif.

Experiments were performed with a continuous Lorentz or $J \times B$ accelerator, using an arc jet plasma source and argon and nitrogen expellants. At flow rates of 0.003

lbm/sec, directly measured thrusts of up to 3.6 lbf, exclusive of the arc jet, were obtained, with acceleration efficiencies as high as 54%. The specific impulse increment due to the plasma accelerator was 1200 sec corresponding to an addition of 300% to the specific impulse of the arc jet used in these experiments.

THE REQUIREMENT for space propulsion engines with thrust levels of the order of 1 to 100 lb and high specific impulse has focused attention on the thermal arc jet as a possible solution. However, there are several factors which limit the stagnation enthalpy obtainable with the arc jet; namely, (a) the energy transferable to the gas is thermally limited because of material properties; (b) joule heating decreases in effectiveness as the gas temperature increases; and (c) the conversion of sensible, ionization, and dissociation energies to directed kinetic energy is incomplete because of the

Received June 9, 1961.

¹ Head, Space Propulsion and Power Laboratory. Member ARS.

² Senior Scientist. Member ARS.

nonequilibrium expansion process in the nozzle.

It appears that the propulsion performance can be considerably increased by transferring the input electrical energy directly into directed kinetic energy instead of first "degrading" it into thermal energy. A continuous $J \times B$ or Lorentz force acting on the propellant gas can accomplish this. A current is passed between two electrodes through the conducting gas. This current is normal to both the flow direction and an applied magnetic field. This causes a Lorentz force to act on the plasma in the flow direction. A propulsion system consisting of an arc jet and a Lorentz plasma accelerator (or magnetogasdynamic driver) is shown schematically in Fig. 1.

To explore the promising potential of this device, an experimental investigation was made of continuous linear plasma acceleration by means of Lorentz forces. The main objectives of this experimental investigation were (a) to demonstrate the feasibility of the $J \times B$ accelerator as a space propulsion device; (b) to determine the thrust and efficiency characteristics of the engine; and (c) to provide accurate and unambiguous experimental thrust data for comparison with theory.

Apparatus

The apparatus is shown schematically in Fig. 2. It consists of a plasma accelerator (MGD driver) mounted on a balance enclosed in a vacuum tank. An arc plasma generator is mounted at one end of the tank. The plasma stream from this source is directed between the electrodes and pole pieces of the accelerator. The accelerator consists of one or more pairs of movable tungsten electrodes, which pass a current through the plasma stream normal to the direction of flow, and a d-c magnet to generate an accelerating field normal to both the electrode axis and the direction of plasma flow. The magnet produces a field strength of up to 4500 gauss in a gap of 3.75 in. and with a maximum power consumption of 1200 w. Power to the electrodes was transmitted to the assembly on the thrust stand through mercury reservoirs to eliminate any restraining forces. Force measurements were made by electric strain gages on the thrust stand which had a sensitivity of 0.2 oz. The arc jet, mounted in the tank door and completely separate from the accelerator, acted solely as a plasma source. The thrust stand measures only the Lorentz accelerator force reactions, i.e., the thrust increment due to magnetogasdynamic forces. The vacuum tank was evacuated by a two-stage mechanical vacuum pump. With a steady mass flow rate of 0.003 lbm/sec, the tank pressure could be regulated to 0.6 mm abs or higher. Further details of the apparatus are given elsewhere (1,2).³

During the course of each experiment, measurements were made of accelerator thrust, magnet current, electrode current, electrode voltage, and arc jet voltage, and these were continuously recorded on a Sanborn 850 eight-channel recorder. Preselected for each test were gas mass flow rate, arc jet current and voltage, and vacuum tank pressure.

The argon tests reported here were run with a mass flow rate of 0.0030 lbm/sec and a power input of 43.5 kw giving a plasma velocity of 10,000 fps at the inlet of the MGD driver. Nitrogen tests were made at 0.0020 lbm/sec and 87.5 kw giving a plasma velocity of 12,000 fps at the inlet of the MGD driver. Results with air were reported by Demetriades (1).

The following experimental procedure was used: First, the thrust stand strain gages were calibrated. The tank was then closed and evacuated. The expellant gas was bled in at the desired flow rate and the tank pressure regulated to the desired value. The recorder was started and then the arc jet turned on to the desired power level. The accelerator electrode current was turned on and the current set to the desired value. Finally, the magnetic field was applied. Normally, the magnetic field was slowly increased from zero to

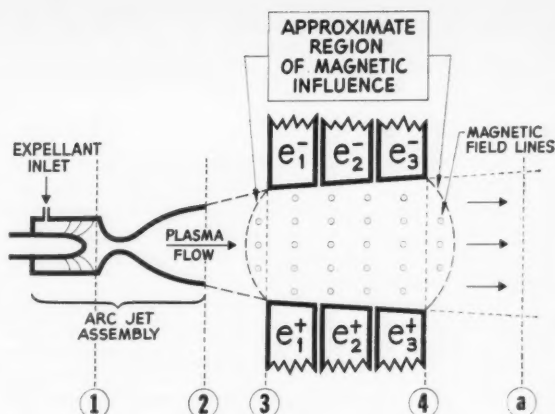


Fig. 1 Schematic diagram of arc jet plasma source and continuous MGD plasma accelerator

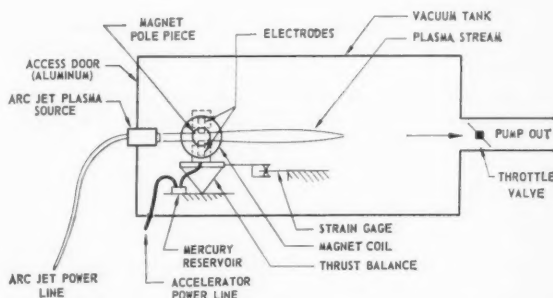


Fig. 2 Schematic diagram of experimental apparatus showing MGD plasma accelerator mounted on thrust stand within vacuum tank; arc jet is mounted in vacuum tank door

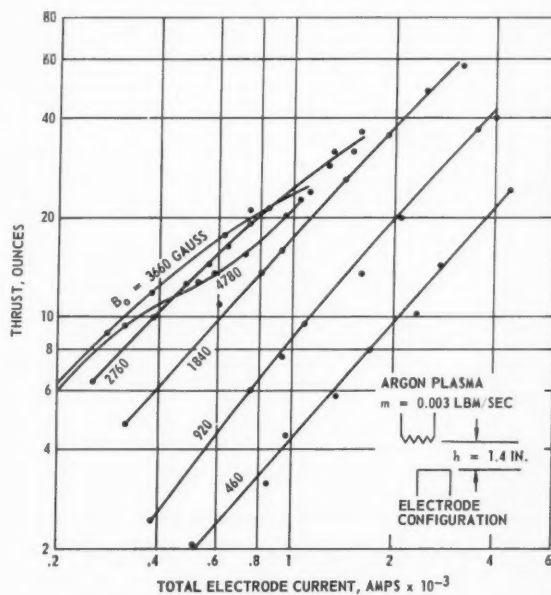


Fig. 3 Directly measured accelerator thrust as a function of total electrode current for various values of the applied magnetic induction

³ Numbers in parentheses indicate References at end of paper

its maximum and then brought back to zero, thereby obtaining a continuous measurement of thrust vs. magnetic induction and thus separating the MGD effects from thermal effects.

Experimental Results

When the electrode current and magnetic field were turned on while the plasma stream was flowing between the accelerator electrodes, a definite reaction, either thrust or drag depending on polarity, was detected by the balance. The following qualitative observations were used as criteria to establish the nature of this effect:

1 When the electrode current was switched on, with the magnetic field off, there was no appreciable balance reaction. When the magnet was switched on, there was a definite reaction of thrust or drag, depending on the polarity of the magnetic field. Reversing the polarity of the magnet caused the force on the balance to reverse direction. Reversing the polarity of both magnet and electrodes does not change the direction of force.

2 As the magnetic field was increased, the current passing through the electrodes decreased because of the reverse potential generated, and the plasma stream became deflected upward as a result of the Hall currents.

3 When the externally applied electric field was switched off, while the magnetic field was on, a small drag force was observed.

4 An increase in the electrode current at constant magnetic induction caused a proportional increase in the thrust. Additional criteria were given by Demetriades (1).

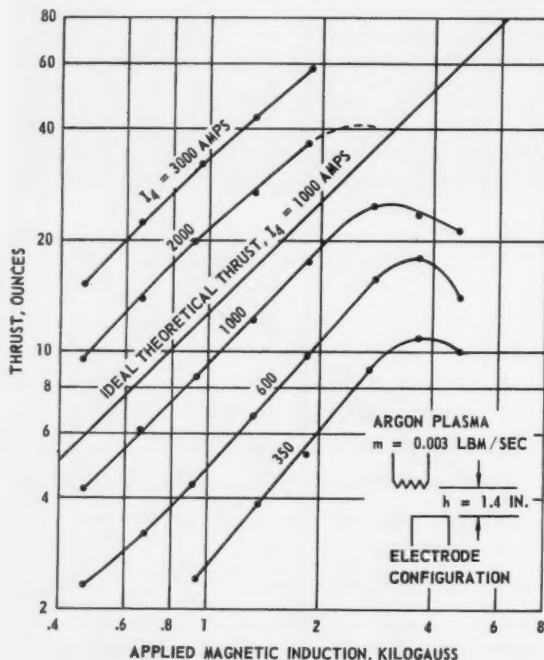


Fig. 4 Cross-plot of experimental data showing accelerator thrust as a function of applied magnetic induction and constant total electrode current

A series of tests were made at various magnitudes of electrode current. The data for argon plasmas, for one electrode configuration, are given in Fig. 3. Measured thrust and electrode current are plotted for several values of the applied magnetic induction B_0 . The experimental results show that for a given B_0 , thrust output is, in general, directly proportional to the electrode current. Also, as B_0 is increased for a given current, thrust reaches a maximum at about 3 kilogauss and then decreases. A maximum thrust increment of 3.6 lbf was obtained with a current of 3200 amp at 82 v and an induction of 1840 gauss.

The theoretical expressions for thrust and efficiency in terms of easily measured parameters have been developed previously (1 through 4). For a constant area accelerator, assuming (U_1, B_2, E_2) -dimensionality, the thrust Θ_d of an MGD driver is given by

$$\Theta_d = I_4 B_0 h$$

in which I_4 is the total electrode current and h is the electrode spacing.

For a better comparison of the experimental results with theory, the data were cross-plotted as thrust vs. B_0 as shown in Fig. 4. The data closely agree with theory up to about 3 kilogauss for all levels of electrode current. Even closer correlation has been achieved with other electrode configurations. The departure above 3 kilogauss indicates a deviation of the plasma and current flow from the (U_1, B_2, E_2) -dimensionality assumed in the theory. For higher magnetic fields it appears that the dimensionality is $(U_{1.2}, B_2, E_{1.2})$ since the Hall effect introduces an axial component to the current (2). In evidence of this is the upward deflection of the plasma stream. Also, end effects could become significant at high B_0 . It must be pointed out that the departure of measured thrust from the ideal theoretical values represents only a deviation of the physical phenomenon from the ideal theoretical model and does not infer any proportional loss of efficiency. At the thrust level of 3.6 lbf the efficiency of conversion of total electrical energy to kinetic energy of the plasma reached $(54 \pm 3)\%$ with argon. With nitrogen the efficiency reached $(22 \pm 1)\%$. No attempt was made to optimize the efficiency of this device but the accuracy of the efficiency measurements was improved over previous results (1).

It is believed that the direct measurements of thrust, efficiency, and specific impulse represent a unique approach to plasma propulsion investigation. The linear acceleration of a plasma stream by continuous Lorentz forces has been demonstrated. The experimental results show that high thrust and efficiency can be readily obtained. There appears to be no limitation to the thrust (or specific impulse) produced if the magnetic induction is kept moderate, i.e., below 3 kilogauss. Acceleration efficiencies higher than 60% and specific impulses of about 5000 sec appear possible with MGD engines.

References

- Demetriades, S. T., "Experimental Magnetogasdynamic Engine for Argon, Nitrogen and Air," ASRL-TM-60-23, Norair Div., Northrop Corp., November 1960; presented at Second Symposium on the Engng. Aspects of Magnetohydrodynamics, Univ. of Penn., March 9-10, 1961 (proceedings to be published).
- Demetriades, S. T. and Ziemer, R. W., "Energy Transfer to Plasmas by Continuous Lorentz Forces," ASG-TM-61-37, Norair Div., Northrop Corp., May 1961; presented at the Fourth Biennial Gas Dynamics Symposium, Northwestern Univ., Evanston, Ill., August 1961 (proceedings to be published).
- Demetriades, S. T., "Magnetogasdynamic Acceleration of Flowing Gases and Applications," NB-59-153, Norair Div., Northrop Corp.; ASTIA Doc. AD-229-672, March 23, 1959; also *Nuclear Sci. Abst.*, USAEC Tech. Info. Service, vol. 14, no. 10, Abstract 10114, May 31, 1960.
- Demetriades, S. T., "Magnetohydrodynamic Orbit Control for Satellites," ASRL-TM-60-6, June 1960; also presented at AIEE Pacific General Meeting, Aug. 8-12, 1960 (CP 60-1087); *Elec. Engng.*, vol. 79, no. 12, December 1960, pp. 987-995.

Time Relationships for Interplanetary Trajectories¹

WERNER M. PAUSON²

Space Sciences Laboratory, General Electric Co.,
Philadelphia, Pa.

A set of curves is presented depicting various classes of flight paths to several planets as functions of the trip time and departure date required for impacting trajectories. Results are based on a two-dimensional model of the solar system with the planets revolving in circular orbits. The only attractive force considered is that of the sun, so that the vehicle trajectory is a Kepler orbit.

NUMEROUS parameters or conditions may be used to specify an interplanetary mission. Quite often it is desired to perform feasibility studies with the known parameters being trip time and departure date. From this information alone, there is no direct method available for determining the orbital elements and other characteristics of the trajectory, due to the transcendental nature of the equations involved. The first problem encountered in attempting to compute the orbital elements, and the subject of this note, is the determination of the route which the vehicle traverses between the departure and destination planets.

Between the orbits of two planets of the solar system the vehicle may follow one of several routes; Fig. 1 shows the case of an elliptic transfer path. Considering P_1 to be the departure planet and P_2 the destination planet these four alternate routes are possible:

Route D	$P_1 P_2'$	Direct route
Route P	$P_1' P_1 P_2'$	Perihelion route
Route A	$P_1 P_2' P_2''$	Aphelion route
Route I	$P_1' P_1 P_2' P_2''$	Indirect route

For a hyperbolic orbit only two alternate routes are possible:

Route D _h	Direct hyperbolic route
Route P _h	Hyperbolic perihelion route

Routes, such as $P_1' P_2''$, which would require retrograde motion to the normal eastward revolution of the planets in the solar system, are not considered in this study.

The following assumptions have been made in this analysis:

- 1 The only attractive force acting on the vehicle is the sun, making the trajectory a Kepler orbit.
- 2 The planets of the solar system revolve in circular orbits.
- 3 The orbital planes of all the planets lie in the ecliptic plane.

The route traversed by the vehicle is uniquely determined by the trip time and departure date. However, since the relation between these quantities is an implicit one, the route cannot be found directly. Charts, depicting the different route areas as functions of trip time and departure date, may be constructed by noting that the various routes are separated by several special trajectories. These limiting trajectories are:

- 1 Tangent to departure planet at departure.
- 2 Tangent to destination planet at arrival.
- 3 Straight line.
- 4 Parabolic.

Received May 18, 1961.

¹ This work was one phase of the research performed under Air Force Contract AF 33(616)-6296 with the Directorate of Advanced Systems Technology, Wright Air Development Div., Air Research and Development Command, USAF.

² Analyst, Celestial Mechanics. Member ARS.

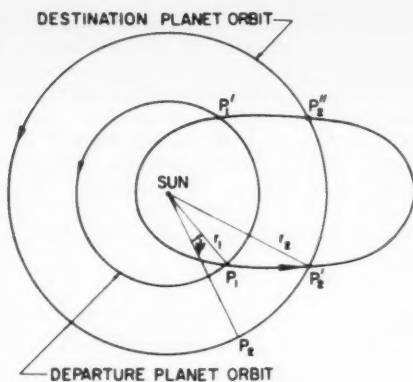


Fig. 1 Elliptic transfer paths

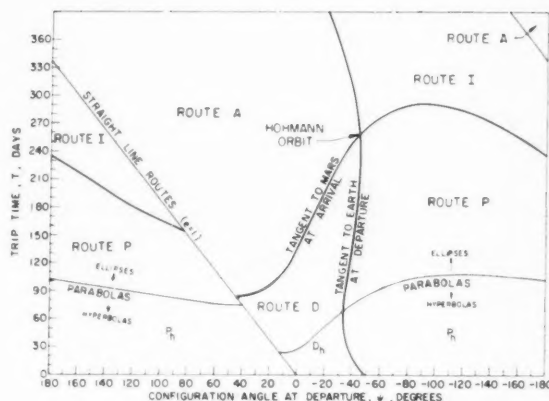


Fig. 2 Earth to Mars transfer orbit characteristics

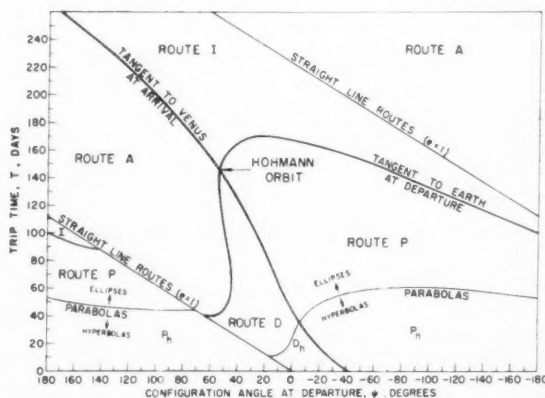


Fig. 3 Earth to Venus transfer orbit characteristics

Figs. 2 through 6 show the route areas for trips to and from several planets. Abbreviated versions of some of these figures have been employed in the trajectory analyses of (1,2).³ The departure date is expressed in terms of ψ , the configuration angle between the planets involved at the moment of departure. ψ is measured positively from the destination planet to the departure planet in the direction of motion.

For the case of a trip to an outer planet (Fig. 2), when the

³ Numbers in parentheses indicate References at end of paper.

transfer path is tangent to the departure planet's orbit, i.e., departure from perihelion, routes D and P become indistinguishable, as do routes A and I. A second boundary condition occurs when the trajectory is tangent to the destination planet's orbit, i.e., arrival at aphelion. In this event route D is identical to route A, and route P to route I. Another class of trajectories separating the various routes are straight line paths arriving at opposition. For example, consider a sequence of trajectories having a constant initial configuration angle and continually increasing trip times.

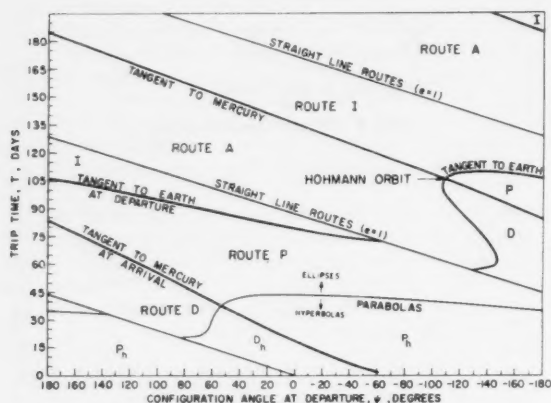


Fig. 4 Earth to Mercury transfer orbit characteristics

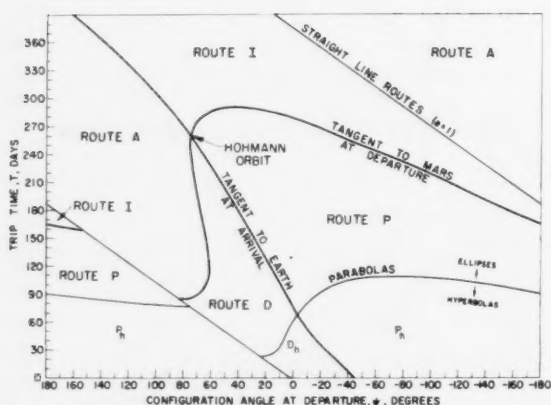


Fig. 5 Mars to Earth transfer orbit characteristics

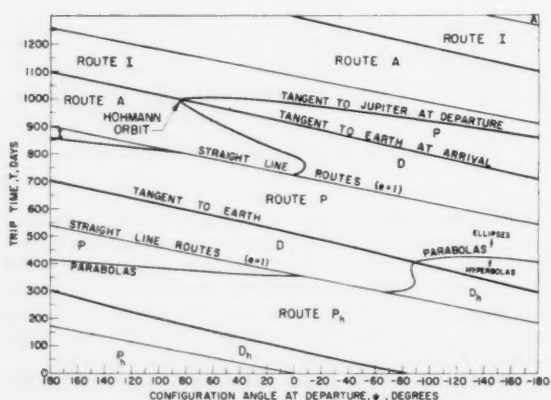


Fig. 6 Jupiter to Earth transfer orbit characteristics

Let the initial trajectory be on route P. Then, increasing the trip time necessitates that impact occur at increasing angular distances from the position of the destination planet at departure. Finally a trip time is reached for which impact must occur at opposition, and the elliptic trajectory degenerates into a straight line path. As the trip time progresses beyond this value, for the given initial configuration angle, the vehicle must follow an elliptical path along route A in order to further increase the angular separation of the impact point from the original position of the destination planet. The final boundary condition is the line representing parabolic trajectories, which separates elliptic from hyperbolic routes. A similar explanation may be presented for the curves of flights to planets whose orbits are closer to the sun than that of the departure planet.

From the above discussion it is seen that the theory underlying the route area curves is quite simple. However, the construction of the curves is rather laborious, since even for the boundary trajectories trip time is implicitly related to configuration angle through a third orbital parameter. In terms of the eccentricity e of the transfer path, the equations appear as follows for an elliptic trajectory tangent to the departure planet on route D to an outer planet

$$T_D = \left(\frac{r_1}{r_e} \right)^{3/2} \frac{(1-e)^{3/2}}{2\pi} \times \left[e \sin \cos^{-1} \frac{1-n(1+e)}{e} - \cos^{-1} \frac{1-n(1+e)}{e} \right] \text{ years}$$

$$\psi_D = \frac{2\pi}{n^{3/2}} T_D + \cos^{-1} \frac{1+e-n}{ne} \text{ radians}$$

where

- $n = r_2/r_1$
- r_1 = radius of departure planet's orbit
- r_2 = radius of destination planet's orbit
- r_e = radius of Earth's orbit
- e = eccentricity of transfer path
- T = trip time
- ψ = initial configuration angle

These equations, as well as those for the other routes and limiting trajectories, are plotted in Figs. 2 through 6. They may easily be derived from the general equations presented in (3). Only for the straight line paths are trip time and configuration angle directly related.

It is interesting to note that the parabolic orbits approach linearity on both routes D and P, yielding two points of contact between the parabolic and straight line boundaries. The section of the straight line boundary between these points differentiates route D from route P, as well as elliptic routes from hyperbolic routes.

From these figures it can be seen that even if the required energy were available, certain combinations of trip time and configuration angle are not feasible for actual interplanetary flights. For example, trajectories on routes P and I in the vicinity of the straight line boundary will pass very close to the sun at perihelion.

The curves also show that the range of departure dates for direct routes increases as the radial distance from the departure planet's orbit to the destination planet's orbit increases. This effect is most noticeable for trips to inner planets (Figs. 4 and 6). In this case, due to the large distance between the planetary orbits and the relatively short period of revolution of the destination planet, only small variations in the location of the impact point are required for large changes in the initial configuration angle.

A method of determining approximate initial conditions, with the aid of the route area curves, for a precision interplanetary trajectory computer program is presented in (4). Also included therein is a complete set of route area curves for

trajectories from Earth to any planet, except Pluto, as well as for return trips.

References

1 Lorell, J., "Two Dimensional Analysis of Interplanetary Flight Schedules," Memo. 30-13, Jet Prop. Lab., C.I.T., Dec. 1, 1959.

2 Dugan, J. F., Jr. and Simsic, C. R., "Analysis of Trajectory Parameters For Probe and Round-Trip Missions to Venus," NASA TN-D-470, November 1960.

3 Vertregt, M., "Interplanetary Orbits," *J. British Interplanetary Soc.*, vol. 16, no. 6, March-April 1958.

4 de Vries, J. P., Coordinator, "Generalized Interplanetary Trajectory Study," Part II, WADD Tech. Rep. 60-502, January 1961.

Summary of Solid Propellant Residual Thrust Studies

J. A. MORRIS¹

ARO, Inc., Arnold Engineering Development Center
Tullahoma, Tenn.

The residual burning of solid rockets after nominal burnout has caused problems in some third-stage space probe applications. This paper deals with the measurement of residual impulse at simulated altitude conditions and the determination of total impulse to extreme accuracies. A method used to protect the payload from an outgassing last stage rocket motor is also explained.

THE TELEMETRY data that have become available from certain satellites and from some rocket payloads have indicated that, on occasion, collisions occur between the final rocket stage and the payload after apparent burnout of the rocket motor. Such collisions, which may damage the payload or cause it to veer off course, are generally attributed to "residual burning," that is, to the burning that takes place after thrust and chamber pressure have nominally returned to zero. This burning, or smoldering over an extended period can only be simulated if the ambient pressure is near zero, as in the case of an altitude test cell. In mid 1958 a series of full scale third-stage rockets were tested in altitude test cells for the first time. Photographic data and thrust instrumentation showed that the motor apparently burned out at 40 sec after ignition, but began to smoke and smolder until combustion at a reduced rate was steady again, building up to a thrust peak of 245 lb 46 sec after apparent burnout. Other difficulties such as marginally designed nozzles were discovered which had not been apparent during sea level firings of this motor. The nozzle was improved and later demonstrated good durability.

Since there had been some indication of outgassing of the solid rocket motor which was to be used as the last stage of the Able IV lunar probe (some flow of gasses from the rocket nozzle after burnout), the third-stage motors were tested in the Rocket Test Facility altitude test cells at the Arnold Center² in October 1959. The purpose of this test was twofold: to determine the total impulse to the extreme accuracy required for such a shot, and to measure any residual thrust due to propellant sliver smoldering or the burning of insulation. To accomplish the latter objective, the NASA requested that motor chamber pressure and thrust be measured for 1000 sec after apparent burnout while the simulated test cell pressure altitude was maintained near 125,000 ft. The former objective would be achieved by firing the motor at an altitude at which the altitude nozzle would flow full, and by accurately measuring the impulse during the nominal firing time. In such a case the vacuum impulse correction is on the

order of only 0.5% of the total impulse as compared with the 17% correction necessary for a sea level firing. Total impulse data were obtained with a maximum interchannel deviation of less than 0.19% for the three firings.

The first attempt to measure the low range thrust was quantitatively unsuccessful, since the low range load cell indicated a zero shift during the test. The expansion of the thrust measuring load column caused the vertical flexures supporting the rocket and test stand to deflect, and a vertical weight component was indicated on the low range load cell. The load cell itself could have been affected by heat during the 1000-sec data acquisition time following nominal motor burnout. However, the qualitative data from the load cell definitely established that some residual thrust was being produced as long as 5 min after apparent burnout (Fig. 1). The low range motor chamber pressure transducers were affected by the temperature, and the shift in the system zeros nullified the quantitative data, even though the pressure data agreed with the thrust data in trend, if not in value. The test also showed a measured total impulse during the main firing approximately 0.7% lower than anticipated; this would equal over 3 lb of propellant left after nominal burnout. If this 0.7% missing impulse were produced after payload separation, it would amount to over 800 lb-sec, more than sufficient impulse to cause collision with and damage to the payload.

Since the Able IV lunar probe was being readied for launching, and since no reliable quantitative values had been obtained, a theoretically calculated value of the impulse obtainable from the burning of the insulation was used to size a heavier separation spring of approximately 50 lb-sec in order to prevent a collision. This expedient was adopted because the data indicated that outgassing was apparently present minutes after the firing, and because the lengthy duration of the outgassing made a simple increase in the payload "hold" time after third-stage burnout before payload separation an insufficient correction. However, the third stage did not

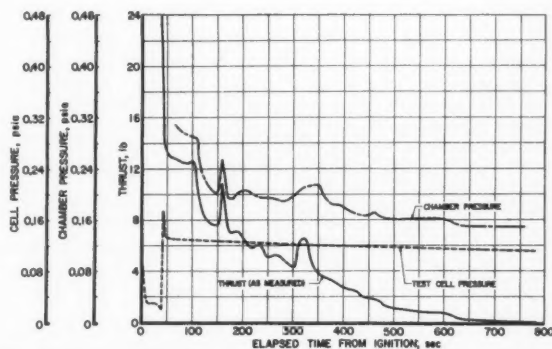


Fig. 1. Outgassing data for solid rocket motor test T-3-13-02

Received May 1, 1961.

¹ Project Engineer, Rocket Branch. Member ARS.

² The Arnold Center is one of the ten research, development, and testing centers of the Air Force Systems Command and is operated by a private concern, ARO, Inc.

have an opportunity to perform during the November 1959 shot because of failure in the lower stages.

In August 1960 three more third-stage rocket motors were secured by the NASA for altitude tests at the Arnold Center (1).³ For these tests the total impulse measurements at

³ Numbers in parentheses indicate Reference at end of paper.

Table 1 Total impulse corrected to vacuum (lb_f-sec)

CHANNEL	TEST NUMBER		
	T3-35-01 (Vac Corr - 1290)	T3-35-02 (Vac Corr - 1055)	T3-35-03 (Vac Corr - 1351)
DIGITAL COUNTER	1	115885	115618
	2	115953	115761
	3	115862	115365
	4	115894	115354
	Average	115898	115524
Maximum Deviation from Average, %		0.05	0.20
MAGNETIC TAPE	1	115790	115428
	2	115990	115629
	3	115790	115529
	4	115890	115329
	Average	115865	115479
Maximum Deviation from Average, %		0.11	0.13
Average for Three Firings (eight channels), 115738 lb _f - sec			
Maximum Deviation from Average for Three Firings, 0.21 %			

altitude were of prime importance because of the necessity of resolving the matter of the correct value of total impulse, that is, whether the impulse is actually lower than the manufacturer anticipated by 0.7% or whether the October 1959 data were incorrect. The average total impulse was therefore obtained from four independent thrust measuring systems. (No attempt was made to measure thrust after nominal burnout, since all available thrust data channels were used to determine total impulse during main burning.) The results agreed with October 1959 results within 0.026% (Table 1). These two values, in turn, agreed with results from two other series of firings of the same motor at the Arnold Center (Table 2). The four series tested over a period of two years had a maximum deviation of the measured total impulse of only 0.7%. (During this interval another series of tests was also made, but a nozzle separation occurred during two of the three firings.)

Since the residual thrust was still a large unknown and a very critical item, another attempt was made to obtain some measurement of the impulse occurring after nominal burnout. If the burning was due to smoldering insulation, the impulse would be small enough to be easily handled by devices such as the stronger separation spring between the payload and the last rocket stage. Residual burning of the propellant would be a much more serious matter. Thus the first question was whether any propellant remained after the main burnout.

In the first test of this series, therefore, a CO₂ quench was applied immediately after thrust had apparently returned to zero. Little information was obtained. The comparison of the motor weight before and after firing with the weight of the same type rockets which had not experienced the quench showed that apparently one pound less was consumed when the CO₂ quench was used.

The motor chamber pressure after apparent burnout was measured on the next two tests using a series of extremely sensitive pressure transducers covering and overlapping the expected range of chamber pressure. This redundancy and overlapping of separate systems gave a high level of confidence to these pressure data for the entire 1000 sec of data acquisition.

Table 2 Data summary of all third-stage motors of this type tested at Arnold Center

SERIES	1 (August 1958)		2 (Sep. 1958)	3 (May 1959)			4 (September 1959)			5 (Current Series)		
Serial Number	SV-17	SV-18	SV-32	SV-43	SV-41	SV-44	SV-77-A5	SV-62-A8	SV-56-A2	SV-131	SV-134	SV-135
Date Fired	7/15/58	7/15/58	9/16/58	5/28/59	5/28/59	5/28/59	9/22/59	9/22/59	9/23/59	8/5/60	8/8/60	8/9/60
Total Impulse at Vac. (avg), lb _f -sec	116,822	116,378	117,521	116,808	116,316	116,495	115,609	115,589	115,926	115,882	115,502	115,829
Specific Impulse at Vac. *, sec	255.9	255.4	257.0	255.9	254.8	255.3	253.5	254.0	254.8	254.5	254.9	254.2
Specific Impulse at Vac. **, sec	250.4	249.6	252.0	251.3	251.0	250.9	248.0	246.7	248.8	249.4	249.2	248.6
Average Specific Impulse for Series*, sec	255.7		257.0	255.3*			254.1			254.5		
Average Total Impulse for Series, lb _f -sec	116,600		117,521	116,540			115,708			115,738		
Deviation of Average Specific Impulse* from that of Series 5, percent	+0.47		+0.98	+0.31			-0.16			Base		
Deviation of Average Total Impulse from that of Series 5, percent	+0.745		+1.541	+0.693			-0.026			Base		

*Based on manufacturer's propellant weight

**Based on weight difference

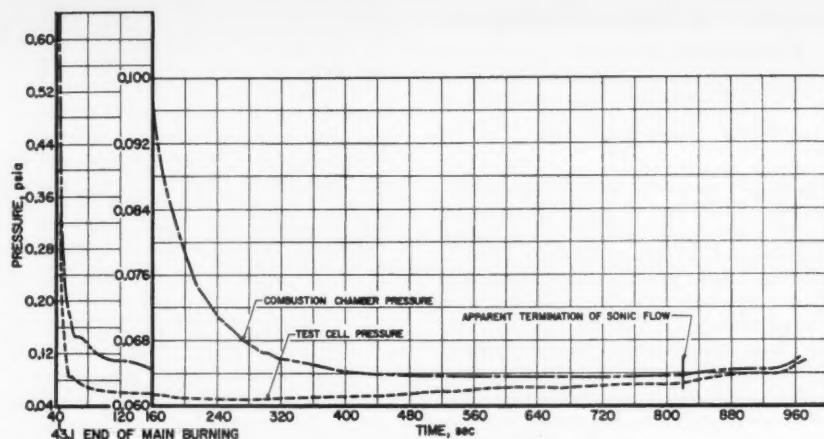


Fig. 2 Outgassing pressure for solid rocket motor test T3-35-03

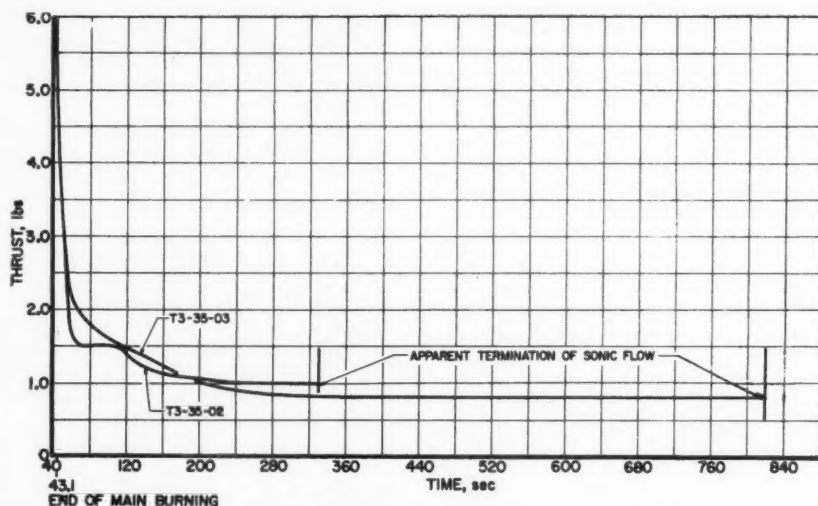


Fig. 3 Thrust as calculated from outgassing chamber pressure data for solid rocket motor test T3-35-02, T3-35-03

tion time following main burnout. The transducers were also shock-mounted in an insulated box to eliminate as much temperature effect as possible. In addition, since the range of the pressure readings expected bordered on the specified accuracy of the instrumentation system, and since some electronic drift must always be anticipated, a unique system was devised whereby the pressure leads to the differential transducers were mechanically reversed every 10 sec during the 1000-sec period of data recording following nominal burnout.

The results not only proved positively the existence of a pressure differential between the motor chamber and test cell but determined the difference quantitatively (Fig. 2). With these pressure data and the nozzle coefficient calculated from normal propellant burning, the outgassing (residual burning) thrust could then be calculated (Fig. 3). For one firing, the impulse calculated for the period of 777 sec following nominal burnout (during which choked flow was plainly evident) had a value of approximately 0.7% of the total impulse; this would amount to approximately 750 lb-sec impulse and almost three pounds of propellant. Such an amount of impulse occurring thus after nominal burnout would cause a collision with an impact of 54 lb-sec between the third stage and the payload 31 sec after separation.

The movie film of the firings also showed outgassing for 270 sec until the camera lens coated over and the poor quality of the film made it useless as data.

In view of the results of this test, both Echo I and the Able V lunar probe adopted a system for forcing the rocket case off course after separation to avoid collision with the payload. A weight is released from the nose of the spin-stabilized rocket, and this weight, attached by a cable, is unwound causing the rocket to stop rotating. The weight, having unwound one circumference and stopped the spinning, is then released and the rocket is forced out of the payload orbit.

A recent test in November 1960 at the Arnold Center of a solid propellant orbiting retro rocket showed outgassing or residual burning still present 8 sec after the 12-sec burn period.

Until it is clearly evident from altitude tests that no appreciable amount of outgassing or residual burning is present in each series of upper atmosphere solid rockets, precautions must be taken to protect the payload from last stage collision. It is also apparent that total impulse at simulated altitudes must be measured with extreme accuracy in order to program the space probes with the precision necessary for a successful mission.

Reference

- 1 Morris, J. A. and Byrd, R. J., "Ballistic Performance and Outgassing Studies of X248-A9 Rockets at Simulated Altitude Conditions," AEDC-TN-60-229, November 1960.

Plateau Ballistics in Nitrocellulose Propellants

R. F. Preckel¹

Hercules Powder Co. Cumberland, Md.

Nitrocellulose propellants normally give straight line ballistics; however, addition of certain lead compounds tend to level the burning rate in pressure intervals below 5000 psi. This phenomenon has been christened the "plateau" effect, and a trivial designation "platonic" propellant has arisen. Burning rates in a plateau are always higher than in the absence of lead compound. Extensive work has been done to characterize the limitations and advantages associated with the effect. This has included studies of heat of explosion, concentrations of ingredients, structure of polymer, inert and explosive plasticizer molecules, per cent nitrogen in nitrocellulose of varying molecular weights, etc. Various lead compounds are effective, including oxides, stearate and 2-ethylhexoate. Platonization occurs without ill effect on temperature coefficient of burning rate, hence the temperature coefficient pressure π_K is radically improved in the plateau where the pressure index n is small. In several instances the π_K of platonic propellants is about 0.1%/°F compared with at least 1%/°F for the high performance propellant JPN. Additionally, since equilibrium pressure is proportional to K to the exponent $1/(1 - n)$, rockets using plateau propellants are relatively insensitive to effects of nozzle erosion or variations in propellant surface.

THE EMPHASIS on low pressure ballistics began in 1939 when the use of rockets became widespread. Low potential nitrocellulose propellants were investigated to reduce nozzle erosion, burning rate and pressure index. Extrusion of massive charges required extrusion lubricants, and fortuitously, a relatively cool formulation was extruded with lead stearate lubricant. Radically unusual ballistic behavior in rockets, which was observed by W. H. Avery (1)², led to extensive study in both rockets and a laboratory strand burning apparatus, which was devised by B. L. Crawford (2).

Plateau Phenomenon

Ordinary nitrocellulose propellants, having burning rates, $r = cP^n$ at 1000 psi in the range 0.2 to 0.6 ips, show a pressure index n ranging from 0.6 to 0.9. Early solventless rocket propellants were high in nitroglycerin NG and low in nitrocellulose NC; for example, JPN, containing 53 NC, 43 NG, 3 diethylphthalate and 1 stabilizer. Such a system is soft and amenable to the standard solventless process. Clearly JPN is a quite "hot" formula, calculating energy of explosion H_{EX} equal to 1250 cal/gm. Its high energy and corresponding flame temperature required thick walled steel motors and made for rapid erosion of steel nozzles. Thus, investigations of "cool" propellants were begun; a 700 cal/gm composition follows: 58.5 NC, 22.5 NG, 8.5 triacetin, 8.0 *s*-diethyldiphenyl urea and 2.5 dinitrotoluene. The addition of small amounts of lead stearate, PbSt, produced the radical alteration in internal ballistics of Fig. 1.

The plateau effect always involves increased burning rates over a range of pressure below some critical value at and above which the plateau is not observed and the r - P relationship is entirely conventional. In the plateau, r tends to be independent of P , leading to higher relative increases at lower

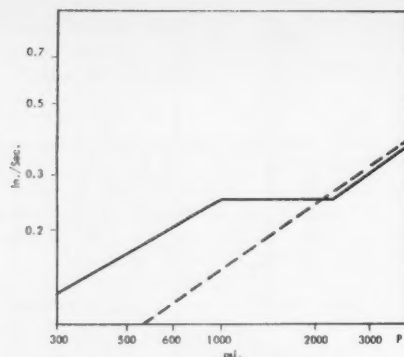


Fig. 1 Plateau effect

pressures until another critical pressure is reached below which n again increases, but usually not to the nonplatonic value. A very hot propellant such as JPN is not susceptible to ballistic modification by PbSt, even though enough salt may be added to bring the calorific value to 700-800 cal/gm. However, the strand burning rate at 1000 psi and 25 °C decreases regularly.

A series of platonic propellants made up with NC, NG, TA and PbSt, retaining PbSt at 2% in each and balancing H_{EX} to about 800 cal/gm shows the following variation of plateau burning rate with NC content:

NC%	60	55	50	45	40
r_{1000}	0.23	0.21	0.20	0.18	0.19

This indicates that one may expect burning rates to decrease with NC. It might be interesting to speculate that a low liquefaction point of such systems leads to a progressively thicker mobile layer at the burning surface with increasing capability of diluting the reactive species. Thus the net rate of regression would be lowered.

PbSt%	H_{EX} , cal/gm	Plateau n	Plateau r , ips
0.0	700	0.70 (no plateau)	0.22 at 1000 psi 0.29 at 1500 psi
0.1	695	0.45	0.31 at 1500 psi
0.4	690	0.20	0.32 at 1500 psi
1.0	675	0.0	0.27 at 1000 psi
4.0	595	0.0	0.22 at 1000 psi
7.0	730	0.0	0.18 at 1000 psi

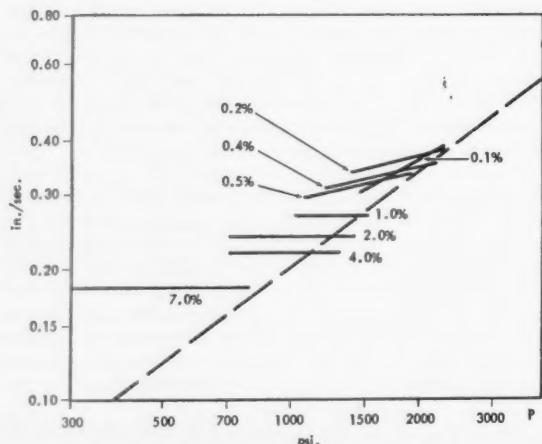


Fig. 2 Plateaus with lead stearate

Presented at the ARS Solid Propellant Rocket Conf., Salt Lake City, Utah, Feb. 1-3, 1961; revision received July 19, 1961.

¹ Senior Scientist, Allegany Ballistics Lab.

² Numbers in parentheses indicate References at end of paper.

Clearly from the evidence (Fig. 2), between 0.5 and 1.0% PbSt will give efficient use of the modifier. Higher lead salt concentrations move the plateau to lower pressures and burning rates.

Omission of all ingredients except NC and PbSt results in retention of plateau ballistics, a system 99 NC, 1 stabilizer and 4 PbSt shows a zero slope plateau at 0.34 ips. Some experiments with liquid nitrate esters have shown plateaus as well.

A number of lead compounds have been investigated in systems similar to that of the original discovery. Ballistics are shown in the following table:

Lead compound	%	Plateau n	Plateau r_{1000}
PbSt	0.5	0.22	0.28 ips
PbO	4.0	0.0	0.17 (at 500 psi)
Pb ₂ O ₄	0.5	0.0	0.24
PbO ₂	0.5	0.0	0.24
L-26*	2.0	0.0	0.25

* L-26 = lead 2-ethylhexoate.

Manufacture of platonic formulations is routine, providing that the generally insoluble salts are thoroughly dispersed. Plateau burning rates generally show a maximum at some lead concentration; such a formulation must be thoroughly mixed, since any local variation in concentration of lead salt decreases the rate. Lead compound toxicity will not be a problem if face masks and gloves, which are standard for dusty ingredients, are used.

Large rocket propellant charges of platonic formulae are made by the cast double-base process, in which solvent extruded "casting powder" is allowed to swell in a "casting" solvent of desensitized nitroglycerin; this gives a monolithic structure of excellent physical properties and ballistic reproducibility. Ballistic quality of the cast charge is dependent only on the properties of the casting powder; sound casting powder gives predictably good cast propellant. This has facilitated use of very large lot sizes without undue difficulty or expense. The platonic propellant system has established an enviable record for reliability and reproducibility in military and civilian applications, including Terrier, Talos, Nike, Honest John, Snark, Altair, aircraft jatos, turbine starters, hot gas servos and many others.

Plateau Internal Ballistics

It is clear that the plateau phenomenon, which is interesting because of its connection with the mechanisms of propellant gasification and combustion, should offer very important ballistic advantages over nonplatonic systems. These advantages have indeed been realized. Thus rockets will suffer little variation in burning time should the pressure be off design for any mechanical reason. Similarly, if burning surface area changes during burning, the change in area ratio of burning surface to nozzle throat area K will cause a less sharp change in pressure than in the absence of the plateau.

The advantage of low n comes from the rocket gas mass rate of discharge equation $m = S\rho r = C_D A_t P$ where propellant ρ and burning surface S is burning at rate r in a chamber at pressure P , discharging through nozzle throat area A_t and C_D is the discharge coefficient, a constant. Dividing $P/r = C'K$, and if $r = cP^n$, then $P^{1-n} = C''K$ or P is proportional to K with exponent $1/(1-n)$. The chamber pressure is then proportional at best to K , when $n = 0$, whereas at $n = 0.75$ as with JPN, P is proportional to K^4 .

The temperature coefficient of burning rate is generally decreased or unchanged in the plateau. Hence π_K , the temperature coefficient of equilibrium pressure at constant K will be very much improved over the nonplatonic case. We may observe that in favorable cases the π_K may be below 0.1%/°F, an order of magnitude less than the value of JPN.

Theoretical Considerations

While no complete theory of the plateau phenomenon is established, much pertinent and important work has been done attempting to understand its phenomenology and relationship to practical internal ballistics. The accepted mechanism of nitrate ester decomposition (3,4,5)³ to NO₂ and an RO' radical, followed by reduction of NO₂ to NO and eventual slower reduction of NO to N₂, has been thought to be involved in a catalytic cycle of reactions with Pb and PbO: Pb is oxidized by NO or NO₂, and the resulting PbO reacts with oxidizable molecules or fragments to regenerate Pb. This action can occur either in the gas phase or in a condensed "foam zone" in extreme outer layers of the burning material. The mechanism seems attractive and appropriate, but no conclusive demonstration of it has been given. Photomicrographs of burning propellant surfaces, and of carbonaceous debris sloughed off during strand burning in the closed bomb, have shown globules of molten lead at all pressures below the upper limit of the plateau. Above the plateau limit the globules are no longer observed. No such particles have ever been observed in vented vessel firings, perhaps only because no effective search has been made. Such observations, of course, have no firm bearing on the nature of the system's microscopic behavior; the entire catalytic action of the lead compound could well involve only oxygen-containing species in either condensed or in attenuated phases.

One approach suggests that the observed presence of carbon or carbonaceous material results from lead compound catalysis. The genesis of underoxidized material may liberate much heat in the condensed phase—more than any fragment evaporation process normally proposed could absorb. Condensed phase surface heat liberation could account for high rates in and below plateau pressures, the carbonaceous surface material progressively diminishing until it is absent at high pressure above the plateau. Cordite burning at relatively low pressure was found by Huffington (6) to show surface blackening, but his results were obtained at low surface regression rates occurring in wedge shaped gaps between propellant surfaces; also it is not known whether he used any lead compounds. It must be concluded that high heat release in surface layers of burning propellants has not been definitely shown.

Spalding (7) has surveyed solid and liquid propellant burning theoretically from a viewpoint he claims is close to that of the laminar gas flame. In the course of his discussions, he arrives at a suggestion of plateau ballistics, finding that the pressure index should tend toward zero at "high" pressures if the temperature dependence of surface decomposition rate is appropriate. However, no complete plateau was arrived at, since the high pressure high slope branch of the rate-pressure curve was not deduced.

The evidence shows that the important plateau mechanism occurs in or very near the burning surface, and that an easily heat-labile compound of lead must be importantly involved. More than this cannot be concluded from the available evidence.

References

- 1 Avery, W. H., Hunt, R. E. and Donin, M. N., "Burning Rate Studies in Double Base Powder," OSRD 5827, ABL/P/1, January 1946.
- 2 Sutton, G. P., *Rocket Propulsion Elements*, John Wiley & Sons, Inc., N. Y., 2nd ed., 1956, pp. 350 et seq.
- 3 Steinberger, R., "Nitrate Ester Flames," *Ind. Eng. Chem.*, vol. 48, 1956.
- 4 Rice, O. K. and Ginell, R., "Theory of Burning of Double-Base Rocket Powders," *J. Phys. and Col. Chem.*, 54, no. 6, 1950.
- 5 Parr, R. G. and Crawford, B. L., Jr., "A Physical Theory of Burning of Double-Base Rocket Propellants," *J. Phys. and Col. Chem.*, vol. 54, no. 6, 1950.
- 6 Huffington, J. D., "Anomalous Rates of Burning in Cordite," *Nature*, 165, May 27, 1950.
- 7 Spalding, D. B., "Theory of Burning of Solid and Liquid Propellants," *Combustion and Flame*, vol. 4, 1960.

³ Steinberger (3) has included a useful bibliography.

Practical Method for Compensation of Erosive Pressure Peaks

WILLIAM C. STONE¹

Rohm & Haas Co., Redstone Arsenal Research Div.
Huntsville, Ala.

Neutral burning characteristics are desirable from the standpoint of efficient case design, since the case must contain the maximum pressure. Rocket motors with a low initial port to throat area ratio $1/J$ show pressure peaks, which result from erosive burning and dynamic pressure drop along the burning surface. High L/D and loading fraction grains fall particularly into this class. One method of compensating for the initial pressure peak and thereby achieving a neutral head-end pressure trace is the reduction of the initial burning surface, i.e., using a progressivity ratio greater than unity. By use of the slotted tube grain design, progressivity ratio adjustments are possible by simple adjustment of the slot length. This method is illustrated in the design and development of a short duration booster motor having a loading fraction of 82%, an L/D of 14.7, and an initial $1/J$ of 1.33. A neutral head-end pressure trace was obtained by experimentally matching surface progressivity ratio with throat erosion and initial pressure peak.

HIGH mass ratio solid propellant rocket motors require light cases and highly loaded grains. Good case strength utilization is achieved when the maximum and working pressures are equal. Hence, a neutral pressure trace is desirable from the standpoint of reducing case weight. This paper presents a method for compensating for initial pressure peaks and thus obtaining a neutral pressure trace in a highly loaded solid propellant rocket motor.

Received June 7, 1961.

¹ Ballistician, Member ARS.

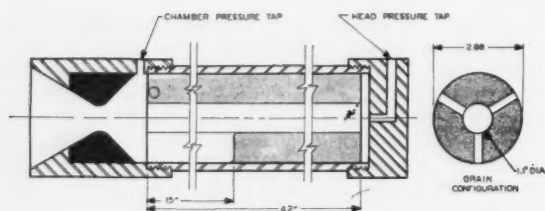


Fig. 1 3 x 42 static test motor

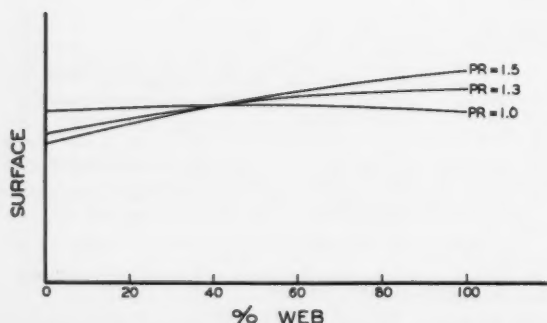


Fig. 2. Surface histories of a slotted tube, $L/D = 14.7$

Analysis

Solid propellant booster motor grains with high loading fractions are generally accompanied by high surface to port area ratios which result in values of J where erosive burning becomes a problem. The throat to port area ratio J determines the gas velocity over the aft portion of the propellant burning surface. Isentropic flow tables show that a J of 0.75 results in a value of 0.50 for the port Mach number, which is related to the amount of erosive burning experienced. It was not the purpose of this work to make a detailed investigation of the phenomena of erosive burning, but simply to assume that the burning rate increase is directly proportional to the velocity of the hot gases flowing over the propellant burning surface. The magnitude of the pressure increase due to erosive burning was left to experimental determination.

The rocket nozzle discharges gas at a rate proportional to chamber pressure, which differs from the head-end pressure. As the combustion products evolve from the burning surface, they are accelerated toward the nozzle by a pressure differential which is here referred to as dynamic pressure drop due to mass addition. The head-end pressure minus the dynamic pressure drop is the grain port pressure which decelerates into the chamber for expulsion through the nozzle. (See Fig. 1.) Application of the momentum equation to the gas flow through the grain perforation yields an expression for the dynamic pressure drop. Assuming no friction and using the ideal gas equation, it may be shown that the head to port pressure ratio is

$$P_h/P_p = 1 + \gamma M_p^2$$

Calculations with this equation yield a ball park value for the head to port pressure ratio of approximately 1.30 when J is 0.75. Some pressure is recovered when the flow is decelerated into the chamber, depending on the chamber to throat area ratio. These numbers show that a considerable initial head-end overpressure is possible due to dynamic pressure drop. Theoretical incorporation of this variation into a grain design is difficult due to the poor accuracy of the idealized calculations. Hence, the final grain design modifications to compensate for the overpressure must be determined experimentally.

The pressure trace of a rocket motor is also affected by the nozzle throat erosion. Data are available on the erosion rates of various throat insert materials, and estimates of the throat erosion and its effect on the shape of the pressure trace may be incorporated into the grain design theoretically. For this study the initial motor grain designs included this variation, but the final adjustments to compensate for throat erosion were made experimentally.

Application

A method of compensating for these burning pressure disturbances and thus obtaining a neutral pressure trace will now be described. Both erosive burning and dynamic pressure drop tend to raise the initial head-end pressure, and the throat erosion lowers the final pressure. These combined effects suggest a reduced initial burning surface to prevent the overpressure, i.e., a theoretical burning surface variation with a progressivity ratio greater than unity. The progressivity ratio must be tailored, through the experimental motor firings, to match the initial overpressure with the final erosion free burning pressure. To perform this experimental matching, a grain configuration with an easily modified progressivity ratio is needed.

The slotted tube grain design (1, 2) was found by this writer to be best suited to the above needs. It has particular utility in the high L/D application because of its low surface to port area ratio as compared with a star geometry. From the viewpoint of this paper, the most attractive feature of the slotted tube is the simple method by which its progressivity ratio is modified. The length of the slots determines the

progressivity ratio which may be varied by simply changing the slot length. Typical theoretical surface histories for the slotted tube are shown in Fig. 2.

Using these principles, a simple static test motor was designed and constructed. The important features of this 3×42 STM are shown in Fig. 1. Provisions for head- and aft-end pressure measurements were incorporated into the design. Casting equipment for the 3×42 STM was designed to permit a variable slot length by a variable length fin section of the mandrel. Plastisol composite double base propellant was used in the motor.

Testing and Results

Initial testing incorporated both head- and tail-end pressure measurements. An experimentally determined head to chamber pressure ratio history is shown in Fig. 3. Since the magnitude of the initial overpressure was not known, the first motors were cast with short slots which resulted in progressive traces as shown in Fig. 4. When an estimate of the overpressure due to erosive burning and dynamic pressure drop was obtained, the progressivity ratio was adjusted to obtain neutral pressure traces. Fig. 5 is a composite showing the effect of erosive burning, dynamic pressure drop, and throat erosion on the head-end pressure. As may be seen from Fig. 5, the 3×42 STM is a high pressure, short burning time motor. Its slotted tube grain configuration was used to design around the initial pressure peak which is normally encountered in high mass ratio solid rocket motors.

Grain geometries other than the slotted tube may be tailored in this same manner, but the surface progressivity ratio modifications are more tedious. As in the case of the star, the mandrel would require modification to alter the surface progressivity. Hence, the slotted tube has particular utility for this type of application.

Acknowledgment

The author wishes to express his appreciation to Max W. Stone for the use of his work on the slotted tube grain designs, and for special calculations on the computer for the $14.7 L/D$ design used in this work.

References

- 1 Stone, M. W., "Slotted Tube Grain Design," ARS JOURNAL, vol. 3, no. 2, February 1961, p. 223.
- 2 Personal conferences with Max W. Stone at Rohm & Haas Co., Huntsville, Ala.
- 3 Stone, M. W., "A Practical Mathematical Approach to Grain Design," JET PROPULSION, vol. 28, no. 4, April 1958, p. 236.

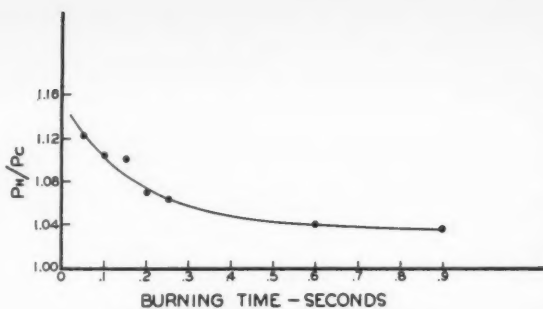


Fig. 3 Head to chamber pressure ratio

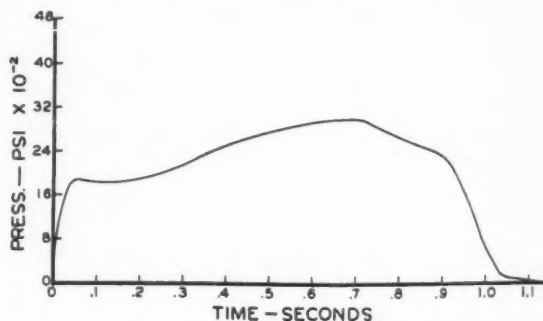


Fig. 4 Progressive pressure trace

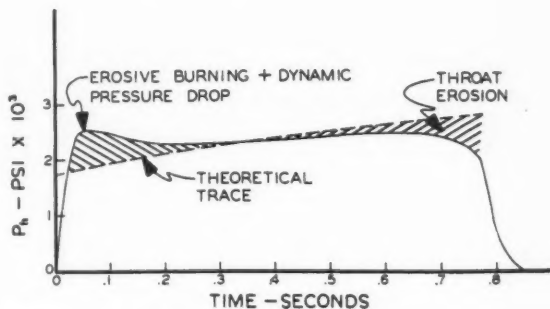


Fig. 5 Neutral pressure trace

Nonuniform Deceleration of a Slender Cone in Supersonic, Transonic and Subsonic Flight¹

CHENG-TING HSU²

Iowa State University, Ames, Iowa

IN A PREVIOUS note (1),³ the effect of constant deceleration on the pressure coefficient of a slender cone has been analyzed for arbitrarily large values of the deceleration

parameter β in all flight speed ranges. Since constant deceleration is less likely to be encountered in practical flight, the present note takes into account the effect of nonuniform deceleration on the pressure coefficient.

It is assumed that the deceleration of the cone is proportional to the drag force and that the drag coefficient decreases linearly with the velocity, i.e., $C_D = C_{D0} U/U_0$. Applying Newton's Second Law of Motion, we have

$$dU/d\tau = -\lambda U^2/U_0 \quad [1]$$

and

$$U = -d\xi/d\tau \quad [2]$$

Integrating Eqs. 1 and 2 and inserting the conditions that $U = U_0$ and $\xi = 0$ at $\tau = 0$ respectively, we obtain the flight path of the cone apex

$$\lambda \xi = 1 - \sqrt{1 + 2\lambda U_0 \tau} \quad [3]$$

Received June 5, 1961.

¹ This research was supported by Engineering Experiment Station of Iowa State Univ.

² Associate Professor, Dept. of Aerospace Eng. Member ARS.

³ Numbers in parentheses indicate References at end of paper.

which is shown in Fig. 1. The asymptotic potential for a slender body of revolution performing arbitrary motion along its axis was obtained by Cole (1 through 3)

where

$$\phi(x, r, t) = (1/2\pi)S(x, t) \log(r/2) - (1/4\pi)\{S[x_1, t - (x - x_1)/a] \log(x - x_1) + S[x_2, t - (x_2 - x)/a] \log(x_2 - x)\} - \frac{1}{4\pi} \int_{x_1}^{x_2} \left[\frac{1}{a} \frac{\partial S(\xi, \tau)}{\partial \tau} + \operatorname{sgn}(x - \xi) \frac{\partial S(\xi, \tau)}{\partial \xi} \right] \times \log|x - \xi| d\xi + \dots \quad [4]$$

$$\tau \doteq t - (|x - \xi|)/a \quad [5]$$

is the retrograde Mach cone. The integral in Eq. 4 is evaluated for those values of ξ which are common to the flight path of the cone apex and the surface of the retrograde cone (1-3). Solving Eqs. 3 and 5 for ξ , we have

$$\lambda x_1 = (M_0 + 1) - \sqrt{(M_0 + 1)^2 - 2\lambda M_0(x - at)} \quad [6a]$$

$$\lambda x_2 = -(M_0 - 1) + \sqrt{(M_0 - 1)^2 + 2\lambda M_0(x + at)} \quad [6b]$$

The source strength $S(x, t)$ is known for a given body shape (2, 3)

$$S(x, t) = U(t)A'(X) \quad [7]$$

where

$$X = x + \int_0^t U(\tau) d\tau$$

is a coordinate fixed in the body. In our case

$$U(\tau) = U_0/\sqrt{1 + 2\lambda U_0\tau} \quad [8]$$

and

$$A(x, t) \doteq \pi\delta^2[x - (1 - \sqrt{1 + 2\lambda U_0t})/\lambda] \quad [9]$$

Substituting Eqs. 8, 9 into 7, we have

$$S(x, t) = 2\pi\delta^2 U_0[1 - (1 - \lambda x)/\sqrt{1 + 2\lambda U_0t}]/\lambda \quad [10]$$

For small values of λU_0t (or $\beta' \ll 1$), Eq. 10 may be expanded, and retaining only the first order terms of λU_0t

$$S(x, t) \doteq 2\pi\delta^2 U_0[x + U_0t - \lambda U_0t(x + 3U_0t/2)] \quad [11]$$

Substituting Eqs. 6a, 6b, 11 into 4 and performing the integration, the velocity potential ϕ can be obtained. The pressure coefficient in unsteady flow, including squared term (3), is

$$C_p = -(2/U^2)(\partial\phi/\partial t) - (1/U^2)(\partial\phi/\partial r)^2 \quad [12]$$

Insert ϕ and Eq. 8 into Eq. 12 and set $t = 0$ and $r \doteq \delta x$; the surface pressure coefficient of a slender cone moving at instantaneous Mach number M_0 with nonuniform deceleration λU_0^2 is

$$C_p/\delta^2 = -1 - 2(1 - 2\beta') \log[\delta x/2\sqrt{(x - x_1)_0(x_2 - x)_0}] + 2\beta'[(1 + 3M_0)(x - x_1)_0 - (1 - 3M_0)(x_2 - x)_0]/x + \{[x_1/(x - x_1)]_0 - M_0 + 2\beta'M_0[x_1 - 3M_0(x - x_1)/2]_0/x\}/\sqrt{(M_0 + 1)^2 - 4\beta'M_0} + \{[x_2/(x_2 - x)]_0 - M_0 + 2\beta'M_0[x_2 - 3M_0(x_2 - x)/2]_0/x\}/\sqrt{(M_0 - 1)^2 + 4\beta'M_0} \quad [13]$$

where x_1 and x_2 are given in Eq. 6 and $\beta' = \lambda x/2$. The subscript "0" for any bracketed term containing x_1 and x_2 indicates the value which is obtained with $t = 0$ for x_1 and x_2 . Eq. 13 is plotted in Figs. 2 and 3 for a cone of semi-angle $\delta = 5$ and 10° respectively. In Fig. 2, the curve of constant deceleration $\beta = 0.5$ is taken from (1) for comparison. Note that since $\beta = \beta'M_0^2$, β may be large even for very small β' in supersonic flight. For example, with $\beta' = 0.01$ and $M_0 = 5$, $\beta = 0.25$. Therefore, it may be concluded that the effect of nonuniform deceleration on the pressure coefficient of a slender cone is also very small in the supersonic range, as

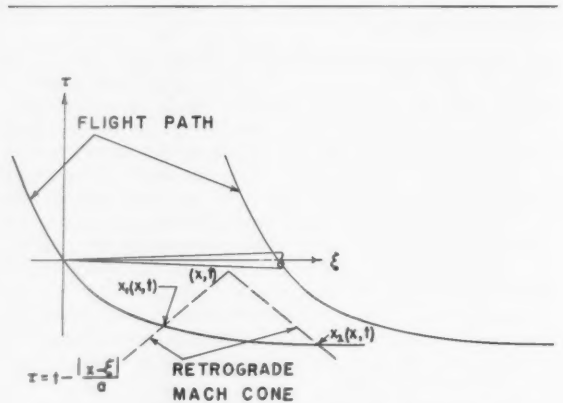


Fig. 1 Body flight path and retrograde Mach cone

in the case of constant deceleration (1). The restriction of small β' used in this analysis further limits the value of β to a much smaller value in the subsonic range. However, it is interesting to note that the use of the new deceleration parameter β' allows a finite value of C_p at $M_0 = 0$, i.e.

$$C_p/\delta^2 = -2 + 5\beta' - 2(1 - 2\beta') \log[\delta\sqrt{\beta'}/2\sqrt{1 - \beta'}] \quad [13a]$$

which may be obtained from Eqs. 13 and 6.

Approximate Expressions for C_p

Supersonic range

Eqs. 6a, 6b may be expanded in terms of $\beta'M_0/(M_0 + 1)^2$ and $\beta'M_0/(M_0 - 1)^2$ respectively at $t = 0$. Retaining only the first-order terms of β' , we have

$$x - x_1 = x/(M_0 + 1) - \beta'M_0^2x/(M_0 + 1)^3 \quad [14a]$$

$$x_2 - x = x/(M_0 - 1) - \beta'M_0^2x/(M_0 - 1)^3 \quad [14b]$$

Substituting Eq. 14 into 13 and retaining only the first-order terms of β' , we obtain

$$C_p/\delta^2 = -1 - 2(1 - 2\beta') \log(\delta/2)\sqrt{M_0^2 - 1} + (10M_0^4 - 18M_0^2 + 4)\beta'/(M_0^2 - 1)^2 \quad [15]$$

Transonic range

For $M_0 = 1$, Eq. 6a may be expanded in terms of β' at $t = 0$. Retaining only the first-order term of β' , we have

$$x_1 = (x/2)[1 + (\beta'/4)] \quad [16]$$

Substituting Eqs. 16, 6b into 13 and retaining only up to the first order of β' , we obtain

$$C_p/\delta^2 = -1 - 2(1 - 2\beta') \log \delta(\beta'/4)^{1/4} + 5\sqrt{\beta'} - (\beta'/4) \quad [17]$$

Subsonic range

Eqs. 6a, 6b may be expanded in terms of $\beta'M_0/(1 + M_0)^2$ and $\beta'M_0/(1 - M_0)^2$ respectively at $t = 0$. Retaining only the first-order terms of β' , Eq. 6a becomes 14a and Eq. 6b becomes

$$x_2 - x = [(1 - M_0)x/\beta'] - (1 - 2M_0)x/(1 - M_0) \quad [18]$$

Substituting Eqs. 14a, 18 into 13 and retaining only first-order terms of β' , we obtain

$$C_p/\delta^2 = -2(1 - 2\beta') \log [\delta\sqrt{(1 + M_0)\beta'}/2\sqrt{1 - M_0}] - 2 + 10M_0 - 9M_0^2 +$$

$$\left[\frac{2 - 12M_0 + 23M_0^2 - 12M_0^3}{(1 - M_0)^2} + \frac{2 + 8M_0 + 5M_0^2}{(1 + M_0)^2} \right] \beta' \quad [19]$$

Eqs. 15, 19 are also plotted in Figs. 2 and 3 for comparison with the exact values obtained from Eq. 13.

Correction on (1)

The first term of Eq. 12 in (1) should be written as

$$-2[1 - 2(M_0^2 - 1)\zeta/M_0^2] \log (\delta/2)\sqrt{M_0^2 - 1}$$

Acknowledgment

The author wishes to acknowledge Laverne Seversike and Fred Stuve of the Aerospace Dept. for checking all the formulas and computing the numerical values using the ISU digital computer.

Nomenclature

$A(X)$	= cross-sectional area
a	= speed of sound in the undisturbed fluid
C_D	= total drag coefficient of the cone, with respect to its base area
C_p	= $(p - p_\infty)/[(1/2)\rho U_0^2]$, pressure coefficient
M_0	= instantaneous Mach number at $t = 0$
$S(x, t)$	= source strength
x, r	= cylindrical coordinates fixed in the undisturbed fluid
t	= time
$U(t)$	= velocity, positive in the direction of the negative x -axis
β	= $-(dU/dt)_{t=0}x/2a^2 > 0$, deceleration parameter at $t = 0$

$$\beta' = -(dU/dt)_{t=0}x/2U_0^2 = \beta/M_0^2, \text{ new deceleration parameter at } t = 0$$

$$\delta = \text{cone semi-angle}$$

$$\lambda = 3C_{D0}\rho/2\rho L, \text{ a constant at } M_0, \text{ where } \rho_0 \text{ is density of the cone and } L \text{ is length of the cone}$$

$$\xi, \tau = \text{variables of } x \text{ and } t, \text{ respectively}$$

$$\rho = \text{density of undisturbed fluid}$$

$$\phi = \text{perturbation velocity potential}$$

Subscript

$$0 = \text{value at } t = 0$$

References

- 1 Hsu, C. T. and Anderson, D. A., "Effect of Deceleration on Pressure Distribution along a Slender Cone in Supersonic, Transonic and Subsonic Flight," *J. Aerospace Sci.*, vol. 28, no. 2, February 1961, pp. 173-174.
- 2 Cole, J. D., "Note on Nonstationary Slender-Body Theory," *J. Aeronaut. Sci.*, vol. 20, no. 11, November 1953, pp. 798-799.
- 3 Cole, J. D., "Acceleration of Slender Bodies of Revolution Through Sonic Velocity," *J. Appl. Phys.*, vol. 26, no. 3, March 1955, pp. 322-327.

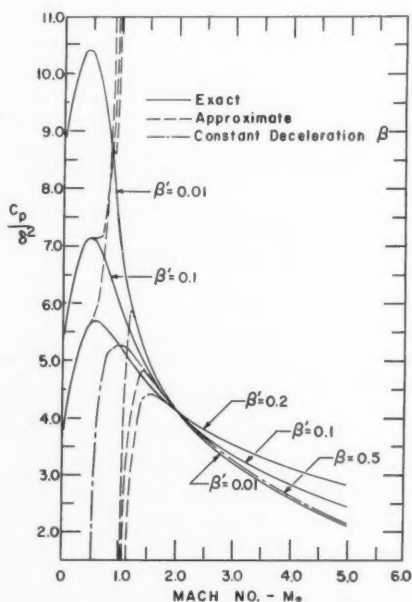


Fig. 2 Effect of deceleration on pressure coefficient, $\delta = 5^\circ$

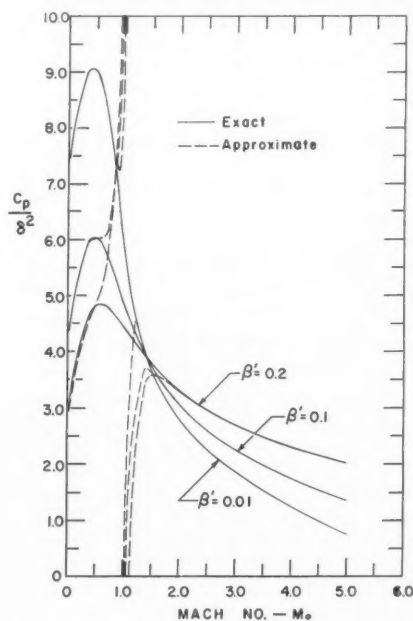


Fig. 3 Effect of deceleration on pressure coefficient, $\delta = 10^\circ$

Technical Comments

Comment on "Rapid Method for Plug Nozzle Design"

M. H. SEIDMAN¹

General Applied Science Laboratories, Inc.,
Westbury, N. Y.

A RECENT paper by Greer (1)² has indicated a rapid means of determining the contour of an ideal plug nozzle. This ideal nozzle is one which yields a uniform, axially parallel exhaust stream. It is the object of this note to point out an error in the analysis (1) and to indicate a proper means of computing the ideal contour.

In the method employed by Greer (1) the flow area was considered to be bounded by the line L_1 . See (1) for figures and nomenclature. The expansion ratio ϵ was then determined from this flow area.

Assuming a Prandtl-Meyer expansion fan at the lip and an ideal nozzle, the flow is uniform, with constant Mach number M along a characteristic line L_3 . The expansion ratio ϵ should be based on the flow region bounded by L_3 . Along L_1 the Mach number varies from the value at the wall to the value in the nozzle exit region M_e , and the area defined in (1) does not correspond to the wall Mach number.

Received May 26, 1961.

¹ Engineer, Aerodynamics Sect. Member ARS.

² Numbers in parentheses indicate Reference at end of paper.

Using this new manner of defining the flow region the flow area becomes

$$A = \pi L_3(r_2 + r_1) \sin \alpha \quad [1]$$

Since

$$\sin \alpha = \frac{1}{M} \quad [2]$$

the flow area becomes

$$A = \pi L_3 \frac{(r_2 + r_1)}{M} \quad [3]$$

Employing $L_3 = L_2/\cos(\alpha - \Psi - \omega)$ and $r_1 = r_2 - L_2$, Eqs. 8 and 9 of (1), there is finally obtained

$$\lambda = \frac{L_2}{r_2} = \frac{1}{\cos(\alpha - \Psi - \omega)} \times \{1 - [1 - \xi M \cos(\alpha - \Psi - \omega)]^{1/2}\} \quad [4]$$

With this equation and Eq. 6 of (1)

$$\Phi = 90 + \alpha - (\Psi + \omega) \quad [5]$$

the contour of an ideal plug nozzle can be determined.

Reference

1 Greer, H., "Rapid Method for Plug Nozzle Design," ARS JOURNAL, vol. 31, no. 4, April 1961, pp. 560-561.

Alternate Form of a Result by Nidey

ROBERT E. ROBERSON¹

Systems Corp. of America, Los Angeles, Calif.

IN A previously published paper (1),² Nidey gives a convenient representation in vector form of the gravitational torque on a satellite vehicle, namely

$$\mathbf{M} \approx 3\omega^2 \sum_i m_i (\mathbf{R}_i \times \mathbf{k})(\mathbf{R}_i \cdot \mathbf{k}) \quad [1]$$

where \mathbf{M} is torque, ω^2 is used to denote the gravitational constant for the central body divided by the cube of the radial distance from the gravitating center to the vehicle center of mass, m_i is the mass of the i th body particle, \mathbf{R}_i is its location relative to the center of mass, and \mathbf{k} is the unit vector along the outward-pointing geocentric vertical at the center of mass. For some purposes, rather than using his particular transformation of coordinate it is desirable to have a general representation in terms of the inertia dyadic, which is invariant under coordinate rotations, and a set of solar components relative to body principal axes.

Received May 25, 1961.

¹ Consultant in Astronautics. Member ARS.

² Numbers in parentheses indicate Reference at end of paper.

It is clear that Eq. 1 can be rewritten

$$\mathbf{M} = 3\omega^2 \mathbf{k} \cdot \left(\sum_i m_i \mathbf{R}_i \mathbf{R}_i \right) \times \mathbf{k} \quad [2]$$

where the terms in parentheses form a dyadic. Call it \mathcal{J}^* . Moreover, the customary inertia dyadic is defined as

$$\mathcal{J} = \sum_i m_i (\mathbf{R}_i \cdot \mathbf{R}_i \mathcal{E} - \mathbf{R}_i \mathbf{R}_i) \quad [3]$$

where \mathcal{E} is the unit dyadic. It is easy to obtain \mathcal{J}^* in terms of \mathcal{J} by expanding in component form. First

$$I_{jk} = I_{ii}^* \delta_{ji} - I_{jk}^* \quad [4]$$

from which $I_{jj} = 3I_{ii}^* - I_{jj}^* = 2I_{jj}^*$, or, $I_{ii}^* = \frac{1}{2}I_{ii} = \frac{1}{2}(\text{diag } \mathcal{J})$. Using this result in Eq. 4, and rewriting the result in dyadic notation,

$$\mathcal{J}^* = \frac{1}{2}(\text{diag } \mathcal{J})\mathcal{E} - \mathcal{J} \quad [5]$$

Using this in turn in Eq. 2,

$$\mathbf{M} = 3\omega^2 \mathbf{k} \cdot [\frac{1}{2}(\text{diag } \mathcal{J})\mathcal{E} - \mathcal{J}] \times \mathbf{k} \quad [6]$$

It is obvious from this form or Eq. 2 that $\mathbf{M} \cdot \mathbf{k} = 0$, i.e., no torque about \mathbf{k} .

Now denote by a_i the direction cosines of \mathbf{k} with respect to principal axes in the body, $\mathbf{e}_1, \mathbf{e}_2, \mathbf{e}_3$, so that $\mathbf{k} = a_i \mathbf{e}_i$. Then Eq. 6 takes the form

$$\begin{aligned} \mathbf{M} &= 3\omega^2 a_i \mathbf{e}_i \cdot \mathbf{e}_k [\frac{1}{2}(I_{jj})\delta_{ki} - I_{ki}] \mathbf{e}_i \times a_m \mathbf{e}_m \\ &= 3\omega^2 a_i [\frac{1}{2}(I_{jj})\delta_{ii} - I_{ii}] \epsilon_{imn} \mathbf{e}_n a_m \\ &= 3\omega^2 \{\epsilon_{imn} a_i a_m [\frac{1}{2}(I_{jj})\delta_{ii} - I_{ii}]\} \mathbf{e}_n \end{aligned} \quad [7]$$

As before, repeated indices denote summation and ϵ_{imn} is the so-called "e-symbol" of tensor analysis. Using the fact that $I_{ii} = 0$ unless $i = i$, it is straightforward to work out this expression to obtain

$$\mathbf{M} = 3\omega^2 [a_2 a_3 (I_{33} - I_{22}) \mathbf{e}_1 + a_3 a_1 (I_{11} - I_{33}) \mathbf{e}_2 + a_1 a_2 (I_{22} - I_{11}) \mathbf{e}_3] \quad [8]$$

a result which decomposes \mathbf{M} directly into body axes. This is a somewhat more convenient form than components relative to the space reference frame given as Nidey's Eq. 17.

As a particular case, suppose that $\mathbf{k} = \mathbf{e}_3$ ($a_1 = a_2 = 0$). Then $\mathbf{M} = 0$, if \mathbf{k} is along either of the other principal axes.

Acknowledgment

These results were obtained in the course of work for the Grumman Aircraft Engineering Corp. and are published with their kind permission.

Reference

- 1 Nidey, R. A. "Gravitational Torque on a Satellite of Arbitrary Shape," *ARS JOURNAL*, vol. 30, no. 2, February 1960, pp. 203-204.

New Patents

George F. McLaughlin, Contributor

Solid composite propellant (2,973,256). J. Linsk, Highland, Ind., assignor to Standard Oil Co. (Ind).

Cellulose binder, a catalyst containing Prussian blue, and the remainder essentially ammonium nitrate.

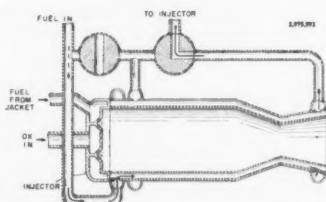
Propellant powder (2,973,257). D. W. Ryker and G. R. Cox, Creve Coeur, Mo., assignors to Olin Mathieson Chemical Corp. (ARS corporate member).

Spherical smokeless powder base grain in which is dispersed metallic lead, lead salts and lead oxides, shaped and solidified into gelatinized droplets.

Full pressure suit helmet and torso tiedown system (2,973,521). R. J. McGowan Jr., Arlington, Tex., assignor to the U. S. Navy.

Inflatable suit with rigid neckband for attaching a helmet by means of outside cables facilitating variation of cable tension on neckband, and bending of suit at waist.

Rocket thrust chamber (2,957,592). Z. Fox (ARS member), Verona N. J., assignor to Thiokol Chemical Corp. (ARS corporate member).



Chamber wall with two distinct sets of coolant passageways. Inlet valves allow

coolant fluid to flow through one set of passageways only for low thrust, and both sets for high thrust.

Accelerometers (2,973,647). H. J. Smith and W. G. Wing, Roslyn Heights, N. Y., assignors to Sperry Rand Corp. (ARS corporate member).

Sensitive element floating in a fluid filled chamber for movement along the axis. Pickoffs provide a signal output with displacement of the element from a null position.

Missile launcher (2,973,691). H. Goldsmith, Washington, D. C.

Magazine for continuously feeding, loading, and launching missiles and selectively jettisoning duds loaded in launching barrel.

Ignition of solid rocket propellants (2,973,713). J. M. Burton, Springfield, Va., assignor to Phillips Petroleum Co.

Ignition sustainer material positioned against a plug and in contact with igniter material. Ignition of a primer causes ignition of an initiator in a perforated sleeve connected to a tubular casing.

Solid composite, smokeless, slow burning, low flame propellant (2,974,026). G. W. Batchelder (ARS member), Glendora, Calif., assignor to Aerojet-General Corp. (ARS corporate member).

Polyester resin, styrene, methyl acrylate, ammonium nitrate, ammonium dichromate, methyl ethyl ketone peroxide, cobalt octoate, and lecithin.

Moving target radar system (2,974,317). H. Klemperer, Belmont, Mass., assignor to Raytheon Co. (ARS corporate member).

Directional radiating and receiving antenna, with means for radiating time-spaced pulses of HF energy and receiving their reflections from targets.

Rocket with gaseous effluent guide (2,974,476). H. M. Fox (ARS member), Bartlesville, Okla., assignor to Phillips Petroleum Co.

Guide formed of slowly combustible

hard carbon and aluminum, positioned in the open end of a shell and against the end of the propellant.

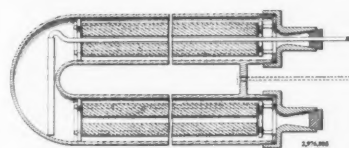
Ignition system for rocket motors (2,974,484). R. A. Cooley (ARS member), Rolla, Mo.

Reactive fluid in a collapsible container within an outer shell. Release of a compressed spring collapses the container, ejecting fluid outside the shell.

Self-destruction switch (2,974,598). Dr. W. B. McLean (ARS member), China Lake, Calif., assignor to the War Department.

Drive shaft turns gears into position to actuate an electrical circuit for firing a detonator after a predetermined number of shaft revolutions.

Rocket construction (2,976,805). A. Africano, G. D. Brewer (ARS members) and W. J. Harrington, Ithaca, N. Y., assignors to the War Dept.



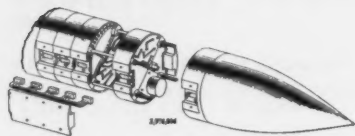
U-shaped connection between parallel rocket tubes. Tubes joined by web to which cable is connected in vertical and horizontal alignment with the c.g., stabilizing rocket and obviating tendency to deflect from course.

High pressure ratio axial flow supersonic compressor (2,974,858). J. K. Koffel (ARS member), and C. A. Lindley, Sierra Madre, Calif., assignor to Thompson Ramo Wooldridge, Inc. (ARS corporate member).

Fluid directed to rotor at velocity above Mach 1, flow diffused between blades at Mach 1, and simultaneously turned and diffused subsonically without flow separation.

EDITOR'S NOTE: Patents listed above were selected from the Official Gazette of the U. S. Patent Office. Printed copies of patents may be obtained from the Commissioner of Patents, Washington 25, D. C., at a cost of 25 cents each; design patents, 10 cents.

Missile structure (2,976,806). D. L. Risk and B. E. Geddes, West Covina, Calif., assignors to General Dynamics Corp. (ARS corporate member).



Electronics section including multiple modules with outer frame surfaces flush with missile surface. Modules fastened to one another, forming a load bearing part of missile structure.

Space vehicle attitude control system (2,974,594). J. Boehm (ARS member), Huntsville, Ala., assignor to the U. S. Army.

Four pairs of reaction motors on after part of vehicle. Each has oppositely directed nozzles actuated by a sensing element to turn vehicle about its various axes.

Propellant grain igniter (2,974,596). R. C. Allen (ARS member), Woodbury, N. J., assignor to E. I. du Pont de Nemours and Co.

High explosive compound, an oxidant, and fuel in a cavity extending the length of the grain, confined in a metal sheath.

Radiant energy source (2,975,375). L. Goldstein, Urbana, Ill., assignor to IT & T Corp.

RF energy source in a missile. Stream of ionized high temperature gases having high electron density produced and mixed with electronegative particles.

Plasma propulsion (2,975,332). W. L. Starr, Palo Alto, Calif., assignor to Lockheed Aircraft Corp. (ARS corporate member).

Plasma introduced between a pair of electrodes causes electrical voltages to break down gap, accelerating plasma away from a metal "backstrap."

Thermal monofuel reactor (2,975,588). L. C. Smith, Livonia, Mich., assignor to Wyandotte Chemicals Corp. (ARS corporate member).

Initiator, extending axially of an annular spray of fuel, heated to initiate autodecomposition of fuel.

Reheat fuel system (2,975,589). J. W. Vdoviak, Cincinnati, Ohio, assignor to General Electric Co. (ARS corporate member).

Wide modulation range for turbojet engine. Selector controls fuel flow to distribution systems in response to movements of throttle, injecting fuel near flameholder or upstream of flameholder.

Proportional coolant flow thrust chamber (2,975,590). A. H. Vonder Esch, Flanders, N. J., assignor to Thiokol Chemical Corp. (ARS corporate member).

Ribs from annular coolant passageways between inner and outer shells of combustion chamber. Part of coolant flows directly to passageways of critical throat section.

Conical injector (2,975,591). Z. Fox (ARS member), Verona, N. J., assignor to Thiokol Chemical Corp. (ARS corporate member).

Injector head for rocket motor. Propellant passageways in a cone with inwardly directed orifices. Alternate passageways are supplied with different propellant fluids.

Pressure-operated systems with ignitable propellants (2,975,595). E. H. Lyons Jr. Elmhurst, Ill., assignor to Chromalloy Corp.

Auxiliary propellant unit for emergency use as power source. Body has interconnected valve and cartridge chambers. A piston-like shuttle valve is mounted for sliding sealing movement within valve chamber.

Variable geometry diffuser control for jet engines (2,976,677). J. E. Taylor, Cleveland, Ohio, assignor to Thompson Ramo Wooldridge, Inc. (ARS corporate member).

Apparatus for sensing position of shock wave formed at transition point of air slowing from supersonic to subsonic velocity. An alpha particle emitting substance ionizes space between members supporting an air streamlining cone.

Restricted solid propellant (2,976,678). D. E. Kennedy (ARS member), Park Forest, Ill., assignor to Standard Oil Co. (Ind.).

Coating of combustible pressure-sensitive tape 0.006 in. thick restrains burning of body material for time equal to burnout time of gas producing material, affording sustained burning of solid propellant grain.

Tubular rocket combustion chamber (2,976,679). J. E. Dalglish, Cleveland, Ohio, assignor to Veet Industries.

Tubes forming a shell of circular cross section and varying diameters. Cross sections reduced at minimum diameter of combustion chamber to increase velocity of tube contents.

Combination igniter and nozzle (2,976,680). D. D. Kobbeman, McGregor, Tex., assignor to the USAF.

Combustion chamber loaded with solid propellant having longitudinally axial perforation through center, and small openings normally closed with coating which fails when subjected to heat.

Clam shell thrust reversers with noise suppressors (2,976,681). H. L. Bohm and W. H. Pearson, Seattle, Wash., assignor to The Boeing Co. (ARS corporate member).

Composite exterior housing enclosing a duct and having jet nozzle for normal exit of gases. Tailcone may be moved rearward to increase gap between housing and terminal element.

Target position computer (2,977,049). E. D. Gittens, Dr. C. D. Brock (ARS members), R. Y. Miner and Q. J. Evans, Floral Park, N. Y., assignor to American Bosch Arma Corp. (ARS corporate member).

Device for continuously determining position of moving target, and for receiving indications of speed, course curvature and course of own ship, and true range and relative bearing of target, providing rectangular coordinates.

Balloon launching method (2,977,069). W. F. Huch and Dr. J. R. Winckler (ARS member), St. Paul, Minn., assignors to the U. S. Navy.

Gathered uninflated part extends laterally from bottom of gas-containing bubble part, tethered by a line from which lift is measured during preparation of launching.

Aircraft having a detachable cabin (2,977,080). H. Ph. von Zborowski, Chateau de Boussy - St. Antoine par Brunoy, France.

Cabin with pilot controls for varying direction of propelling rocket through a variety of angles after detachment of cabin from body.

Tip-jet driven ducted fan for aircraft (2,978,205). C. V. Constant, San Diego, Calif., assignor to Ryan Aeronautical Co. (ARS corporate member).

Plenum chamber in hub of fans in duct at inner portions of aircraft wing panels.

Chamber leads to blade interior. Blades have jet units mounted at tips.

Radial flow lift device (2,978,206). D. S. Johnson, Dunn Loring, Va.

Airfoil having fixed concave circular surface. An impeller comprising a disk with blades rotates in central opening of airfoil. Gas at high velocity is discharged over outside of fixed surface.

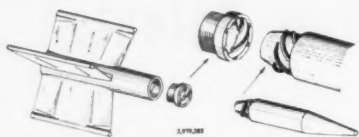
Hydrofuel (2,978,304). R. B. Cox (ARS member), Pomona, Calif., assignor to Aerojet-General Corp. (ARS corporate member).

Alloy containing 2 to 5% of sodium, 30 to 44% of calcium, and 51 to 68% of lithium.

Propellant compositions (2,978,305). Dr. R. W. Lawrence (ARS member), Glendora, Calif., assignor to Aerojet-General Corp. (ARS corporate member).

Solid composition comprising a non-metallic inorganic oxidizing salt, an unsaturated polyester resin, and a burning rate acceleration catalyst.

Missile structures (2,979,285). E. Plautner, Nürtingen, Württemberg, Germany.



Coupling for head and body, having e.g. adjustment in form of fine thread connection of small lead with body, and cross thread connection of large lead with head.

Ammonium perchlorate-asphalt base and catalyst consisting of a mixture of chromium sesquioxide and acid activated aluminium silicate.

Turbo-jet aircraft design (190,064). L. B. Rellis, Chicago, Ill.

Body of circular constant section, wings of low aspect ratio, and multiple jet engines mounted at tail surface.

Adjustable nozzle for rocket (2,978,866). K. Clark, Bloomfield Hills, Mich., assignor to Curtiss-Wright Corp.

Nut threaded on exhaust throat. Cams between nut and throat alter outlet as nut is turned. Index mark on nut indicates relative position of cams.

Powder reactor for self-propelled projectiles (2,978,867). C. A. Somville, Burcht-lez-Anvers, Belgium.

Piston partitions combustion chamber powder charge. When overpressures occur, piston moves to increase combustion volume and reduce overpressures.

Combustion system with cooled dividing partition (2,978,868). S. R. Puffer, Hartland, Vt., assignor to General Electric Co. (ARS corporate member).

Ducted fan type turbine with afterburner. Cylindrical walls of vaporizing chamber cooled internally by vaporization of fuel, and externally by vaporized fuel injected into passages between walls.

Missile guidance system (2,979,284). S. A. Genden and H. D. Paget (ARS members), Detroit, Mich., assignors to Continental Aviation & Engineering Corp. (ARS corporate member).

Adjustable means on ballistic missile increases drag coefficient to alter trajectory in vertical plane only, within predetermined limits.

Book Notes

Numerical Weather Analysis and Prediction, Philip D. Thompson, (Chief, Development Section, Joint Numerical Weather Prediction Unit, Washington, D. C.) Macmillan Co., N. Y., 1961, 170 + xiv pp., 18 figs. \$6.50.

Chapters: 1. Introduction; 2. Fundamental Physical Principles and Their Mathematical Expression; 3. Dynamical Weather Prediction as a Mathematical and Numerical Process; 4. Pure Types of Wave Motion in the Atmosphere; 5. Finite-Difference Methods of Solving the Linear Equations for Sound, Gravity and Rossby Waves; 6. Mixed Types of Wave Motion in the Atmosphere: The Filtering Problem; 7. The Equivalent-Barotropic Model; 8. Numerical Methods for Solving the Modified Nonlinear Equations; 9. The Cyclogenesis Problem and the Modified Equations for Baroclinic Flow; 10. Baroclinic Instability and Other Aspects of Cyclogenesis; 11. Reexamination of the Filtering Problem; 12. Solution of the Primitive Equations; 13. Numerical Weather Analysis and Forecasting in Routine Practice; 14. A Miscellany of Errors and Unsolved Problems; 15. Outlook for the Future.

This is the first book length treatment of new techniques of weather forecasting by means of high speed automatic digital computers, stressing fundamental physical and mathematical aspects of the subject. The author explains that the book is a compromise between two slightly conflicting purposes, since it is designed both for those with a general background in mathematics and physics but without any special knowledge of meteorology, and as a textbook on numerical weather prediction for students of dynamical meteorology on the graduate level.

Concepts from Tensor Analysis and Differential Geometry, Tracy Y. Thomas (Graduate Institute for Mathematics and Mechanics, Indiana Univ., Bloomington, Ind.) Academic Press, N. Y., 1961, 119 + vii pp. \$5.60.

Chapters: 1. Coordinate Manifolds; 2. Scalars; 3. Vectors and Tensors; 4. A Special Skew-Symmetric Tensor; 5. The Vector Product. Curl of a Vector; 6. Riemann Spaces; 7. Affinely Connected Spaces; 8. Normal Coordinates; 9. General Theory of Extension; 10. Absolute Differentiation; 11. Differential Invariants; 12. Transformation Groups; 13. Euclidean Metric Space; 14. Homogeneous and Isotropic Tensors; 15. Curves in Space. Frenet Formulae; 16. Surfaces

The books listed here are those recently received by the ARS from various publishers who wish to announce their current offerings in the field of astronautics. The order of listing does not necessarily indicate the editors' opinion of their relative importance or competence.

in Space; 17. Mixed Surface and Space Tensors. Coordinate Extension and Absolute Differentiation; 18. Formulae of Gauss and Weingarten; 19. Gaussian and Mean Curvature of a Surface; 20. Equations of Gauss and Codazzi; 21. Principal Curvatures and Principal Directions; 22. Asymptotic Lines; 23. Orthogonal Envelopes and Normal Congruences; 24. Families of Parallel Surfaces; 25. Developable Surfaces. Minimal Surfaces.

First in a new series of monographs and textbooks entitled "Mathematics in Science and Engineering," this book is an introductory textbook designed for a one-semester course at the graduate level, for students of pure mathematics as well as for those whose primary interest lies in the study of certain aspects of applied mathematics including the theory of relativity, fluid mechanics, elasticity and plasticity theory.

The Abundance of the Elements, Lawrence H. Aller (Observatory of the Univ. of Michigan, Ann Arbor, Mich.), Interscience Publishers, N. Y., 1961, 283 + xi pp. \$10.

Chapters: 1. The Nature and Scope of the Problem of Elemental Abundance; 2. Composition of the Earth and Its Crust; 3. Meteorites; 4. Abundances Derived From Gaseous Nebulae; 5. Abundances of Elements From Normal Stellar Atmospheres; 6. Abundances From Cosmic Rays; 7. Isotope Abundances; 8. General Abundance Compilations; 9. Composition Differences Between Stars; 10. Theories of the Origin of the Elements. Author Index. Subject Index. Index of Stars, Clusters and Nebulae.

Vol. VII in the series titled "Interscience Monographs and Texts in Physics and Astronomy," this work, which includes a large number of figures and tables, discusses the Earth's crust and meteorites in a brief, descriptive manner and concentrates on abundances derived from celestial objects. A short summary of theories of element building in stars is given in the last chapter.

Satellite Environment Handbook, Francis S. Johnson, ed. (Manager of Space Physics, Lockheed Missiles and Space Div., Palo Alto, Calif.), Stanford Univ. Press, Stanford, Calif., 1961, 155 + xii pp., 57 figs., 17 tables. \$5.50.

Chapters: Introduction; 1. Structure of the Upper Atmosphere by Francis S. Johnson; 2. Structure of the Ionosphere by W. B. Hanson; 3. Penetrating Radiation by A. J. Dessler; 4. Solar Radiation by Francis S. Johnson; 5. Micrometeorites by J. F. Vedder; 6. Radio Noise by O. K. Garriott; 7. Thermal Radiation From the Earth by Francis S. Johnson; 8. Geomagnetism by A. J. Dessler. *Appendix* (Supplementary Data): Solar-System Data; Earth Satellites and Space Probes—April 24, 1961; Conversion Factors; Useful Physical Constants.

Satellite-environment data presented here have been compiled principally in response to questions from engineering projects to Lockheed's Space Physics Research organization. Available data describing the geophysical environment encountered by satellites are presented in a comprehensive survey, with the major satellite-environment factors discussed and existing data evaluated.

Missile Configuration Design, S. S. Chin (Chief Aerodynamics Engineer, The Martin Co., Orlando, Fla.), McGraw-Hill Book Co., N. Y., 1961, 279 + xvi pp. \$11.

Chapters: 1. Introduction; 2. General Aerodynamic Design Considerations; 3. Aerodynamic Characteristics of Airframe Components; 4. Missile Performance; 5. Static Longitudinal Stability and Control; 6. Maneuvering Flight; 7. Directional Stability and Control; 8. Lateral Stability and Control; 9. Dynamic Stability; 10. Air Loads; 11. Aerodynamic Launching Problems; 12. Free-Flight Dispersions; 13. Powerplant Design Characteristics; 14. Structural Design Characteristics. *Appendices:* Determination of Radius and Volume of Tangent Ogives; Expression and Coordinates of Different Nose Shapes; Optimum Wing Study; Derivation of Incremental Velocity Due to Boost; Derivation of Expression for V for Iteration Method; Determination of Downwash From Wind-Tunnel Test Results; Determination of Damping Derivatives From Wind-Tunnel Test Results; Determination of Aerodynamic Derivatives From Flight-Test Data.

The purpose of this book is to present some of the basic principles in configuration design of guided missiles. Containing a large number of figures and tables, with each chapter referenced, the book is slanted primarily toward the aerodynamicist in preliminary design and is also intended for use as a working handbook for aeronautical engineers in their first assignments in the missile industry, or by missile engineers not directly concerned with external design.

Meteor Science and Engineering, D. W. R. McKinley (Associate Director, Radio and Electrical Engineering Div., National Research Council, Ottawa, Canada), McGraw-Hill Book Co., N. Y., 1961, 309 + ix pp., illustrated. \$12.50.

Chapters: 1. Historical Survey; 2. Some Elements of Astronomy and Radio; 3. Visual and Photographic Techniques; 4. Radio Techniques; 5. Observational Data on Meteors; 6. Astronomical Aspects of Meteors; 7. Physical Theory of Meteors; 8. Radio Echo Theory; 9. Forward-Scatter From Meteor Trails; 10. Other Effects of Meteor Trails. *Appendix:* Upper-Atmosphere Data. Bibliography. Name Index. Subject Index.

Part of the McGraw-Hill "Series in Engineering Sciences," this work summarizes the major observational and theoretical developments in meteor science. The book is aimed primarily at the man who has not specialized in meteor research but who would like to learn something of the background, possibly because he is a scientist or engineer engaged in work in which meteors may play some part.

Plasmas and Controlled Fusion, David J. Rose and Melville Clark Jr. (Professor and Associate Professor of Nuclear Engineering, respectively, at M.I.T.), M.I.T. Press, Cambridge, Mass., and John Wiley & Sons, N. Y., 1961, 493 + xiv pp. \$10.75.

Chapters: 1. Energy Needs and Resources; 2. Collision Phenomena: Basic Theory and Fusion Cross Sections; 3. Collision Phenomena: Atomic and Surface Effects; 4. Velocity Distributions and Averages; 5. Maxwell's Equations and Electromagnetic Energy; 6. The Hydro-magnetic Equations; 7. Macroscopic Motions of a Plasma; 8. Coulomb Interactions and Their Consequences; 9. Plasma Waves of Small Amplitudes; 10. Motion of Individual Charges; 11. Radiation Losses From a Plasma; 12. Plasma Stability; 13. Energy Balance and Material Problems; 14. Devices Based upon the Pinch Effect; 15. Mirror-Like Devices; 16. The Stellarator. **Appendices:** Glossary; Conversion of Units; Frequently Used Vector Relations; Frequently Used Physical Constants.

This is a graduate level textbook on the principles underlying plasma physics and controlled fusion, planned for a two-semester course. Each chapter contains a set of problems and a reference list, and the subject matter moves from first principles to advanced concepts. The reader is assumed to have a moderate knowledge of atomic physics, differential equations, electricity and magnetism, and thermodynamics.

Axial Flow Fans, R. A. Wallis (Senior Scientific Officer, Aeronautical Research Laboratories, Department of Supply, Melbourne, Australia), Academic Press,

N. Y., 1961, 366 + x pp., illustrated. \$10.

Chapters: 1. Introduction; 2. Introduction to the Fluid Mechanics of Ducted Fans; 3. Boundary Layer and Skin Friction Relations; 4. Aerofoil Data for Blade Design; 5. Vortex Flows in Ducting and Fan; 6. Ducts; 7. Introduction to Fan Design Methods; 8. Rotor: Momentum Considerations—Free Vortex Flow; 9. Rotor: Blade Element Considerations—Free Vortex Flow; 10. Rotor Losses; 11. Stator Design; 12. Stator Losses; 13. Tail Fanning Design and Associated Losses; 14. Overall Efficiencies; 15. Torque, Thrust and Power; 16. Design of Fan Unit with Arbitrary Vortex Flow; 17. Noise; 18. Design Examples; 19. Rotor Analysis; 20. Stator Analysis and Overall Fan Unit Performance; 21. Variable Pitch Rotors and Examples of Fan Analysis; 22. Fan Testing; 23. Review of Design Assumptions. **Appendix:** Free Fans.

This book seeks to fulfill the need for a modern comprehensive treatment of the aerodynamics of ducted axial flow fans, and is designed primarily for the ventilating engineer. The material is presented in a modern aerodynamic manner, with the traditional hydraulic notation discarded. The results of aerodynamic research are analyzed and then presented as a consistent and working theory, capable of being used by engineers in the solution of problems. Containing a large number of figures, the work also includes 22 tables of numerical data.

The Theory of Subsonic Plane Flow, L. C. Woods (Fellow of Balliol College, Oxford, formerly Nuffield Professor of Mechanical Engineering, Univ. of New South Wales, Australia), Cambridge University Press, N. Y., 1961, 594 + xxii pp. \$22.50.

Contents: **Part I, Fluid Motion Theory:** 1. Introductory Theory; 2. General Theory of Two-Dimensional Flow. **Part II, Complex Variable Theory:** 3. Cauchy Integrals and Their Application to Harmonic Function Boundary Value Problems; 4. Mixed and Periodic Boundary Conditions; 5. Conformal Mapping. **Part III, Applications:** 6. General Account of Methods—Sources, Doublets and Vortices; 7. Flow in Channels; 8. Aerofoil

Theory; 9. Unsteady Aerofoil Theory; 10. Flow Past Semi-Infinite Profiles; 11. Wakes and Cavities; 12. Cascades of Aerofoils; 13. Lifting Aerofoils in Channels and Jets; 14. Unsteady Motion of Aerofoils in Channels and Jets; Concluding Remarks.

Vol. III of the "Cambridge Aeronautical Series," this book is designed to provide a concise and systematic treatment of two-dimensional, subsonic, inviscid fluid motion by employing the same mathematical methods and variables throughout. Another aim is to present some recent developments in a text for the first time. It is claimed to be the first book to give an extensive account of mixed boundary-value problems and to treat such examples of these problems as occur in ventilated wind-tunnel theory, jet flaps and unsteady Helmholtz motions.

Methods of Celestial Mechanics, Dirk Brouwer and Gerald M. Clemence (Director of the Yale Univ. Observatory, New Haven, Conn., and Scientific Director of the U. S. Naval Observatory, Washington, D. C., respectively), Academic Press, N. Y., 1961, 598 + xx pp. \$15.50.

Chapters: 1. Elliptic Motion; 2. Expansions in Elliptic Motion; 3. Gravitational Attraction Between Bodies of Finite Dimensions; 4. Calculus of Finite Differences; 5. Numerical Integration of Orbits; 6. Aberration; 7. Comparison of Observation and Theory; 8. The Method of Least Squares; 9. Differential Correction of Orbits; 10. General Integrals. Equilibrium Solutions; 11. Variation of Arbitrary Constants; 12. Lunar Theory; 13. Perturbations of the Coordinates; 14. Hansen's Method; 15. The Disturbing Function; 16. Secular Perturbations; 17. Canonical Variables.

Intended to provide a comprehensive background for practical applications, this volume is designed for graduate and advanced undergraduate students, as well as for engineers and others desiring to acquire some knowledge of celestial mechanics. It may also be used as a reference volume by specialists, since the presentation and arrangement have been designed to facilitate numerical work as much as possible.

Technical Literature Digest

M. H. Smith, Associate Editor

The James Forrestal Research Center, Princeton University

Propellants and Combustion

Research on the Hazard Classification of New Liquid Rocket Propellants, by

EDITOR'S NOTE: Contributions from Professors E. R. G. Eckert, E. M. Sparrow and W. E. Ibele of the Heat Transfer Laboratory, University of Minnesota, are gratefully acknowledged.

T. Spring, *North Amer. Aviation Inc., Rocketdyne Div.*, R-2452-4, *Quar. Prog. Rep.*, Jan. 31, 1961, 47 pp.

Methane-Oxygen Flame Structure, III. Characteristic Profiles and Matter and Energy Conservation in a One Twentieth Atmosphere Flame, by R. M. Fristrom, C. Gunfelder and S. Favin, *J. Phys. Chem.*, vol. 65, no. 4, April 1961, pp. 587-590.

Peroxides and Peroxy Radicals in

Propane Oxidation, by M. Seakins, *Royal Soc., London, Proc.* vol. A 261, no. 1305, April 1961, pp. 281-290.

Materials and Structures

A Closed-Cycle System for Gas Bearings, by J. H. Laub and H. D. McGinness, *Calif. Inst. Tech., Jet Propulsion Lab. Tech. Release* 34-174, Jan. 1961, 17 pp.

- Nonlinear Theories for Thin Shells**, by J. Lyell Sanders Jr., *Harvard Univ., Div. Engng. and Appl. Phys. Tech. Rep.* 10, Feb. 1961, 29 pp.
- Electrets**, by Dorothy Sweitzer, *Calif. Tech., Jet Propulsion Lab. Literature Search* 308, Feb. 1961, 32 pp.
- The Design of Flat Scored High-Pressure Diaphragms for Use in Shock Tunnels and Gas Guns**, by J. J. Rast, *Nav. Ord. Lab. NAVORD Rep.* 6865, Sept. 6, 1960, 7 pp., illus., charts, tables, dagrams. (*Ballistics Res. Rep.* 29.)
- Structural and Insulative Characteristics of Ablating Plastics**, by Franklin A. Vassallo, Norman E. Wahl, Gerald A. Sterbutzel and John L. Beal, *Cornell Aeron. Lab.*, 22 pp., 14 figs.
- A Note on the Use of Sandwich Structures in Severe Acoustic Environments**, by D. J. Mead, *Southampton Univ., Dept. Aeron. Astron. Rep.* 145, July 1961, 34 pp.
- Reaction of Copper and Fluorine From 800° to 1200°F**, by Patricia M. O'Donnell and Adolph E. Spakowski, *NASA Tech. Note D-768*, April 1961, 15 pp.
- Third Annual Conference on Aviation and Astronautics**, Tel-Aviv and Haifa, Israel, Inst. of Tech., Dept. Aeron. Engng. (reprint from *Bull. Research Council of Israel*, vol. 9C, no. 1-2, Feb. 1961), Feb. 1961, 121 pp.
- Buckling of Thin Circular Conical Shells Subjected to Axisymmetrical Temperature Distributions**, by J. Singer, pp. 49-50.
- The Mechanical Properties and Structure of Some High Tensile Alloy Steels**, by S. Becker and M. G. Bader, pp. 61-78.
- High Speed Testing**, Plas-Tech Equipment Corporation, vol. 1. A Symposium held at Boston, Mass., Dec. 8, 1958, Interscience Publishers, N. Y., 1960, 112 pp.
- Review of a High-Speed Tensile Testing Program for Thermo-Plastics**, by Richard E. Ely, pp. 3-25.
- High-Rate Tension Testing of Plastics**, by Stephen Strella, pp. 27-40.
- Stress Relaxation-Theory and Practice**, by Henry M. Morgan, pp. 83-96.
- Effect of Strain Rate and Temperature on the True Stress-True Strain Properties of Commercially Pure Titanium**, by Thomas S. DeSisto and David E. Driscoll, pp. 97-105.
- Studies of Metals at Ballistic Rates of Loading**, by J. O'Brien and R. S. Davis, pp. 107-112.
- Ballistic Missile and Space Technology**, v. IV, Reentry and Vehicle Design, Donald P. LeGalle, ed., Symposium on Ballistic Missile and Space Technology, Los Angeles, August 1960, Academic Press, N. Y., 1960, 422 pp.
- The Pyrolysis of Plastics in a High Vacuum Arc Image Furnace**, by Henry L. Friedman, pp. 3-29.
- Aerothermodynamic Feasibility of Graphite for Hypersonic Glide Vehicles**, by S. M. Scala and E. J. Nolan, pp. 31-63.
- An Engineering Analysis of the Weights of Ablating Systems for Manned Re-entry Vehicles**, by Robert T. Swan, pp. 65-86.
- Rocket Casing Behavior Predicted by Laboratory Tests**, by J. D. Marble, pp. 153-172.
- The Numerical Solution of Axis-Symmetric Problems in Elasticity**, by S. D. Conte, K. L. Miller and C. B. Sensing, pp. 173-202.
- The Effect of Radiation on Materials**, J. J. Harwood, Henry H. Hansner, J. G. Marse and W. G. Rauch, eds., (Office of Naval Research), Reinhold Publishing Corp., N. Y. 1958, 355 pp.
- Defects in Solids and Current Concepts of Radiation Effects**, by G. J. Dienes, pp. 1-47.
- Radiation Effects on Physical and Metallurgical Properties of Metals and Alloys**, by E. S. Billington, pp. 99-125.
- Influence of Radiation Upon Corrosion Behavior and Surface Properties of Metals and Alloys**, by M. Simmad, pp. 126-143.
- Effects of Radiation on Electrodes and Optical Properties of Inorganic Dielectric Materials**, by R. Smoluchowski, pp. 144-158.
- Effects of Radiation on Semiconductors**, by H. Y. Fan and K. Lark-Horovitz, pp. 159-190.
- Experimental Techniques and Current Concepts-Organic Substances**, by M. Burton, pp. 243-260.
- Effects of Radiation on Behavior and Properties of Polymers**, by A. Charlesby, pp. 261-286.
- Bibliography "Effect of Irradiation on Solids"**, by H. Friedmann, pp. 305-339.
- Stability of a Cylindrical Shell under Twisting, External Pressure and Compression**, by O. I. Terebushko, *ARS JOURNAL*, vol. 31, no. 3, March 1961, pp. 378-386.
- Saint-Venant's Problem for Thin-Walled Tubes with a Circular Axis**, by K. F. Chernykh, *Appl. Math. Mech. (PMM)*, vol. 24, no. 3, 1960, pp. 619-632.
- The Strength of Ceramic Materials**, by Winston H. Duckworth and Alfred Rudnick, *Battelle Tech. Rev.*, vol. 10, no. 4, April 1961, pp. 3-8.
- Recent Developments in Lubricants**, by Stanley L. Cosgrove and Richard L. Jentgen, *Battelle Tech. Rev.*, vol. 10, no. 4, April 1961, pp. 9-13.
- Testing Techniques for Full-Scale Missile Structures Under Simulated Re-entry Environment**, by R. T. Nichols, *Experimental Mech.*, vol. 1, no. 1, Jan. 1961, pp. 8-15.
- Experimental Study of Large-Diameter Thin-Wall Pressure Vessels**, by A. J. Durelli, J. W. Dally and S. Morse, *Experimental Mech.*, vol. 1, no. 2, Feb. 1961, pp. 33-42.
- Experimental Investigation of the Buckling Instability of Monocoque Shells**, by R. H. Homewood, A. C. Brine and Aldie E. Johnson, Jr., *Experimental Mech.*, vol. 1, no. 3, March 1961, pp. 88-96.
- Measuring Repeated Strains With a Modified Null-Balancing Strain Indicator**, by R. S. Loubser and W. W. Schroeder, *Experimental Mech.*, vol. 1, no. 4, April 1961, pp. 136-140.
- Spherically Symmetric Thermal Shock in a Medium With Thermal and Elastic Deformations Coupled**, by G. A. Nariboli, *Quarterly J. Mech. and Appl. Math.*, vol. 14, part 1, Feb. 1961, pp. 75-84.
- On Recent Developments in Shell Theory**, by W. Zerna, *Zeitschrift für Angewandte Math. und Mech.*, vol. 41, no. 3, March 1961, pp. 97-100. (In German.)
- Effect of Target Thickness on Cratering and Penetration of Projectiles Impacting at Velocities to 13,000 feet per second**, by William H. Kinard, C. H. Lambert Jr., David R. Schryer and Francis W. Casey Jr., *NASA Mem.* 10-18-58L, Dec. 1958, 20 pp. (Declassified by authority of NASA TPA no. 45, May 11, 1961).
- Thermal Stresses in Multi-Layer Spherical Shells**, by G. R. Cowper, *Canada National Res. Council, NRC LR-300*, Feb. 1961, 13 pp., 8 figs.
- Phase Relationships in Tantalum-Rich Tantalum-Ruthenium Alloys at 1500°C**, by 1/Lt. C. S. Hartley, W. L. Baun, D. W. Fisher and E. J. Rappoport, *Wright Air Dev. Div. Tech. Note* 60-228, March 1961, 22 pp.
- Method for Finding Approximate Emissivity of Various Surfaces**, by F. K. Deaver, *Atomic Energy Commission SCDR* 167-59, Oct. 1959, 11 pp.
- Aeronautics and Astronautics, Proceedings (Durand Centennial Conference, Stanford University, Aug. 5-8, 1959)** Nicholas John Hoff and Walter Guido Vincenti, eds., Pergamon Press, N. Y. 1960, 460 pp. (*AOSR TR* 59-108)
- Frontiers of Flight Structures Design**, by Richard R. Heldenfels, pp. 29-50.
- Transient Temperature and Thermal Vibrations in Space Structures**, by Luigi Broglio, pp. 52-75.
- New Developments in the Non-linear Theories of the Buckling of Thin Cylindrical Shells**, by W. F. Thielemann, pp. 76-121.
- Creep Buckling of Plane Frameworks**, by Jan Hult, pp. 227-246.
- Thermodynamic Foundations of the Theory of Deformation**, by J. F. Besseling, pp. 247-266.
- Leading Edge Structures of Hypersonic Vehicles**, by Wilfred H. Dukes, pp. 267-287.
- Thermoelectric Materials and Devices**, Irving B. Cadoff and Edward Miller, eds., Reinhold Publishing Corp., N. Y. 1960, 344 pp.
- Properties Affecting the Utility of Thermoelectric Materials**, by Philipp H. Klein, pp. 55-83.
- Measurement of Pertinent Thermoelectric Properties**, by Theodore C. Harman, pp. 84-97.
- Thermoelectric Properties of Bi₂Te₃ and some Bi₂Te₃ Alloys**, by E. H. Lougher, pp. 133-142.
- Lead Telluride Alloys and Junctions**, by R. W. Fitts, pp. 143-162.
- Thermoelectric Properties of Refractory Materials**, by John R. Gambino, pp. 163-172.
- Ionic Materials**, by R. W. Christy, pp. 173-183.
- Liquids as Thermoelectric Materials**, by Rudolph Marcus and Clinton M. Kelley, pp. 184-193.
- Molten Salts as Thermoelectric Materials**, by Benson Sundheim, pp. 194-198.
- Modern Dielectric Materials**, J. B. Birks, ed., Heywood and Co., London, 1960, 253 pp.
- Paper**, by H. C. Hall and E. Kelk, pp. 26-44.
- Hydrocarbon Insulating Oils**, by N. Pilpel and E. H. Reynolds, pp. 45-67.
- Chlorinated Hydrocarbons**, by J. B. Birks, pp. 68-78.
- Natural and Synthetic Rubbers**, by W. J. Green and S. Verne, pp. 79-94.
- Synthetic High Polymers**, by J. B. Birks, pp. 95-144.
- Silicones**, by D. J. Dowling, pp. 145-163.
- Ceramics**, by P. Popper, pp. 164-195.
- Glass**, by H. E. Taylor, pp. 196-220.
- Mica and Micanite**, by J. B. Birks, pp. 221-229.
- Fibers and Textiles**, by J. W. S. Hearle, pp. 230-253.



Mechanical
or Aeronautical
Engineers with
**MASTERS
DEGREES...**

Mechanical or Aeronautical Engineers with M.S. Degrees and some research or development experience are required for an extensive research program in advanced rocket propulsion concepts. A comprehensive knowledge of fluid mechanics is required (compressible viscous flows, turbulence, transport phenomena) along with the ability to apply this knowledge to unusual fluid flow problems. Both theoretical and experimental programs are being conducted. This program has strong corporate sponsorship with all that this implies in personal stability. Available are excellent experimental, computational, and library facilities with experienced supporting personnel. Attractive salary levels and benefits are available to qualified individuals.

We invite you to contact Mr. W. F. Walsh

**RESEARCH LABORATORIES
UNITED AIRCRAFT CORPORATION**

400 Main Street, East Hartford 8, Conn.

All qualified applicants will receive consideration for employment without regard to race, creed, color or national origin.

Non-Crystalline Solids, (Conference on Non-Crystalline Solids, Alfred, New York, Sept. 3-8, 1958) V. D. Frechette, ed., John Wiley & Sons, N. Y. 1960, 536 pp.

Structure of Vitreous Silica by Total Neutron Scattering, by R. M. Delaney and A. H. Weber, pp. 96-116.

High Temperature X-Ray Diffraction Methods Applied to the Study of Non-Crystalline media. Structure of Molten Fluoride and Chlorides, by Jerzy Zarzycki, pp. 117-143.

X-Ray Absorption Edge Spectroscopy of Compounds of Chromium, Manganese and Cobalt in Crystalline and Non-Crystalline Systems, by Robert A. Van Nordstrand, pp. 168-198.

Magnetic Resonance Studies of Glasses, by W. P. Slichter, pp. 199-231.

Liquid Relaxation Phenomena and the Glass State, by Theodore A. Litovitz, pp. 252-268.

Kinetics of Mechanical Relaxation Processes in Inorganic Glasses, by P. L. Kirby, pp. 269-296.

The Thermal Conductivity of Glass, by P. G. Klemens, pp. 508-530.

Mechanisms of Surface Removal from Metals in Space, by John L. Ham, *Aero/Space Engng.*, vol. 20, no. 5, May 1961, pp. 20-21, 49-52.

Development of an All-Welded Tubular Truss Core Sandwich, by Bertram Klein, *Aero/Space Engng.*, vol. 20, no. 5, May 1961, pp. 22-24, 54-55.

Thermostructural Design - Entry Vehicles for Mars and Venus, by Henry T. Ponsford, Robert M. Wood, Robert E. Lowe and James F. Madewell, *ARS JOURNAL*, vol. 31, no. 4, April 1961, pp. 474-481.

Ablation Mechanisms in Plastics with Inorganic Reinforcement, by Norman Beecher and Ronald E. Rosenzweig, *ARS JOURNAL*, vol. 31, no. 4, April 1961, pp. 532-539.

Effect Upon Shock Spectra of the Dynamic Reaction of Structures, by G. J. O'Hara, *Experimental Mech.*, vol. 1, no. 5, May 1961, pp. 145-151.

Stresses of Nozzle Connections of Pressure Vessels, by D. E. Hardenbergh, *Experimental Mech.*, vol. 1, no. 5, May 1961.

Electron Microscope Study of Radiation Damage in Graphite, by W. Bollmann, *J. Appl. Phys.*, vol. 32, No. 5, May 1961, pp. 869-879.

Bi-harmonic Solutions to the Steady-State Thermoelectric Problems in Three Divisions, by J. Nowinski, *Zeitschrift Angewandte Math Phys.*, vol. 12, no. 2, March 25, 1961, pp. 132-148.

Fluid Dynamics, Heat Transfer, and MHD

A Variational Principle in Aerodynamics and Its Application to Hypersonic Flow, by P. T. Hsu and Haim Kennet, *Mass. Inst. of Tech., Fluid Dynamics Res. Lab. Rep.* no. 60-5, Nov. 1960, 30 pp.

Review of Hypersonic Research, by Ting Y. Li, *Rensselaer Polytech. Inst., Dept. Aeron. Engng. TRAE 6104*, March 1961, 13 pp. 22 refs. (AFOSR 440)

Approximate Solutions of the Hypersonic Laminar Boundary Layer Equations With Heat Transfer and Arbitrary Pressure Gradient and Their Applications, by Humio Naruse, *Tokyo Univ., Aeron. Res. Inst. Rep.* 361, Feb. 1961, 30 pp.

Stability of the Compressible Boundary Layer Along a Curved Wall Under Gortler-

Type Disturbances, by Yasuhiko Aihara, *Tokyo Univ., Aeron. Res. Inst. Rep.* 362, Feb. 1961, 7 pp.

Center-Point Mass Flow Through a Circular Orifice Using the Integral Iteration Method, by D. Roger Willis, *Stockholm, Royal Inst. Tech., Div. Gas Dynamics, Tech. Note* 31, Dec. 1960, 44 pp. (AFOSR 535)

Heat Transfer Rate Distribution for Conical Afterbody at 0, 5, and 10 Degrees Angle of Attack, by E. Offenhartz and H. Weisblatt, *Avco Corp., Res. Dev. Div. RAD-2-TM-58-105*, Aug. 1958, 25 pp.

Investigation of Annular-Two Phase Flow and Heat Transfer to and From Gases With Large Temperature Differences, by C. F. Warner and J. M. Murphy, *Purdue Univ. Jet Propulsion Center Rep.* F-61-1, March 1961, 19 pp.

Wall Heating of a Supersonic Gas Flow, by A. A. Pomerantsev, *The Johns Hopkins Univ., Appl. Phys. Lab. Tech. Transl. Series*, TG 230-T217, Feb. 1961, 11 pp. (Transl. from *Inzhenerno-Fizicheskii Zhurnal*, vol. 3, no. 8, Aug. 1960, pp. 39-46.)

Shock Profiles in Hypersonic Flow of a Relaxing Gas About a Wedge, by Frederick R. Dressler, *Cornell Univ. Grad. School Aeron. Engng.*, Feb. 1961, 32 pp. (AFOSR 263)

Plasma Sheath and Screening Around a Rapidly Moving Body, by E. H. Walker, *Maryland Univ., Dept. Phys.*, March 1961, 17 pp. (AFOSR 460)

Theoretical Investigation in Linear and Nonlinear Problems, the Determination of Surface Interactions and Examination of Development of Shock Wave in Rarefied Gas Dynamics, by D. Roger Willis, *Stockholm, Royal Inst. Tech. Div. of Gas Dynamics, Final Tech. Rep.*, Jan. 1961, 9 pp. (AFOSR 481)

Investigation of the Development of a Shock Wave for Times Smaller Than the Average Collision Time, by D. Roger Willis, *Stockholm, Royal Inst. Tech. Div. Gas Dynamics Tech. Note* 4, Dec. 1960, 42 pp. (AFOSR 536)

Thermal Conductivity of a Completely Ionized Plasma, by Ira A. Pekar, *The Johns Hopkins Univ., Appl. Phys. Lab. Tech. Transl. Series*, TG 230-T174, Feb. 1961, 5 pp. (Transl. from *Izvestiya Vysshikh Uchebnykh Zavedenii Fizika*, no. 2, March-April 1960, pp. 99-102.)

Applied Probability (Proceedings of Symposia in Applied Mathematics, Vol. 7) McGraw-Hill Book Co., N. Y. for the Amer. Math. Soc., 1961.

On the Application of Functional Calculus to the Statistical Theory of Turbulence, by Eberhard Hopf, pp. 41-50.

The Singularity in the Spectrum of Homogeneous Turbulence, by G. K. Batchelor, pp. 67-72.

Advance in Chemical Physics, Vol. 3, L. Prigogine, ed., Interscience Publishers, N. Y., 1961, 372 pp.

Nonlinear Problems in Thermodynamics of Irreversible Processes, by Thor A. Bak, pp. 33-57, 20 refs.

Variational Principles in Thermodynamics and Statistical Mechanics of Irreversible Processes, by Syu Ono, pp. 267-321, 63 refs.

Spaceflight Technology, *Commonwealth Spaceflight Symposium 1st*, London, 1959, Kenneth W. Gatland, ed., Academic Press, N. Y., 1960, 365 pp.

Heating Problems of Entry into Planetary Atmospheres, by D. J. Shapland, pp. 173-203.

Generalized Heat Transfer Formulas

ARS JOURNAL

and Graphs for Nose Cone Re-Entry Into the Atmosphere, by R. W. Detra and H. Hidalgo, *ARS JOURNAL*, vol. 31, no. 3, March 1961, pp. 318-321.

Linearized Magnetogasdynamical Channel Flow With Axial Symmetry, by F. Edward Ehlers, *ARS JOURNAL*, vol. 31, no. 3, March 1961, pp. 334-341.

Stagnation Point Radiative Transfer, by H. Kennet and S. L. Strack, *ARS JOURNAL*, vol. 31, no. 3, March 1961, pp. 370-371.

Calibration of Hypersonic High Temperature Wind Tunnels, S. E. Neice and R. W. Rutowski, *ARS JOURNAL*, vol. 31, no. 3, March 1961, pp. 372-373.

Entrance Effects in the High Temperature Heat Transfer From Dissociated Gases, by P. Bro and S. Steinberg, *ARS JOURNAL*, vol. 31, no. 3, March 1961, pp. 375-376, 433.

Comparison of Some Approximate Methods for Calculating Re-Entry Ablation of a Subliming Material, by Sheldon Blecher and George W. Sutton, *ARS JOURNAL*, vol. 31, no. 3, March 1961, pp. 433-435.

Radiated Power From a 2-in. Sphere of High Temperature Air at Pressures to 50 atm., by Domenico Ragusa, *ARS JOURNAL*, vol. 31, no. 3, March 1961, pp. 445.

Effect of Two-Dimensional Heat Transfer on Wall Temperatures in a Tubular Thrust Chamber, by John P. Sellers Jr., *ARS JOURNAL*, vol. 31, no. 3, March 1961, pp. 445-447.

On the Calculation of Flow Past Axisymmetric Bodies With Detached Shock Waves Using an Electronic Computing Machine, by O. M. Belotserkovskii, *Appl. Math. Mech. (PMM)* vol. 24, no. 3, 1960, pp. 745-755.

On the Theory of Hypersonic Gas Flow With a Power-Law Shock Wave, by V. V. Sychev, *Appl. Math. Mech. (PMM)*, vol. 24, no. 3, 1960, pp. 656-764.

On the Flow in a Diffuser in the Presence of a Magnetic Field, by A. B. Vatazhin, *Appl. Math. Mech. (PMM)*, vol. 24, no. 3, 1960, pp. 765-772.

On the Propagation of Disturbances in Plane Magnetohydrodynamic Flows, by M. N. Kogan, *Appl. Math. Mech. (PMM)*, vol. 24, no. 3, 1960, pp. 773-782.

On a Certain Form of Exact Particular Solutions of a Plane Vortex Free Gas Flow, by E. D. Tomilov, *Appl. Math. Mech. (PMM)*, vol. 24, no. 3, 1960, pp. 783-789.

On the Flow of An Electrically Conducting Fluid in Tubes of Arbitrary Cross-Section in the Presence of a Magnetic Field, by S. A. Regirer, *Appl. Math. Mech. (PMM)*, vol. 24, no. 3, 1960, pp. 790-793.

Fundamental Relations Across a Strong Steady Shock Wave Giving Rise to a Discontinuity in Conductivity, by Iu. L. Zhilin, *Appl. Math. Mech. (PMM)*, vol. 24, no. 3, 1960, pp. 794-800.

Free-Flight Skin-Temperature and Surface-Pressure Measurements on a Highly Polished Nose Having a 100° Total-Angle Cone and a 10° Half-Angle Conical Flare Section Up to a Mach Number of 4.08, by Bernard Rashis and Aleck C. Bond, *NASA Tech. Note D-807*, April 1961, 23 pp.

Aerodynamic Interaction Effects Ahead of a Sonic Jet Exhausting Perpendicularly From a Flat Plate Into a Mach Number 6 Free Stream, by David J. Romeo and James R. Sterrett, *NASA Tech. Note D-743*, April 1961, 26 pp.

An Experimental Investigation of the

A General Chemical-designed tank trailer for the bulk shipment of liquid fluorine.



320-million lb.-miles of LIQUID FLUORINE from ALLIED CHEMICAL

Multiply the number of pounds of liquid fluorine that we've produced by the number of miles we've shipped it . . . and you come up with a total of 320-million pound-miles! This notable record is one more proof that liquid fluorine is no harder to handle than other advanced propellants.

Allied Chemical's General Chemical Division is a prime source for fluorine . . . your number one fluorine authority. We have supplied tonnage quantities to every major propulsion program using this ultimate oxidizer . . . and we can make bulk shipments to any part of the country.

Our experience in producing, storing and shipping large quantities of liquid fluorine has led to the development of handling and storage techniques that make this super-high-energy oxidizer completely practical to use. Let us share our experience and knowledge with you. If you'd like our fluorine technical bulletins, just mail the coupon below.

First in
Fluorine
Chemistry



**GENERAL CHEMICAL
DIVISION**

40 Rector Street, New York 6, N.Y.

GENERAL CHEMICAL DIVISION

ARS-81

40 Rector Street, New York 6, N.Y.

Please send me bulletin(s) checked:

☐ Fluorine (Pd-TA-85413)

☐ Liquid Fluorine Unloading Procedure (PD-TB-85411)

Name _____

Company _____

Address _____

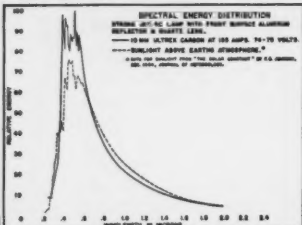
City _____ Zone _____ State _____

Title _____

Strong SOLAR RADIATION SIMULATOR

The Strong blown type Jetarc, the most powerful carbon arc, has proved to be the best artificial simulator of solar energy in the development and testing of space vehicle components.

Useful radiation is efficiently collected by first surface reflectors and concentrated at the reimaging point from where it can be projected by a quartz objective system in a pattern shaped to fit the work area. A circular radiation pattern totals 374 watts with an 80% uniformity of field or a total of 668 watts with a 60% uniformity of field. Higher or lower energy unit areas, can be obtained by variation in optics or projection distance. Large areas can be covered by multiple employment of lamps using either superimposed or overlapping pattern technique. Other, less powerful carbon arc sources, are also available for smaller work areas.



A continuous spectrum is available from .25 to 5+ microns, with the spectral energy distribution very close to solar energy distribution above the earth's atmosphere.

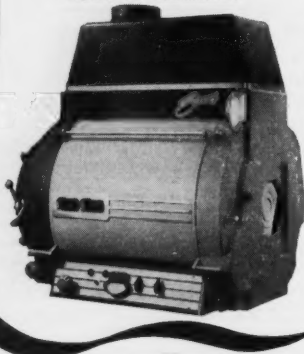
The Jetarc source can be oriented in any plane without loss of stability.

You are invited to consult with Strong Electric on your particular problems.

THE STRONG ELECTRIC CORP.
395 CITY PARK AVE. • TOLEDO 1, OHIO



A SUBSIDIARY OF GENERAL PRECISION EQUIPMENT CORPORATION



Flow Phenomena Over Bodies at High Angles of Attack at a Mach Number of 2.01, by John P. Gapeynski, *NACA Res. Mem.* L55H29, Oct. 1955, 23 pp. (Declassified by authority of NASA TPA no. 45, May 11, 1961.)

Wind-Tunnel Investigation at Mach 1.9 of Multijet-Missile Base Pressures, by L. Eugene Baughman, *NACA Res. Mem.* E54L14, Mar. 1955, 13 pp. (Declassified by authority of NASA TPA no. 45, May 11, 1961.)

The Effect on Thrust Minus Base Drag of Exchanging Base Area for Nozzle Expansion in Supersonic Nozzles at Transonic Mach Numbers, by Travis H. Slocumb Jr. and Earl H. Andrews Jr., *NASA Tech. Note D-754*, Apr. 1961, 30 pp.

Effect of a Hot-Jet Exhaust on Pressure Distributions and External Drag of Several Afterbodies on a Single-Engine Airplane Model at Transonic Speeds, by Harry T. Norton Jr. and John M. Swihart, *NACA Res. Mem.* L57J04, Mar. 1958, 58 pp. (Declassified by authority of NASA TPA no. 45, May 11, 1961.)

Measurement of Temperature Profiles in Laminar and Turbulent Axisymmetric Boundary Layers on a Cylinder With Non-uniform Wall Temperature, by E. R. G. Eckert, Roger Eichhorn and Thomas L. Eddy, *Air Force Res. Div., Aeron. Res. Lab., ARL Tech. Note 60-161*, Dec. 1960, 40 pp.

The Effects of Boundary-Layer Separation Over Bodies of Revolution With Conical Tail Flares, by David H. Dennis, *NACA Res. Mem.* A57130, Dec. 1957, 35 pp. (Declassified by authority of NASA TPA no. 45, May 11, 1961.)

Film Condensation With and Without Body Force in Boundary-Layer Flow of Vapor Over a Flat Plate, by Paul M. Chung, *NASA Tech. Note D-790*, April 1961, 35 pp.

Turbulent Skin Friction at High Mach Numbers and Reynolds Numbers in Air and Helium, by Fred W. Matting, Dean R. Chapman, Jack R. Nyholm and Andrew G. Thomas, *NASA Tech. Rep. T-82*, 1961, 39 pp.

The Theory of Differential Catalytic Probes for the Determination of Atom Concentrations in High Speed, Non-equilibrium Streams of Partially Dissociated Gases, by Daniel E. Rosner, *AeroChem Res. Labs., Inc. TP-19*, Oct. 1960, 37 pp. (AFOSR TN 18)

Notes on Magneto-Hydrodynamics—VIII, Non-Linear Wave Motion, by K. O. Friedrichs and H. Kranzer, *Atomic Energy Commission, NYO 6486*, Pt. VIII, July 1958, 61 pp.

Notes on Magneto-Hydrodynamics—Number I, General Fluid Equations, by Harold Grad, *Atomic Energy Commission, NYO 6486*, Pt. I, Aug. 1956, 18 pp.

Alignment Charts for Transport Properties, Viscosity, Thermal Conductivity, and Diffusion Coefficients for Nonpolar Gases and Gas Mixtures at Low Density, by Richard S. Brokaw, *NASA Tech. Rep. R-81*, 1961, 23 pp.

Axially Symmetric Laminar Free Mixing With Large Swirl, by Martin H. Steiger and Martin H. Bloom, *Brooklyn Polytech. Inst., Dept. Aerospace Engng. Applied Mech. Rep. 636*, Jan. 1961, 22 pp. (AFOSR 400)

Effects of Yaw on the Heat Transfer to a Blunt Cone-Cylinder Configuration at Mach Number of 1.98, by Roland D. English, *NASA Mem.* 10-8-58L, Nov. 1958, 20 pp. (Declassified by authority of NASA TPA no. 45, May 11, 1961.)

Measurements of Aerodynamic Heat

Transfer in Turbulent Separated Regions at a Mach Number of 1.8, by Benjamin J. Garland and James R. Hall, *NACA Res. Mem.* L57L09, Feb. 1958, 16 pp. (Declassified by authority of NASA TPA no. 45, May 11, 1961.)

Observation of Laminar Flow on an Air-Launched 15° Cone-Cylinder at Local Reynolds Numbers to 50×10^6 at Peak Mach Number of 6.75, by Leonard Rabb and Milan J. Krasnican, *NACA Res. Mem.* E56L03, March 1957, 33 pp. (Declassified by authority of NASA TPA no. 45, May 11, 1961.)

Preliminary Investigation of Lithium Hydride as a High-Temperature Internal Coolant, by Jerry L. Modissette, *NACA Res. Mem.* L57F12a, Oct. 1957, 10 pp. (Declassified by authority of NASA TPA no. 45, May 11, 1961.)

Heat-Transfer Characteristics of Blunt Two- and Three-Dimensional Bodies at Supersonic Speeds, by Glen Goodwin, *NACA Res. Mem.* A55L13a, Feb. 1956, 18 pp. (Declassified by authority of NASA TPA no. 45, May 11, 1961.)

A Theoretical Analysis of Effects of Ablation of Heat Transfer to an Arbitrary Axisymmetric Body, by Robert T. Swann and Jerry South, *NASA Tech. Note D-741*, April 1961, 49 pp.

Basic Studies in Heat Transfer and Fluid Flow, *Columbia Univ., Dept. Chem. Engng. Quar. Prog. Rep. IX-QPR-2-60*, April 1-June 30, 1960, 79 pp.

An Experimental Study of the Transient Vaporization of Liquid at a Solid Surface, by Robert C. Lummis, *Columbia Univ., Dept. Chem. Engng. Quar. Prog. Rep. IX-QPR-2-60*, April 1-June 30, 1960, 43 pp. (Appendix A)

An Experimental and Analytical Investigation of Flow Patterns in Forced-Circulation Boiling Flow, *Columbia Univ. Dept. Chem. Engng. Quar. Prog. Rep. IX-QPR-2-60*, April 1-June 30, 1960, 17 pp. (Appendix B)

Automatic Control of Laboratory Representation of Kinetic Heating, by J. Taylor Great Brit., *Aeron. Res. Council, Current Paper 532*, July 1960, 10 pp., 9 figs.

Effusion of Charged Particles From a Shock Heated Gas, by Bradford Sturtevant, *Calif. Inst. Tech., Guggenheim Aeron. Lab.*, 1960, 129 pp. (Thesis, Ph.D.)

Statistical Mechanics and Thermodynamics of Irreversible Processes Vol. 4 Electrodifussion, by W. Cauman and T. Bak, *Brussels, Free Univ., Tech. Rep. EOARDC PR 59-18*, 1959, 146 pp. (AFOSR TR 59-44D) (ASTIA AD 214,529)

Statistical Mechanics and Thermodynamics of Irreversible Processes, by L. Prigogine, M. Toda and S. Ono, *Brussels, Free Univ., Tech. Rep. EOARDC PR 59-18*, 1959, 41 pp. (AFOSR TR 59-44C) (ASTIA AD 214,528)

Collision-Free Plasmas, by Harry E. Petschek, *Avco-Everett Res. Lab. AMP 52 AFOSR 360*, Nov. 1960, 12 pp.

An Absolute Definition of Phase Shift in the Elastic Scattering of a Particle From Compound Systems, by Aaron Temkin, *NASA Tech. Note D-698*, April 1961, 14 pp.

Quarterly Bulletin of the Division of Mechanical Engineering and the National Aeronautical Establishment, *Canada, National Res. Council, Rep. DME/NAE 1961(1)*, Jan.1-March 31, 1961, 85 pp.

Heat Transfer Across Contact Surfaces, by E. H. Dudgeon, pp. 27-37, 32 refs.

Aeronautics and Astronautics, Proceedings (Durand Centennial Conference,

Stanford Univ., Aug. 5-8, 1959) Nicholas John Hoff and Walter Guido Vincenti, eds., Pergamon Press, N. Y., 1960, 460 pp. (AFOSR TR 59-108)

Similarity Solutions of Hydrodynamic Problems, by Geoffrey Taylor, pp. 21-28.

Recent Trends in the Mechanics of Highly Rarefied Gases, by G. N. Patterson, pp. 122-152, 42 refs.

A Study of Effusive Flow, by H. W. Liepmann, pp. 153-160.

A New Look at Transition, by Leslie S. G. Kovasznay, pp. 161-172.

Rapid Evaluation of Radiant Heating During Re-Entry Into the Atmosphere, by H. de L'Estoile and L. Rosenthal, pp. 173-206, 26 refs.

Magnetogasdynamic Problems From the Point of View of Particle Dynamics, by J. M. Bergers, pp. 288-304.

Plasma Dynamics, by Francis H. Clauser, pp. 305-343.

Some Heat Transfer Problems in Hypersonic Flow, by Antonio Ferri, pp. 344-377.

Ballistic Missile and Space Technology, vol. 1: Bioastronautics and Electronics and Invited Addresses (Symposium on Ballistic Missile and Space Technology, 5th, Los Angeles, Aug. 1960) Donald P. Le Galley, ed., Academic Press, N. Y., 1960, 494 pp.

The Expansion of a Gas Cloud Into a Vacuum, by W. G. Strang and I. Tarnove, pp. 471-494.

Ballistic Missile and Space Technology vol. II: Propulsion and Auxiliary Power Systems, (Symposium on Ballistic Missile and Space Technology, 5th, Los Angeles, Aug. 1960) Donald P. Le Galley, ed., Academic Press, N. Y. 1960, 441 pp.

Experimental Determination of a Solid Rocket Nozzle Heat Transfer Coefficient, by S. E. Colucci, pp. 303-343.

Thermoelectric Materials and Devices, Irving B. Cadoff and Edward Miller, eds., Reinhold Publishing Corp., N. Y., 1960, 344 pp.

Thermal Conductivity Mechanisms, by Wendell S. Williams, pp. 98-112.

The Measurement of Thermal Conductivity, by Defoe C. Ginnings, pp. 113-132.

Design Calculations for Peltier Cooling, by Robert H. Vought, pp. 250-274.

Experimental Cooling Devices, by R. L. Eichhorn, pp. 318-336.

Non-Crystalline Solids, (Conference on Non-Crystalline Solids, Alfred, N. Y., Sept. 3-8, 1958) V. D. Frechette, ed., John Wiley & Sons, 1960, N. Y. 536 pp.

The Use and Limitations of Irreversible Thermodynamics in the Study of Relaxation Processes, by R. O. Davies, pp. 232-251.

Outer Inviscid Hypersonic Flow With Attached Shock Waves, by Richard A. Scheuing, ARS JOURNAL, vol. 31, no. 4, April 1961, pp. 486-505, 49 refs.

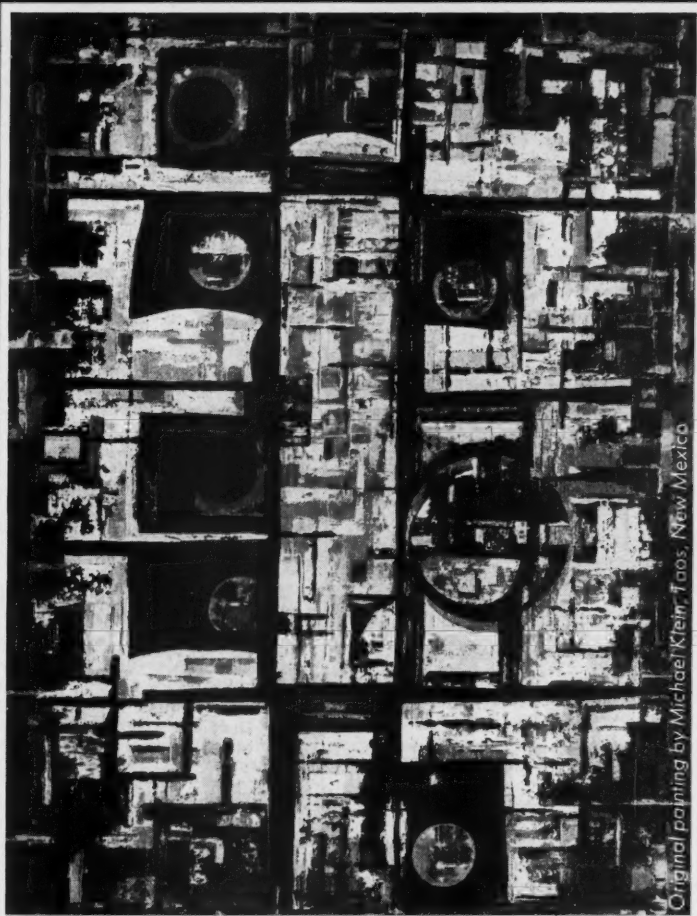
Application of the Mangler Transformation in Boundary Layer Flow, by S. deSoto and H. Wolf, ARS JOURNAL, vol. 31, no. 4, April 1961, pp. 553-555.

Similar Solutions of the Free Convection Boundary Layer Equations for an Electrically Conducting Fluid, by Barry L. Reeves, ARS JOURNAL, vol. 31, no. 4, April 1961, pp. 557-558.

Growth of Magnetohydrodynamic Boundary Layers, by J. C. Wu, ARS JOURNAL, vol. 31, no. 4, April 1961, pp. 562-564.

Mathemagical Machines ?

Maybe they are not really magical, but modern computers are marvelous aids to solving the complex problems arising from research. With the addition of an IBM 7090 and the super-computer STRETCH, Los Alamos Scientific Laboratory has become one of the most advanced electronic computer centers in the world. Such machines are required to perform in a reasonable time the billions of computations involved, for example, in the design of nuclear weapons and nuclear reactors, and, in problems of molecular biology and magnetohydrodynamics.



Original painting by Michael Klein, Taos, New Mexico

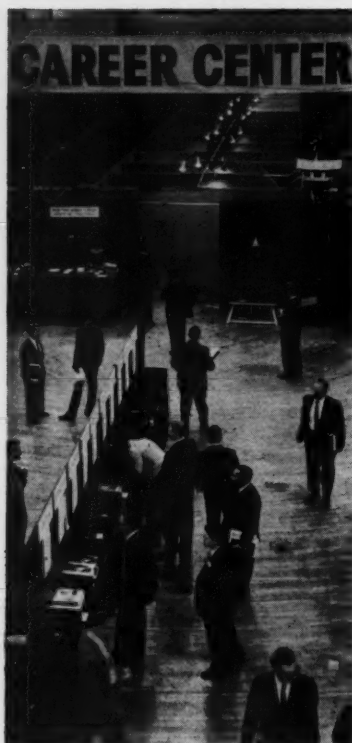
Qualified applicants are invited to send resumes to: Director of Personnel, Division 61-71

los alamos
scientific laboratory
OF THE UNIVERSITY OF CALIFORNIA
LOS ALAMOS, NEW MEXICO

All qualified applicants will receive consideration for employment without regard to race, creed, color, or national origin. U.S. citizenship required.

Employers Sponsor Career Center

Interview Engineers In
New York, October 10-13



LOCATION:

**HENRY HUDSON
HOTEL**

358 W. 58th St. (opp. Coliseum)

PHONE: Circle 6-5015

TIME: 10 A.M. to 9 P.M. daily

NOTE TO EMPLOYERS:

Employer participations are still available. Call Miss Dowlin at Careers Incorporated, PLaza 2-7733.

**CAREER
CENTER**

Career Centers are a service of Careers Incorporated, 770 Lexington Avenue, New York 21, N. Y.

All qualified applicants will receive consideration for employment without regard to race, creed, color or national origin.

Liquid Flow in Tubes, IV. The Transition Process and Turbulent Flow Related to Tube Diameter and Microscopic Surface Properties, by E. R. Lindgren, *Arkiv för Fysik*, vol. 18, no. 5, 1961, pp. 449-464.

Vertex Generated Waves Outside Metallic Wedges, by W. E. Williams, *Cambridge Philosophical Soc. Proc.*, vol. 57, part 2, April 1961, pp. 393-400.

Approach to Thermodynamic Equilibrium, by J. E. Mayer, *J. Chem. Phys.*, vol. 34, no. 4, April 1961, pp. 1207-1223.

Wall Temperature and Heat Flux Measurement in a Round Tube, by A. I. Morgan, Jr. and Robert A. Carlson, *J. Heat Transfer (ASME Trans., Series C)* vol. 83, no. 2, May 1961, pp. 105-110.

The Viscosity of Steam and Water at Moderate Pressure and Temperatures, by J. R. Moszynski, *J. Heat Transfer (ASME Trans., Series C)* vol. 83, no. 2, May 1961, pp. 111-121.

Thermal Conductivity and Prandtl Number of Carbon Dioxide and Carbon-Dioxide Air Mixtures at One Atmosphere, by Jerome L. Novotny and Thomas F. Irvine, Jr., *J. Heat Transfer (ASME Trans., Series C)* vol. 83, no. 2, May 1961, pp. 122-132.

The Influence of Sound on Free Convection From a Horizontal Cylinder, by R. M. Fand and J. Kaye, *J. Heat Transfer (ASME Trans., Series C)* vol. 83, no. 2, May 1961, pp. 133-148.

A Model for Correlating Two-Phase, Steam-Water, Burnout Heat-Transfer Fluxes, by H. S. Isbin, R. Vanderwater, H. Fauske and S. Singh, *J. Heat Transfer (ASME Trans., Series C)* vol. 83, no. 2, May 1961, pp. 149-157.

Burnout in Turbulent Flow-A Droplet Diffusion Model, by K. Goldmann, H. Firstenberg, and C. Lombardi, *J. Heat Transfer (ASME Trans., Series C)* vol. 83, no. 2, May 1961, pp. 158-162.

Heat Transfer by a Turbulent Flowing Fluid-Solids Mixture in a Pipe, by C. L. Tien, *J. Heat Transfer (ASME Trans., Series C)* vol. 83, no. 2, May 1961, pp. 183-188.

Heat Transfer and Pressure Drop in an Annular Gap With Surface Spoilers, by G. A. Kemeny and J. A. Cyphers, *J. Heat Transfer (ASME Trans., Series C)* vol. 83, no. 2, May 1961, pp. 189-198.

Radiation Heat Transfer in a Spherical Enclosure Containing a Participating Heat-Generating Gas, by E. M. Sparrow, C. M. Usiskin and H. A. Hubbard, *J. Heat Transfer (ASME Trans., Series C)* vol. 83, no. 2, May 1961, pp. 199-206.

Analysis, Results, and Interpretation for Radiation Between Some Simply-Arranged Gray Surfaces, by E. M. Sparrow, J. L. Gregg, J. V. Szel and P. Manos, *J. Heat Transfer (ASME Trans., Series C)* vol. 83, no. 2, May 1961, pp. 207-214.

Radiative Transport Within an Ablating Body, by Leo P. Kadanoff, *J. Heat Transfer (ASME Trans., Series C)* vol. 83, no. 2, May 1961, pp. 215-225.

Radiant Heat-Transfer Analysis of a Furnace or other Combustion Enclosure, by J. T. Bevens, *J. Heat Transfer (ASME Trans., Series C)* vol. 83, no. 2, May 1961, pp. 226-232.

Boundary-Layer Displacement and Leading-Edge Bluntness Effects in High-Temperature Hypersonic Flow, by H. K. Cheng, J. Gordon Hall, T. C. Golian, and A. Hertzberg, *J. Aerospace Sci.*, vol. 28, no. 5, May 1961, pp. 353-381, 410, 71 refs.

Statistical Thermodynamics of Plasmas, by H. S. Green, *Nuclear Fusion*, vol. 1, no. 2, 1961, pp. 69-77.

Fluctuations of Plasmas (I), by N. Rostoker, *Nuclear Fusion*, vol. 1, no. 2, 1961, pp. 101-120.

Vaporization Processes in the Hypersonic Laminar Boundary Layer, by Sinclair M. Scala and Guido L. Vidale, *International J. Heat & Mass Transfer*, vol. 1, no. 1, June 1960, pp. 4-22.

Experimental Methods Applied to the Determination of Some Temperature Radiation Parameters, by D. T. Kokorev, *International J. Heat & Mass Transfer*, vol. 1, no. 1, June 1960, pp. 23-27.

Thermal Radiation Between Parallel Plates Separated by an Absorbing-Emitting Nonisothermal Gas, by C. M. Usiskin and E. M. Sparrow, *International J. Heat & Mass Transfer*, vol. 1, no. 1, June 1960, pp. 28-36.

Highly Intensive Heat and Mass Transfer in Dispersed Media, by Y. Mikhailov, *International J. Heat & Mass Transfer*, vol. 1, no. 1, June 1960, pp. 37-45.

Turbulent Boundary Layer on a Flat Plate in a Stream of Dissociating Gas, by S. I. Kosterin and Yu. A. Koshmarov, *International J. Heat & Mass Transfer*, vol. 1, no. 1, June 1960, pp. 46-49.

A Non-Stationary Method of Measuring Heat Conduction From Fluids and Gases, by P. Grassmann and W. Straumann, *International J. Heat & Mass Transfer*, vol. 1, no. 1, June 1960, pp. 50-54. (In German)

Evaluation of Bulk Velocity and Temperature for Turbulent Flow in Tubes, by G. F. C. Rogers and Y. R. Mayhew, *International J. Heat & Mass Transfer*, vol. 1, no. 1, June 1960, pp. 55-67.

Heat Convection in the Laminar Regime in the Case of a Pressure Gradient and Any Wall Temperature, the Fluid Having Constant Physical Properties, by B. Le Fur, *International J. Heat & Mass Transfer*, vol. 1, no. 1, June 1960, pp. 68-80. (In French)

One-Dimensional Energy Transfer in Radiant Media, by Robert and Madeleine Goulard, *International J. Heat & Mass Transfer*, vol. 1, no. 1, June 1960, pp. 81-91.

Heat Transfer to Mercury in a Circular Tube and Annular Channels With Sinusoidal Heat Load Distribution, by V. I. Petrovichev, *International J. Heat & Mass Transfer*, vol. 1, no. 2-3, Aug. 1960, pp. 115-120.

A Mechanism of Turbulent Heat Transfer in Liquid Metals, by N. Z. Azer and B. T. Chao, *International J. Heat & Mass Transfer*, vol. 1, no. 2-3, Aug. 1960, pp. 121-138.

Thermal Contact Resistance Between Mercury and a Metal Surface, by T. Mizushima, S. Iuchi, T. Sasano and H. Tamura, *International J. Heat & Mass Transfer*, vol. 1, no. 2-3, Aug. 1960, pp. 139-146.

Local and Average Heat Transfer Coefficients at an Air Stream in a Tube With a Pointed Inlet, by V. K. Ermolin, *International J. Heat & Mass Transfer*, vol. 1, no. 2-3, Aug. 1960, pp. 147-151.

The Theory of Thermal Regular Regime and its Application to the Determination of Thermal Characteristics, by G. N. Dulnev, *International J. Heat & Mass Transfer*, vol. 1, no. 2-3, Aug. 1960, pp. 152-160.

Application of Variational Methods to the Thermal Entrance Region of Ducts, by E. M. Sparrow and R. Siegel, *International J. Heat & Mass Transfer*, vol. 1, no. 2-3, Aug. 1960, pp. 161-172.

Analysis of the Flow and Energy Separation in a Turbulent Vortex, by R. G. Deissler and M. Perlmutter, *International J. Heat & Mass Transfer*, vol. 1, no. 2-3, Aug. 1960, pp. 173-191.

A Standard Formulation of the Steady Convective Mass-Transfer Problem, by D. B. Spalding, *International J. Heat & Mass Transfer*, vol. 1, no. 2-3, Aug. 1960, pp. 192-207.

The Steady and Transient Free Convection Boundary Layer on a Uniformly Heated Vertical Plate, by R. G. Goldstein and E. R. G. Echeert, *International J. Heat & Mass Transfer*, vol. 1, no. 2-3, Aug. 1960, pp. 208-218.

On the Correlation of Nucleate Boiling Heat Transfer, by K. Nishikawa and K. Yamagata, *International J. Heat & Mass Transfer*, vol. 1, no. 2-3, Aug. 1960, pp. 219-235.

On the Investigation of Heat Transfer in the Presence of Chemical Conversions, by S. I. Anisimov and T. L. Percelman, *International J. Heat & Mass Transfer*, vol. 1, no. 4, Jan. 1961, pp. 269-272.

The Experimental Investigation of Heat and Mass Transfer in the Presence of Chemical Conversions, by A. V. Ralko, *International J. Heat & Mass Transfer*, vol. 1, no. 4, Jan. 1961, pp. 273-279.

Mixing and Chemical Reaction in an Initially Non-Uniform Temperature Field, by S. I. Cheng and H. H. Chiu, *International J. Heat & Mass Transfer*, vol. 1, no. 4, Jan. 1961, pp. 280-293.

Convection Heat Transfer Coefficients for Turbulent Flow Between Parallel Plates with Unequal Heat Fluxes, by Henry Barrow, *International J. Heat & Mass Transfer*, vol. 1, no. 4, Jan. 1961, pp. 306-311.

Decay of Temperature Fluctuations in Homogeneous Turbulence Before the Final Period, by A. L. Loeffler, Jr. and R. G. Deissler, *International J. Heat & Mass Transfer*, vol. 1, no. 4, Jan. 1961, pp. 312-324.

An Analysis of Laminar Film Boiling with Variable Properties, by P. W. McFadden and R. J. Grosh, *International J. Heat & Mass Transfer*, vol. 1, no. 4, Jan. 1961, pp. 325-335.

Heat Transfer Bibliography, by E. R. G. Eckert, J. P. Hartnett and E. M. Sparrow, *International J. Heat & Mass Transfer*, vol. 1, no. 4, Jan. 1961, pp. 336-345.

Flow of Condensing Vapour With Temporary Supersaturated State Due to Heat-Removal Effect, by Keishiro Niu, *Phys. Soc. Japan, J.*, vol. 16, no. 4, April 1961, pp. 798-804.

On Cylindrical Magnetohydrodynamic Shock Waves, by Carl Greifinger and Julian D. Cole, *Phys. of Fluids*, vol. 4, no. 5, May 1961, pp. 527-534.

Viscosity of Dissociated Gases From Shock - Tube Heat - Transfer Measurements, by R. A. Hartunian and P. V. Marrone, *Phys. of Fluids*, vol. 4, no. 5, May 1961, pp. 535-543.

Viscous Magnetohydrodynamic Boundary Layer, by A. Sherman, *Phys. of Fluids*, vol. 4, no. 5, May 1961, pp. 552-557.

Magnetically Insulated Shock Tube, by Richard G. Fowler and Eugene B. Turner, *Phys. of Fluids*, vol. 4, no. 5, May 1961, pp. 544-551.

Mechanically Insulated Shock Tube, by Richard G. Fowler and Eugene B. Turner, *Phys. of Fluids*, vol. 4, no. 5, May 1961, pp. 544-551.

Experimental Heat Transfer Characteristics of a Liquid in Couette Motion and With Taylor Vortices, by F. C. Haas and A. H. Nissan, *Royal Soc., London*

Proc. vol. A 261, no. 1305, April 1961, pp. 215-226.

Dispersion of Gases in Laminar Flow Through a Circular Tube, by A. Bournia, J. Coulland and G. Houghton, *Royal Soc. London Proc.* vol. A 261, no. 1305, April 1961, pp. 227-236.

Fluctuation Thermodynamics of Non-equilibrium Processes, by R. L. Stratovich, *Soviet Phys. JETP*, vol. 12, no. 6, June 1961, pp. 1150-1164.

Thermodynamics of Turbulent Systems, by V. G. Nevzglyadow, *Soviet Phys. JETP*, vol. 12, no. 6, June 1961, pp. 1206-1209.

The Influence of Turbulence on the Transfer of Heat to Cylinders Near the Stagnation Point, by J. Kestin, P. F. Meader and H. H. Sogin, *Zeitschrift Angewandte Math. Phys.*, vol. 12, no. 2, March 25, 1961, pp. 115-131.

On the Dynamics of Turbulent Vortical Flow, by A. Reynolds, *Zeitschrift Angewandte Math. Phys.*, vol. 12, no. 2, March 25, 1961, pp. 149-158.

On the Quasi-One-Dimensional Steady Flow of a Compressible Conducting Gas in a Pipe of Constant Cross-Section in the Presence of Transverse Magnetic and Electric Fields, by I. B. Chekmarev, *Appl. Math. Mech. (PMM)*, vol. 24, no. 3, 1960, pp. 801-803.

The Automodelling (Similarity) Case of Hypersonic Flow Past a Body of a Viscous Heat-Conducting Gas, by V. V. Lunev, *Appl. Math. Mech. (PMM)*, vol. 24, no. 3, 1960, pp. 804-809.

On the Problem of the Excitation of Standing Waves by a Wave Generator in a Channel of Finite Length, by V. S. Cherkasov, *Appl. Math. Mech. (PMM)*, vol. 24, no. 3, 1960, pp. 810-815.

Determining Electron Density and Distribution in Plasmas, by H. L. Bunn, *Electronics*, vol. 34, no. 14, April 7, 1961, pp. 71-75.

Rate of a Transfer Unit-A New Correlating Factor for Heat and Mass Transfer, by E. H. Lebel Jr., *I/EC; Ind. Engng. Chem.*, vol. 53, no. 5, May 1961, pp. 349-356.

Thermal Conductivity of Two-Phase Materials, by G. T.-N. Tsao, *I/EC; Ind. Engng. Chem.*, vol. 53, no. 5, May 1961, pp. 395-397.

A Study of the Magnetohydrodynamic Boundary Layer on a Flat Plate, by M. B. Glauert, *J. Fluid Mech.*, vol. 10, part 2, March 1961, pp. 276-288.

Effect of a Magnetic Field Upon the Stability of Free Boundary Layers Between Two Uniform Streams, by Kanefusa Gotoh, *Physical Soc. Japan, J.*, vol. 16, no. 3, March 1961, pp. 559-564.

Density Field for Rarefied Flow Through an Orifice, by Weston M. Howard, *Phys. of Fluids*, vol. 4, no. 4, April 1961, pp. 521-529.

Surface and Solid Phase Reactions at High Temperatures, by John L. Margrave, *Planetary and Space Sci.*, vol. 3, Feb. 1961, pp. 3.

The Boltzmann Equation for Flows With Chemical Reactions, by J. M. Burgers, *Planetary and Space Sci.*, vol. 3, Feb. 1961, pp. 4-11.

Systematic Trends in Vaporization and Thermodynamic Properties of Oxides, by R. J. Ackermann, R. J. Thorn and G. H. Winslow, *Planetary and Space Sci.*, vol. 3, Feb. 1961, pp. 12-23.

Rate of Vaporization of Refractory Substances, by R. F. Walker, J. Efimenko and N. L. Lofgren, *Planetary and Space Sci.*, vol. 3, Feb. 1961, pp. 24-30.

NOW AVAILABLE

High Speed Aerodynamics And Jet Propulsion: Volume VIII

HIGH SPEED PROBLEMS OF AIRCRAFT AND EXPERIMENTAL METHODS

Edited by A. F. Donovan, H. R. Lawrence, F. E. Goddard, and R. R. Gilruth. Topics include methods of performance calculation at high speed; stability and control; aerelasticity and flutter; principles of model testing; design considerations, wind tunnel measurements, objectives of free flight research, instrumented models in free flight, piloted aircraft testing and free flight range methods. 994 pages. \$22.50.

At all booksellers



Princeton University Press
Princeton, New Jersey

An Investigation of the Effects of Gaseous Diffusion on the Rate of Oxidation of a Metal Forming a Volatile Oxide, by D. R. Schryer and J. L. Modisette, *Planetary and Space Sci.*, vol. 3, Feb. 1961, pp. 31-37.

Nitrogen Atom Recombination on Surfaces, by F. M. Prok, *Planetary and Space Sci.*, vol. 3, Feb. 1961, pp. 38-45.

A Study of the Interaction Between Carbon and Dissociated Gases, by W. Zinman, *Planetary and Space Sci.*, vol. 3, Feb. 1961, pp. 46-52.

A Non-Catalytic Surface for Dissociated Combustion Gases, by J. C. Cutting, J. A. Fay, W. T. Hogan and W. C. Moffat, *Planetary and Space Sci.*, vol. 3, Feb. 1961, pp. 53-60.

Heterogeneous Flash Pyrolysis of Hydrocarbon Polymers, by L. S. Nelson and N. A. Kuebler, *Planetary and Space Sci.*, vol. 3, Feb. 1961, pp. 61-67.

Behavior of Plastic Laminates at Elevated Temperatures, by S. Ruby, J. B. Cohen and F. K. Ward, *Planetary and Space Sci.*, vol. 3, Feb. 1961, pp. 68-72.

Behavior of "Teflon" Fluorocarbon Resins at Elevated Temperatures, by P. H. Settlege and J. C. Siegle, *Planetary and Space Sci.*, vol. 3, Feb. 1961, pp. 73-84.

Summary of Discussion of the Pyrolysis of Plastics in Ablation, by R. Simha, *Planetary and Space Sci.*, vol. 3, Feb. 1961, p. 82.

The Ablation of Thermosetting Plastics, by P. J. Friel, *Planetary and Space Sci.*, vol. 3, Feb. 1961, pp. 83-84.

Introduction-Gas Phase Reactions and Kinetics, by S. S. Penner, *Planetary and Space Sci.*, vol. 3, Feb. 1961, p. 85.

Comparative Studies of Vibrational Relaxation in Nitric Oxide, by R. Monson, J. J. Allport and F. Robben, *Planetary and Space Sci.*, vol. 3, Feb. 1961, pp. 86-93.

The Influence of Periodic Pressure Variations on Chain Reactions, by H. M. Wight, *Planetary and Space Sci.*, vol. 3, Feb. 1961, pp. 94-98.

Shock Layer Electron Densities Considering the Effects of both Chemical Reactions and Flow Field Variation, by M. H. Bortner, *Planetary and Space Sci.*, vol. 3, Feb. 1961, pp. 99-103.

Measurements of Electron Attachment, Recombination, Elastic and Inelastic Collision in Atmospheric Gases, by M. A. Bionde, *Planetary and Space Sci.*, vol. 3, Feb. 1961, pp. 104-112.

Thermodynamic Relaxation of Atmospheric Gases in Shock Waves, by B. Steverding and L. Uerner, *Planetary and Space Sci.*, vol. 3, Feb. 1961, pp. 113-117.

A Survey of Methods for the Chemical Analysis of Transient Species, with Microsecond Resolution, by S. Bauer, N. Rol and J. Kiefer, *Planetary and Space Sci.*, vol. 3, Feb. 1961, pp. 118-131.

Radiation From the Nonequilibrium Region of Normal Shocks in Oxygen, Nitrogen and Air, by B. Kivel, P. Hammerling and J. D. Teare, *Planetary and Space Sci.*, vol. 3, Feb. 1961, pp. 132-138.

Spectroscopic Measurement of the Temperature of Shock-Heated Oxygen, by W. Wurster, *Planetary and Space Sci.*, vol. 3, Feb. 1961, pp. 158-161.

Thermodynamic and Transport Properties of Gases, by Charles Curtiss, *Planetary and Space Sci.*, vol. 3, Feb. 1961, pp. 204.

The Present Status of Intermolecular Potentials for Calculations of Transport Properties, by R. A. Buckingham, *Planetary and Space Sci.*, vol. 3, Feb. 1961, pp. 205-216.

Intermolecular Potentials for Ionic Systems, by A. Dalgarno, *Planetary and Space Sci.*, vol. 3, Feb. 1961, pp. 217-220.

High Temperature Gaseous Diffusion Experiments and Intermolecular Potential Energy Functions, by R. E. Walker, L. Monochick, A. A. Westenberg and S. Favin, *Planetary and Space Sci.*, vol. 3, Feb. 1961, pp. 221-227.

An Experimental Approach to the De-

termination of Gaseous Transport Properties at Very High Temperatures, by I. Amdur, *Planetary and Space Sci.*, vol. 3, Feb. 1961, pp. 228-235.

Transport Properties of Atomic Hydrogen, by A. Dalgarno, *Planetary and Space Sci.*, vol. 3, Feb. 1961, pp. 236-237.

Energy Transport in High Temperature and Reacting Gases, by R. S. Brokaw, *Planetary and Space Sci.*, vol. 3, Feb. 1961, pp. 238-252.

Molecular Interactions at High Temperatures, by C. E. Treanor and G. T. Skinner, *Planetary and Space Sci.*, vol. 3, Feb. 1961, pp. 253-256.

Thermodynamic Effects of Coulombic Interactions in Ionized Gases, by H. Myers, J. H. Buss and S. W. Benson, *Planetary and Space Sci.*, vol. 3, Feb. 1961, pp. 257-270.

The Thermodynamic and Electrical Properties of Mercury Vapor at Pressures Below Atmospheric and High Temperatures, by A. Sherman and F. Martinek, *Planetary and Space Sci.*, vol. 3, Feb. 1961, pp. 271-282.

A Class of Exact Solutions of the Magnetohydrodynamic Navier-Stokes Equations, by Ching-Sheng Wu, *Quar. J. Mech. and Appl. Math.*, vol. 14, part 1, Feb. 1961, pp. 1-19.

The Final Stage of Decay of a Localized Disturbance in a Conducting Fluid in a Uniform Magnetic Field, by P. G. Saffman, *Quar. J. Mech. and Appl. Math.*, vol. 14, part 1, Feb. 1961, pp. 20-28.

On Certain Functions Arising in the Linearized Theory of the Supersonic Jet, by H. Portnoy, *Quar. J. Mech. and Appl. Math.*, vol. 14, part 1, Feb. 1961, pp. 29-35.

Method for Measuring Time-Average Concentration in a Turbulent Wake of Electrolyte, by Robert E. Sparks and H. E. Hoelscher, *Rev. Sci. Instr.* vol. 32, no. 4, April 1961, pp. 417-420.

Shock Waves in Magnetohydrodynamics, by R. V. Polovin, *Soviet Phys: Uspekhi*, vol. 3, no. 5, March-April 1961, pp. 677-688.

Flight Mechanics

Theory of the Secular Variations in the Orbit of a Satellite of an Oblate Planet, by William A. Mersman, *NASA Tech. Rep. R-99*, 1961, 77 pp.

Ballistic Missile and Space Technology, vol. 4. Reentry and Vehicle Design,

Donald P. LeGalley, ed., Symposium on Ballistic Missile and Space Technology, Los Angeles, Aug. 1960, Academic Press, N. Y., 1960, 422 pp.

Trajectories of Lifting Bodies Entering Planetary Atmospheres at Shallow Angles, by E. Bendor, C. Kottler and A. R. Krenkel, pp. 89-112.

Anomalies of the Geomagnetic Retardation of the Spin of Satellite Vanguard I (1958 Beta), by P. R. Arendt, *ARS JOURNAL*, vol. 31, no. 3, March 1961, pp. 286-289.

Eddy Current Torque Compensation in a Spin Stabilized Earth Satellite, by L. H. Grasshoff, *ARS JOURNAL*, vol. 31, no. 3, March 1961, pp. 290-293.

Characteristic Velocity Requirements for Impulsive Thrust Transfers Between Non Co-Planar Circular Orbits, by L. Rider, *ARS JOURNAL*, vol. 31, no. 3, March 1961, pp. 345-351.

Probability of Satellite Interception by an Air Launched Preguided Missile, by Edgar M. Jacobs, George W. Morgenthauer and Robert A. Sebastian, *ARS JOURNAL*, vol. 31, no. 3, March 1961, pp. 352-355.

Effect of Geometrical Libration on the Damped Motion of an Earth Satellite, by L. N. Rowell and M. C. Smith, *ARS JOURNAL*, vol. 31, no. 3, March 1961, pp. 361-363.

Variables That are Determinate for any Orbit, by Robert R. Newton, *ARS JOURNAL*, vol. 31, no. 3, March 1961, pp. 364-366.

Minimum Time Ballistic Interplanetary Trajectory, by Vernon A. Lee and Dwight E. Florence, *ARS JOURNAL*, vol. 31, no. 3, March 1961, pp. 435-436.

Approximate Velocity, Position and Time Relationship for Ballistic Re-Entry, by B. P. Miller, *ARS JOURNAL*, vol. 31, no. 3, March 1961, pp. 437-438.

Graphical Method for Prediction of Time in Sunlight for a Circular Orbit, by G. B. Patterson, *ARS JOURNAL*, vol. 31, no. 3, March 1961, pp. 441-442.

Aerodynamic Influences on Satellite Librations, by D. M. Schrello *ARS JOURNAL*, vol. 31, no. 3, March 1961, pp. 442-444.

Divergence From Equilibrium Glide Path at Supersatellite Velocities, by Raymond North and Jason L. Speyer, *ARS JOURNAL*, vol. 31, no. 3, March 1961, pp. 448-450.

The Geometry of the Orbits of Artificial Satellites, by R. A. Struble, *Archive Rational Mech. Analysis*, vol. 7, no. 2, Feb. 1961, pp. 87-104.

Estimating the Mean Square Deviation From a Given Trajectory, by E. A. Barbashin, *Automation and Remote Control*, vol. 21, no. 7, July 1960, pp. 661-667.

Vehicle Design, Testing and Performance

Measured Response to Wind-Induced Dynamic Loads of a Full-Scale Scout Vehicle Mounted Vertically on a Launching Tower, by George W. Jones Jr. and Jean Gilman Jr., *NASA Tech. Note D-757*, April 1961, 28 pp.

The Characteristics of a Two-Dimensional Supersonic Sail, by E. A. Boyd, *Cranfield, College of Aeron., CoA Rep.* 143, Dec. 1960, 5 pp.

An Analysis of Ablation-Shield Requirements for Manned Reentry Vehicles, by Leonard Roberts, *NASA Tech. Rep. R-62*, 1960, 25 pp.

CHANGE-OF-ADDRESS NOTICE

In the event of a change of address, it is necessary to include both your old and new addresses, as well as your membership number and coding, when notifying ARS headquarters, in order to insure prompt service. If you are moving or have moved, send the following form to Membership Dept., American Rocket Society, 500 Fifth Ave., New York 36, N. Y.:

Name _____

Membership Card No. _____ Coding _____

Old Address _____

New Address _____

